KOVINE ZLITINE TEHNOLOGIJE

METALS ALLOYS TECHNOLOGIES

LETO 1996 / 6

Glavni urednik / Editor: F. Vodopivec, IMT Ljubljana, Slovenija
Gostujoči urednik / Guest Editor: M. Jenko, IMT Ljubljana, Slovenija

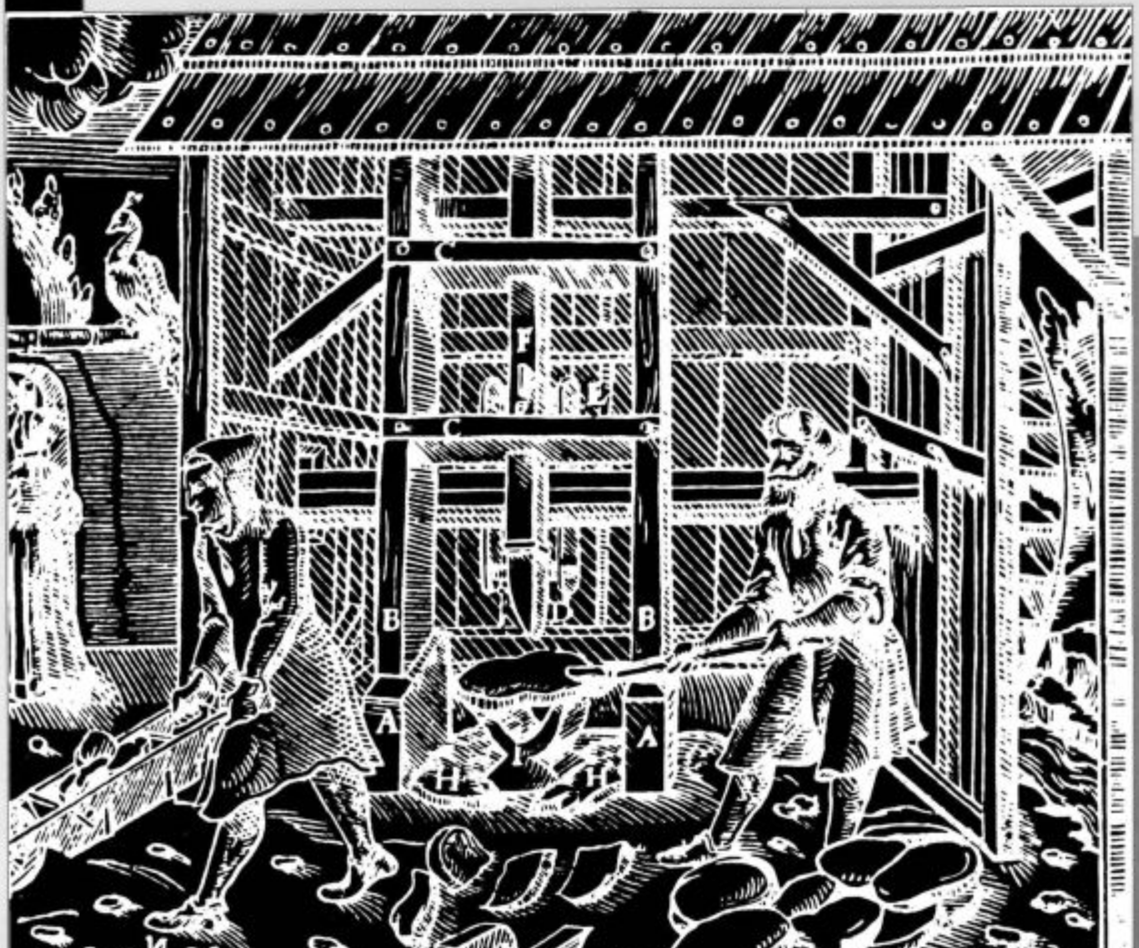

Izdajatelji / Publishers: Inštitut za kovinske materiale in tehnologije Ljubljana, ACRONI Jesenice, Institut Jožef Stefan, IMPOL Slovenska Bistrica, Kemijski inštitut Ljubljana, Koncern Slovenske železarne, Metal Ravne, Talum Kidričevo

KOVINE ZLITINE TEHNOLOGIJE	LETNIK 30 VOLUME	ŠTEV. 6 NO.	STR. 477-579 P.	LJUBLJANA SLOVENIJA	NOV.-DEC. 1996

ISSN 1318-0010

Navodilo avtorjem

Prosimo avtorje, da pri pripravi rokopisa za objavo članka dosledno upoštevajo naslednja navodila:
- Članek mora biti izvirno delo, ki ni bilo v dani obliki še nikjer objavljeno. Deli članka so lahko že bili podani kot referat.
- Avtor naj odda članek oz. besedilo napisano na računalnik z urejevalniki besedil:
- WORDSTAR, verzija 4, 5, 6, 7 za DOS
- WORD za DOS ali WINDOWS.

Če avtor besedila ne more dostaviti v prej naštetih oblikah, naj pošlje besedilo urejeno v ASCII formatu.
Prosimo avtorje, da pošljejo disketo z oznako datoteke in računalniškim izpisom te datoteke na papirju. Formule so lahko v datoteki samo naznačene, na izpisu pa ročno izpisane.

Celoten rokopis članka obsega:
- naslov članka (v slovenskem in angleškem jeziku),
- podatke o avtorju,
- povzetek (v slovenskem in angleškem jeziku),
- ključne besede (v slovenskem in angleškem jeziku),
- besedilo članka,
- preglednice, tabele,
- slike (risbe ali fotografije),
- podpise k slikam (v slovenskem in angleškem jeziku),
- pregled literature.

Članek naj bi bil čim krajši in naj ne bi presegal 5–7 tiskanih strani, pregledni članek 12 strani, prispevek s posvetovanj pa 3–5 tiskanih strani.

Obvezna je raba merskih enot, ki jih določa zakon o merskih enotah in merilih, tj. enot mednarodnega sistema SI.

Enačbe se označujejo ob desni strani besedila s tekočo številko v okroglih oklepajih.

Preglednice (tabele) je treba napisati na posebnih listih in ne med besedilom.
V preglednicah naj se – kjer je le mogoče – ne uporabljajo izpisana imena veličin, ampak ustrezni simboli.

Slike (risbe ali fotografije) morajo biti priložene posebej in ne vstavljene (ali nalepljene) med besedilom. Risbe naj bodo izdelane praviloma povečane v merilu 2:1.
Za vse slike po fotografskih posnetkih je potrebno priložiti izvirne fotografije, ki so ostre, kontrastne in primerno velike.

Vsi podpisi k slikam (v slovenskem in angleškem jeziku) naj bodo zbrani na posebnem listu in ne med besedilom.

V pregledu literature naj bo vsak vir oštevilčen s tekočo številko v oglatih oklepajih (ki jih uporabljamo tudi med besedilom, kadar se želimo sklicevati na določeni literarni vir).

Vsak vir mora biti opremljen s podatki, ki omogočajo bralcu, da ga lahko poišče:
knjige: – avtor, naslov knjige, ime založbe in kraj ter leto izdaje (po potrebi tudi določene strani):
H. Ibach and H. Luth, Solid State Physics, Springer, Berlin 1991, p. 245
članki: – avtor, naslov članka, ime revije in kraj izhajanja, letnik, leto, številka ter strani:
H. J. Grabke, Kovine zlitine tehnologije, 27, 1993 , 1–2, 9

Avtorji naj rokopisu članka priložijo povzetek v omejenem obsegu do 10 vrstic v slovenskem in angleškem jeziku.

Rokopisu morajo biti dodani tudi podatki o avtorju:
- ime in priimek, akademski naslov in poklic, ime delovne organizacije v kateri dela, naslov stanovanja, telefonska številka, E-mail in številka fax-a.

Uredništvo KZT
- odloča o sprejemu članka za objavo,
- poskrbi za strokovne ocene in morebitne predloge za krajšanje ali izpopolnitev,
- poskrbi za jezikovne korekture.

Rokopisi člankov ostanejo v arhivu uredništva Kovine zlitine tehnologije.

Instructions to Authors

Authors are kindly requested to prepare the manuscripts according to the following instructions:
- The paper must be original, unpublished and properly prepared for printing.
- Manuscripts should be typed with double spacing and wide margins on numbered pages and should be submitted on floppy disk in form of:
- WORDSTAR, version 4, 5, 6, 7 for DOS,
- WORD for DOS or WINDOWS,
- ASCII text without formulae, in which case formulae should be clearly written by hand in the printed copy.

Preparation of Manuscript:
- the paper title (in English and Slovenian Language)*
- author(s) name(s) and affiliation(s)
- the text of the Abstract (in English and Slovenian Language)*
- key words (in English and Slovenian Language)*
- the text of the paper (in English and Slovenian Language)*
- tables (in English Language)
- figures (drawings or photographs)
- captions to figures (in English and Slovenian Language)*
- captions to tables (in English)
- acknowledgement
- references

* The Editorial Board will provide for the translation in Slovenian Language for foreign authors.

The length of published papers should not exceed 5–7 journal pages, of review papers 12 journal pages and of contributed papers 3–5 journal pages.

The international system units (SI) should be used.
Equations should be numbered sequentially on the right-hand side in round brackets.

Tables should be typed on separate sheets at the end of manuscript. They should have a descriptive caption explaining displayed data.

Figures (drawings or photographs) should be numbered and their captions listed together at the end of the manuscript. The drawings for the line figures should be twice the size than in the print. Figures have to be original, sharp and well contrasted, enclosed separately to the text.

References must be typed in a separate reference section at the end of the manuscript, with items refereed too in the text by numerals in square brackets.

References must be presented as follows:
- books: author(s), title, the publisher, location, year, page numbers
  H. Ibach and H. Luth, Solid State Physics, Springer, Berlin 1991, p. 245
- articles: author(s), a journal name, volume, a year, issue number, page
  H. J. Grabke, Kovine zlitine thenologije, 27, 1993 , 1–2, 9

The abstract (both in English and in Slovenian Language) should not exceed 200 words.

The title page should contain each author(s) full names, affiliation with full address, E-mail number, telephone and fax number if available.

The Editor
- will decide if the paper is accepted for publication,
- will take care of the refereeing process,
- language corrections.

The manuscripts of papers accepted for publication are not returned.

KOVINE ZLITINE TEHNOLOGIJE

METALS ALLOYS TECHNOLOGIES

KOVINE ZLITINE TEHNOLOGIJE

Izdajatelj (Published for):
Inštitut za kovinske materiale in tehnologije Ljubljana
Soizdajatelji (Associated Publishers):
SŽ ŽJ ACRONI Jesenice, IMPOL Slovenska Bistrica, Institut Jožef Stefan, Kemijski inštitut Ljubljana, Koncern Slovenske Železarne, Metal Ravne, Talum Kidričevo

Izdajanje **KOVINE ZLITINE TEHNOLOGIJE** sofinancira: Ministrstvo za znanost in tehnologijo Republike Slovenije
(Journal **METALS ALLOYS TECHNOLOGIES** is financially supported by Ministrstvo za znanost in tehnologijo, Republika Slovenija)

Glavni in odgovorni urednik (Editor-in-chief):
prof. Franc Vodopivec, Inštitut za kovinske materiale in tehnologije Ljubljana, 1000 Ljubljana, Lepi pot 11, Slovenija

Urednik (Editor):
mag. Aleš Lagoja

Tehnični urednik (Technical Editor):
Jana Jamar

Lektorji (Linguistic Advisers):
dr. Jože Gasperič in Jana Jamar (slovenski jezik), prof. dr. Andrej Paulin (angleški jezik)

Članki objavljeni v periodični publikaciji KOVINE ZLITINE TEHNOLOGIJE so indeksirani v mednarodnih sekundarnih virih:
(Articles published in journal are indexed in international secondary periodicals and databases):
- METALS ABSTRACTS
- ENGINEERED MATERIALS ABSTRACTS
- BUSINESS ALERT ABSTRACTS (STEELS, NONFERROUS, POLYMERS, CERAMICS, COMPOSITES)
- CHEMICAL ABSTRACTS
- ALUMINIUM INDUSTRY ABSTRACTS
- REFERATIVNYJ ŽURNAL: METALLURGIJA

Naslov uredništva (Editorial Address):
KOVINE ZLITINE TEHNOLOGIJE
IMT Ljubljana
Lepi pot 11
1000 Ljubljana, Slovenija
Telefon: +386 61 125 11 61
Telefax: +386 61 213 780
Žiro račun: 50101-603-50316 IMT pri Agenciji Ljubljana

Na INTERNET-u je revija KOVINE ZLITINE TEHNOLOGIJE dosegljiva na naslovu: http : // www. ctk. si /kovine/
(INTERNET LINK: http://www.ctk.si/kovine/)

Elektronska pošta (E-mail):
cobissimtlj @ ctklj.ctk.si

Oblikovanje ovitka: Ignac Kofol
Tisk (Print): Tiskarna PLANPRINT, Ljubljana

Po mnenju Ministrastva za znanost in tehnologijo Republike Slovenije št. 23-335-92 z dne 09. 06. 1992 šteje KOVINE ZLITINE TEHNOLOGIJE med proizvode, za katere se plačuje 5-odstotni davek od prometa proizvodov.

Laudation in honour of Professor Dr. Franc Vodopivec on the occasion of his 65th birthday

Professor Dr. Franc Vodopivec, scientific councillor, former director of Institute of Metals and Technology and member of the State Council of Republic Slovenia is celebrating his 65th birthday. This birthday is the occasion to look at the background and the development of this well known scientist and at the influence which his research work has in the field of elaboration, transformation and use of metals and alloys in Slovenia and abroad.

F. Vodopivec was born in Rakitnik, a small village in the former Italy on 8th October 1931. After finishing with distinction the secondary school education, he studied Metallurgy at the University of Ljubljana. In 1956 he passed the final examinations and second degree thesis as the first of his class. During the university study he was for three years assistant-student for lectures of Mechanics and Kinematics. In 1956 he joined Metallurgical Institute, present Institute of Metals and Technology in Ljubljana directed by the founder Professor Ciril Rekar. After the military service 1958/59 he received through the International Agency of Atomic Energy in Vienna a scholarship from the French Government. Working in the Institute de Recherché de la Siderurgie, in St.Germain en Laye, France, from 1960 to 1962 he prepared his Dr.-thesis and graduated in 1962 at the University of Paris, France with the thesis: *Study of the behaviour of arsenic and phosphorous by selective oxidation of iron alloys with low contents of both elements.*

He returned in 1962 to the Metallurgical Institute and worked as founder and head of the Laboratory for Metalography to 1972, head of Technology Department to 1978, assistant director to 1990 and director from 1990 to April 1996 when he retired. In 1992, Professor Vodopivec was elected in the Council State of Republic Slovenia by the community of researchers and engineers.

He is the editor-in-chief of Slovenian scientific journal *Metals Alloys Technologies* since 1994.

Professor Vodopivec is full of development spirit and creative ideas. He has been doing research work on the behaviour of metals in oxidative atmosphere, microstructure characterization of metals by optical and electron microscopy, electron probe analysis, mechanical testing; behaviour of material in use at medium and high temperature, hot and cold working of metals, recovery, recrystallization and grain growth. His present research interest includes: ductile permanent magnet alloys, non oriented electrical steel sheets, grain growth induced by selective surface segregation, topology of microstructure and behaviour of metals in use.

Professor Vodopivec has published over 150 papers in international journals and conferences and 240 papers in Slovenian journals and conferences on topics of science, technology and use of metals and alloys.

Professor Vodopivec has been supervisor to several Ph.D. and Master Degree students at the Universities of Ljubljana, Maribor, Belgrade and Zagreb. He is also very active in the international academic field. He was a chairman of international scientific conferences and project evaluator in EU COST actions.

He is the president of Slovenian Society of Materials, member of executive council of Slovenian Vacuum Society, member of Slovenian Electron and Microelectronics Society, Slovenian Society of Chemistry, Historical Society of Ljubljana, chairman of the R&D group of the Slovenian Association of Engineers, chairman of annual Conferences on Materials and Technologies from 1990 to present, and member of Vacuum Metallurgy scientific division of IUVSTA - International Union for Vacuum Science, Technique and Applications. He wrote in Slovenian newspaper several tens of articles of industrial and research policy. In 1978 he was awarded by the Boris Kidrič Foundation Award and in 1984 the Boris Kidrič State Award for Science.

His many projects were supported by 21 industrial societies and associations in Slovenia and the former Yugoslavia from Metallurgy, over mechanical industry to power stations as well as the Slovenian and the Yugoslav governments. He was involved also in the projects of international cooperations EU RD actions and USA- Slovenia projects.

He prepared forensic analysis of several industrial failures which qualified Slovenian societies to win arbitration for retributions of damages from foreign companies suppliers of industrial equipment.

His colleagues hope very much that he will instead of the retirement, take part in discussions, lectures and publications. Most of all we would like to wish him and his family many years to come in good health.

Monika Jenko

Vsebina - Contents

ZNANSTVENI PRISPEVKI - SCIENTIFIC PAPERS

Kovinski materiali - Metallic Materials

Kovine, zlitine, tehnologije/30/1996/6/483-495

Surface and Grain Boundary Segregation of Antimony and Tin - Effects on Steel Properties

Segregacija antimona in kositra na površini in po mejah zrn - vpliv na lastnosti jekel

H. J. Grabke[1], Max-Planck-Institut, Düsseldorf, Germany

Dedicated to Prof. Dr. F. Vodopivec on the occasion of his 65th birthday.
Prof. dr. Francu Vodopivcu za njegov 65. rojstni dan.

Prejem rokopisa - received: 1996-10-01; sprejem za objavo - accepted for publication: 1996-11-04

The tramp elements Sb and Sn have a strong tendency to surface segregation on iron. By LEED and AES surface structures and concentrations of Sb and Sn segregated on single crystal were determined. The surface segregation is strongly dependent on orientation, therefore recrystallization of steel sheet is affected since the surface energies of different grains are reduced to different extent - this effect may be used to obtain advantageous textures of electrical steel sheet and deep drawing steels. Surface segregation of Sb and Sn retards surface reaction kinetics as was shown for the gas carburization of case hardening steels. Surface segregation of tin in creep cavities of turbine steels was shown to accelerate the creep fracture. The grain boundary segregation of both elements in iron is minor, and furthermore Sb and Sn are displaced from grain boundaries by carbon so that most steels are not endangered by grain boundary embrittlement due to Sb and Sn, but some low alloy turbine steels are susceptible to temper and long-term embrittlement.

Key words: surface and grain boundary segregation Fe-Sb alloys, Fe-Sn alloys, Fe-Sb-C alloys, Fe-Sn-C alloys, intergranular fracture embrittlement

Elementa v sledeh Sb in Sn močno segregirata na površini železa. Površinska struktura in koncentracija Sb in Sn v segregirani plasti sta bili določeni z metodami LEED in AES. Površinska segregacija je odvisna od kristalografske orientacije, rekristalizacija jeklenih pločevin je aktivirana, ker imajo posamezna kristalna zrna različno znižano površinsko energijo - pojav se lahko uporabi za pridobivanje prednostnih tekstur elektro pločevin in pločevin za globoki vlek. Površinska segregacija Sb in Sn zavira kinetiko površinske reakcije kar je prikazano pri procesu naogljičevanja jekel. Površinska segregacija kositra v vdolbinah pri lezenju jekel za turbine povzroča pospešenje lezenja do preloma. Segregacija obeh elementov po mejah kristalnih zrn je v železu minimalna zato ker Sb in Sn na mejah zrn izpodrine ogljik. Tako večina jekel ni ogroženih zaradi krhkosti kristalnih mej, ki bi jih povzročala Sb in Sn, le nekatera nizka ogljična turbinska jekla so občutljiva na popuščno krhkost.

Ključne besede: površinska segregacija, segregacija po mejah zrn, Fe-Sb zlitine, Fe-Sn zlitine, Fe-Sb-C, Fe-Sn-C, interkristalna krhkost

1 Introduction

1.1 The role of tramp elements in steels

The effects of the so-called tramp elements in steels, Ni, Cu, P, S, Pb, As, Sb, Sn etc. are generally deleterious, the greatest problems they cause are 'hot shortness' and 'temper embrittlement' of steels. The hot shortness, a lack of hot workability can have different reasons, one possible reason is the copper enrichment due to surface scaling[1,2]. Beneath the scale the more noble elements Cu, As, Sb, Sn are enriched and form a liquid phase which causes surface cracking by grain boundary penetration. Sb and Sn greatly reduce the solubility of Cu in austenite and hence lead to precipitation of a molten phase and its grain boundary penetration, under conditions of much less enrichment and down to lower temperatures. The enrichment of tramp elements below the oxide scale upon reheating or hot rolling of steels and could be detected by electron microprobe (EPMA). This enrichment also can have strong effects on the scale adherence and morphology as has been studied extensively by F. Vodopivec et al. in work started at the IRSID[3-11]: by the presence of the more noble elements Cu, Ni, Sb, Ag, S the scale adherence is enhanced whereas the elements Si, Al, P and B which are oxidized and form silicate, aluminate, phosphate or borate layers cause formation of voids and cavities at the scale/metal interface.

The other way of enrichment which leads to deleterious effects of tramp elements is equilibrium segregation, so the 'temper embrittlement' is caused by segregation of P, Sn or Sb in the temperature range 400 - 700°C to the steel grain boundaries, e.g. during slow cooling after tempering, but also during application of steels in this temperature range. It was suspected since long that temper embrittlement is caused by grain boundary segregation, but this suspect could be confirmed only after the arrival and spreading of interfacial analysis by Auger-electron spectroscopy (AES) in the eighties. But the tramp elements do not have only deleterious effects, e.g. it is known that Cu can enhance the resistance against atmospheric corrosion. Even positive effects of Sb and Sn were detected and studied at the IMT Ljubljana and the MPI für Eisenforschung Düsseldorf[12-20], these tramp elements can improve the texture and magnetic proper-

---

[1] Prof.Dr.Sc. Hans Jürgen GRABKE
Max-Planck-Institut für Eisenforschung GmbH
Postfach 140444, 40074 Düsseldorf, Germany

ties of nonoriented silicon steel sheets, caused by surface segregation and its effect on surface energies as discussed in the following chapter.

1.2 Fundamentals of surface and grain boundary segregation

In this review the *equilibrium segregation* of Sb and Sn will be described and only the effects will be discussed which are caused by equilibrium surface and grain boundary segregation. Most elements which are dissolved in iron tend to enrich at elevated temperatures at surfaces, grain boundaries and interfaces[21-25], and distribution equilibria are established at sufficiently high temperature.

$$\text{A (dissolved)} \leftrightarrow \text{A (segregated)} \qquad (1)$$

There are different driving forces for such equilibrium segregation:

1. free bonds at the surface or interface can be saturated by interaction with the atoms A

2. the iron surface may be covered with a layer of atoms A which has a lower surface energy than the initial iron surface

3. the release of atoms A from the bulk solution leads to release of elastic energy, especially in the case of in-

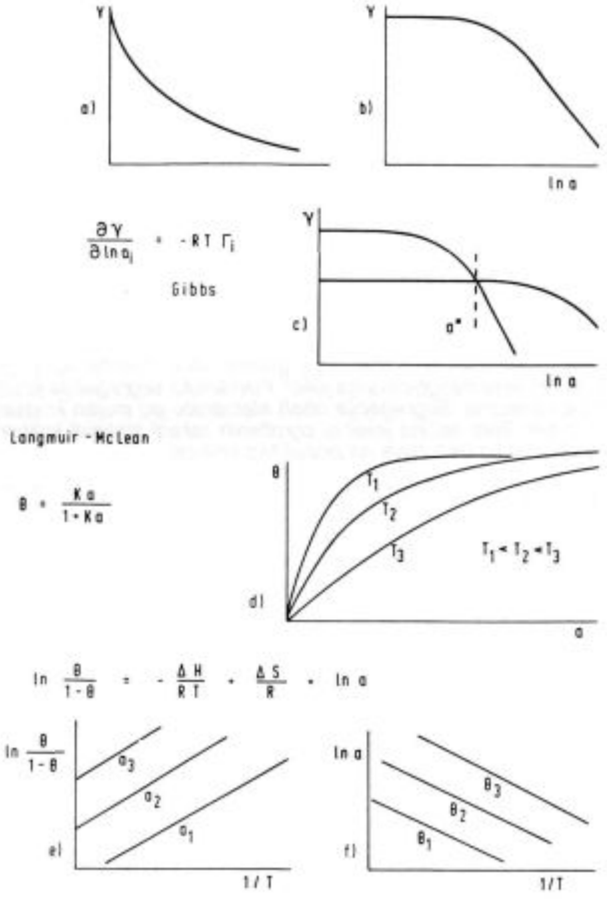

Figure 1: Schematic diagrams on the Gibbs isotherm (a-c) and the Langmuir-McLean isotherm (d-f)
a) surface energy γ vs activity a of the adsorbed or segregated element A,
b) γ vs ln a and
c) the latter plot for two orientations with different surface energies and different adsorption or segregation behaviour - upon increasing activity a and coverage Θ the surface firstly instable becomes stable, a reason for tertiary recrystallization or facetting,
d) degree of coverage Θ vs activity of the absorbed or segregated element A,
e) plot for the evaluation of studies at constant activity or concentration of the element A,
f) isosteres for determination of the thermodynamic data at constant coverage

Slika 1: Shematski diagrami Gibbsove izoterme (a-c) in Langmuir-McLeanove izoterme (d-f)
a) površinska energija γ v odvisnosti od aktivnosti a adsorbiranega ali segregiranega elementa A, **b)** γ v odvisnosti od ln a in
c) zadnji grafikon za dve orientaciji z različnimi površinskimi energijami in različno adsorbcijo oziroma segregacijo - po zvišanju aktivnosti a in pokritja Θ je sprva nestabilna površina postala stabilna, vzrok za terciarno rekristalizacijo ali facetiranje,
d) stopnja pokritja Θ v odvisnosti od adsorbiranega ali segregiranega elementa A,
e) grafični prikaz za ovrednotenje študij pri konstantni aktivnosti ali koncentraciji elementa A,
f) izostere za določitev termodinamičnih podatkov pri konstantnem številu atomov A

terstitial atoms or substitutional atoms larger than the iron atoms.

The latter effect is certainly true for Sb and Sn since both elements have large atoms, causing a strain in the iron lattice and increase of lattice parameter[26]. In fact, all equilibrium segregation processes should lead to a decrease in surface energy (or interfacial energy) according to Gibbs' law

$$\frac{d\gamma}{d \ln a_A} = -RT\,\Gamma_A \qquad (2)$$

where γ is the surface energy, a_A the thermodynamic activity of the segregating species A and Γ_A the surface concentration (mol/cm^2), R gas constant, T temperature (K) (**Figure 1a-c**). The effect of adsorption or segregation on surface energy can be measured by the so-called zero creep method[27] but only at very high temperatures. One example of the result for a measurement on Fe-Sn foils with different Sn concentrations at 1420°C[28,29] is given in **Figure 2a**. Combining such a study with measuring 'grain boundary grooving', i.e. the dihedral angle of the thermally etched grain boundary grooves at the surface gave the ratio of the grain boundary to surface energies and thus the dependence of grain boundary energy was derived as a function of the bulk tin content (**Figure 2b**). From these 'Gibbs isotherms' also the isotherms for surface resp. grain boundary segregation could be derived[27-29]. However, these techniques were time consuming, difficult and tedious and since the arrival and spreading of AES they are no more used.

In many cases, segregation can be described by a simple equation, the Langmuir-McLean isotherm (**Figure 1d-f**), describing segregation to a limited number of sites which leads to a maximum coverage Γ_A^{sat} when all sites are occupied, and with a free energy ΔG_A which is independent of coverage.

Then the degree of coverage

$$\Theta = \Gamma_A/\Gamma_A^{sat} \qquad (3)$$

is given by

$$\Theta_A/(1-\Theta_A) = x_A \exp(-\Delta G_A/RT) \qquad (4)$$

Since

$$\Delta G_A = \Delta H_A - T\,\Delta S_A \qquad (5)$$

this leads to the form of the Langmuir-McLean equation

$$\ln\frac{\Theta_A}{1-\Theta_A} = -\frac{\Delta H_A}{RT} + \frac{\Delta S_A}{R} + \ln x_A \qquad (6)$$

which is used to derive the enthalpy and entropy of segregation from measurements of Θ_A at a constant bulk concentration x_A of the segregating species in dependence on temperature. Such measurements have been conducted, e.g. for the surface segregation of C, Si, N, P and S on iron and also for the grain boundary segregation of P, Sb and Sn (see **Figure 6 and 8**). The surface analyses were conducted by AES, observing the concentrations in situ on single or polycrystalline surfaces in dependence on temperature[30-40].

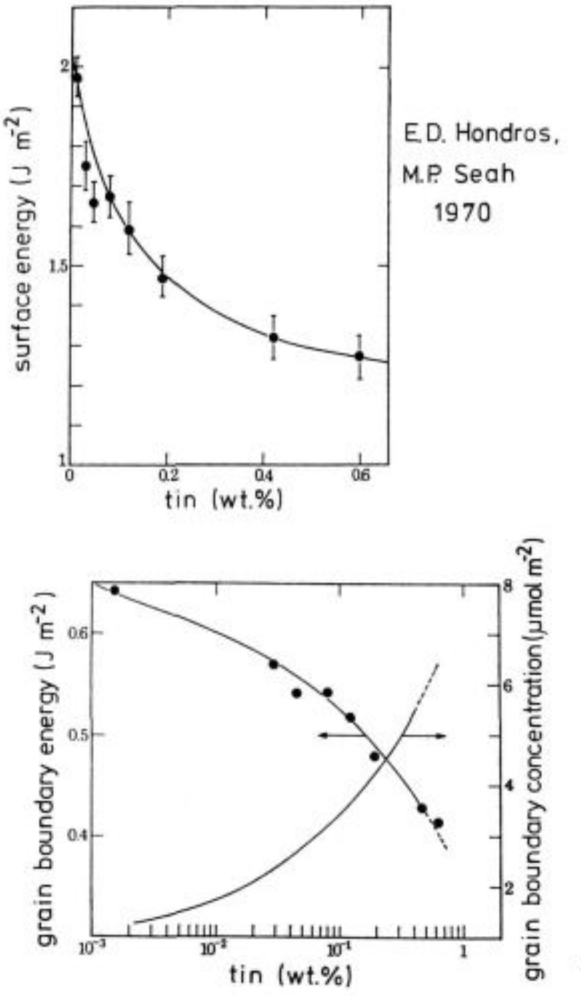

Figure 2: **a)** Surface energy and **b)** grain boundary energy of iron-tin alloys at 1420°C plotted as a function of the bulk tin content[28,29] in (b) also the grain boundary segregation isotherm is given, which can be derived from the measurements

Slika 2: **a)** površinska energija in **b)** energija kristalnih mej zlitine železo-kositer pri 1420°C kot funkcija vsebnosti kositra v osnovni zlitini[28,29] (b) podana je tudi izoterma segregacije po mejah zrn, ki jo lahko izračunamo iz meritev

The grain boundary analyses are also performed by AES, but after annealing the specimens for sufficient time at elevated temperature, then introducing them into the UHV system and fracturing in-situ by impact or tensile test[35,36,39,40]. The analysis of intergranular fracture facets yields the grain boundary concentration, assuming that the content of impurity A has been distributed equally to both sides upon fracture.

The sites and structures attained in surface segregation can be elucidated using LEED (=low energy electron diffraction). In most cases the elements A are enriched on Fe(100) up to half a monolayer, corresponding to a c(2x2) structure, only for oxygen a complete monolayer and p(1x1) structure is attained. At grain boundaries rather high coverages are possible, for P in ferrite coverages nearly up to one monolayer have been observed. The observation of the LEED structures on single crystal surfaces gives a good possibility for calibrating the AES measurements, also at grain boundaries, since the coverage for the saturated LEED structures in known.

Further information on segregated species can be obtained using photoelectron spectroscopy (XPS), the photolines obtained can indicate the ionization state of ions and the charge transfer between substrate and segregated atom[41-45]. Generally, there is a transfer of negative charge (electrons) to the segregated atoms, which means that these (C, N, S, O, P etc.) are present as negatively charged atoms (anions) on the metal surface. This most probably is also the case in the grain boundary segregation, and it is supposed that such charge transfer weakens the cohesion of grain boundaries[46,47] - leading to temper embrittlement of steels.

In the case that two elements are segregating simultaneously to a surface or a grain boundary, there is generally a competition for the sites available and the relative amount of both species in the surface depends on their free energy of segregation and concentrations in the bulk. Cases of competitive segregation have been studied on the iron surface for carbon and silicon[38], and at grain boundaries: carbon-phosphorus[36], carbon-sulfur[48], nitrogen-phosphorus[37]... The simple formalism for competitive segregation without further energetic interaction of the segregating species is given by

$$\Theta_A / (1-\Theta_A-\Theta_B) = x_A \cdot \exp(-\Delta G_A / RT) \qquad (7)$$

$$\Theta_B / (1-\Theta_A-\Theta_B) = x_B \cdot \exp(-\Delta G_B / RT) \qquad (8)$$

which could be applied in the cases mentioned above. In the literature on temper embrittlement there is a lot of fuss about 'cosegregation', the mutually enhanced segregation of two species where attractive energetic interaction is to be assumed. In some cases the enhanced segregation can be explained in a different way - in other cases which are important here (Ni-Sn, Ni-Sb) formation of two- or three-dimensional phases at the grain boundaries may be suspected (see below, chapters 2.2 and 3.4).

1.3 Systems Fe-Sn and Fe-Sb

The solid solutions of Sn in α-Fe were determined by lattice parameter measurements[49,50]. Accordingly, the solubility ranges from a maximum at 9,2 at% (17,7 wt%) at 900°C to 3,2 at% (6,56 wt%) at 600°C. The solubility limit in γ-Fe has been determined[24,26] the γ-loop extends to 0,92 at% (1,93 wt%). Own investigations on Fe-0,054 wt% Sn and Fe-0,080 wt% Sn [unpublished], however, showed precipitation of Sn-rich particles on the grain boundaries after long-term annealing at 550°C; accordingly, there are uncertainties on the solubility at temperatures <600°C.

The solubility of Sb in α-Fe has been determined by several authors, the results are in substantial agreement[49]. The solubility at 900°C is 4,19 at% Sb (8,71 wt%) decreasing at 600°C to 2,58 at% (5,46 wt%). The γ-loop extends till 1,1 at% Sb (2,36 wt%).

Experimental and theoretical studies have been conducted on the effects of other alloying elements on the antimony solubility, they were found to be the largest for M = Ti, Mn and Ni and small for M = Cr, Co. The presence of Ni e.g. reduces the solubility strongly, the phase precipitating is a hexagonal NiAs type: $Fe_{96}Sb_2Ni_2$. A cubic $CaFe_2$ type $Fe_{97}Sb_2Ti$ is formed with Ti, which reduces the solubility at 900°C to 1,91 at%[52]. Strong interaction of Ni and Sb is also observed in surface segregation[53].

2 Interfacial segregation of Sn and Sb on and in iron and steels

2.1 Surface segregation of Sn and Sb on iron

The surface segregation of tin on Fe-Sn single crystals has been studied in the temperature range 450°C to 650°C, mainly on crystals with relatively high Sn concentrations so that always saturation coverages were observed, no dependence of coverage on temperature, so that the segregation enthalpy was not obtained[54,55]. Each of the low index orientations exhibits a characteristic behaviour of the segregating Sn, the coverages attained are governed by segregation kinetics (**Figure 3a**). After heating the specimen for a short time a c(2x2) structure is observed, corresponding to half a monolayer coverage. But the segregation continues which leads to an order-disorder transition and a coverage somewhat higher than a monolayer (corresponding to $1{,}4 \cdot 10^{15}$ atoms Sn/cm²). The transition is accompanied by a shift of the photolines observed by XPS to values closely corresponding to the values characteristic for pure elemental tin, **Figure 3b**. Most probably the transition can be explained by formation of a two-dimensional nearly close packed layer of tin on Fe(100) with a high surface mobility. This segregation behaviour is different from the segregation in most systems Fe-A (A = C, N, S, P, Sb...) which always leads to a saturation at a surface coverage of 0,5. The driving force for the segregation of tin to higher coverages is probably the strong decrease of surface energy by the presence of a layer of tin. This layer at high coverage has properties similar to a layer of pure molten tin on iron, as indicated by the results of the XPS measurements. The segregation behaviour on Fe-Sn(111) is similar, there is an inflection point in the kinetics when the p(1x1) structure with one monolayer coverage is reached, which corresponds to $7 \cdot 10^{14}$ atoms Sn/cm² on Fe(111). After this surface structure is reached, further Sn segregation occurs, an order-disorder transition is observed and a Sn monolayer is attained. The segregation behaviour is different on Fe-Sn(110), here no intermediate adsorption structures were observed, but only structures with high Sn content, firstly a hexagonal structure corresponding to one monolayer of grey tin. Upon fur-

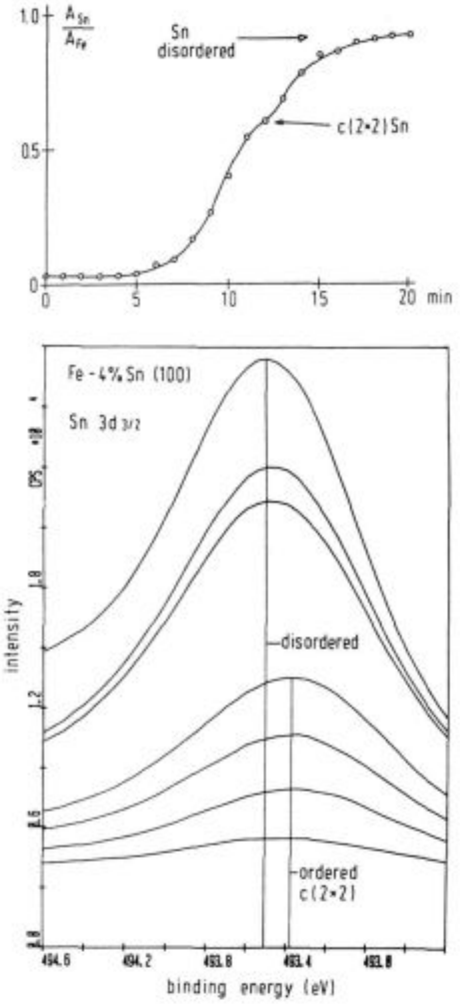

Figure 3: **a)** Kinetics of the tin surface segregation on Fe-4 wt% Sn(100) during heating to 650°C[54], at the inflection point indicated the structural phase transition from the ordered monolayer c(2x2)Sn to the disordered multilayer occurs; **b)** photolines observed during increasing surface concentration demonstrating the shift caused by the transition

Slika 3: **a)** Kinetika površinske segregacije na zlitini Fe-4 ut.% Sn(100) med žarjenjem do 650°C[54], prevoj označuje strukturni fazni prehod iz urejene monoplasti c(2x2)Sn v neurejeno večplastnost; **b)** fotolinije med naraščanjem površinske koncentracije prikazujejo kemijski premik, nastal zaradi prehoda

ther segregation a structure is formed which corresponds to a layer of the intermetallic compound FeSn of one unit cell thickness, **Figure 4a**.

The segregation behaviour of Sb on Fe-4 wt% Sb[55,56] is similar on the orientations (100) and (111) to the behaviour of tin, on both orientations on ordered adsorption structure is formed, c(2x2) on (100), see **Figure 5**, and p(1x1) on (111) but upon continued segregation no elevated Sb surface concentration were observed, in contrast to Sn. On Fe(110) the presence of Sb caused faceting, the LEED patterns indicated formation of (111) and (111) planes, **Figure 4b**. Accordingly, the segregation enthalpy of Sb to Fe(111) must be very exothermic (negative), due to a strong decrease of the surface energy of Fe(111) which compensates the increase of total surface area by the faceting.

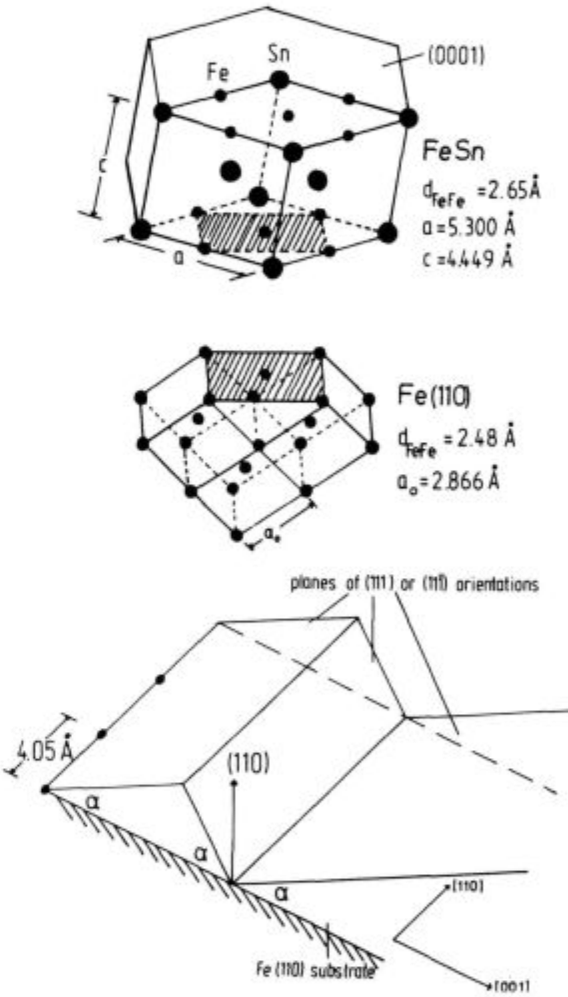

Figure 4: Phenomena on the Fe(110) face caused by segregation of Sn or Sb;

a) *Supposed structure of the surface compound 'FeSn' formed by* epitaxial stabilization on Fe-Sn(110) as the final saturation structure[54];

b) Faceting on Fe-Sb(110) under formation of (111) faces due to Sb segregation[56]

Slika 4: Pojav na Fe(110) ploskvi, ki ga je povzročila segregacija Sn ali Sb;

a) predpostavljena struktura zlitine na površini 'FeSn', ki je nastala z epitaksialno stabilizacijo na Fe-Sn(110) kot končna nasičena struktura[54];

b) facetiranje na površini monokristala Fe-Sb(110), zaradi segregacije Sb se tvorita (111) in (111) ploskvi

Three possibilities are demonstrated in the systems Fe-Sn and Fe-Sb for the behaviour upon segregation, (i) formation of adsorption structures such as c(2x2) or p(1x1), (ii) formation of surface phases such as two-dimensional grey tin and two-dimensional FeSn, or (iii) formation of facets to attain surface energies.

2.2 Grain boundary segregation of Sn and Sb

A fundamental study on grain boundary segregation in Fe-Sn alloys has been conducted after annealing in the temperature range 500-750°C for up to 5000 h[39]. The results of the grain boundary analyses show a wide scatter

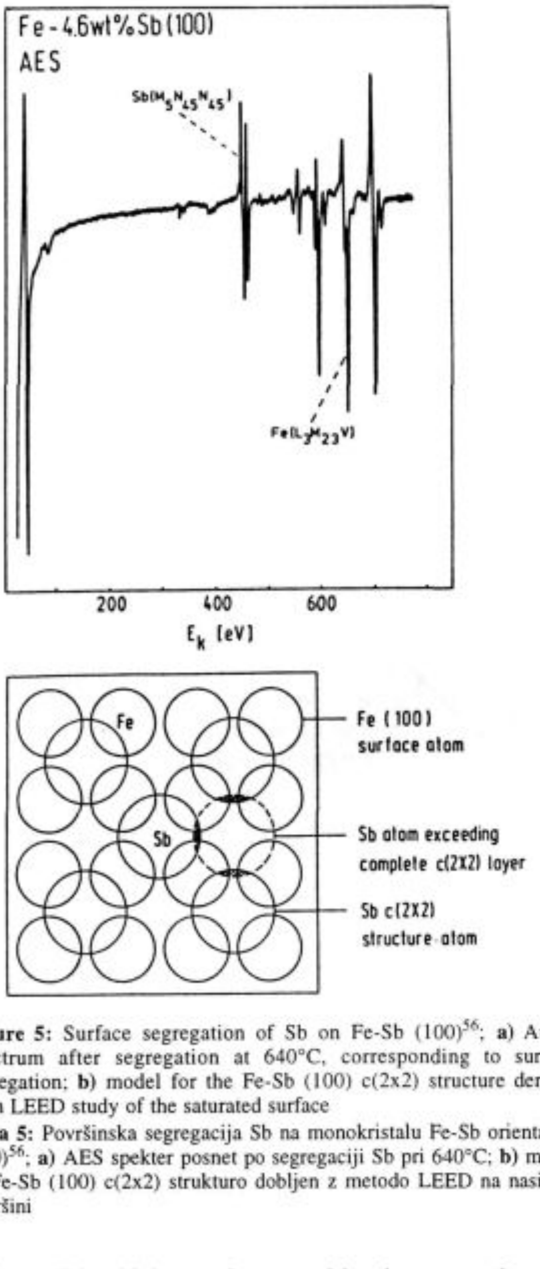

Figure 5: Surface segregation of Sb on Fe-Sb (100)[56]; **a)** Auger spectrum after segregation at 640°C, corresponding to surface segregation; **b)** model for the Fe-Sb (100) c(2x2) structure derived from LEED study of the saturated surface

Slika 5: Površinska segregacija Sb na monokristalu Fe-Sb orientacije (100)[56]; **a)** AES spekter posnet po segregaciji Sb pri 640°C; **b)** model za Fe-Sb (100) c(2x2) strukturo dobljen z metodo LEED na nasičeni površini

(Figure 6a) which may be caused by the strong dependence of tin segregation on grain boundary orientation. All data have been obtained for Sn concentrations within the α-solid solution range, no precipitates of intermetallic compounds should have formed. The tin concentrations are always below a monolayer, in contrast to the surface segregation behaviour. In spite of the large scatter the data were evaluated according to the Langmuir-McLean equation **(Figure 6b)**, yielding the values for segregation enthalpy and entropy

$$\Delta H = -22{,}5 \text{ kJ/mol} \qquad \Delta S = 26 \text{ J/mol K}$$

for 550°C results in good agreement with previous results of E. D. Hondros and M. P. Seah[28,29].

The enthalpy value is relatively low (P: ΔH = -34,3 kJ/mol[35,36]), this indicates the rather low tendency for grain boundary segregation of Sn! Furthermore, due to its low segregation enthalpy Sn is kept from the grain boundaries effectively by the presence of carbon such as in plain carbon steels **(Figure 7)**. As described in the introduction, an equilibrium of site competition between Sn and C occurs according to

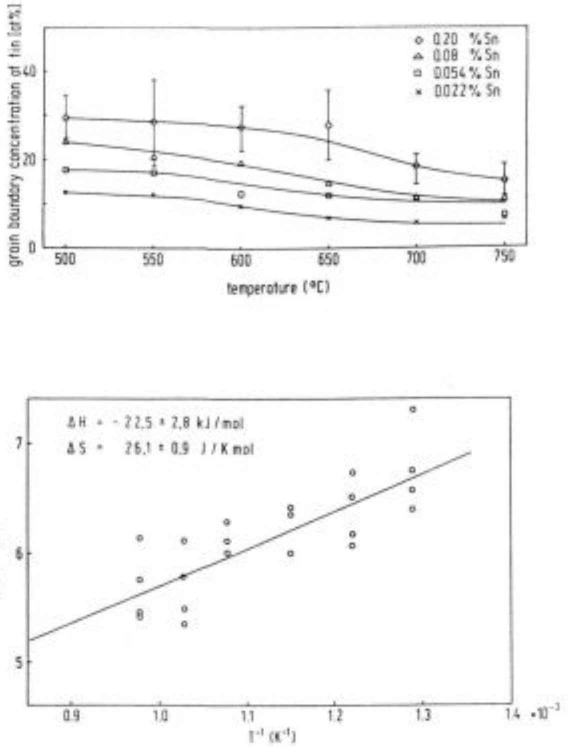

Figure 6: a) Grain boundary concentrations of tin in Fe-Sn alloys after annealing at elevated temperatures, measured by AES on intergranular fracture faces[39]; **b)** evaluation of the measurements in (a) applying the Langmuir-McLean equation (6)

Slika 6: a) Koncentracija kositra v segregirani plasti na mejah zrn po žarjenju pri povišanih temperaturah, merjeno z metodo AES na interkristalnih prelomnih ploskvah[39]; **b)** ovrednotenje meritev (a) z uporabo Langmuir-McLean enačbe (6)

$$\begin{aligned} &\text{C(dissolved)} + \text{Sn(segregated)} \\ &\qquad = \text{C(segregated)} + \text{Sn(dissolved)} \end{aligned}$$

In the presence of some ppm dissolved carbon, the tin is effectively removed from the grain boundaries.

However, in low alloy steels the concentration of dissolved C is reduced due to the formation of less soluble carbides with Cr and Mn. Tin segregation is possible if not Sn is displaced from the grain boundaries by segregated phosphorus. For rotor steels, CrMoV steels it is even dangerous to have too low phosphorus contents, since in application at high temperature if Sn segregation prevails, this easily leads to formation of creep cavities, due to the strong tendency for surface segregation of tin. The surface segregation of Sn decreases the surface energy of pores and cavities, stabilizes such defects and accelerates their growth (see chapter 3.2).

In must be kept in mind that the data given above are average values and have an integral character, since the grain boundary segregation of tin in iron is strongly de-

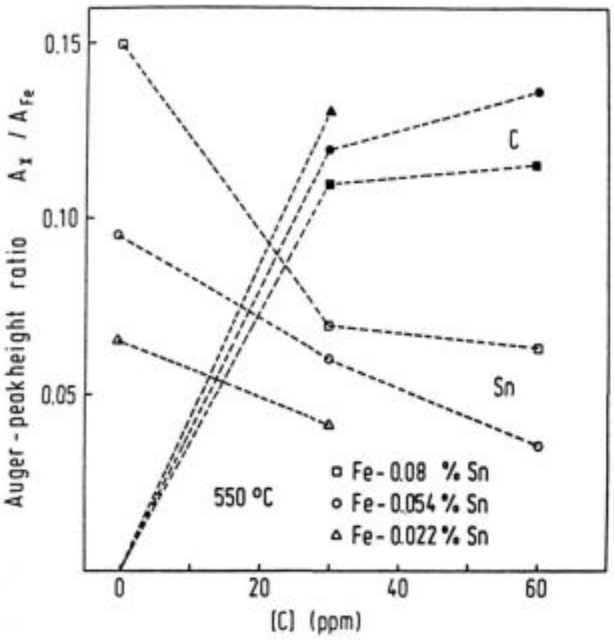

Figure 7: Grain boundary segregation of Sn and C in Fe-Sn-C alloys in dependence on the bulk carbon concentration after equilibration at 550°C, demonstrating the displacing effect of carbon on segregated Sn[39]

Slika 7: Segregacija Sn in C po mejah zrn v Fe-Sn-C zlitinah v odvisnossti od koncentracije ogljika v osnovnem materialu pri ravnotežju pri 550°C

pendent on the misorientation, increasing with the tilt angle of misorientation between the grains[57]. Sn causes grain boundary hardening, excess hardness extending to many microns on either side of the grain boundary, also increasing with the misorientation. This is a well documented effect but not well understood[57,58].

For temper embrittled Ni-Cr steels there are strong indications that Sn is present at the grain boundaries coupled with Ni in an bidimensional phase corresponding to an intermetallic compound such as Ni_3Sn_2, this has been concluded from Mössbauer spectroscopy and TEM work[59-61].

The grain boundary segregation of Sb was investigated for Fe-Sb and Fe-Sb-C alloys after equilibration at temperatures between 550°C for sufficient time[62,63]. The analysis of intergranular fracture faces by AES calibrated on the base of the surface segregation studies shows relatively low interfacial concentrations, see **Figure 8**, and a wide scatter of results. The plot of the data according to the Langmuir-McLean equation leads to the values for segregation enthalpy and entropy:

$$\Delta H = -19 \text{ kJ/mol} \qquad \Delta S = 28 \text{ J/mol K}$$

Thus, the segregation enthalpy is even lower than for Sn, which emphasizes the low tendency for grain boundary segregation of Sb. However, even small grain boundary concentrations of Sb cause marked grain boundary embrittlement and prevailing intergranular fracture. Also the segregant Sb is effectively displaced from grain boundaries by carbon, small concentrations of dissolved carbon < 60 wtppm can shift the displacement equilibrium to low Sb segregation and also lead to a marked reduction of intergranular fracture, see **Figure 9**[64]. Carbon not only removes Sb from the grain boundaries, but also enhances the grain boundary cohesion and enforces transgranular fracture. The effect of carbon also was demonstrated by notch-impact tests on Fe-Sb-C alloys, see **Figure 10**. As in the case of Sn, for unalloyed carbon steels the danger of embrittlement by Sb is minor, there will be always enough dissolved and segregated carbon to avoid Sb grain boundary segregation. Only for alloyed steels, in which the carbon is tied up by carbide forming elements, Cr, Mn, etc., embrittlement is possible during heat treatment or use of steels in an elevated temperature range.

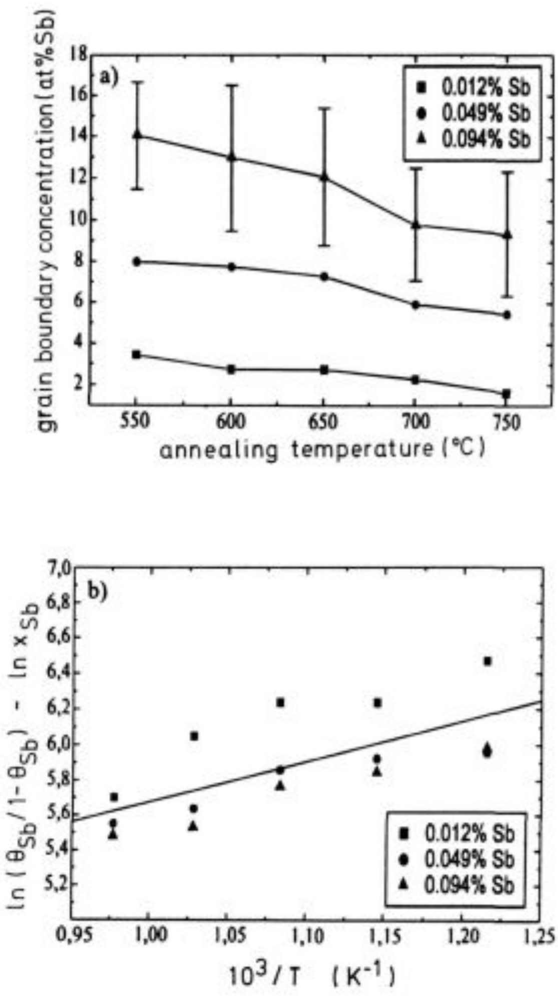

Figure 8: **a)** Grain boundary concentrations of Sb in Fe-Sb alloys, plotted vs equilibration temperature[62]; **b)** plot of the data in (a) according to the Langmuir-McLean aquation (6)

Slika 8: **a)** Segregacija Sb po mejah zrn v Fe-Sb zlitini v odvisnosti od ravnotežne temperature[62]; **b)** prikaz podatkov v (a), ki ustrezajo Langmuir-McLean enačbi (6)

Several authors have claimed an effect of nickel, enhancing the grain boundary segregation of Sb, however, this effect could not be reproduced in recent studies on

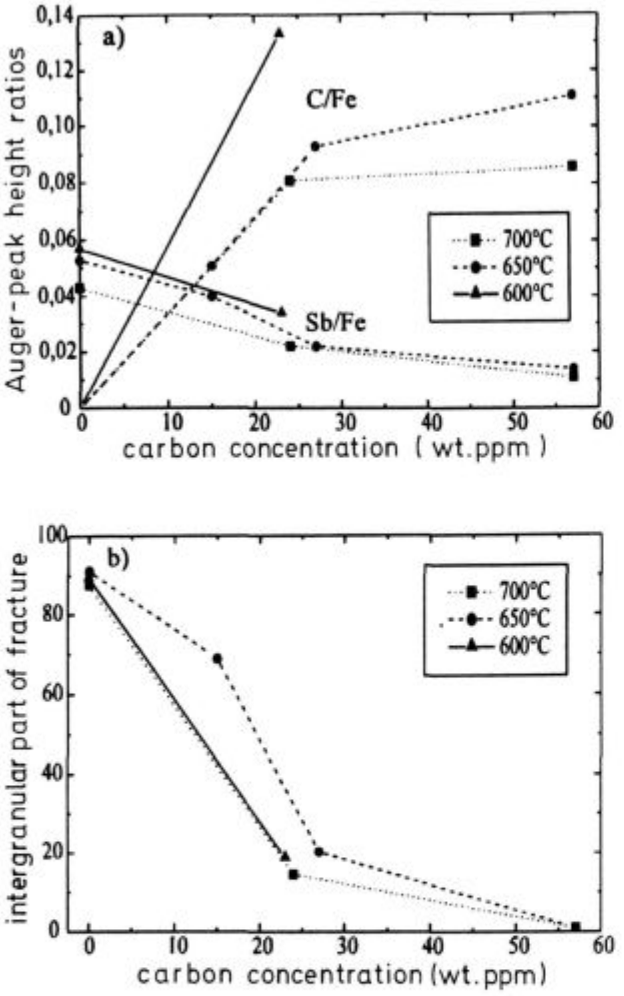

Figure 9: **a)** Grain boundary segregation of Sb and C in Fe-Sb-C alloys after equilibration at different temperatures, plotted in dependence on the bulk concentration, demonstrating the displacing effect of carbon on segregated Sb[62,63]; **b)** intergranular part of fracture in dependence on bulk carbon concentration

Slika 9: **a)** Ravnotežna koncentracija Sb v segregirani plasti na mejah zrn v zlitini Fe-Sb-C pri različnih temperaturah, prikazana v odvisnosti od koncentracije C v osnovnem materialu, prikazuje pojav ko ogljik izrine Sb v segregirani plasti[62,63]; **b)** interkristalna ploskev preloma v odvisnosti od koncentracije ogljika v osnovnem materialu

Fe-Ni-Sb alloys[64]. In earlier studies[65,66] of Fe-Sb and Fe-Ni-Sb alloys at 560°C an increase of Sb segregation was observed with hte Ni-content and Ni also segregates to the grain boundaries, its segregation being only slightly affected by the presence of Sb. For low alloy Ni-Cr steels the authors[65,66] conclude that the Sb-segregation is a complex function of the total alloy composition. When Mn is present in these steels it causes precipitation of an antimonide and greatly reduces Sb-segregation. A detailed investigation of a 3,5 Ni-1Cr-steel after embrittlement at 480°C demonstrates a dependence on the microstructure[67]. Intergranular embrittlement in a quenched and tempered martensitic microstructure was associated with the segregation of phosphorus, which is possible since the carbon activity is reduced by precipitation of chromium rich carbides at the grain boundaries. the embrittlement in the bainitic microstructure was associated with the segregation of antimony, since the carbon activity is relatively high due to the formation of cementite type carbides. Prolonged embrittlement of the bainite produced a low energy fracture. Increased nickel and antimony concentrations at the grain boundaries were associated with the formation of a fine grain boundary precipitate. The increased carbon activity continued to prevent appreciable P segregation but could not inhibit the 'cosegregation' of Ni and Sb[67].

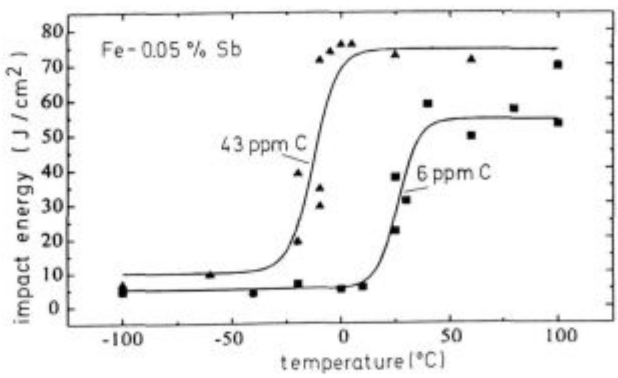

Figure 10: Results of notch impact tests on an Fe-Sb alloy with different carbon concentrations[63]. The ductile-brittle transition temperature is shifted to lower temperatures by carbon, due to the removal of Sb from the grain boundaries and increase of grain boundary cohesion by segregated carbon

Slika 10: Rezultati udarnih preizkusov na zlitini Fe-Sb z različnimi vsebnostmi ogljika[63]. Temperatura prehoda duktilno-krhko je premaknjena k nižjim temperaturam zaradi ogljika, le-ta izpodrine Sb z mej zrn in poviša kohezijo

2.3 Segregation of Sb and Sn at internal interfaces

Sb can be trapped by TiC precipitates in Fe. A dense dispersion of TiC, produced by ion implantation and annealing at 600-700°C, ties up Sb effectively[68]. Continued annealing leads to slow release of Sb into the matrix in a diffusion and trapping process. The Sb is present at the interface TiC/ferrite, and not in the TiC, the binding enthalpy is -35,6 kJ/mol[68-70]. This interfacial segregation may provide a means for keeping Sb from grain boundaries in ferritic steels to suppress embrittlement. Similar trapping has been observed at TaC and Cu precipitates in Fe at 600°C[71].

Trapping or segregation of Sn at MnS particles has been observed in Fe-3% Si doped with tin. The Sn was clearly enriched compared to the grain boundaries, this segregation retards the growth rate of the MnS particles so that in Sn doped alloy they are much smaller than in Sn-free Fe-3% Si[72]. The size of the precipitates affects the primary and secondary recrystallization, thus influencing the magnetic properties of Si steels, see chapter 3.1.

In the eutectoid transformation of austenite to cast iron, minor additions of Sb (0,08 wt%) or Sn (0,12 wt%)

were found to inhibit the $\gamma \rightarrow \alpha$ + graphite and the $Fe_3C \rightarrow \alpha$ + graphite reaction paths, but did not significantly affect the metastable $\gamma \rightarrow \alpha + Fe_3C$ reaction[73]. Scanning Auger microprobe analysis indicated that Sn and Sb adsorb at the graphite/metal interface. The segregated layer acts as a barrier for the access of carbon to the graphite nodules. With the graphite disabled as a sink for carbon, the metal transforms as a nongraphite steel.

3 Effects of interfacial segregation of Sn and Sb on steel properties

3.1 Effects of surface segregation on the texture of electrical sheet

A (100) [001] texture of Fe-Si can be achieved with the aid of adsorption or segregation of different species: O, S, Sb, Sn etc. The (100) [001] texture cannot compete losswise with the (110) [001] texture if unidirectional magnetization is important. In applications where the magnetization must occur in all directions in the plane of the sheet such as in motors or generators the (100) [001] texture is favourable since the plane of the sheet does not contain the hard (111) direction of magnetization, but even in transformers lower losses can be obtained by using some (100) [001] texture. After the primary recrystallization, the growth of grains is governed by the surface energy, preferential growth of grains with a low surface energy occurs in the secondary recrystallization. In absence of oxygen or other adsorbing or segregating species γ_{110} is the lowest surface energy and (110) [001] grains grow. When sufficient oxygen or sulfur is present γ_{110} and (100) grains become stable in the surface[74-76], see also **Figure 1**.

Presence of oxygen and sulfur is not well possible in the production process of non-oriented electrical sheet. The annealing for secondary recrystallization is done in dry hydrogen at about 900°C. Presence of sulfur would cause precipitation of MnS particles in the steels which may hinder the reorientation of the magnetic domains. Thus, other elements such as Sn and Sb were successfully used as alloying additions to improve the texture and magnetic properties of non-oriented steel sheet[77,78]. The alloying additions may not be too high to obtain the wanted (100) [001] texture, for too high activities and surface coverages the surface energies of nearly all orientations are decreased so strongly that no preferential growth of (100) is attained. Sb has proved to have another advantageous effect, it suppresses widely the internal oxidation of the alloying elements Si, Al and Mn which is possible during the decarburization treatment and causes increasing permeability deterioration with increasing subscale depth[79]. Also in the production of high induction and high permeability grain oriented Fe-Si, the presence of Sb and Sn can have positive effects, yielding a more precise (110) [001] secondary recrystallization texture than in conventional Fe-Si. In earlier work it was assumed that Sb and Sn are effective on the primary recrystallization, retarding primary grain growth in cooperation with BN and S, less S being necessary than without Sb and Sn. But in recent studies it was found that grain boundary segregation of Sb and Sn is negligibly low in the silicon steel sheet after the usual thermal treatment. Obviously, the effect of Sb and Sn is caused by the surface segregation during recrystallization annealing. The surface segregation decreases the surface energy of grains with (100) orientation in the plane of the steel sheet and the grains with low surface energy grow on account of grains with other space orientation in the sheet plane. The role of the surface segregation has been confirmed by extended studies on silicon steel doped with Sb and Sn[12-20]. Only a controlled surface segregation promotes the wanted selective grain growth. For too high Sb and Sn concentrations the surface energy of all orientations are strongly decreased and no preferential growth of (100) is obtained. For steels with a high Sb content rather the unwanted growth of (111) is to be expected, since the surface concentration on that plane is highest[56]. Furthermore, it has been stated that Sb and Sn retard the decarburization[79], which is also a very important process in the production of electrical steel sheet - so this again would be a negative effect of Sb and Sn surface segregation.

3.2 Effect of surface segregation in creep of steels

Due to their strong tendency to surface segregation Sn and Sb can very negatively affect the creep behaviour of heat resistant CrMo- and CrMoV- steels used for turbine rotors and blades[80]. The failure of such steels occurs by formation of creep cavities at the grain boundaries and in the steel matrix and the coalescence of the cavities to cracks. The nucleation of the cavities mostly starts at inclusions, such as sulfides (MnS) and oxides[81]. But the nucleation is favoured and accelerated by the presence of Sn or Sb which will immediately segregate to the free metal surface of a pore forming at an inclusion or at a grain bondary. The segregation decreases the surface energy, the pores are stabilized and can grow to cavities under further surface segregation. This effect of Sn has been observed for a CrMoV- steel[39,40] measuring creep curves for melts doped with different Sn-concentrations. The higher the Sn content of the steel the earlier they failed by rupture in the creep test, **Figure 11**.

3.3 Effects on the carburization of case hardening steels

Surface segregation on Sn and Sb can effectively retard the carburization of case hardening steels[82]. The carburization is generally conducted at about 930°C in $CO\text{-}H_2\text{-}H_2O$ atmospheres. In the beginning its rate is controlled mainly by the surface reaction sequence

$$CO(g) = C\ (dissolved) + O\ (adsorbed)$$

$$O\ (adsorbed) + H_2(g) = H_2O(g)$$

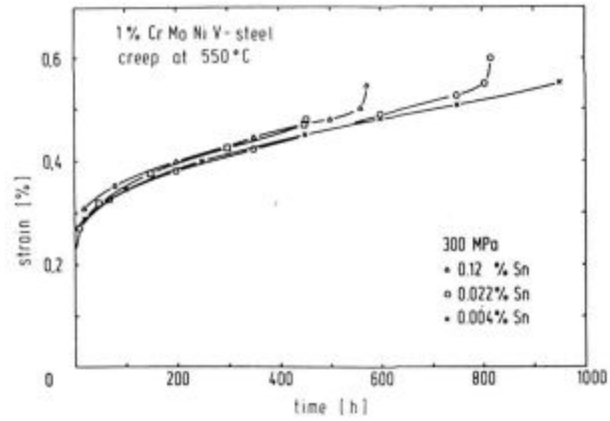

Figure 11: Creep curves for 1% CrMoNiV- steel at 300 MPa and 500°C[39], effect of different Sn-contents - with increasing Sn-content the rupture time is markedly decreased

Slika 11: Krivulje lezenja za jeklo 1% CrMoNiV pri 300 MPa in 550°C[39], vpliv različnih vsebnosti Sn - z naraščajočo vsebnostjo Sn je prelomni čas opazno znižan

and later on a coupled surface reaction and diffusion control determines the rate of carburization. The surface reaction rate can be described by

$$r = \beta([C]_{eq} - [C]_s)$$

where $[C]_{eq}$ and $[C]_s$ are the equilibrium and the actual surface concentration of carbon and β is the carbon transfer coefficient, which contains dependencies on partial pressures and temperature[83]. Extended thermogravimetric studies of carburization on steels doped with Sn, Sb, Cu, P or Pb demonstrated a strong effect of Sb on the coefficient β (see **Figure 12a**), whereas the effect of the other elements is much less. This retardation of carbon transfer is caused by the blocking of surface sites for reaction, the adsorption and dissociation of CO, by segregated Sb. The surface segregation of Sb and Sn on the case hardening steels was demonstrated by AES studies, after exposure in the carburization atmosphere at 900°C, see **Figure 12b**. Segregation in the UHV chamber leads to displacement of Sb and Sn by sulfur, however, in the carburization atmosphere the sulfur would be removed by the reaction S (absorbed) + $H_2(g) = H_2S(g)$. The presence of too high levels of Sb in case hardening steels would lead to too low carbon contents after the usual carburization period and insufficient hardening of the workpieces, see **Figure 12c**. Thus, a specification for Sb-content < 25 wt ppm was recommended for case hardening steels, whereas concentration of the other tramp elements may be in the usual range[84].

3.4 Temper embrittlement

Reversible temper embrittlement occurs upon slowly cooling of steels through the temperature range 550 to 350°C after annealing (tempering) at higher temperatures or during application of steels in this range. Temper em-

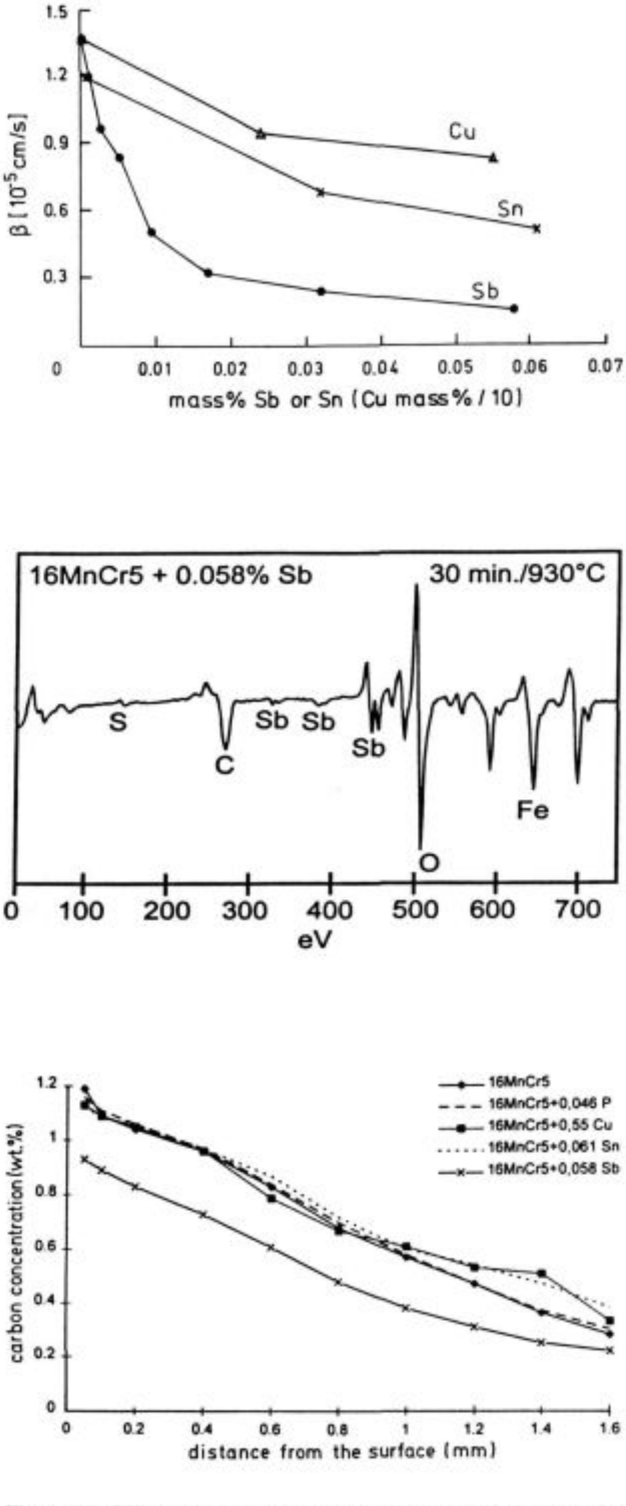

Figure 12: Effects of Sb, Sn and Cu on the gas carburization of a case-hardening steel at 930°C[82,84], **a)** carbon transfer coefficient β in dependence on bulk concentrations of Sb, Sn or Cu, **b)** Auger spectrum of the Sb-doped steel after heating in hydrogen to 930°C, **c)** carbon concentration profiles after gas carburization of samples in an industrial furnace

Slika 12: Vpliv Sb, Sn in Cu na plinsko naogljičenje jekla za cementacijo pri 930°C[82,84], **a)** β prenosni koeficient ogljika v odvisnosti od koncentracije Sb, Sn ali Cu v osnovnem materialu, **b)** AES spekter jekla legiranega z Sb po žarjenju v vodiku pri 930°C, **c)** koncentracijski profil ogljika po plinskem naogljičevanju vzorcev v industrijski peči brittlement is caused by grain boundary segregation of P, Sn, Sb and As[61-72] but severe embrittlement is observed only if the alloying elements Ni, Cr and Mn are present, such as in low alloy turbine steels. In earlier years this fact was explained by 'cosegregation', e.g. of Cr and P, however especially for this case it could be clearly shown that Cr alone has no enhancing effect on P-segregation[35,36]. In fact, Cr and Mn decrease the carbon solubility in steels, and the effect of carbon on P-segregation, i.e. removal of P from the grain boundaries by displacement by C, is reduced in the presence of Cr and Mn, thereby allowing more P-segregation. 'Cosegregation' was also suspected for Ni and Sb, and Ni and Sn, but most probably the strong effect of these combinations on embrittlement are due to interfacial formation of intermetallic compounds of these elements. Steels without Ni do not show embrittlement by Sn or Sb[85-96].

Temper embrittlement is a particular problem for low alloy steels, e.g. Ni-Cr-Mo-V rotor steels and Cr-Mo pressure vessels. Temper embrittlement does not occur in plain carbon steels with less than 0,5% Mn. At high Mn concentrations, however, P-segregation is possible in plain carbon steels and also a 'cosegregation' of Mn and Sb is supposed to occur. However, the effect of Mn can easily be explained by the reduction of carbon activity caused by formation of Mn-rich carbides[97]. Thereby, carbon segregation is reduced which allows grain boundary segregation of P, Sn and Sb.

3.5 Hydrogen induced cracking

The threshold stress intensity for cracking of a Ni-Cr-Mo steel is strongly reduced by grain boundary segregation of Sb, Sn and P[98-100]. In the presence of hydrogen this threshold stress intensity is lowered further, but it is the impurity effect which is dominant, the hydrogen merely accentuates the tendency for brittleness already present.

If must be emphasized again that for embrittlement of steels by Sb the presence of Ni and Cr is necessary. Sb causes intergranular fracture in the constant strain rate test, it is five times more effective in inducing intergranular fracture at cathodic potentionals than S, the results are consistent with H-permeation studies in Fe as affected by Sb and S[101,102].

3.6 Possible effects of grain boundary segregation in interstitial free steels

One may expect that grain boundary segregation of Sn and Sb is possible in interstitial free steels (i.f. steels). Such steels have very low concentrations of C and N in order to attain good deep drawing properties, and thus the tramp elements are not kept away from the grain boundaries by segregated carbon (**see Figure 10**). The effects of Sn and Sb in deep drawing steels were not studied as yet, but a behaviour similar to P[103,104] may be expected. Brittle behaviour was found for steels with very low C content (< 300 ppm), caused by P at grain boundaries. Some i.f. steels are alloyed with Ti to tie up the interstitial elements, but Ti is also effective in scavenging the phosphorus forming a very stable phosphide. Also TiC as a precipitate is able to trap phosphorus and to keep it from the grain boundaries to a certain extent, such trapping effect has also been reported for Sb at the TiC/ferrite interface[68-70]. Anyway, similar as P can be deleterious for the properties of certain deep drawing steels with low C and no TiC or excess Ti, also Sn and Sb may adversely affect the ductility of such steels. Especially if steels with high Sn and/or Sb contents are slowly cooled after batch annealing or coiling, they may segregate to grain boundaries and cause embrittlement. On the other hand, also positive effects may occur on the texture, as in the case of electrical steel sheet. Effects of Sb and Sn on the texture of deep-drawing steels are currently investigated[105].

4 Conclusions

Generally, tramp elements such as Sn and Sb can have effects on steel properties only if they enrich at interfaces, the enrichment by equilibrium segregation leads to coverages in the range of a monolayer depending on bulk concentration and decreases with temperature. Utilizing Auger-electron spectroscopy the thermodynamics of segregation to surfaces and grain boundaries can be elucidated.

The solubilities of Sn and Sb in the ferritic matrix are relatively high, the solubility is strongly decreased in the presence of some elements such as Ni which form intermetallic compounds with Sn and Sb.

The tendency for surface segregation of Sn and Sb is very high, as yet no thermodynamic data have been determined since always saturation was observed. The segregation coverages and structures are very different for different crystallographic orientations, therefore the decrease of surface energy will be strongly dependent on orientation and marked effects of Sn and Sb on the stability of different crystallographic planes are to be expected.

Sn and Sb segregate to grain boundaries in ferrite, the extent of segregation strongly depends of the misfit of the grains. The tendency for grain boundary segregation of Sn and Sb is relatively low, as indicated by the results on equilibrium segregation in binary alloys in the temperature range 500 to 750°C. This can also be seen from the segregation enthalpies: -22,5 kJ/mol Sn and -19 kJ/mol Sb.

Sn and Sb also segregate to interfaces, for Sb at interfaces ferrite/TiC and for Sn at the interface ferrite/MnS.

In the annealing of steel sheet the surface segregation of Sn and Sb affects the stability of certain orientations. For intermediate concentrations the (100) orientation appears to be stabilized, for higher contents the (111) orientation becomes stable. These effects are of importance in the production of electrical Fe-Si steel sheet and may also be useful in the production of deep-drawing steels.

The strong tendency for surface segregation of Sn (and Sb) plays a role in the creep of heat resistant steels, since formation and growth of creep cavities is enhanced by surface segregation decreasing the surface energy of the cavities. This was demonstrated for Sn doped CrMoV-steels.

Surface segregation of Sn and Sb affects the carburization of case hardening steels. Especially Sb strongly retards the carbon transfer and may cause insufficient carburization.

Grain boundary segregation of Sn or Sb causes embrittlement. Temper embrittlement of low alloy steels only occurs in the presence of Ni and Cr. Obviously, reduction of carbon activity by Cr and formation of intermetallics Ni_xSn_y resp. Ni_xSb_y is necessary for temper embrittlement.

Hydrogen induced cracking can be favoured by Sn and Sb grain boundary segregation. However, as for temper embrittlement the presence of Ni and Cr appears to be a precondition of such effect of Sn and Sb.

In interstitial free steels one may expect strong effects of Sn and Sb since these elements are not kept away from the grain boundaries by carbon. Addition of Ti may scavenge Sn and Sb, either by direct interaction or by trapping effect of TiC.

5 References

[1] D. A. Melford: *Phil. Trans. Roy. Soc. London*, A295, 1980, 89
[2] M. Torkar, F. Vodopivec: *Železarski zbornik*, 15, 1981, 61
[3] F. K. Peters, H. J. Engell: *Archiv Eisenhüttenwes.*, 30, 1959, 275
[4] F. Vodopivec, A. Kohn, J. Benard: *Comptes Rendus A. S.*, 255, 1962, July, 296-298
[5] F. Vodopivec: *Métaus-Corrosion-Industries*, 452, 1963, April, 159-170
[6] F. Vodopivec, A. Kohn: *Comptes Rendus A. S.*, 253, 1963, July, 448-450
[7] F. Vodopivec, A. Kohn, J. Philibert, J. Manenc: *Mem. Scient. Rev. de Métallurgie*, 60, 1963, 11, 808-818
[8] F. Vodopivec, L. Kosec: *Comptes Rendus A. S.*, 262, 1966, April, 1124-1127
[9] F. Vodopivec, L. Kosec: *Archiv Eisenhüttenwes.*, 40, 1969, 2, 118-121
[10] L. Kosec, F. Vodopivec, R. Tixier: *Métaux-Corrosion- Industries*, 1969, May-525, 1-17
[11] F. Vodopivec, L. Kosec: *Radex-Rundschau*, 8, 1969, 4, 639-649
[12] F. Vodopivec, F. Marinšek, F. Grešovnik, D. Gnidovec, M. Praček, M. Jenko: *Journal of Magnetism and Magnetic Materials*: 97, 1991, 281-285
[13] F. Vodopivec, M. Jenko, F. Marinšek, F. Grešovnik: *Vacuum*, 43, 1992, 497-500
[14] M. Jenko, F. Vodopivec, B. Praček: *Vacuum*, 43, 1992, 449-451
[15] M. Jenko, F. Vodopivec, B. Praček: *Appl. Surface Science*, 1993, 70/71, 118
[16] M. Jenko, F. Vodopivec, B. Praček, M. Godec, D. Steiner: *Journal of Magnetism and Magnetic Materials*: 133, 1994, 229-232
[17] M. Jenko, F. Vodopivec, H. J. Grabke, H. Viefhaus, B. Praček, M. Lucas, M. Godec: *Steel Research*, 65, 1994, 500-504
[18] M. Jenko, F. Vodopivec, H. Viefhaus, M. Milun, T. Valla, M. Godec, D. Steiner-Petrovič: *Fizika*, A4, 1995, 3, 91-98
[19] M. Jenko, F. Vodopivec, H. J. Grabke, H. Viefhaus, M. Godec, D. Steiner-Petrovič: *Journal de Physique IV*, Colloque C7, 5, 1995, C7-225-231
[20] R. Mast, H. J. Grabke, M. Jenko, M. Lucas: *Materials Sci. Forum*, 207-209, 1996, 401
[21] E. Hondros, M. P. Seah: *Int. Metals Review*, 222, 1977, 262
[22] C. L. Briant, S. K. Banerji: *Int. Materials Reviews*, 232, 1978, 164
[23] C. L. Briant, H. J. Grabke: *Mat. Sci. Forum*, 46, 1989, 253
[24] H. J. Grabke: *J. Iron Steel Inst. Japan Int.*, 29, 1989, 529-538
[25] H. J. Grabke: Grain Boundary Segregation of Impurities in Iron and Steels and Effects on Steel Properties, in *Impurities in Engineering Materials*, Ed. C. L. Briant, M. Dekker, in press
[26] W. B. Pearson: *A Handbook of Lattice Spacings and Structures of Metals and Alloys*, Pergamon Press, London, issued as N.R.C. No. 4303
[27] E. D. Hondros, M. P. Seah: *Proc. Roy. Soc. London*, A 286, 1965, 479
[28] M. P. Seah, E. D. Hondros: *Proc. Roy. Soc. London*, A 335, 1973, 191
[29] E. D. Hondros, M. P. Seah: *Met. Trans.*, 8A, 1977, 1363
[30] H. J. Grabke, G. Tauber, H. Viefhaus: *Scr. Metall.*, 9, 1975, 1181
[31] H. J. Grabke, W. Paulitschke, G. Tauber, H. Viefhaus: *Surf. Sci.*, 63, 1977, 377
[32] H. J. Grabke, H. Viefhaus, G. Tauber: *Archiv Eisenhüttenwes.*, 49, 1978, 391
[33] H. J. Grabke: *Mater. Sci. Eng.*, 42, 1980, 91
[34] H. Viefhaus, H. J. Grabke: *Surf. Sci.*, 109, 1981, 1
[35] H. Erhart, H. J. Grabke: *Železarski zbornik*, 15, 1981, 33, Proceed. Int. Conf. 'Residuals in Iron and Steel', 1980 Ljubljana
[36] H. Erhart, H. J. Grabke: *Met. Sci.*, 15, 1981, 401
[37] H. Erhart, H. J. Grabke: *Scripta Met.*, 15, 1981, 531-534
[38] H. de Rugy, H. Viefhaus: *Surf. Sci.*, 173, 1986, 418
[39] W. Jäger, H. J. Grabke, R. Möller: *Proc. Int. Conf.*, on 'Residuals and Trace Elements in Iron and Steel', Portorož, Oct. 1985, ed. by F. Vodopivec, Inst. Metall., Ljubljana, 1986, 217-237
[40] W. Jäger, H. J. Grabke, Jin Yu: *Proc. 2nd Int. Conf. on Creep and Fracture of Engineering Materials and Structures*, ed. B. Wilshire, D. R. Owen, Pineridge Press, 1984, 649-659
[41] B. Egert, G. Panzner: *Surface Sci.*, 118, 1982, 345-368
[42] B. Egert, G. Panzner: *Physical Review B*, 28, 1983, 8
[43] G. Panzner, B. Egert: *Surface Sci.*, 144, 1984, 651-664
[44] G. Panzner, W. Diekmann: *Surface Sci.*, 160, 1985, 253-270
[45] W. Diekmann, G. Panzner, H. J. Grabke: *Surf. Interface Analysis*, 2, 1986, 184
[46] W. Losch: *Acta Metall.*, 27, 1979, 1885
[47] R. P. Messmer, C. L. Briant: *Acta Metall.*, 30, 1980, 457
[48] G. Tauber, H. J. Grabke: *Ber. Bunsenges. Physikal. Chemie*, 82, 1978, 298
[49] O. Kubaschewski: *Iron - Binary Phase Diagrams*, Springer Verlag, 1982
[50] M. Nageswararao, C. J. McMahon, Jr., H. Herman: *Met. Trans.*, 5, 1974, 1061
[51] M. Arita, M. Ohyama, K. S. Goto, M. Someno: *Z. Metallkde.*, 72, 1981, 244
[52] M. C. Cadeville, M. Maurer: *Mat. Sci. a. Engineering*, 51, 1981, 147
[53] Ph. Dumoulin, M. Guttmann: *Mat. Sci. a. Engineering*, 42, 1980, 249
[54] H. Viefhaus, M. Rüsenberg: *Surf. Sci.*, 159, 1985, 1
[55] M. Rüsenberg, H. Viefhaus. *Ber. Bunsenges. Phys. Chem.*, 90, 1986, 301
[56] M. Rüsenberg, H. Viefhaus: *Surf. Sci.*, 172, 1986, 615
[57] T. Watanabe, S. Kitamura, S. Karashima: *Acta Met.*, 28, 1980, 455
[58] M. Braunovic: *Canadian Metallurg. Quart.*, 13, 1974, 211
[59] J. M. Titchmarsh, B. C. Edwards, G. Gabe, B. L. Eyre: *Nature*, 278, 1979, 38
[60] B. C. Edwards, B. L. Eyre, T. E. Cranshaw: *Nature*, 269, 1977, 47
[61] T. E. Cranshaw: *J. Physique*, Colloque C2, supplément No. 3, 40, 1979, C2-167
[62] R. Mast, H. J. Grabke, M. Jenko, M. Lucas: *Materils Science Forum*, 207-209, 1996, 401-404
[63] R. Mast, H. Viefhaus, M. Lucas, H. J. Grabke: in *Nichtmetalle in Metallen 96*, ed. D. Hirschfeld, 51-60
[64] R. Mast, H. Viefhaus, M. Lucas, H. J. Grabke: *4th Conf. on Materials and Technology*, Oct. 1996, Portorož, Slovenia
[65] C. L. Briant, A. M. Ritter: *Acta Met.*, 32, 1984, 2031
[66] C. L. Briant: *Acta Met.*, 35, 1987, 149
[67] A. Wirth, I. Andreoni, G. Gregory: *Surface a. Interf. Anal.*, 9, 1986, 157
[68] S. M. Myers, D. M. Follstaedt, H. J. Rack: *Met. Trans.*, 11A, 1980, 1465
[69] J. A. Knapp, D. M. Follstaedt: *Appl. Phys. Lett.*, 37, 1980, 9, 810

[70] J. A. Knapp, D. M. Follstaedt: *Nucl. Instr. and Meth.*, 182/183, 1981, 1017

[71] S. M. Myers, D. M. Follstaedt: *J. Appl. Phys.*, 52, 1981, 6, 4007

[72] S. Suzuki, K. Kuroki, H. Kobayashi, N. Takahashi: *Mater. Transactions JIM*, 33, 1992, 1068

[73] W. C. Johnson, B. V. Kovacs: *Met. Trans.*, 9A, 1978, 219

[74] D. Kohler: *J. Appl. Physics Suppl.*, 31, 1960, 5, 408S

[75] C. G. Dunn, J. L. Walter: *Trans. AIME*, 224, 1962, 518

[76] J. J. Kramer: *Met. Trans.*, 23A, 1992, 1987

[77] H. C. Fiedler: *J. Magnetism a. Magnetic Materials*, 26, 1982, 22

[78] G. Lyudkovsky, P. K. Rastogi: *Met. Trans.*, 15A, 1984, 257

[79] G. Lyudkovsky: *IEEE Trans. Magnetics. vol. Mag.*, 22, 1986, 5, 508

[80] B. L. King: *Phil. Trans. R. Soc. Lond.*, 295, 1980, 235

[81] W. Hartweck, H. J. Grabke: *Scripta Met.*, 15, 1981, 653

[82] A. Ruck, D. Monceau, H. J. Grabke: *Steel Research*, 67, 1996, 240

[83] H. H. Grabke: *Härterei-Techn. Mitteilungen*, 45, 1990, 110-118

[84] A. Ruck, H. J. Grabke: *Effects of Impurities and Tramp Elements in Case Hardening Steels*, ECSC research project, final report, in press

[85] P. A. Restaino, C. J. McMahon, Jr.: *Trans. ASM*, 60, 1967, 699

[86] J. R. Low, Jr., D. F. Stein, A. M. Turkalo, R. P. Laforce: *Trans. AIME*, 242, 1968, 14

[87] J. R. Rellick, C. J. McMahon, Jr.: *Met. Trans.*, 5, 1974, 2439

[88] C. L. Smith, J. R. Low, Jr.: *Met. Trans.*, 5, 1974, 279

[89] H. Ohtani, H. C. Feng, C. J. McMahon, Jr., R. A. Mulford: *Met. Trans.*, 7A, 1976, 87

[90] H. Ohtani, H. C. Feng, C. J. McMahon, Jr., R. A. Mulford: *Met. Trans.*, 7A, 1976, 1123

[91] R. A. Mulford, C. J. McMahon, Jr., D. P. Pope, H. C. Feng: *Met. Trans.*, 7A, 1976, 1269

[92] A. K. Cianelli, H. C. Feng, A. H. Ucisik, C. J. McMahon, Jr.: *Met. Trans.*, 8A, 1977, 1059

[93] J. Yu, C. J. McMahon, Jr.: *Met. Trans.*, 11A, 1980, 277

[94] T. Wada, W. C. Hagel: *Met. Trans.*, 9A, 1978, 691

[95] J. Kameda, C. J. McMahon, Jr.: *Met. Trans.*, 12A, 1981, 31

[96] M. Guttmann, P. R. Krahe, F. Abel, G. Amsel, M. Bruneaux, C. Cohen: *Met. Trans.*, 5, 1974, 167

[97] H. J. Grabke, K. Hennesen, R. Möller, W. Wei: *Scripta Met.*, 21, 1987, 1329-1334

[98] R. Viswanathann, S. J. Hudak, Jr.: *Met. Trans.*, 8A, 1977, 1633

[99] R. O. Ritchie: *Met. Trans.*, 8A, 1977, 1131

[100] N. Bandyopadhyay, J. Kameda, C. J. McMahon, Jr.: *Met. Trans.*, 14A, 1983, 881

[101] R. H. Jones, S. M. Bruemmer, M. T. Thomas, D. R. Baer: *Met. Trans.*, 13A, 1982, 241

[102] R. H. Jones, M. T. Thomas, D. R. Baer: *Met. Trans.*, 16A, 1985, 123

[103] H. J. Grabke, R. Möller, H. Erhart, S. S. Brenner: *Surf. Interface Anal.*, 10, 1987, 202

[104] H. Erhart, H. J. Grabke, R. Möller: *Archiv Eisenhüttenwes.*, 54, 1983, 285

[105] H. G. Beyer, H. J. Grabke: *Development of new deep drawing steels by doping with surface active elements*, current ECSC project

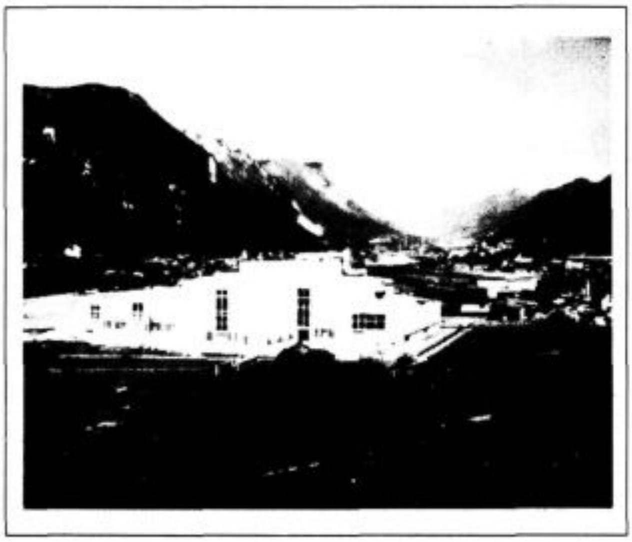

Kovine, zlitine, tehnologije/30/1996/6/497-507

Applications of Surface Analytical Techniques in Corrosion Research (Mainly High Temperature Corrosion)

Uporaba površinskih analiznih tehnik v raziskavah korozije

H. Viefhaus[1], Max-Planck-Institut, Düsseldorf, Germany

Prejem rokopisa - received: 1996-10-01; sprejem za objavo - accepted for publication: 1996-11-04

The application of materials under various environmental conditions strongly depends on the corrosion properties of those materials. This is in particularly true for high temperature materials to be used in power plants, petrochemical, chemical and automobil industry, where during application high temperatures and aggressive environments may cause great problems. At low temperatures the corrosion of metals is often inhibited by a passive layer on the metal surface. To understand the phenomenon of passivity the formation and nature of this surface film, quite often only a few nm's thick, has to be characterized. Corrosion protecting layers on high temperature materials, either grown during application or precovered before application, have a much larger thickness. In order to study the growth mechanisms, nature and properties of corrosion protecting layers thin films have to be characerized spreading over a quite large range of thicknesses, from a few nm's for the passive layers up to several μm's for the protecting layers on high temperature materials. Different methods for thin film analysis using surface analytical methods will be presented and illustrated by examples from different areas of corrosion research.

Key words: corrosion, high temperature corrosion, surface analytical techniques

Uporaba materialov v različnih okoljih zavisi od njihovih korozijskih lastnosti. To je posebno pomembno pri uporabi materialov pri visokih temperaturah in agresivnih medijih npr. v elektrarnah, petrokemijski, kemijski in avtomobilski industriji, kjer lahko pride do hudih industrijskih havarij. Pri nizkih temperaturah se na površini kovin tvori tanka pasivna plast, ki zavira korozijo. Razumevanje pojava nastanka in narave tanke pasivne plasti, ponavadi debele le nekaj nanometrov je mogoče samo s karakterizacijo teh plasti. Protikorozijske zaščitne plasti materialov, ki se uporabljajo pri visokih temperaturah in nastajajo med samo uporabo ali pa so bile predhodno nanesene, so debelejše. Študij mehanizma rasti, narave in lastnosti protikorozijskih prevlek je mogoč z raziskavami protikorozijskih prevlek. Te so različnih debelin, od nekaj nanometrov debelih pasivnih tankih plasti do nekaj mikronov debelih prevlek za zaščito na visokih temperaturah. Za analizo protikorozijskih plasti se uporabljajo različne metode površinske analize, ki so prikazane v članku, kakor tudi primeri z različnih področij korozije.

Ključne besede: korozija, visokotemperaturna korozija, metode površinske analitike

1 Introduction

A metal is normally described as beeing passive, if for the existing surrounding atmosphere a high corrosion rate would be expected, instead of the very low corrosion rate to be observed. This passivity is caused by very thin dense oxide (and/or hydroxide) layers which are formed on the metal by the corrosion process. In order to get a better understanding on the effect of those passive layers they have to be analysed with respect to composition and thickness by very surface sensitive methods. High temperature oxidation and corrosion can cause great problems in power plants, petrochemical and chemical industry. A very important precondition for the practical application of a metalic material at high temperature is its oxidation or high temperature corrosion resistance. This precondition may be fulfilled if on the surface of the material protecting oxide layers are formed. These oxide layers can grow under use of the material by reaction of the material elements with the surrounding oxygen atmosphere or by a specific preoxidation at suitable temperatures in oxygen containing atmospheres. The protecting effect of those oxide layers relys on their property to act as a diffusion barrier between the metallic and the corrosive atmosphere surrounding it. Oxyde layers therefore have a key function for the application of materials in high temperature technology and there is a great need for doing research and testing the materials for such applications.

2 Methods

In order to study the growth mechanisms, nature and properties of corrosion protecting layers thin films have to be analysed spreading over a large range of thicknesses, from a few nm's for the passive layers up to several tenth of mµ's for the protecting layers on high temperature materials.

To analyse thin films with respect to layer composition and thickness different depth profiling methods can be applied depending on the thickness of the layer under study and on various sample preparation methods. Following the mainly applied surface analytical methods to be used for depth profiling of homogeneous and inhomogeneous surface layers are listed.

Depthprofiling

homogeneous layers	inhomogeneous layers
AES	AES
XPS	SIMS
SIMS	
SNMS	
GDOES	

---

[1] Dr. Sc. H. VIEFHAUS
Max-Planck-Institut für Eisenforschung GmbH
40074 Düsseldorf, Postfach 140 444 Germany

AES is Auger electron spectroscopy, XPS is X-ray excited photoelectron spectroscopy, SIMS is secondary ion mass spectroscopy, SNMS is secondary neutrals mass spectroscopy and GDOES is glow discharge optical emission spectroscopy.

To analyse inhomogeneous surface layers laterally resolving methods like AES and SIMS have to be applied. For this paper a restriction to the electron spectroscopic methods will be carried out. More detailed information on the application of the remaining methods may be found elsewhere[1].

To get a depth profile in most cases destruction of the layer to be analysed has to be performed by one of the following methods:

a) Sputter depth profiling
b) Angle lapping
c) Crater edge profiling
d) ball cratering

For sputter depth profilling the layer is decomposed by bombardement with noble gas ions and parallel or successive analysis of the momentary interface by a surface analytical method is carried out.

Angle lapping means that by using normal metal polishing equipment a layer covered sample is polished under a very flat angle. Using polishing angles down to about 1° a spreading of the surface layer up to a factor of about 100 is possible and this spreaded part of the layer may be analysed after transfer into a surface analytical system by AES point or line analysis for example.

For crater edge profiling the crater edge resulting from ion beam etching accompanying a single sputter depth profile is exploited. The crater edge of such a profile exposes the strata of the interface in a manner related to that produced by angle lapping, but the striking difference is that for crater edge profiling the resulting angles between surface and interface are 3 orders of magnitude less.

In the case of ball cratering a rotating, spherical, steel ball coated with fine diamond paste, is used to grind a spherical crater into the sample surface and after that the sample is transferred into the surface analytical system to analyse the sputter cleaned crater walls.

Advantages and disadvantages of the different methods are discussed in some detail in[2].

3 Results

a) Very thin surface layers (passive layers)

The only nondestructive method to depth profile very thin surface films is by angle dependent XPS - or AES - measurements. The first example to be presented concerns an oxide layer which was formed at room temperature in air on a pure zinc sample. The thickness of this layer was assumed to be only a few nm's and it should be less than the information depth of the applied electron spectroscopic methods AES or XPS.

The next **figure 1** compares the Zn - LMM Auger spectrum of a clean zinc sample (sputter cleaned by Ar^+ ion bombardment) with the same sample after oxidation at room temperature in air. The comparison makes clear that for the oxidized sample additional features can be recognized if the analyser energy resolution is adequate (0.05%).

XPS studies on the same sample lead to the results that also for the Zn 3d- and Zn 2p- photoelectron signals a distinction between metal and oxide is possible, but the difference is most pronounced for the Zn - LMM Auger signal (in this case X-ray excited), **figure 2**.

If the information depth for the Zn - LMM Auger signal corresponding to the oxidized state of Zn is less than the thickness of the oxide layer, angle dependent measurements should reveal a more pronounced oxide signal at lower angles of analysis. This is illustrated by **figure 3**. The results of an angle dependent measurement on the X-ray excited Zn - LMM Auger signal are depicted in **figure 4** and clearly demonstrate, for angles of analysis ranging from 25° to 90°, that the information deepth is less than the thickness of the oxide layer.

For a smooth, homogeneous, contamination free thin oxide layer the measured signals of the metallic and oxide components may be used to determine the oxide thickness according to equation (1):

$$\frac{I_m}{I_{ox}} = \frac{N_m}{N_{ox}} \times \frac{\lambda_m}{\lambda_{ox}} \times \frac{\exp[-d/\lambda_{ox}\sin\beta]}{1-\exp[-d/\lambda_{ox}\sin\beta]} \qquad (1)$$

where I_m, I_{ox} are the intensities of the metal and oxide signals, N_m, N_{ox} are the densities of the metal and the oxide, λ_m, λ_{ox} are the inelastic mean free pathes of the Auger electrons in the metal and in the oxide, β is the angle of analysis in relation to the sample surface, see **figure 3**.

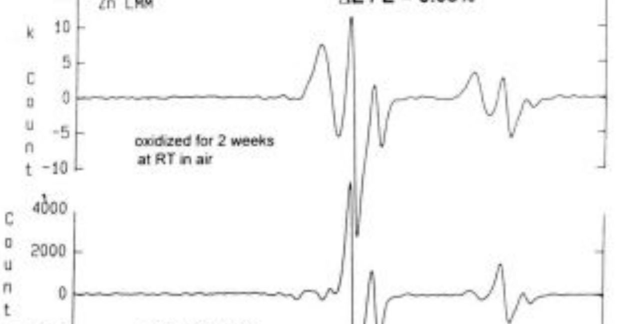

Figure 1: Comparison of the Zn - LMM - Auger spectrum for a clean zinc sample and after oxidation at room temperature in air for 2 weeks
Slika 1: Primerjava AES spektrov čistega Zn - LMM pred in po oksidaciji dva tedna na zraku pri sobni temperaturi

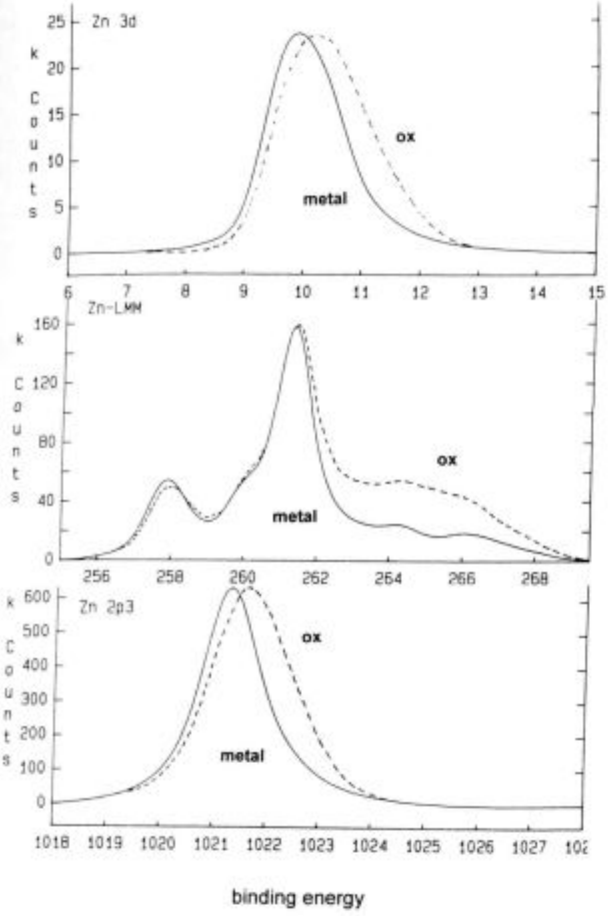

Figure 2: Zn - 3d-, Zn - 2p - photoelectron and Zn - LMM - Auger - signal for clean and oxidized zinc sample (see **figure 1**)
Slika 2: Zn - 3d, Zn - 2p XPS signal in Zn - LMM AES signal za čisti in oksidirani cink (glej **sliko 1**)

The above equation (1) may be changed to equation (2):

$$\frac{d}{\sin\beta} = \lambda_{ox} \ln\left[\frac{N_m}{N_{ox}} \times \frac{\lambda_m}{\lambda_{ox}} \times \frac{l_{ox}}{l_m}\right] \tag{2}$$

For a determination of the layer thickness values for the λ's are necessary. There are no experimental data for the λ - values of zinc, therefore the corresponding λ's of zinc and zinc oxide (of zinc hydroxide as well, which will be needed lateron) were calculated according to a relation derived by Tanuma et al.[3]. The calculated values are (in Å):

Table 1: The calculated λ values (in Å)

	zinc	zinc oxide	zinc hydroxide
λ^{LMM}	17.7	20	21
λ^{2p}	6.7	8	7

According to equation (2) a plot of 1/sinβ against the term on the right hand side of equation (2) should give a straight line and from the slope of this straight line the thickness may be derived.

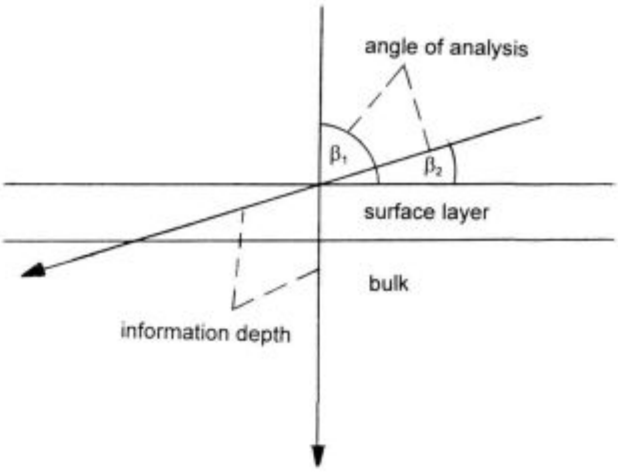

Figure 3: Shematic illustration of the higher surface sensitivity at lower angles of analysis
Slika 3: Shematični prikaz višje površinske analizne občutljivosti pri nizkih kotih

The angle dependence of the peak areas of the Zn - LMM Auger signal and the Zn - 2p photo electron signal are plotted in **figure 5** for the metallic and the oxide contributions. From this plot and by using additionally the known values for N_m, N_{ox} and λ_m, λ_{ox} **figure 6** can be derived. The observed straight line for the dependence of the Zn - LMM Auger signal leads to a thickness of 15Å for the oxide.

If we have a closer look to the well resolved oxygen O - 1s photo electron signal corresponding to the oxide layer, **figure 7**, we can detect that the assumption of a pure oxide layer was not correct, additionally to the oxide signal centered at about 530 eV peak energy a second signal caused by some hydroxide contribution is observed around 532 eV peak energy. Results of angle dependent measurements on the oxygen O - 1s signal in **figure 8** indicate that we have an inner oxide layer and an outer hydroxide layer.

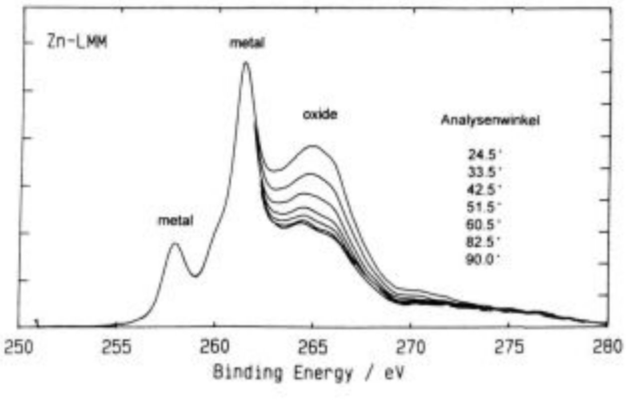

Figure 4: Angle dependence of the Zn - LMM Auger signal for an oxidized zinc sample (as for **figure 1**)
Slika 4: Kotna odvisnost Zn - LMM AES signala za oksidiran cink (kot na **sliki 1**)

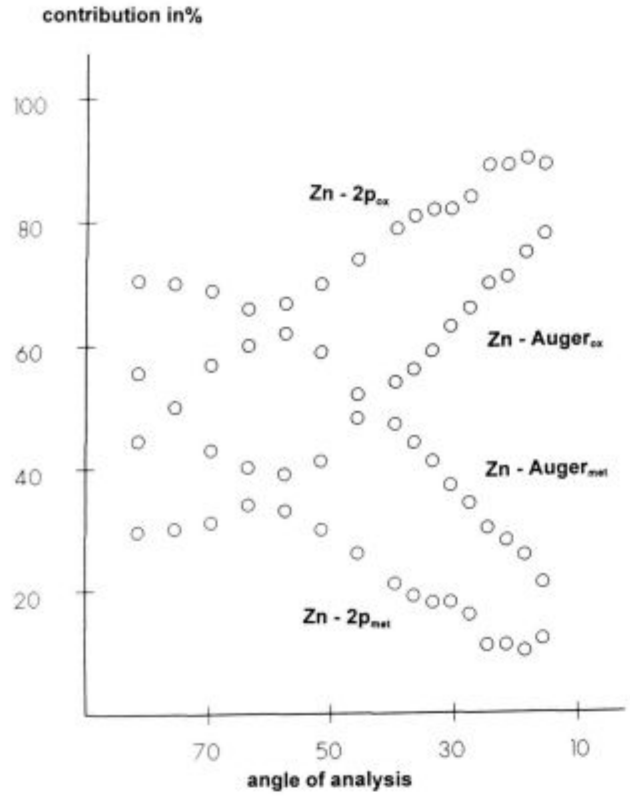

Figure 5: Angle dependence of the Zn - LMM Auger signal and Zn - 2p photoelectron signal for an oxidized zinc sample (as for **figure 1**), metal and oxide contributions are plotted

Slika 5: Kotna odvisnost Zn - LMM AES signala in Zn - 2p XPS signal za oksidiran cink (kot na **sliki 1**), prikazana sta deleža kovine in oksida

Looking more detailed to the angle dependence of the Zn - LMM Auger signal it can be recognized, **figure 9**, that also for this signal the "oxide" - component exhibits some peak shape variations in dependence on the angle of analysis. If we try to fit the Zn - LMM Auger signal for the oxidized sample at first, **figure 10b**, by a metal contribution according to **figure 10a** and the remaining peak area for the oxide contribution by a single peak this is not possible. We need two different peaks as shown in **figure 10c**, to get an acceptable fit of the whole Zn - LMM spectrum. We can now try evaluate the thickness of the oxide and the hydroxide separately.

Again we assume that the oxide and hydroxide layer are homogeneous layers. The intensity ratios of the signals of the different layers with respect to the signal of the zinc substrate are given according to S. Lecuyer et al.[4] by:

$$\frac{I_{ZnOH}}{I_{Zn}}(\Theta) = \lambda_{ZnOH}\, C_{ZnOH}\, [1-\exp(d_{ZnOH}/\lambda_{ZnOH} \cos\Theta)]\ /$$

$$/\ \lambda_{Zn}\, c_{Zn} \exp(-\frac{d_{ZnO}}{\lambda_{ZnO}\cos\Theta}) \exp(-\frac{d_{ZnOH}}{\lambda_{ZnOH}\cos\Theta}) \qquad (3)$$

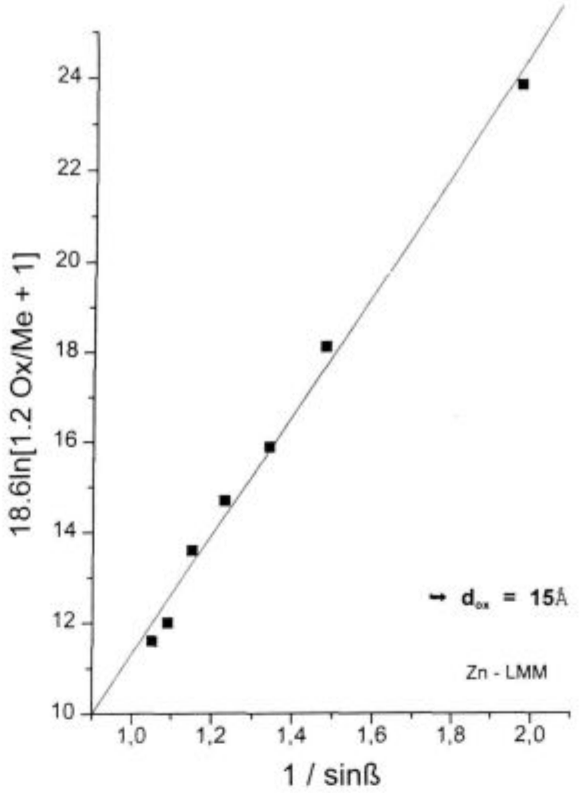

Figure 6: Determination of the oxide thickness according to equation (2), see text

Slika 6: Določitev debeline oksidne plasti po enačbi (2), glej tekst

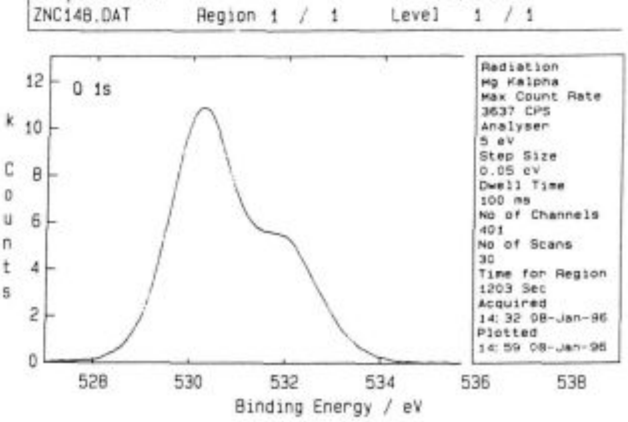

Figure 7: XPS - O - 1s signal for an oxidized zinc sample (as for **figure 1**)

Slika 7: XPS - O - 1s signal za oksidiran vzorec cinka (kot na **sliki 1**)

$$\frac{I_{ZnO}}{I_{Zn}}(\Theta) = \lambda_{ZnO}\, C_{ZnO}\, [1-\exp(-\frac{d_{ZnO}}{\lambda_{ZnO}\cos\Theta})]\ /$$

$$/\ \lambda_{Zn}\, c_{Zn} \exp(-\frac{d_{ZnO}}{\lambda_{ZnO}\cos\Theta}) \qquad (4)$$

where c_i is the concentration within layer i and d_i is the layer thickness.

For all the angle dependent measurements of the Zn - LMM Auger signal recorded for the oxidized zinc sam-

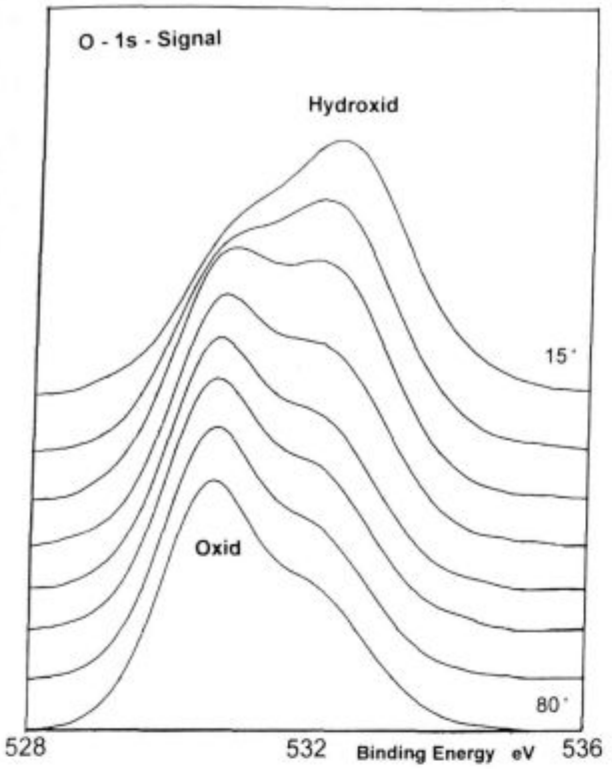

Figure 8: Angle dependent measurements for the XPS - O - 1s signal of an oxidized zinc sample (as for **figure 1**)

Slika 8: Meritve XPS - O - 1s signala za oksidiran vzorec cinka (kot na **sliki 1**) v odvisnosti od kota

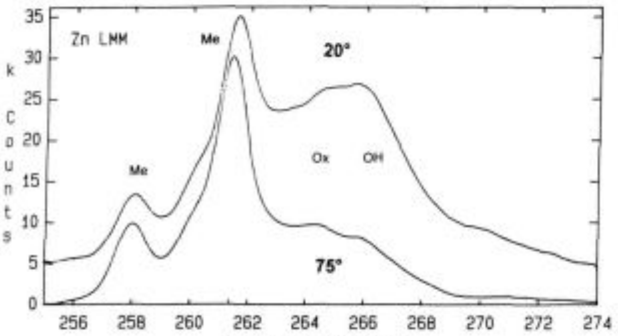

Figure 9: Zn - LMM Auger signal for an oxidized zinc sample (as for **figure 1**) recorded at 20° and 75° angle of analysis

Slika 9: Zn - LMM AES signal oksidiranega cinka (kot na **sliki 1**) posnet pri kotih analize 20° in 75°

ple a peak fitting for the total LMM signal was performed in a similar way as discussed before. The measured peak area ratios I_{ox}/I_{me} and I_{OH}/I_{me} for the oxide and the hydroxide layer in dependence on the angle of analysis ŽN1 = 0 are listed in the **table 2** together with the same peak area ratios calculated according to equation (3) and (4) by using a thickness of 13Å for the oxide layer and a thickness of 4Å for the hydroxide layer.

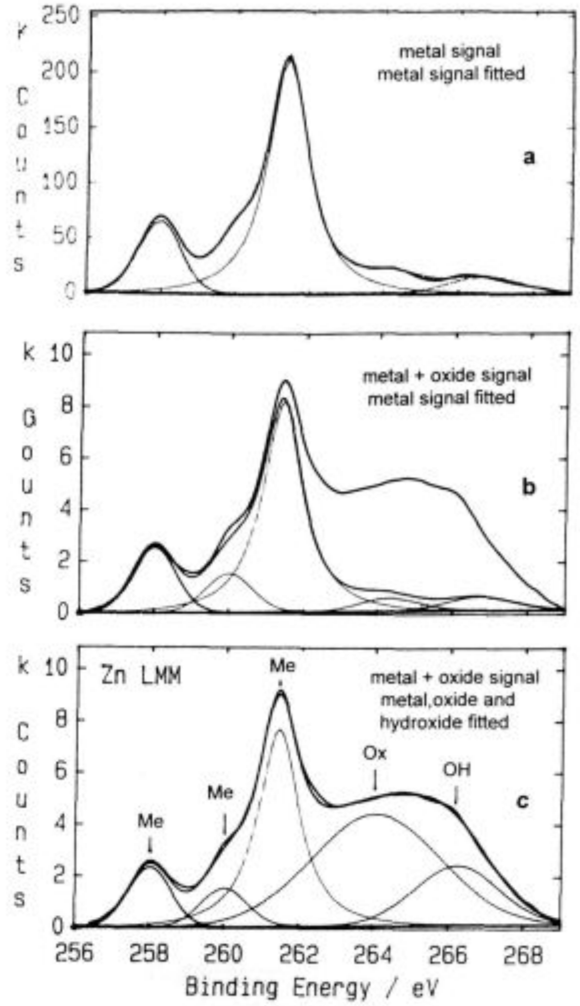

Figure 10: a) Zn - LMM Auger signal for a clean zinc sample, metal signal fitted; **b)** Zn - LMM Auger signal for an oxidized zinc sample (as for **figure 1**), metal part fitted; **c)** Zn - LMM Auger signal for an oxidized zinc sample (as for **figure 1**), metal oxide and hydroxide parts fitted

Slika 10: a) Zn - LMM AES signal za čisti cink; **b)** Zn - LMM AES signal za oksidiran cink (kot na **sliki 1**) kovinski del se prilega; **c)** Zn - LMM AES signal za oksidiran cink (kot na **sliki 1**) kovinski in hidroksidni del se prilega krivulji

Table 2: The angle dependent measurements of the Zn - LMM Auger signal for the oxide and hydroxide layer

Θ	I_{ox}/I_{me} (exp.)	I_{ox}/I_{me} (calc.)	I_{OH}/I_{me} (exp.)	I_{OH}/I_{me} (calc.)
78.1	13	14.7	11.7	10.5
76	9	9.05	5.8	4.1
73	5.6	5.44	2.8	2.2
70.5	3.5	3.9	1.8	1.65
68	3.15	3.1	1.25	1.05
64	2.3	2.25	0.8	0.7
60.5	1.9	1.8	0.6	0.54
58	1.5	1.6	0.5	0.42
45.4	1	1	0.25	0.28
32.9	0.79	0.77	0.18	0.18
21.4	0.65	0.67	0.15	0.17
13	0.66	0.63	0.14	0.14

For the first thickness determination, assuming a single oxide layer, a thickness of 15Å resulted, which is in very good agreement with a thickness of 17Å for the double layer consisting of a 13Å thick oxide and a 4Å thick hydroxide layer.

b) Thick layers (high temperature oxidation)

For future power plants high strength 9% Cr steels are being considered as construction materials for steam piping, headers and superheater tubes up to 600°C. For those materials it was found that the destruction of the protective oxide scale occurs during eposure in simulated combustion gas by the presence of water vapour. Although this detrimental effect of water vapour on the oxidation resistance of ferritic Cr - steels is known already for a long time no conclusive mechanism has been elucidated.

According to **figure 11**, illustrating schematically the variation with alloy Cr content of the oxidation rate and oxide scale structure, several different oxides are expected to appear for a Fe 9% Cr alloy and the above mentioned oxidation conditions.

The Fe 9% Cr alloys were oxidized isothermally in N_2 - 1% O_2 with and without various H_2O contents at 650°C. Using the crater ball equipment a crater was ground into the different oxidized samples. The crater ball process is illustrated in **figure 12**. After transferring the samples into the scanning Auger system the samples were sputter cleaned and SEM images recorded. Two examples will be presented to show the possibilities of this method. The first sample was oxidized in N_2 - 1% O_2 - 4% H_2O at 650°C for 3 hours and the second one for 10 hours, **figure 13 to 16**.

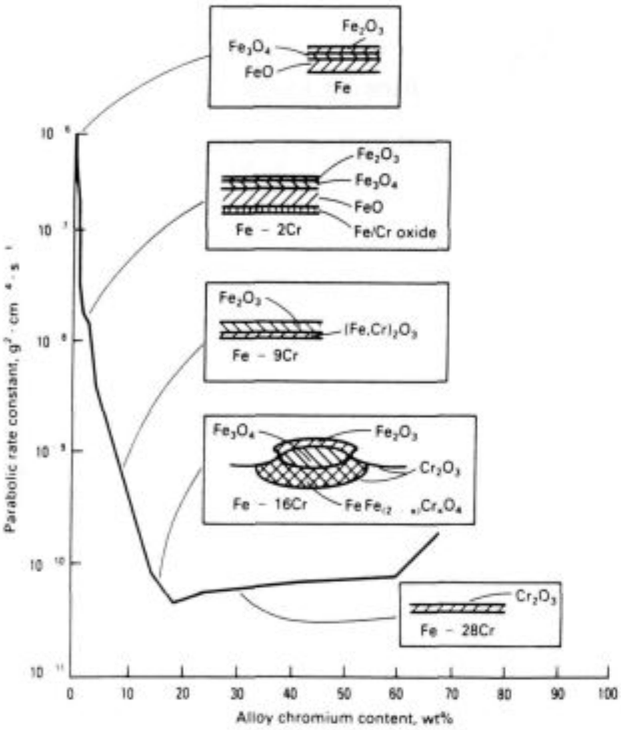

Figure 11: Schematics of the variation with alloy chromium content of the oxidation rate and oxide scale structure (based on isothermal studies at 1000°C in 0.13 atm oxygen)

Slika 11: Shematičen prikaz vpliva različnih vsebnosti kroma na stopnjo oksidacije in struktura oksida (izotermna oksidacija pri 1000°C in 0.13 atm kisika)

For the application of high temperature materials the formation of even, slow growing and well adherend oxide layers are desired. Al_2O_3 layers would be the thermodynamically most stable layers for nearly all conditions occuring during the use of the material. Quite often however the nucleation and adherence of the Al_2O_3 layers are not satisfactory. The improve the adherence of those layers oxidation of a model alloy Fe - 6% Al - 0,5% Ti and 50 to 100 ppm C were studied.

After oxidation of this alloy the samples were investigated by surface analytical methods. The oxide layers were fine grained, well adherent and represented an excellent protection against carburizing atmospheres. This was tested by long term investigations.

In order to find out the reason for this improvement of the protecting properties Auger depth profiles of the oxide layer on top of the model alloy were recorded. A typical example is shown in **figure 17**. The most striking feature of this depth profile is the simultaneous enrichment of carbon and titanium at the oxide metal matrix interface. This observation leads to the assumption that by formation of a TiC layer at the interface this improvement of the corrosion protecting properties could be realized.

By further detailed surface analytical investigations on a single crystal model alloy of the same composition and applying LEED (low energy electron diffraction) and AES it could be found out that on several low indexed crystal surfaces this TiC layer grows epitaxially.

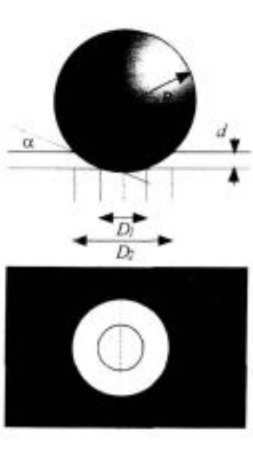

$$d = \frac{D_2^2 - D_1^2}{8R}$$

Figure 12: Schematic illustration of the crater ball etching process

Slika 12: Shematski prikaz kraterja dobljenega s procesom jedkanja s kroglico

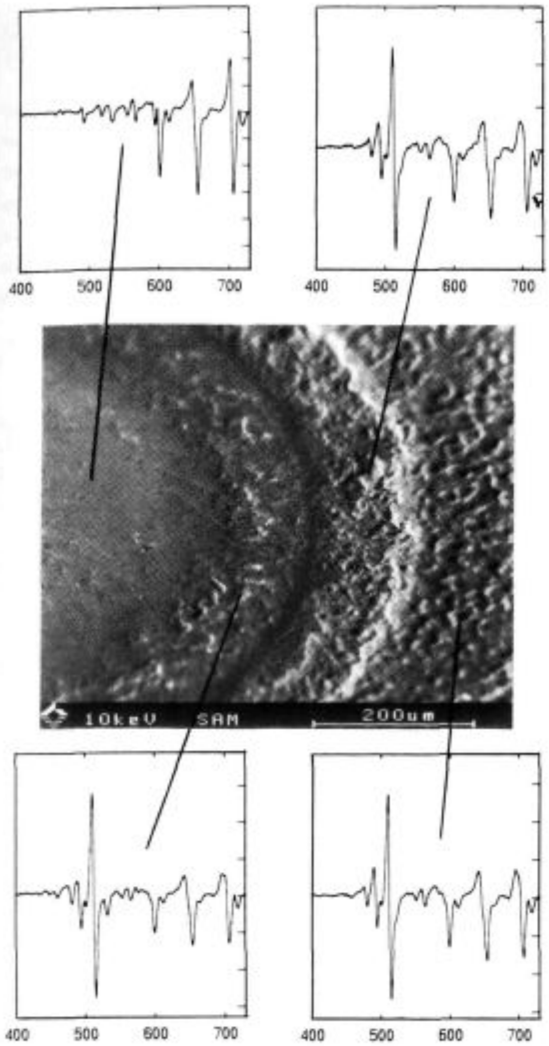

Figure 13: SEM of a part of the crater etched area of the Fe 9% Cr sample oxidized for 3 h (see text) and characteristic Auger point spectra for the different areas

Slika 13: SEM posnetek dela jedkalnega kraterja vzorca zlitine Fe 9% Cr, po 3 urah oksidacije (glej tekst) in karakteristični AES spektri, posneti na označenih mestih

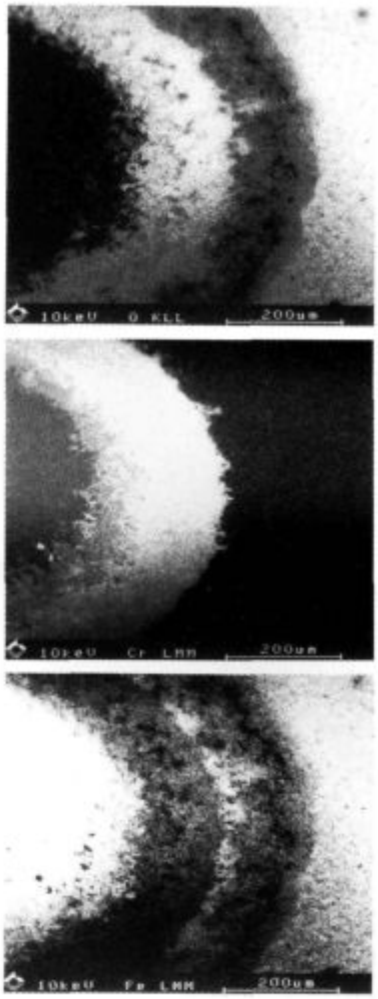

Figure 14: a) oxygen; **b)** chromium; **c)** and iron - images of the same surface area as shown in the SEM image in **figure 13**

Slika 14: a) kisik; **b)** krom; **c)** in železo - slike delov površin prikazanih na SEM posnetku **slike 13**

Metal dusting is known to be a dangerous high temperature corrosion phenomenon in petrochemistry and in reformer and direct reduction plants. In strongly carburizing atmospheres and temperatures from 400 to 800°C low alloyed Fe, Ni and Co base alloys are subject to a catastrophic carburization leading into a desintegration of the material into a dust composed of fine metal particles and carbon. For the reaction mechanism of the metal dusting process it was assumed that instable carbides form as an intermediate before they decompose to metal and carbon dust.

In order to get a more detailed picture of the metal dusting process an iron sample from the initial stages of the metal dusting process (680°C, 78% H_2, 15% CO and 0.5% H_2O) was removed from the carburizing atmosphere and using the crater ball equipment a crater was etched into the sample surface. After transferring the etched sample into the scanning Auger system a clean surface of the crater area was produced by Ar ion bombardement. Immediately afterwards Auger spectra and Auger images were recorded. The different chemical states of carbon within graphite and in carbide may easily be distinguished by Auger electron spectroscopy because of a characteristic Auger signal peak shape for the individual compounds. This is demonstrated by the Auger spectra in **figure 18**, which were recorded for different areas of the etched crater. Because of the different peak shape and a slight difference in peak energy graphite and carbide may be imaged separately. This is illustrated by the following figures, **figure 19a to figure 19d**, which show additional to a SEM image Auger elemental maps for carbidic carbon, carbon in graphitic form and iron of the crater region.

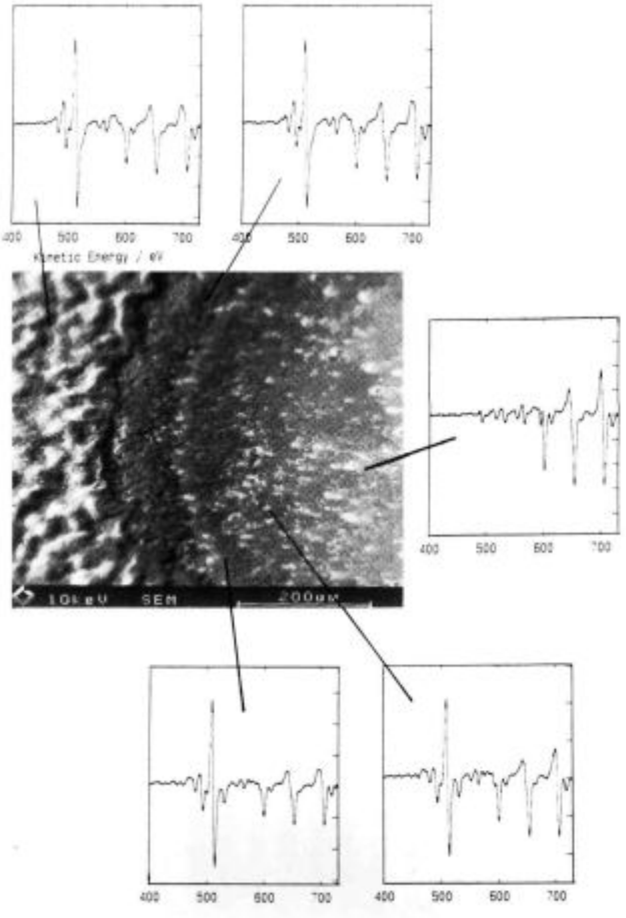

Figure 15: SEM of a part of the crater etched area of the Fe 9% Cr sample oxidized for 10 h (see text) and characteristic Auger point spectra for the different areas

Slika 15: SEM posnetek dela jedkalnega kraterja zlitine Fe 9% Cr, po 10 urah oksidacije (glej tekst) in karakteristični AES spektri, posneti na označenih mestih

The sum up the results from different kinds of investigations the following development of surface layers during the metal dusting process can be derived (schematically):

surface	surface	surface	surface
metal (Fe) +C diss.	Fe_3C	graphite	coke(Fe+C)
	metal(Fe) +C diss.	Fe_3C	graphite
		metal(Fe) +C diss.	Fe_3C
			metal (Fe) +C diss.

Well adherent and corrosion protecting oxide layers are of great importance for high temperature alloys. The adherence of the oxide layers is affected by the morphology and the chemical composition of the oxide/metal interface. In this study scanning Auger microscopy (SAM) is used to investigate the oxide/alloy interface of oxidized Fe-Cr-Al alloys (undoped or doped with Ti, Ce and

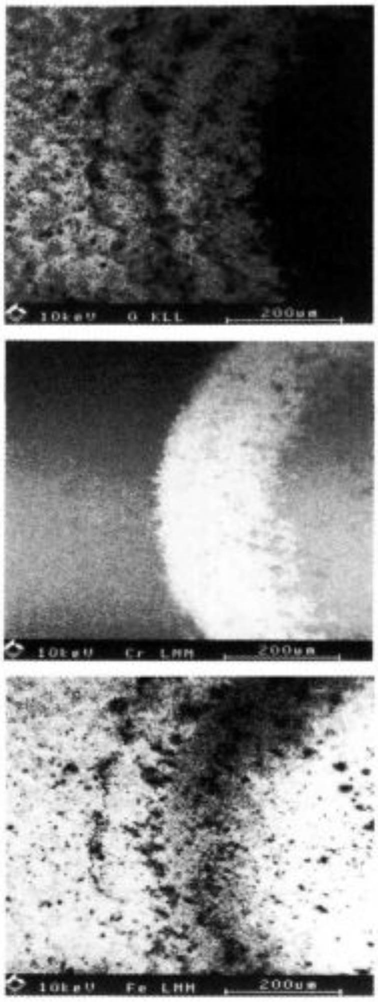

Figure 16: **a)** oxygen; **b)** chromium; **c)** and iron - images of the same surface area as shown in the SEM image in **figure 15**

Slika 16: **a)** kisik; **b)** krom; **c)** in železo - slike istih delov površin prikazanih na SEM posnetku **slike 15**

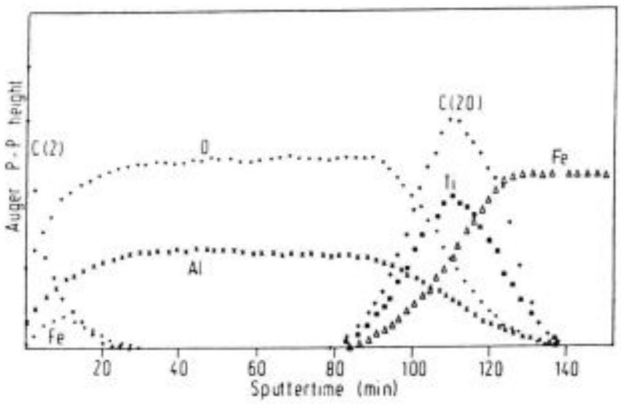

Figure 17: AES depth profile of a polycrystalline Fe-6Al-0,5Ti-0,01C sample oxidized for h at 1000°C and 10^{-19} bar oxygen partial pressure

Slika 17: AES profilni diagram polikristalne zlitine Fe-6Al-0,5Ti-0,01 C po 1/2 urni oksidaciji na temperaturi 1000°C in parcialnemu tlaku kisika 10^{-19} bar

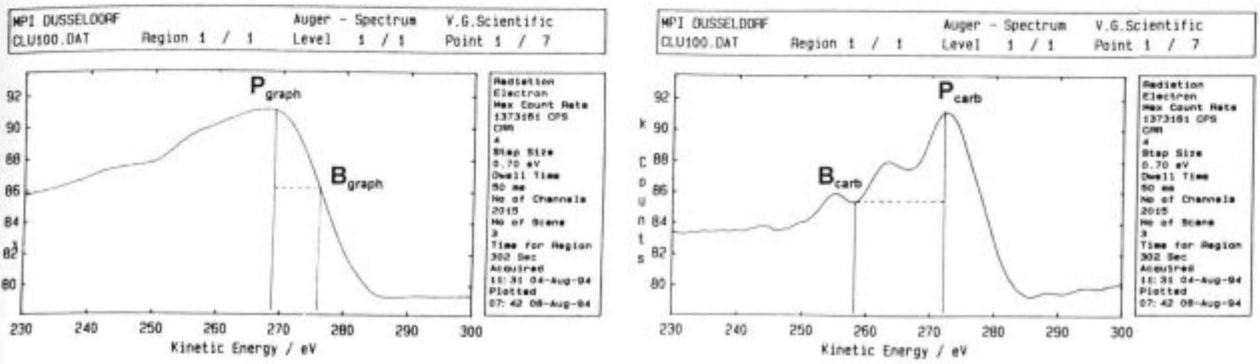

Figure 18: 'graphitic' (upper spectrum) and 'carbidic' carbon - KVV Auger signal of a crater ball etched Fe metal dusting sample indicating the different peak shapes and illustrating the peak (P_i) and background (B_i) energy positions for recording the Auger images

Slika 18: 'grafitni' (zgornji spekter) in 'karbidni ogljik' - KVV Augerjev signal s kroglico jedkanega Fe prašnatega vzorca z različnimi oblikami vrhov prikazuje vrh (P_i) in ozadje (B_i) in energijske pozicije za posnete AES spektre

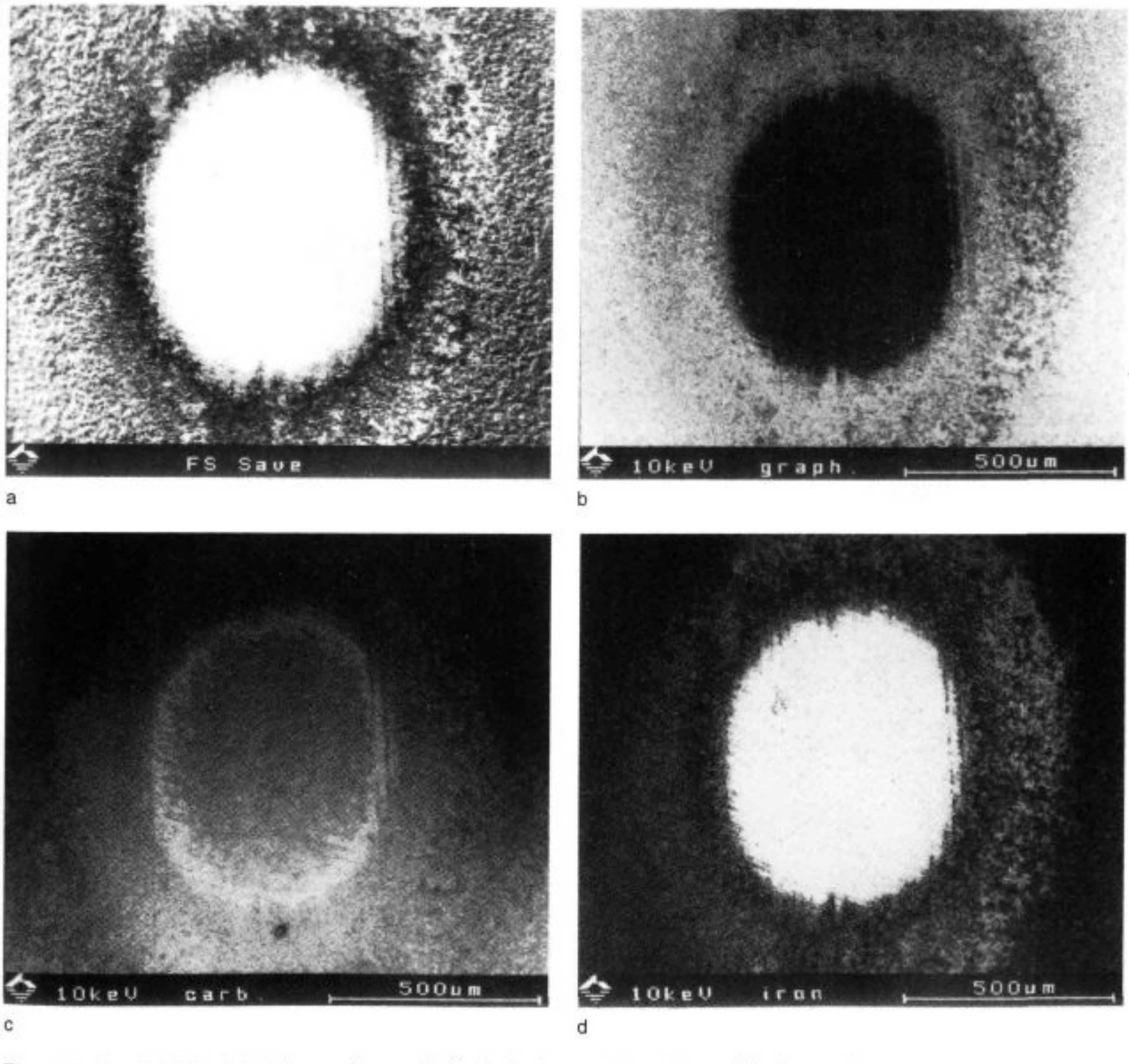

Figure 19: **a)** to **d)** SEM and SAM images of a crater ball etched and sputter cleaned Fe metal dusting sample

Slika 19: **a)** do **d)** SEM in SAM posnetki s kroglico jedkanega Fe prašnatega vzorca in z Ar^+ ioni jedkan Fe prašnat vzorec

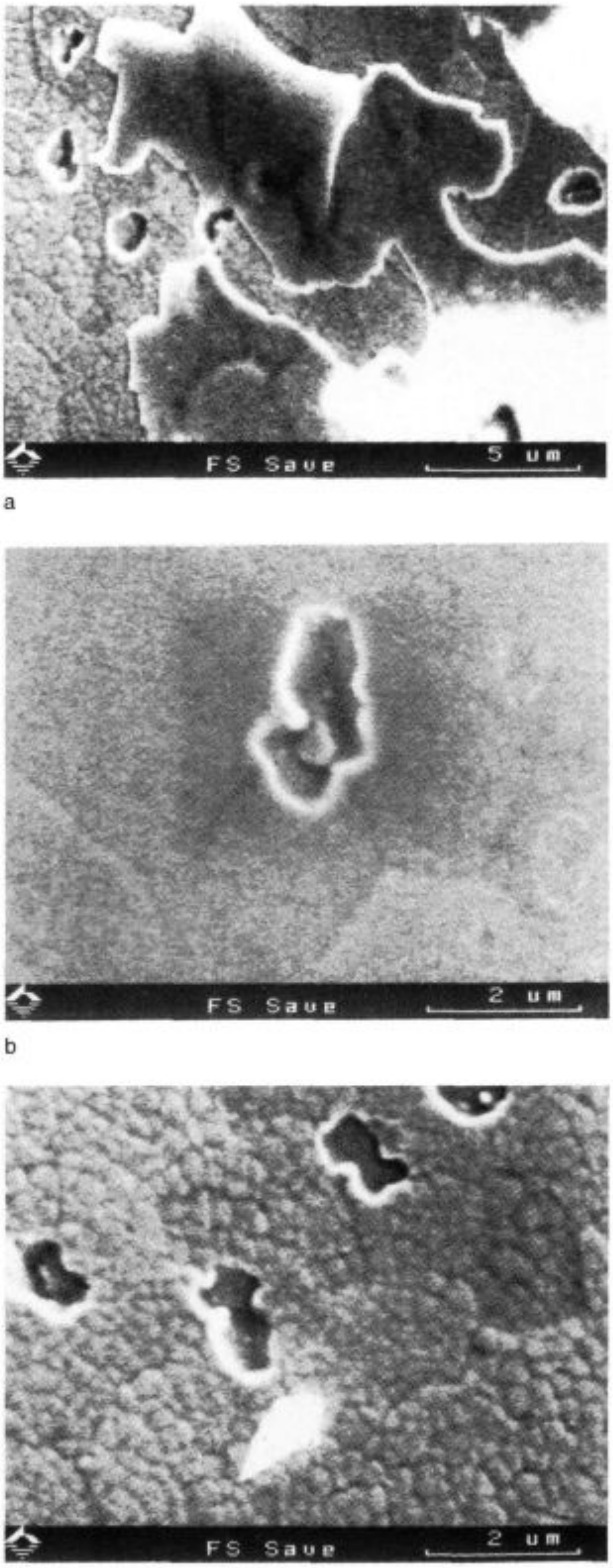

a

b

c

Figure 20: a) to c) SEM images of surface areas where the oxide layer is partly (or completely) removed
Slika 20: a) do c) SEM posnetki površine, kjer je bila oksidna plast delno (ali popolnoma) odstranjena

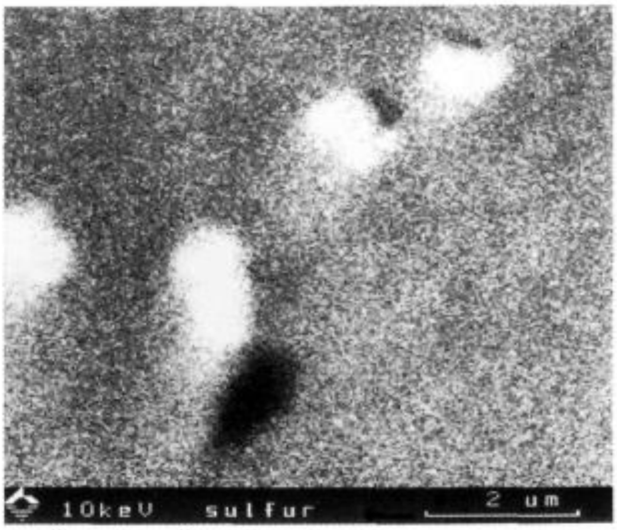

Figure 21: Sulfur image of the same surface area as shown in the SEM image of **figure 20 c)**
Slika 21: Posnetek žvepla na površini, prikazani na **sliki 20 c)**

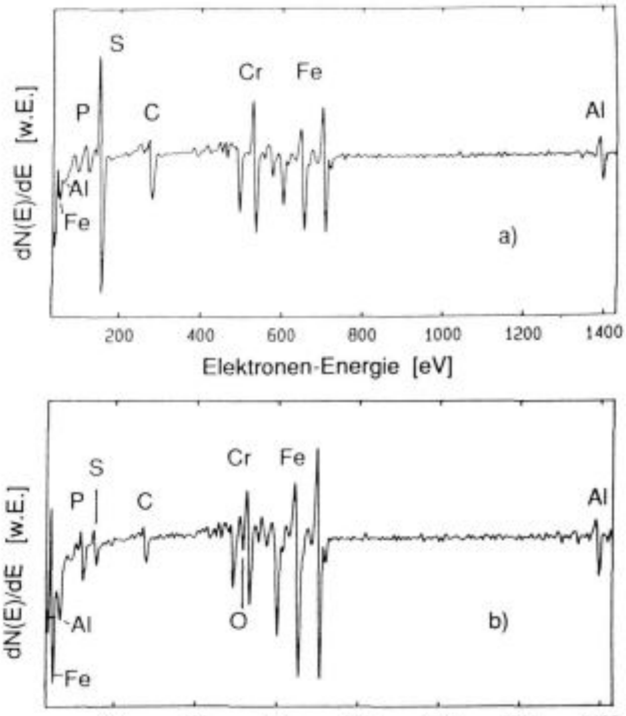

Figure 22: Auger point spectra of **a)** a void area; **b)** a rugged surface area
Slika 22: AES spekter posnet **a)** v vrzeli; **b)** na hrapavi površini

Y) after partly removing the oxide layer by in situ bending.

Thin Fe-Cr-Al ribbons, doped and undoped, were produced by meltspinning. Rectangular specimens were cut from the ribbons and ultrasonically cleaned in acetone. The samples were oxidized at 1273 K in a controlled He - O_2 gas mixture at an oxygen partial pressure of 133 mbar.

Bending of the specimens was performed in UHV at a residual pressure of 5×10^{-9} Pa to spall off parts of the oxide layer. The stripped oxide/metal interface was investigated by in situ SEM and SAM.

The metal surface shows individual voids and rugged parts, indicating imprints of the removed oxide, see SEM **figures 20a to 20c**. For the undoped alloy poor adherence of the oxide layer is observed. Sulphur is strongly enriched at the surface of the voids, **figure 21** shows a sulphur image of the sample area as for the SEM image in **figure 20c and 22a and 22b** Auger point spectra of a void surface and a rugged part of the interface.

On the Ti containing alloys the oxide layer is again poorly adherent. Sulphur is also strongly enriched at the surface of voids. On the Y- and Ce- containing alloys the oxide layer is well adherent and the sulphur concentration is below the detection limit.

The poor adherence of the oxide layers on undoped and Ti doped Fe-Cr-Al alloys is correlated to the presence of sulphur at the alloy surface. Sulphur enrichment is explained by sulphur segregation to the free alloy surface and by additional sulphide formation for the Ti containing alloys. The positive effect of Y and Ce on the adherence of the oxide layers is explained by sulphide precipitation in the bulk and thus preventing sulphur segregation to the free surface of the alloy.

4 Summary

Depending on the thickness of the surface layers to be analysed by surface analytical methods with respect to composition and thickness, different methods of depth profiling have to be applied. Valuable information may be derived from the results of the surface analytical investigations, leading to a better understanding of the growth mechanisms and the corrosion protecting properties of oxide layers on metal surfaces.

5 References

[1] Guidelines for methods of testing and research in high temperature corrosion, European Federation of Corrosion Publications 14, The Institute of Materials, London, 1995, 189

[2] in *Practical Surface Analysis*, eds. D. Briggs and M. P. Seah, Wiley, Chichester, 1990

[3] S. Tanuma, C. J. Powell and D. R. Penn, *Surf. Interface Anal.*, 20a, 1993, 77

[4] S. Lecuyer, A. Quemerais and G. Jezequel, *Surf. Interface Anal.*, 18, 1992, 257

I M T®

INŠTITUT ZA KOVINSKE
MATERIALE IN TEHNOLOGIJE

INSTITUTE OF METALS
AND TECHNOLOGY

1001 LJUBLJANA, LEPI POT 11, SLOVENIJA, POB 431
Phone.: +386 61/125 11 61, Fax: +386 61/213 780

VACUUM HEAT TREATMENT LABORATORY

Vacuum Brazing

Universally accepted as the most versatile method of joining metals. Vacuum Brazing is a precision metal joining technique suitable for many component configurations in a wide range of materials.

ADVANTAGES

- Flux free process yields clean, high integrity joints
- Reproducible quality
- Components of dissimilar geometry or material type may be joined
- Uniform heating & cooling rates minimise distortion
- Fluxless brazing alloys ensure strong defect free joints
- Bright surface that dispense with expensive post cleaning operations
- Cost effective

Over five years of Vacuum Brazing expertise at **IMT** has created an unrivalled reputation for excellence and quality.

Our experience in value engineering will often lead to the use of Vacuum Brazing as a cost effective solution to modern technical problems in joining.

INDUSTRIES

- Aerospace
- Mechanical
- Electronics
- Hydraulics
- Pneumatics
- Marine
- Nuclear
- Automotive

QUALITY ASSURANCE

Quality is fundamental to the **IMT** philosophy. The choice of process, all processing operations and process control are continuously monitored by **IMT Quality Control Department**.

The high level of quality resulting from this tightly organised activity is recognised by government authorities, industry and International companies.

Kovine, zlitine, tehnologije/30/1996/6/509-516

Aluminium and Magnesium Based Metal Matrix Composites

Kompoziti na osnovi Al in Mg

K. U. Kainer[1], Technische Universität Clausthal-Zellerfeld, Germany

Prejem rokopisa - received: 1996-10-01; sprejem za objavo - accepted for publication: 1996-11-04

In motor-cars metal matrix composites (MMC's) are employed in braking systems and engine components. Other applications for these materials have been developed in energy and in information applications. The potentional of composite materials is very great because the properties can be tailored according to the application. There are many possible material combinations and processing techniques which can be employed. For structural applications standard light metal are often strengthened by ceramic fibres or particles. The performance and potential of composites will be discussed using examples of reinforced aluminium and magnesium alloys.

Key words: Al and Mg based MMC's, Al and Mg alloys, SiC and Al_2O_3 as reinforcement, properties, applications, processing techniques

Kompoziti s kovinsko osnovo, ojačani s keramičnimi delci ali vlakni se danes že uporabljajo kot deli zavornega sistema in motorjev z notranjim izgorevanjem. Razvite so tudi posebne vrste teh materialov, ki so uporabni na področju energetike in informatike. Uporabnost kompozitnih materialov je vsestranska, ker lahko njihove lastnosti prilagajamo potrebam uporabe. Možne so številne kombinacije materialov (kovinska osnova / keramična ojačitev) in postopkov njihove izdelave. Kompoziti, ki se uporabljajo kot konstrukcijski materiali so najpogosteje sestavljeni iz lahke kovinske osnove in keramičnih delcev ali vlaken. Prispevek obravnava predvsem dosežene lastnosti in možnosti uporabe kompozitov z osnovo iz Al ali Mg zlitin, ki so diskontinuirno ojačane z SiC ali Al_2O_3 delci oziroma kratkimi vlakni.

Ključne besede: kompoziti s kovinsko osnovo, Al in Mg zlitine, SiC in Al_2O_3 kot ojačitvena faza, lastnosti, uporaba, postopki izdelave

1 Introduction

The strenuous efforts to develop metal matrix composites with light metal matrices in the eighties have paid off with successful applications in automobile and transport systems. Worthy of mention are partially reinforced pistons, hybrid reinforced engine blocks for cars or trucks as well as particle reinforced brake discs for light lorries, motocycles, cars or rail vehicles. Further fields of applications are military aircraft and space craft. The innovative materials are interesting possibilities in the development of modern materials because the properties of MMC's can be tailored for a particular application and hence MMC's can fulfill all requirements of the designer. Such materials become important when the property profile cannot be achieved by the conventional light metal alloys. The specific strength as outstanding advantage of light metal MMC's is however under pressure from competing technologies such as powder metallurgy of polymer technology. The advantages of composites are only realised if a resonable cost performance ratio is achievable on production of the component. In this respect it is important for economic and ecological reasons to recycle scrap components, production waste, etc.

The aims in the reinforcement of metal matrix functional or structural materials are on the one hand the optimisation of some critical properties at the same time as maintaining other properties and on the other hand a complete change in the property profile of a class of materials. The reinforcement of light metals opens, for example, an extension of the application potential where weight reduction of components is very desirable at the same time as optimisation of component properties. The development aims of light metal matrix composites thus can be sumarised as follows:

- increase in yield strength, ultimate tensile strength and fatigue strength at room temperature whilst maintaining minimum values of ductility or toughness,
- increase in hot strength, fatigue strength and creep resistance at elevated temperatures compared to conventional materials,
- reduction in the coefficient of thermal expansion of light metal alloys to values comparable with steels,
- improvement in the stability of light metals to temperature changes,
- improvement in damping behaviour,
- improvement in the wear resistance through addition of hard materials,
- improvement in weight specific properties (strength and E-modulus).

Discontinuous particle, fibre or whisker reinforced light alloys are most likely to fulfill design criteria because the components are relatively cheap and production of components in large numbers is possible. Further advantages are the relatively high isotropy of properties compared to the long continuous fibre reinforced light metals and the possibility of further forming by forging and machining.

---

[1] Dr.-Ing. habil. K. U. KAINER
Technische Universität Clausthal
Institut für Werkstoffkunde und Werkstofftechnik, Clausthal-Zellerfeld, Germany

2 Combination of materials for light alloy composites

The obvious candidates for light metal matrices for composite materials are the easily workable, conventional alloys. Particulary when powder metallurgical (P/M) production techniques are employed it is possible to consider special alloys with specific compositions. P/M technology allows the use of alloys with super satorated or metastable phases. The alloys are free from segregation problems as often observed after conventional solidification.

Examples of extensively investigated matrix alloys are[1-8]:

Conventional Casting Alloys:
  Al alloys: AlSi12CuMgNi
    AlSi9Mg
    AlSi7 (A 356)
  Mg alloys: MgAl9Zn1 (AZ91)
    MgAl2RE2Zr1 (MSR, QE 22)
Conventional wrought alloys:
  Al alloys: AlMgSiCu (6061)
    AlCuSiMn (2014)
    AlZnMgCu1 5 (7075)
  Mg alloys: MgAl3Zn (AZ 31)
    MgZn6Zr (ZK 60)
    MgZn6Cu3 (ZC 63)
Special alloys:
  Al alloys: Al-Cu-Mg-Li (8090)
  Mg alloys: Mg99,5 + RE, Ca, Zr, Ba, Br, Sb or Sn (1-2.4%)

A wide variety of reinforcement materials are available with a wider range of properties. The choice depends on the method chosen for production and on the matrix alloy system. In general the requirements are:

- low density,
- mechanical compatability (a thermal coefficient of expansion which matches the matrix),
- chemical compatability,
- thermal stability,
- high elastic modulus, high compressive and tensile strength,
- good workability,
- economicy.

These demands can be fulfilled virtually only by inorganic reinforcing materials. Often only ceramic particles or fibres or carbon fibres are used to reinforce metals. The use of metallic fibres results in prohibitive increases in density. Which component is chosen depends on the matrix material and the property profile of the particular application. Information of available particles, short fibres, whiskers and continuous fibres for reinforcement of metals is collected in **Table 1** and in references[9,10]. The preparation, working and means of applications of the various reinforcements depends on the method chosen to produce the composite (see[1]). A combinated application of two and more reinforcement material is possible (hybrid technique)[1,9].

3 Production of light metal composites

There are several possible methods of producing semi finished material and components in light metal composites, which depend primarily on the component geometry and the material systems (matrix / reinforcement). The process must be divided into preparation of suitable starting material, production of the semi finished material or component and finishing operations. For economic reasons near net shape production should be attempted to minimise mechanical finishing operations. In general the following production techniques are available:

- *Casting techniques*
  - infiltration of short fibres, particle or hybrid preforms by squeeze casting, vacuum infiltration or pressure infiltration[1,4,7,8],

Table 1: Examples of particles, whisker, continuous and discontinuous fibres used a reinforcements in metal alloys (*CTE = coefficient of thermal expansion, [1)]PAN based fibres, [2)]pitch based fibres)

reinforcement	producer	diameter (μm)	density (gcm^{-3})	E-modulus (GPa)	tensile strength (MPa)	CTE* ($10^{-6}K^{-1}$) axial
FP α-Al_2O_3	Du Pont	20	3.9	380	> 1400	7.6
Altex alumina fibre	Sumitomo	17	3.2	300	2000	8.8
Nicalon SiC-fibre	Nippon Carbon	15	2.6	185	2700	3.5
Torayca T-300[1)]	Toray	7	1.8	230	3530	-0.26
Torayca M-40[1)]	Toray	5.5	1.8	392	2650	-1.3
Thornel P 75[2)]	Amoco	10	2.0	520	2370	-1.4
Saffil RF disk α-Al_2O_3	ICI plc.	1-5	3.3	300	2000	4.7
SiC-whiskers Silar	DWA Composites Specialities	0.6	3.2	690	6900	4.1
SiC-particles	Norton AS, ESK, Kempten	various	3.2	ca.400	-	4.7
alumina platelets	Elf, ESK, Kempten	various	3.9	ca.380	-	3.6
alumina particles	H.C. Starck, ESK, Kempten	various	4.0	ca.380	-	9.5

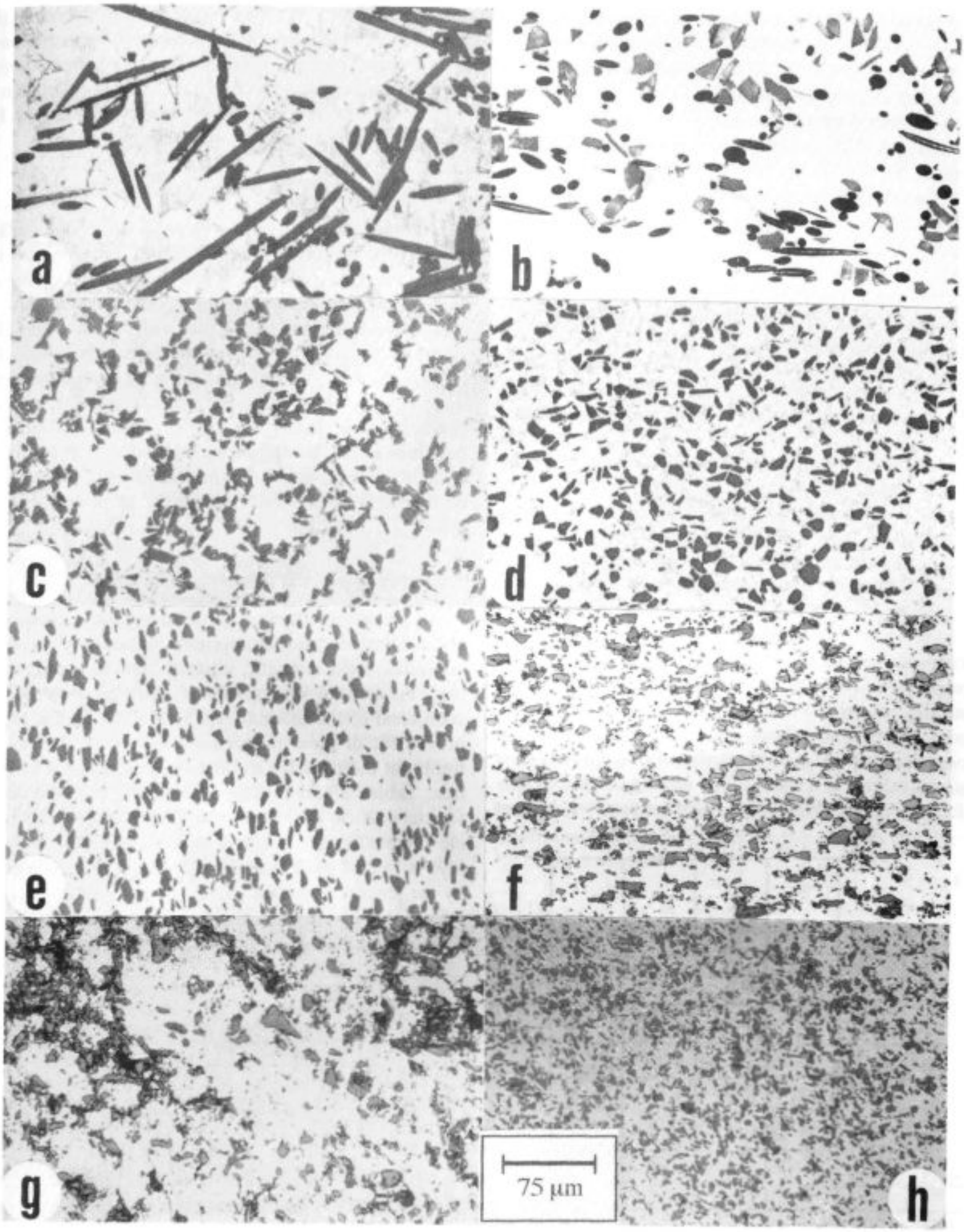

Figure 1: Collection of typical microstructures of various light metal composites as a function of reinforcement and production process.
a) Al_2O_3 short fibre reinforced magnesium.
b) Al_2O_3-SiC hybrid reinforced magnesium.
c) SiC particle reinforced aluminium (chill cast).
d) SiC particle reinforced aluminium (pressure die cast).
e) SiC particle reinforced aluminium (cast and extruded).
f) SiC particle reinforced aluminium (extruded powder blend).
g) SiC particle reinforced magnesium (spray formed).
h) SiC particle reinforced magnesium (spray formed and extruded)

  - reaction infiltration of fibre or particle preforms[11,12],
  - production of prematerial by stirring particles into metallic melts with subsequent sand casting, chill casting or pressure casting[2,3].
- *Powder metallurgy techniques*
  - extrusion or forging of metal powder - particle mixtures[5,6],
  - extrusion or forging of spray formed semi finished material[1,13,14].
- Further processing of semi finished cast material by thixocasting or forming, extrusion[15], forging, cold forming or superplastic forming,
- Joining or welding of semi finished products,
- Finishing by machining.

4 Structure and properties of light metal composites

The structure of composites is determined by the nature and shape of the reinforcing components, their distribution and orientation by the production process. Typical microstructures of various short fibre and particle reinforced light metals are shown in **Figure 1**. In the case of short fibre reinforced composites a planar isotropic distribution of the short fibres is formed as a result of the production of the fibre preform. The pressure supported sedimentation technque leads to a layer like structure **(Figures 1a & b)**[10]. The direction of infiltration is generally normal to these planes. The cast particle reinforced light metals show, depending on the working processing, typical particle distributions. Gravity cast material exhibit as a result of the casting conditions particle free regions **(Figure 1c)**, whereas pressure die cast materials show a much better particle distribution **(Figure 1d)**. An even distribution is achieved by extrusion of semi finished material **(Figure 1e)**. An extremely homogeneous particle distribution is obtained by extrusion of mixed powders or spray formed materials **(Figures 1 f-g)**.

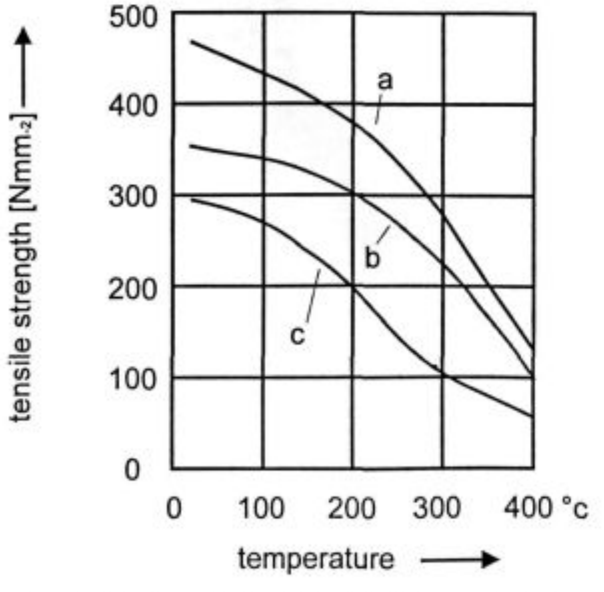

Figure 2: Comparison of the temperature dependence of the tensile strength of the unreinforced and reinforced piston alloy AlSi12CuMgNi (KS 1275)[7]

a) KS 1275 with 20 vol.% SiC whiskers,

b) KS 1275 with 20 vol.% Al_2O_3 short fibres,

c) KS 1275 unreinforced

Properties of short fibre reinforced aluminium

An increase in strength with increasing fibre content in short fibre reinforced aluminium is actually observed as the example AlSi12CuMgNi with 20 vol.% Al_2O_3 shows in **Figure 2**. Composites of light metal casting alloys is not made just to increase only the strength. The effect alone would not be justifiable economically. The improvement of the properties at high temperature with a doubling of the strength **(Figure 2)** and the rotating bending fatigue strength at 300°C **(Figure 3)**, opens up possibilities for use as piston material or cylinder liners. A dramatic increase of the thermal shock resistance can be achieved at temperature of 350°C as is shown in **Figure 4**.

Properties of particle reinforced aluminium

In general addition of particles to light metals, such as magnesium and aluminium increases the elastic modulus, yield strength, ultimate tensile strength, the hardness and the wear resistance and also decreases the coefficient of the thermal expansion. The degree of improvement of these properties depends on the volume fration of the particles and the chosen means of production. **Tables 2 and 3** show a collection of properties of various particle reinforced aluminium alloys. The particle volume fraction in stirred in particle reinforced Al alloys is limited to about 20 vol.%. This limit is imposed by the process. A maximum tensile strength of over 500 MPa and E-moduli of 100 GPa are possible for this particle content. Higher particle contents can be achieved by

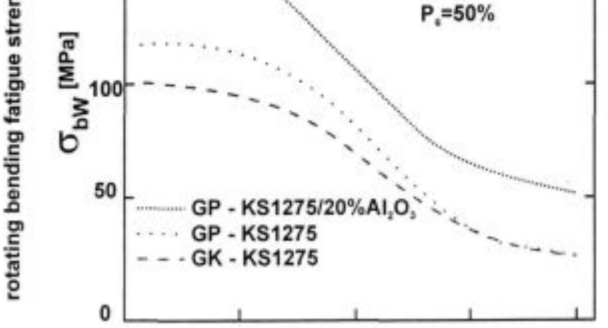

Figure 3: Change in the rotating bending fatigue strength of the unreinforced and reinforced (20 vol.% Al_2O_3) piston alloy AlSi12CuMgNi (KS 1275) with increasing temperature[8] (GK = chill cast GP = squeeze cast)

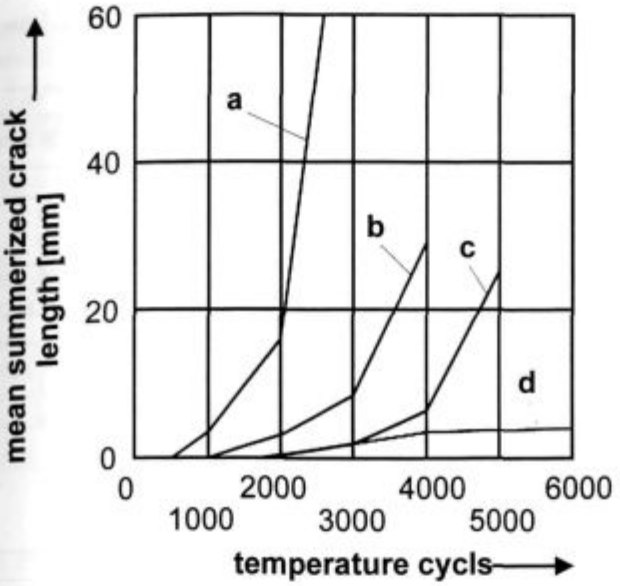

Figure 4: Temperature shock resistance of the fibre reinforced piston alloy AlSi12CuMgNi as a function of the fibre content for a temperature of 350°C[7]:
a) unreinforced,
b) 12 vol.% Al_2O_3 short fibres,
c) 17.5 vol.% Al_2O_3 short fibres,
d) 20 vol.% Al_2O_3 short fibres

infiltration of particle preforms with higher particle volume fraction. The materials then assume increasingly the characteristics of ceramics. On tensile loading premature failure occurs. The small thermal expansion is an excellant characteristic despite the metallic features.

There is a limit to the particle content of about 13-15 vol.% also for spray formed materials. The use of special alloys e.g. with lithium additions can nevertheless lead to high specific properties. If powder metallurgical technique involving extrusion and forging are applied then the particle content can be increased to more than 40 vol.%. As the result of high particle content and the resultant fine grain of the matrix very high strength of up to 760 MPa, very high E-Moduli of 125 GPa and low coefficients of expansion of 17 x $10^{-6}K^{-1}$ can be achieved. Unfortunately the elongation to fracture and the fracture toughness deteriorate. The values lie, however, in part above those for casting alloys.

Properties of discontinuously reinforced magnesium alloys

In general the strengthening effects in discontiuous reinforced composites is smaller than in continuous fibre reinforced materials but the properties are more isotropic. In the following the properties of short fibre or particle reinforced magnesium composites are listed. **Table 4** shows the 0.2 yield strength, the temperature dependence of the ultimate tensile strength and the ductility of different magnesium alloys reinforced with 20 vol.% Saffil short fibre. The properties are compared with of these of unreinforced alloys. Information about hardness, Young's modulus and coefficient of thermal expansion (CTE) are included. The results show that the main advantages of this type of composite material are the high specific strength at elevated temperatures, the increase of Young's modulus and the reduction of the CTE. The improvement of the properties depends on the volume content of the short fibres. In the range of 15 -22 vol.% short fibres the most promising properties were measured[4,16]. With a higher fibre content problems in the infiltration arises which reduces the strength and ductility of the composites.

Table 2: Selected properties of typical cast aluminium composites, prepared by chill, pressure die casting or reaction infiltration[2,3,11]. (T6 = solution annealed and aged, T5 = aged; *after ASTM G-77: cast iron 0,66 mm³; **CTE = coefficient of thermal expansion, a) after ASTM E-399 and B-645; b) after ASTM E-23), n.i. = no information

Material		Yield stress (MPa)	Tensile strength (MPa)	Elongation to fracture (%)	Young's modulus (GPa)	a) Fracture toughness. b) impact strength	Wear* volume decrease (mm³)	Thermal conductivity 22°C (cal/cm s K)	CTE** 50-100°C ($10^{-6}K^{-1}$)
Identification	Composition								
Gravity casting (chill casting)						a) (MPa $m^{1/2}$)			
A356-T6	AlSi7Mg	200	276	6.0	75.2	17.4	0.18	0.360	21.4
F3S.10S-T6	AlSi9Mg10SiC	303	338	1.2	86.9	17.4	n.i.	n.i.	20.7
F3S.10S-T6	AlSi9Mg20SiC	338	359	0.4	98.6	15.9	0.02	0.442	17.5
F3K.10S-T6	AlSi10CuMgNi10SiC	359	372	0.3	87.6	n.i.	n.i.	n.i.	20.2
F3K.20S-T6	AlSi10CuMgNi20SiC	372	372	0.0	101	n.i.	n.i.	0.346	17.8
Die casting					b) (J)				
A390	AlSi17Cu5Mg	241	283	3.5	71.0	1.4	0.18	0.360	21.4
F3D.10S-T5	AlSi10CuMnNi10SiC	331	372	1.2	93.8	1.4	n.i.	0.296	19.3
F3D.20S-T5	AlSi10CuMnNi20SiC	400	400	0.0	113.8	0.7	0.018	0.344	16.9
F3N.10S-T5	AlSi10CuMnMg10SiC	317	352	0.5	91.0	1.4	n.i.	0.384	21.4
F3N.20S-T5	AlSi10CuMnMg20SiC	338	365	0.3	108.2	0.7	0.018	0.401	16.6
Reaction infiltration		Bending strength (MPa)		Density (g/cm³)		a) (MPa $m^{1/2}$)			
MCX-693™	Al+55-70 %	SiC	300	2.98	255	9.0	n.i.	0.430	6.4
MCX-724™	Al+55-70 %	SiC	350	2.94	226	9.4	n.i.	0.394	7.2
MCX-736™	Al+55-70 %	SiC	330	2.96	225	9.5	n.i.	0.382	7.3

Table 3: Properties of aluminium wrought alloy composites, manufactures information after[5,6,13-15]. (T6 = solution annealed and aged), *after ASTM G-77: cast iron 0,66 mm^3; **CTE = coefficient of thermal expansion, n.i. = no information.

Material Identification	Composition	Yield stress (MPa)	Tensile strength (MPa)	Elongation to fracture (%)	Young's modulus (GPa)	a) Fracture toughness. b) impact strength	Wear* volume decrease (mm^3)	Thermal conductivity 22°C (cal/cm s K)	CTE** 50-100°C ($10^{-6}K^{-1}$)
Cast starting material (extruded or forged)									
6061-T6	AlMg1SiCu	355	375	13	75	30	10	0.408	23.4
6061-T6	+ 10% Al_2O_3	335	385	7	83	24	0.04	0.384	20.9
6061-T6	+ 15% Al_2O_3	340	385	5	88	22	0.02	0.336	19.8
6061-T6	+ 20% Al_2O_3	365	405	3	95	21	0.015	n.i.	n.i.
Powder metallurgically prepared starting material (extruded)									
6061-T6	AlMg1SiCu	276	310	15	69.0	n.i.	n.i.	n.i.	23.0
6061-T6	+ 20% SiC	397	448	4.1	103.4	n.i.	n.i.	n.i.	15.3
6061-T6	+ 30% SiC	407	496	3.0	120.7	n.i.	n.i.	n.i.	13.8
7090-T6	AlZn8Mg2Co1.5Cu1	586	627	10.0	73.8	n.i.	n.i.	n.i.	n.i.
7090-T6	+ 30% SiC	676	759	1.2	124.1	n.i.	n.i.	n.i.	n.i.
6092-T6	AlMg1Cu1Si17.5SiC	448	510	8.0	103.0	n.i.	n.i.	n.i.	n.i.
6092-T6	AlMg1Cu1Si25SiC	530	565	4.0	117.0	20.3	n.i.	n.i.	n.i.
Spray formed starting material (extruded)									
6061-T6	+ 15% Al_2O_3	317	359	5	87.6	n.i.	n.i.	n.i.	n.i.
2618-T6	+ 13% SiC	333	450	n.i.	89.0	n.i.	n.i.	n.i.	19.0
8090-T6	AlLi2.5CuMg	480	550	n.i.	79.5	n.i.	n.i.	n.i.	22.9
8090-T6	+ 12% SiC	486	529	n.i.	100.1	n.i.	n.i.	n.i.	19.3

Table 4: Properties of short as cast fibre reinforced magnesium composites (CTE = coefficient of thermal expansion, n.d. = not determined, rt = room temperature, 0.2 YS = 0.2 yield strength, UTS = ultimate tensile strength)[4]

	Cp-Mg		AS 41		AZ 91		QE 22	
	matrix	comp.	matrix	comp.	matrix	comp.	matrix	comp.
0.2 YS (MPa) (rt)	70	220	125	240	160	230	180	250
UTS (MPa) (rt)	80	240	193	270	220	280	250	300
Elongation (%) (rt)	5.0	2.2	9.0	1.0	4.8	1.8	4.5	1.6
Young's modulus (GPa)	46	56	49.8	77.7	46	64	46	74
UTS (100°C) (MPa)	65	240	175	250	200	270	240	285
UTS (200°C) (MPa)	45	180	150	240	120	220	200	245
UTS (300°C) (MPa)	30	120	n.d.	n.d.	60	130	125	180
Vickers hardness HV10 (kp/mm^2)	40	75	n.d.	n.d.	65	140	75	125
CTE ($10^{-6}K^{-1}$)*	26.5	21.5	24.0	18.0	27.0	20.5	26.0	20.0

The second group of discontinuous reinforced composites are particle reinforced magnesium alloys. The high range of properties is achieved by the limitless variation possibilities of alloys, type of particle and production techniques. In general only a modest improvement in the strength by addition of particles is observed. But with the increase in hardness, wear resistance and Young's modulus together with the reduction of the CTE the material becomes interesting for commercial application[17]. The **Tables 5 and 6** show the propety profiles of different produced particle reinforced magnesium composites. The SiC particles used for composite materials in **Table 5** have irregular blocky shape. These particles were treated to achieve a smooth surface without sharp tips. The result are composites with high strength and very good ductility combinated with high hardness, Young's modulus and low CTE values. The P/M production technique unfluences the properties of the particle reinforced composites, as shown in **Table 6**. The highest strength but with low ductility is measured for spray formed and extruded composites. The best properties were achieved for direct powder forged composites, a near net shape production technique. With a special preform technique it is possible to produce particle or hybrid reinforced composites by squeeze casting. The properties of material system investigated are listed in **Table 5**. As reinforcement a SiC-particles-fibre hybrid preform and aluminia platelets were used. The material shows lower strength and ductility due to the solidification mi-

Table 5: Properties profile of P/M produced or squeeze cast QE 22 composites with different additions of reinforcement (SiC-particles, hybrid SiC-Al_2O_3-preforms, Al_2O_3-platelets in vol.%)[17]

	0.2 yield strength (MPa)	UTS (MPa)	Elongation to fracture (%)	Young's modulus (GPa)	Brinell hardness HB31,25/2,5	CTE rt-300°C ($10^{-6}K^{-1}$)
Powder metallurgy produced composites (T6) condition						
P/M QE 22 - T6	175	260	18	43	70	27.1
QE 22 + 10% SiC	200	265	10	48	87	21.4
QE 22 + 15% SiC	210	290	10	58	95	20.0
QE 22 + 20% SiC	225	315	6.5	66	120	18.2
QE 22 + 25% SiC	245	325	4.0	73	108	16.6
Squeeze cast composites						
Sq/C QE 22 - T6	185	262	5.2	69	48	27.0
QE 22+20%SiC hybrid	265	285	2.4	74	120	18.9
QE 22+25%SiC hybrid	270	282	1.0	80	125	17.5
QE 22 + 20% Al_2O_3 platelets	177	250	1.0	85	110	19.8

crostructure which is different to the rapid solidified structure by use of P/M technologies.

Table 6: Influence of the production technique on the properties of P/M QE 22 + 15 vol% SiC-particles-composites

	Unreinforced QE22	Spray formed and extruded	Extruded powder blends	Forged powder blends
0.2 yield strength (MPa)	180	300	250	220
UTS (MPa)	252	320	300	300
Elongation to fracture (%)	16.0	1.0	4.0	4.5
Vickers hardness (HV10 kp/mm^2)	82	92	88	94
Young's modulus (GPa)	46	69	70	79
CTE (10^{-6}K^{-1})	27.1	20.5	21.1	20.8

5 Possible uses and applications for metallic matrix composites

Light metal composites are interesting materials for automobile components in the engine (*oscillating parts:* valve system, connecting rod, pistons and piston pin; *covers:* cylinder head, crankshaft main bearing; *motor block:* partially reinforced cylinder liner). An example for a successful application involving aluminium composites is the partially reinforced short fibre aluminium pistons in which the combustion chamber is reinforced with Al_2O_3 short fibres. Comparable component properties are only possible in powder metallurgical produced aluminium alloys or in iron pistons. The reason for the use of composites are, as explained above, improved high temperature properties. Similar considerations apply to partially reinforced cylinder blocks. In this case the critical areas, the bridges and cylinder surfaces are reinforced. The same applies to the reinforcement of aluminium cylinder heads where cracking in the combustion chamber is the life limiting factor. **Figure 5** shows the development goal on increasing the component temperature for reinforced aluminium cylinder heads.

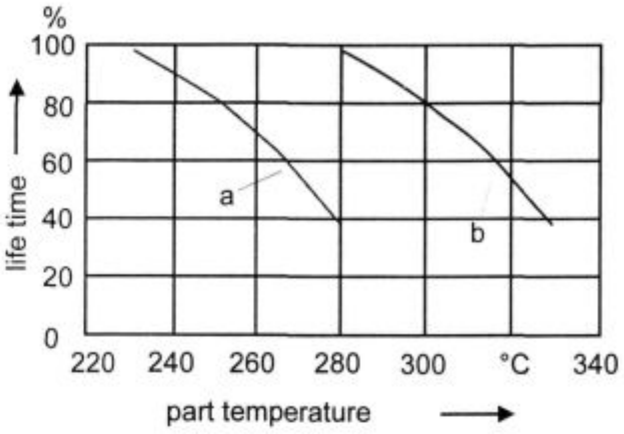

Figure 5: Component life for aluminium cylinder heads for car diesel engines (The life limiting factor is cracking in the combustion chamber area)[7]

Potential applications can be found also in the propulsive components e.g. transverse link and particle reinforced brake discs. The latter are also employed in rail transport (tube trains, railway trains). In air and space applications, the high strength, the high E-modulus, the low thermal coefficient of expansion, the temperature stabillity and the high conductivity of reinforced light metals compared to polymer materials make composites interesting for stiffening parts, load bearing tubes, rotors, covers, and containers and supports for electronic devices. A collection of potential actual applications of the various metal matrix components (MMC's) is given in **Table 7**.

In history, the first technical applications of MMC's were in the fields of energy and information engineering, e.g. carbon brushes (Cu-graphite) or contact materials. There is still scope for further development in conductor materials, support materials for printed circuits or structures for electronic components. Further economically interesting applications are to be found in leisure applications e.g. extruded and welded particle reinforced alu-

Table 7.1: Potential and actual technological applications of metal matrix composites (part 1)

Application	Required property	Material system	Production method
automobile and commercial vehicles			
stiffeners, connecting rod, frames, piston, piston pins, valve spring retainer, brake disks, brake, brake linings, drive shaft.	high specific strength and stiffness, temperature stability, low coefficient of thermal expansion, wear resistance, thermal conductivity.	Al-SiC, Al-Al_2O_3, Mg-SiC, Mg-Al_2O_3, discontinuous reinforcements.	melt infiltration, extrusion, forging, gravity casting, pressure die casting, squeeze-casting.
accumulator plate	high stiffness, creep resistance	Pb-C, Pb-Al_2O_3	melt infiltration
military and civil aircraft			
supporting tubes, stiffeners, wings- and gear boxes, ventilation and compressor blades.	high specific strength and stiffness, temperature stability, fracture toughness, fatigue resistance	Al-B, Al-SiC, Al-C, Ti-SiC, Al-Al_2O_3, Mg-Al_2O_3, Mg-C continuous and discontinuous reinforcements.	melt infiltration, hot pressing, diffusion welding and soldering, extrusion, squeeze-casting.
turbine blade	high specific strength and stiffness, temperature stability, fracture toughness, fatigue resistant.	W, superalloys, intermetallics e.g. Ni_3Al, Ni-Ni_3Nb	melt infiltration, directional solidification of near net shape components

Table 7.2: Potential and actual technological applications of metal matrix composites (Part 2)

Application	Required property	Material system	Production method
space			
frames, stiffeners, antennas, joints, bolds.	high specific strength and stiffness, temperature stability, low coefficient of thermal expansion, thermal conductivity	Al-SiC, Al-B, Mg-C, Al-C, Al-Al_2O_3, continuous and discontinuous reinforcements.	melt infiltration, extrusion, diffusion bonding and joining (spatial structures)
energy engineering (electrical contacts and conductive material)			
carbon brushes	high electrical and thermal conductivity wear resistance	Cu-C	melt infiltration, powder metallurgy.
electrical contacts	high electrical conductivity, temperature and corrosion resistance, switch capacity, resistance to burn.	Cu-C, Ag-Al_2O_3, Ag-C, Ag-SnO_2, Ag-Ni	melt infiltration, powder metallurgy, extrusion, hot pressing
superconductor	superconductivity, mechanical strength, ductility.	Cu-Nb, Cu-Nb_3Sn, Cu-YBaCO	extrusion, powder metallurgy, coating techniques.
other applications			
spot welding electrodes	resistance to burn.	Cu-W	powder metallurgy, infiltration.
bearings	load bearing capacity, wear resistance.	Pb-C, bronze-Teflon	powder metallurgy, infiltration

minium-mountain bike frames and golf clubs with particle reinforced inserts. Baseball bats are another possible application because the higher damping would result in a completely different striking behaviour.

6 Recycling

The necessity of integrating production waste and scrap of newly developed materials is of particular importance. Since ceramic materials are used in the form of particles, short fibres or continuous fibres as reinforcement it is not possible to separate the components with aim of reutilising of matrix *and* the reinforcement. But conventional melting techniques can be employed to recover the matrix alloy. In the case of cast or powder metallurgically produced discontinuously reinforced light metals (short fibre or particle) it is possible under certain conditions to reuse the swarf. This is particular so for particle reinforced aluminium casting alloys where no problems arise by remelting the swarf and directly use of the cast ingots without modification. The paper[18] provides an overview of the various recycling concepts for light alloy matrix composites taking into account alloy composition, reinforcement type and the production and working history.

7 Conclusion

The development of metal matrix composites can be used to improve critical properties of metal alloys e.g. high temperature strength, stiffness, wear resistance and thermal expansion. With high variability of materials combination and manufacturing techniques it is possible to produce tailor-made materials. Which combination and production techniques are choosen depends on the requirement of the possible application. The production processes allow the manufacture of semi-finished products or near net shape parts.

8 Literature

[1] K. U. Kainer (ed.): *Metallische Verbundwerksoffe*, DGM Informationsgesellschaft, Oberursel, 1994

[2] DURALCAN Composites for Gravity Castings, Duralcan USA, San Diego, 1992

[3] DURALCAN Composites for High-Pressure Die Castings, Duralcan USA, San Diego, 1992

[4] K. U. Kainer: Guss Produkte 91, Verlag Hoppenstedt, Darmstadt, 1991, 261-262

[5] C. W. Brown, W. Harrigan, J. F. Dolowy, Proc. Verbundwerk 90, Demat, Frankfurt, 1990, 20.1. - 20-15

[6] Manufactures of Discontinuously Reinforced Aluminium (DRA), DWA Composite Specialities, Inc., Chatsworth USA, 1995

[7] W. Henning, E. Köhler, *Maschinenmarkt*, 101, 1995, 50-55

[8] S. Mielke, N. Seitz, Grosche, *Int. Conf.on Metal Matrix Composites*, The Institute of Metals, London, 1987, 4/1-4/3

[9] K. U. Kainer, Keramische Partikel, Fasern und Kurzfasern für eine Verstärkung von metallischen Werkstoffen in *Metallische Verbundwerkstoffe*, K. U. Kainer (ed.), DGM Informationsgesellschaft, Oberursel, 1994, 43-64

[10] H. Hegeler, R. Buschmann, I. Elstner: Herstellung, Eigenschaften und Anwendungen von Kurz- und Langfaserpreforms in *Metallische Verbundwerkstoffe*, K. U. Kainer (ed.), DGM Informationsgesellschaft, Oberursel, 1994, 101-116

[11] Lanxide Electronic Components, Lanxide Electronic Components, Inc., Newark USA, 1995

[12] C. Fritze, K. U. Kainer: *Proc. Conf. Verbundwerkstoffe und Werkstoffverbunde*, G. Ziegler (ed.) DGM Informationsgesellschaft, Oberursel, 1996, 483-486

[13] A. G. Leatham, A. Ogilvy, L. Elias, *Proc. Int. Conf. P/M in Aerospace, Defence and Demanding Applications, MPIF*, Princeton, USA, 1993, 165-175

[14] Cospray Ltd. Banbury, U.K., 1992

[15] Keramal Aluminium-Verbundwerkstoffe, Aluminium Ranshofen GmbH, Ranshofen, Austria, 1992

[16] K. U. Kainer, B. L. Mordike, *Metall*, 44, 1992, 436-439

[17] K. U. Kainer, *Proc. Int. Conf. New and Alternative Materials for the Transportation Industries, ISATA*, Croydon, 1994, 463-470

[18] K. U. Kainer: Konzepte zum Recycling von Metallmatrix- Verbundwerkstoffen, in press Proc. Recycling von Verbundwerkstoffen und Werkstoffverbunden, DGM Informationsgesellschaft, Frankfurt

Kovine, zlitine, tehnologije/30/1996/6/517-520

Microstructural Considerations Limiting the Mechanical Properties of HSLA Steel

Mikrostrukturne omejitve mehanskih lastnosti HSLA jekel

Ľ. Parilák[1], IMR SAS, Košice, Slovakia

Prejem rokopisa - received: 1996-10-01; sprejem za objavo - accepted for publication: 1996-11-04

The influence of chemical composition, grain and subgrain size, and precipitation on yield strength, transition temperature and the work strengthening exponent was analyzed for HSLA (high strength, low alloy) steel. The relationships are quantified and transferred to graphic charts - nomogram for steel with polygonal as well as non polygonal microstructure. The limits of mechanical properties (the highest combinations of yield strength and transition temperature) were quantified for the polygonal HSLA microstructure.

Key words: microstructure, mechanical properties, HSLA steels

Vpliv kemijske sestave, velikosti zrn in podzrn ter izločanja na mejo plastičnosti, prehodno temperaturo žilavosti in keficienta deformacijske utrditve je bil analiziran za HSLA jekla. Odvisnosti so kvantificirane in zapisane v grafih - nomogramih za jekla s poligonalno in acirkularno mikrostrukturo. Mejne mehanske lastnosti (kombinacije največje meje plastičnosti in prehodne temperature žilavosti) so bile kvantificirane za poligonalno mikrostrukturo.

Ključne besede: HSLA jekla, mikrostrukture, mehanske lastnosti

1 Introduction

At the development of new steel types the key problem is to understand the influence of chemical composition and obtainable parameters of microstructure on strength, plasticity and brittle fracture resistance. It is essential to obtain the quantitative description of the relation, and the description should be based on the knowledge concerning the nature of the mechanical properties in question. This way a valuable information can be obtained for the production technology, first for the prime chemical composition and heat treatment. In the presented work descriptions of correlations between chemical composition and parameters of microstructure on one side, and yield strength, work strengthening exponent, and transition temperature on the other, are compiled. They are quantified enabling direct application in engineering. In the second part of the work the limits of mechanical properties - combinations of strength, plasticity and brittle fracture resistance, are shown for the polygonal microstructure.

2 Microstructural essence of mechanical and fracture properties of microalloyed steels

Investigated were low-carbon microalloyed steels based on Ti, V, Nb, with eventual addition of Mo, in polygonal and non-polygonal microstructures. Introductory studies were devoted to the kinetics of precipitation of carbides, nitrides or carbonitrides of microalloying elements from the viewpoint of its intensity and effectiveness. Furthermore, investigated were also questions of laws of interphase precipitation and precipitation in austenite and ferrite. The main objective was to gain the knowledge of laws of the effect of precipitation states on strength as well as, plastic and brittle fracture properties. Analyses were carried out on several hundreds of structural states in the state after rolling at hot rolling mill in VSŽ JSC Košice, or in the state after thermal processing. Main attention was paid to the yield point, work strengthening exponent and transition temperature of notch toughness.

2.1 Yield point

The analyses were based on the assumption of an additive character of individual strengthening contributions to the yield point R_e and the following relationship was proposed for the studies set of steels:

$$R_e = R_{PN}+R_{IN}+R_G+R_{SG}+R_S+R_{PR}+R_P+R_D \qquad (1)$$

where R_{PN} - is the contribution of lattice friction stress; R_{IN} - contribution to strengthening on account of interstitially dissolved atoms of additives; R_D - contribution of dislocation strengthening; R_G - strengthening contribution resulting from the size of grains; R_{SG} - contribution resulting from the effect of subgrains; R_{PR} - pearlitic contribution; R_S - substitution contribution; R_P - precipitation contribution.

Their quantitative expression is based on relations comprised in [1].

Analyses provided a quantitative expression of the substitution effect of manganese R_{Mn} and confirmation of the effect of silicon and pearlite on strengthening contributions (R_{Si}, R_{PR}).

In addition to that a quantitative effect of polygonal ferrite grains d, or formations delimited by large angle boundaries (d_F) in non-polygonal microstructures was

---

[1] Ass. Prof. Dr. L'udovít PARILÁK
Institute of Materials Research SAS
Watsonova 47, 04353 Košice, Slovakia

described. The quantitative expression of subgrain strengthening with intensity $R_{SG} = Gb \cdot d_{SG}^{-1} = 0.1 \cdot d_{SG}^{-1}$ (the size of a subgrain d_{SG} in mm) in a very good agreement with the Landford-Cohen relation, was used. The interchangeability of R_G and R_D was demonstrated, with R_D representing a contribution of transformation or of "geometrically inevitable" dislocations.

The analyses of the influence of precipitation on precipitation strengthening, employing all available theoretical models, were carried out. These analyses resulted in a quantitative relation for precipitation strengthening:

$$R_p = k_p^R \cdot \lambda^{-2} \tag{2}$$

where λ is the average planary interparticle distance of precipitates. The physical interpretation of this relation is following: Precipitation strengtheningis inversely proportional to the mean size of a free sliding area, corresponding to one precipitate (obstacle) standing in the way of the moving dislocation. The strengthening intensity constant k_p^R acquires a force dimension and can represent a mean value of force interaction phenomena between dislocations and precipitations, leading to a critical stress for the passing of dislocations trough obstacles. Its value $k_p^R = 76.8 \cdot 10^{-8}$ N is of the order corresponding to the size of an interaction of an edge dislocation with an elastic field of a particle $F \approx 10^{-7}$ N).

The quantitative behaviour of a thermaly dependent constituent of the yield point (R^*) was determined in the range -196 to +20°C, together with parameters C_1, B, appearing in the relation:

$$R^* = C_1 \cdot \exp(-T/B) \tag{3}$$

2.2 Transition temperature

Our analyses were based on Cottrell's energetic balance of cohesion of tough/brittle transition and Petch's condition of equality of the yield point R_e and fracture stress R_{FR} for determination of the transition temperature of brittleness T_K. Contrary to Petch's formulation, we have assumed a general interaction between individual parameters of microstructure and chemical composition and the friction stress R_{OFR}, appearing in the relation for fracture stress

$$R_{FR} = R_{OFR} + k_f \cdot d^{-1/2} \tag{4}$$

which resulted in the development of a corresponding model and analytical formulation. The k_f parameter represents a barrier effect of grain boundaries directed against the propagation of cracks across boundaries of grains.

The performed analyses provided the following relation for the transition temperature

$$T_{K(35)} = A - B \cdot \ln(d^{-1/2}) + \sum_{(i)} \Delta T_i \tag{5}$$

where A is the so-called threshold value of brittleness, dependent on the intensity of the thermal change of yield point B (relation (3)). The surface-plastic energy γ, shear modulus of elasticity G, parameters k_y, k_f and the mode of stressing q are connected to the values A and B in the relation

$$A = B \cdot \ln\left(\frac{4\gamma \cdot q \cdot G}{k_y} - k_f\right) \tag{6}$$

ΔT_i is the shift of transition temperature and depends from the structural parameter i or eventually from the chemical composition.

The positive effect of grain refining on an improvement of brittle fracture resistance has been demonstrated and a direct relationship of its intensity and a thermal change of the yield point has been observed. A good agreement of the parameter B in relations (3) and (5) was detected. An embrittlement effect of pearlite and silicon has been demonstrated.

The influence of precipitation on the shift of transition temperature was demonstrated to follow the relation

$$\Delta T_p = k_p^T \cdot \lambda^{-2} \tag{7}$$

An estimate of the barrier effect of grain boundaries against propagation of cleavage cracks ($k = 55$ Nmm$^{-3/2}$) was provided together with a value of surface plastic energy at T_K ($\gamma = 10^{-2}$ Nmm^{-1}). In case of polygonal microstructures analyses did not exclude a positive effect of manganese on the improvement of brittle fracture resistance and the quantitative expression corresponded to results of Pickering. In case of non-polygonal microstructures an absence of significant effect of subgrains on transition temperature changes was observed.

2.3 Complex relations

In our previous works[1,2,3] we presented simplified relations for the evaluation of the influence of microstructure on yield strength R_e, transition temperature T_{35} and work strengthening exponent n. For a polygonal microstructure it is expressed as:

$$R_e = R_G + R_{Mn} + \Delta R \tag{8}$$

$$T_{35} = A - B \cdot \ln(d^{-1/2}) + C \cdot \Delta R \tag{9}$$

$$n = a + \frac{b}{\Delta R} \tag{10}$$

where $R_G = 15 \cdot d^{-1/2}$ is the strengthening by ferrite grain size d (mm); $R_{Mn} = 50 \cdot x_{Mn}$ is the strengthening share of manganese x_{Mn} (%); ΔR is the part of embrittlement caused by strengthening, for microalloyed steel including mainly precipitation strengthening R_P, and also the influence of strengthening by silicon content R_{Si}, pearlite content R_{PR}, Peierls-Nabarro stress R_{PN}, and by interstitial strengthening R_{IN} ($\Delta R = R_P + R_{Si} + R_{PR} + R_{PN} + R_{IN}$); A = 147°C, B = 110°C, C = 0.4°C/MPa is an embrittlement constant, a, b are regression coefficients. For non polygonal microstructure similar relation were derived:

$$R_e = R_G + R_{SG} + R_{Mn} + \Delta R \qquad (11)$$

$$T_{35} = A - B \cdot \ln(d^{-1/2}) + C \cdot \Delta R \qquad (12)$$

where $R_G = 19 \cdot d^{-1/2}$; $A = 143°C$; $B = 100°C$, $C = 0.4$ °C/MPa while $R_{SG} = 0.1 \cdot d_{SG}^{-1}$ is the strengthening contribution of the subgrain size d_{SG} (mm).

The graphic interpretation of the relations is shown in **Fig.1** for the polygonal microstructure (eq. 8-10) and in **Fig.2** for the non-polygonal one (eq. 11-12).

It is important to note that the yield strength is controlled by a set of strengthening contributions with different influences on the brittle fracture resistance. The embrittlement from strengthening ΔR is resulting for every 100 MPa of strengthening a 40°C shift of the transition temperature into the wrong direction, causing the worsening of plastic properties, too, as shown by the work strengthening exponent. There is an influence of manganese content and subgrain size on strengthening too, though their influence on the transition temperature is not significant. Practically only one microstructural parameter is known, the increasing of the yield point together with the increase of brittle fracture resistance. It is the ferrite grain size d, or described more generally the size of the microstructural object limited by large angled borders. It is of prime importance to constitute the chemical composition and microstructure in the way to obtain first this microstructural parameter in the quality reflecting the desired complex of properties. The relations given in the work are simplified theoretical descriptions with coefficients calculated by regression analysis made on more than 300 microstructure types of steel produced in ironworks VSŽ, a.s. Košice, Slovakia.

3 Limits of polygonal microstructures

We decided to define the limits of the complex of mechanical properties for a steel with polygonal microstructure. With this aim the HSLA steel, with yield strength from 420 to 700 MPa were evaluated. The basic features of the evaluation are shown in the graphic chart in **Fig.3**, which was calculated for a 1% Mn content. The straight lines are representing the yield strength R_e. The nomo-

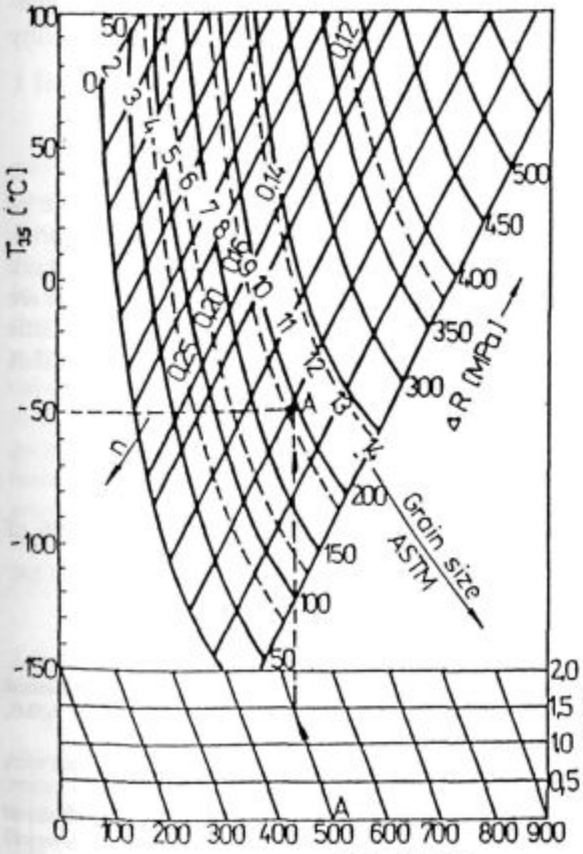

Figure 1: A complex nomogram for relation between microstructural parameters and mechanical properties of HSLA steels with polygonal microstructure

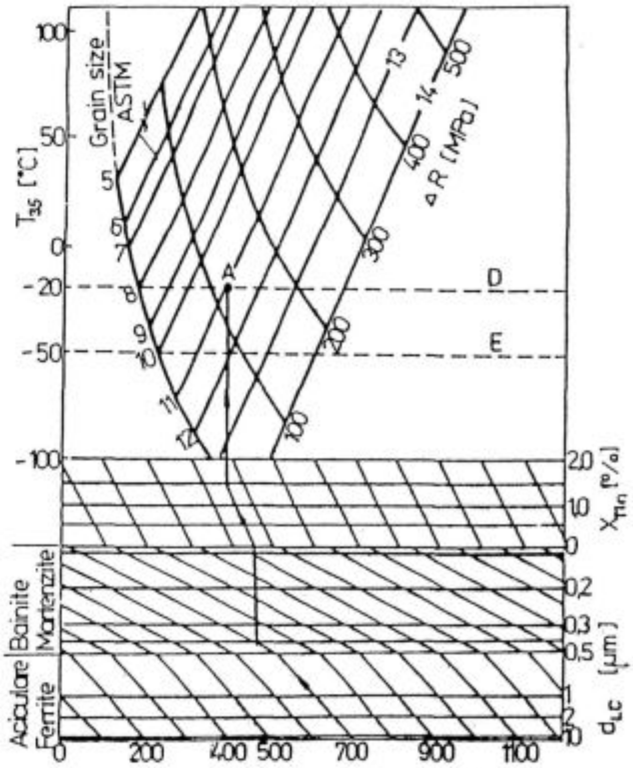

Figure 2: A complex nomogram for relation between microstructural parameters and mechanical properties of HSLA steels with non-polygonal microstructure

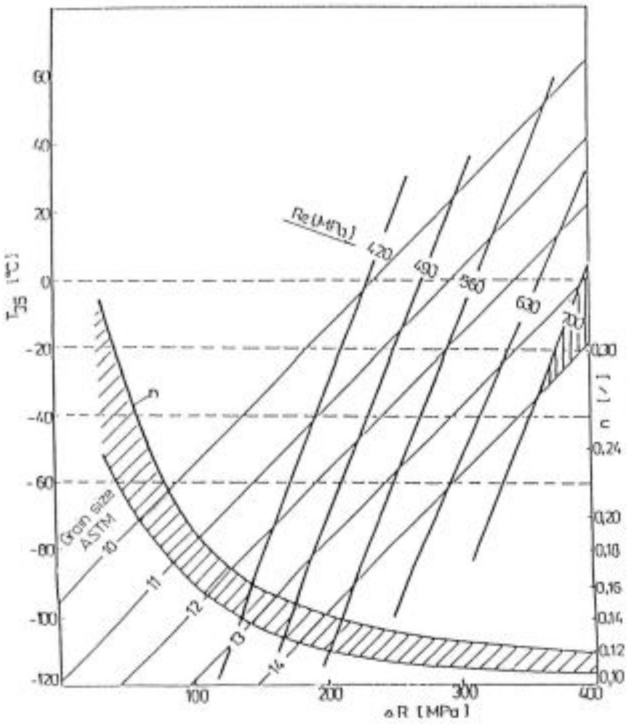

Figure 3: Microstructural considerations limiting mechanical properties of HSLA steels with polygonal microstructure

gram shows the possible combination of embrittlement ΔR and ferrite grain size d, necessary to obtain the selected yield point. The transition temperature T_{35} and the work strengthening exponent n are shown also.

In **Tab. 1** the combinations of embrittlement ΔR and ferrite grain size d in grades according to ASTM are shown, which are necessary for a steel with the desired combination of yield strength R_e and transition temperature T_{35}.

Table 1: Required ferrite grain size d and embrittlement by strengthening ΔR necessary for the combination of properties R_e and T_{35}

T_{35}(°C)	0		-20		-40		-60	
R_e (MPa)	d	ΔR (MPa)	d	ΔR (MPa)	d	ΔR (MPa)	d	ΔR (MPa)
420	10	230	11-10	220	11	190	11-12	170
490	11-10	275	11	260	12-11	230	12-13	210
560	11-12	320	12	290	12-13	270	13	250
630	12-13	370	13	340	13-14	320	14	290
700	13-14	420	14	400	14	350	?	?

In all cases a fine ferrite grain is required. Knowing the manufacturing technology and the limits of the wide strips hot rolling mill the production of steel with ferrite grain size under grade 14 cannot be experted. To obtain the grade 13 is very difficult, grade 12 is demanding, while the more coarse grains are currently obtained. Consequently, **Tab. 1** was simplified to **Tab. 2** which show that the elaboration of polygonal steel with the yield strength R_e = 700 MPa and the transition temperature T_{35} under -40°C, is not be reliable. It is also not realistic to desire expert a limit of elasticity R_e = 630 MPa with the transition temperature T_{35} better than -60°C.

Table 2: Limits of the polygonal microstructure for different combinations of R_e and T_{35}

R_e	T_{35} (°C)			
(MPa)	0	-20	-40	-60
420	1	1	1	1
490	1	1	2	2
560	1	2	2	3
630	2	3	3	4
700	3	3	4	4

The possibilities are denoted: 1 - realistic, 2 - demandig, 3 - very difficult, 4 - fiction.

In **Fig. 3** it can be also seen, that for the mentioned R_e and T_{35} values the ductility is very low, the work strengthening exponent in the range 0.10 to 0.16 (for the lower strength) because for high R_e values the embrittlement by ΔR is necessarily high, degrading the ductility and brittle fracture resistance.

4 Conclusion

Starting from theoretical relations the influence of chemical composition and parameters of the microstructure on strength, transition temperature and work strengthening exponent were investigated. The results are compiled and the limit combinations of strength, plastic properties and resistance to brittle fracture for HSLA steel with polygonal microstructure are calculat

5 Acknowledgment

The work is supported by Project No. 2/1106/96 of the Slovak Scientific Grant Agency - VEGA.ed.

6 References

[1] L'. Parilák, M. Šlesár, B. Štefan: Structural Prediction of Mechanical Properties of HSLA Steels. In.: *Proc. of Microalloying 88*, ASMI, USA, 1988, 559

[2] B. Štefan: Fyzikálna metalurgia a vývoj konštrukčných zvaritetl'ných ocelí. *Doktorská dizertačná práca*, ÚEM SAV Košice, 1990

[3] L'. Parilák: Štruktúrna podstata mechanických a lomových vlastností materiálov. In.: *Predikce mechanických vlastností kovových materiálů na základě strukturních charakteristik. I.díl.* Nové Město na Morave, 11.-14.5.1993 Brno, P MSVTS VÚ 070 1993, 125

Kovine, zlitine, tehnologije/30/1996/6/521-526

Predicting of Reactions During Carburization and Decarburization of Steels in Controlled Atmospheres

Napovedovanje reakcij, ki potekajo med naogljičenjem in razogljičenjem jekla v kontroliranih atmosferah

B. Koroušič[1], IMT Ljubljana, Slovenija
M. Stupnišek, Faculty of Mechanical Engineering and Naval Architecture, Zagreb University, Croatia

Prejem rokopisa - received: 1996-10-01; sprejem za objavo - accepted for publication: 1996-11-04

The knowledge of the thermodynamics of complexe systems consisting of gases and metal should be valuable for the control of industrial processes. The Gibbs energy minimization model has been implemented in the software program GPRO® and associated with a powerfull and reliable database. The computer package can perform computation of the equilibrium composition in very complex chemical and metallurgical systems. Some examples in this paper illustrate the simplicity of the computation and the use of the program in the field of some typical metallurgical applications.

Key words: equilibrium reactions, NO_x modelling, combustion of fossil fuels, active gas-atmospheres, decarburizing of non-oriented electrical steels, carburizing of alloyed steels with in situ produced atmospheres

Poznavanje termodinamičnih odnosov v kompleksnih sistemih plin - kovina ima lahko izreden pomen za kontrolo industrijskih procesov. Gibbsov model o minimizaciji energije je implementiran v programsko opremo GPRO®, ki mu služi kot osnova močna baza verificiranih termodinamičnih podatkov. Programska oprema omogoča izračunavanja ravnotežnih sestav v zelo kompleksnih kemijskih in metalurških sistemih. Navedeni primeri v tem članku ilustrirajo enostavnost izračunavanj in način uporabe programa na področju metalurških reakcij, ki jih večinoma izvajajo strokovnjaki na tem področju.

Ključne besede: ravnotežne reakcije, tvorba NO_x, zgorevanje fosilnih goriv, aktivne plinske atmosfere, razogljičenje neorientirane elektropločevine, naogljičenje legiranih jekel

1 Introduction

The application of thermodynamics to a system gas/solid enables to calculate the composition at equilibrium, direction and extent of change which can take place under specified conditions.

Rapid developments have taken place in recent years in efficiency of thermodynamics in the engineering as thermodynamic can be defined as being the meeting point between physical - chemical principles and practical applications[1]. In this paper an attempt has been made to demonstrate use of a personal computer software program as an ellegant and sensitive method for numerous metallurgical applications especially for the analysis of gaseous systems. It is hoped, that users of this method will be in a good position to go more deeply into learning thermodynamic laws.

2 Principles of the Gibbs method

In the fields of heat treatment of metals like *annealling, carburizing, decarburizing, nitrocarburizing and many other operations*, the metallurgist is concerned not with the pure gases but with the mixture of various species (gaseous and solids) which form the atmosphere in the furnace.

The thermodynamics of such complex systems can be treated by two methods:

- The classical method of numerical solution of an equilibrium problem when the equilibrium constant (K_r) or free energy change $\Delta G°$ of the involved reactions are known.
- The general Gibbs method for the numerical solution of an equilibrium. The problem is to determine the values of the species which minimize the state of total free energy at the given temperature and pressure.

Both treatments are thermodynamically equivalent, however, it seems that the later method has significant advantages for calculating the equilibrium conditions in complex systems, in mixtures containing both gaseous and condensed species.

During the last 20 years, SOLGASMIX computer program, as the method of attacking chemical and metallurgical problems, has influenced our approach to the study of a branch of scientific knowledge in physical chemistry.

There can be no doubt that to attack such a complex application of thermodynamics is only possible with the use of computer technology.

---

[1] Prof. Dr. Blaženko KOROUŠIĆ
Inštitut za kovinske materiale in tehnologije
1000 Ljubljana, Lepi pot 11, Slovenija

3 Description of the method used for the calculation of complex equilibrium conditions

Several excellent software programs for calculating equilibria reactions at high temperatures, have been developed in the last two decades (SOLGASMIX, THERMOCALC, FACT, CHEMSAGE...)[2,3]. However, most of them are designed and written in a complex form using very strong computer units, while few are intented as a simply a tool to be applied for the purposes of solving practical problems. Therefore, it seemed worthwile to develop a program which would combine these two computer program designs. The new software program, called GPRO is based on the method of free energy minimization and extended to systems containing numerous gaseous and condensed phases in accordance with SOLGASMIX-principles. GPRO-program is dimensioned for 16 elements and 100 species. If necessary, this figure can be increased or new included datasets, which if necessary are written by the user (private databases are open and can be easily included also).

3.1 Thermodynamical approaches to the Gibbs-method

The power of Gibbs method energy minimization lies in its simplicity for the description of chemical reactions in complex systems, and its ability to facilitate the determination of the effect, on equilibrium state, of changes in the external influences which can be brought to bear on the system. In our software program, the user needs only to specify the type, the species present and the conditions (for example: *temperature of the system*) for the calculation. The program will automatically perform equilibrium thermodynamic computions typically associated with complex chemical equilibria from a defined database. With the aid of the GPRO-program, a user is able to perform most of the following operations:

1. The energy for pre-heating the initial mixture from the initial temperature T_0 to the reaction temperature T,
2. The reaction heat,
3. The computation of the complex chemical equilibria in gaseous mixtures and activity of solid compounds,
4. Displaying and printing data for compounds and solutions at selected temperature and composition.

An additional scientific and engineering benefit of this program is the software able to develop a more basic understanding of chemical equilibria at high temperatures and its applications. Although the power software program will automatically perform the thermodynamical computation (no danger of pluging wrong numbers in wrong equations), however, the user must have some knowledge of the chemical nature of the considered system. In this paper the attempt is made to demonstrate the breadth and diversity of the modern software program in simple way so that a user may be able to understand the thermodynamical method and apply it to metallurgical problems. Most of the examples are chosen with the aim to show superiority of the computer program, over traditionally manual methods, which are particularly stressed for the engineers and students.

3.2 Databases associated for the equilibrium thermodynamic comptutations

From many excellent standard treatises on thermodynamics it is known, that without reliable thermodynamic data most equations are ineffective and the numerical answers will be therefore wrong. GPRO software program is based on the use of both the expressions for calculations of the standard Gibbs energies of the formation of a selected phase:
in the form:

$$\Delta G^{\circ}{}_{T} = \frac{A}{T} + B + CT + DT^{2} + ET^{3} + + FT\ln T$$

or using thermodynamical data on enthalpy $\Delta H^{\circ}{}_{T}$, entropy $\Delta S^{\circ}{}_{T}$ and heat capacity $C_p(T)$:

$$\Delta G^{\circ}{}_{T} = \Delta H^{\circ}{}_{298} + \int_{T_0}^{T} C_p(T)dt - T\Delta S^{\circ}{}_{298} - T\int_{T_0}^{T} \frac{C_p(T)}{T}\,dT$$

Both methods used from the database involve the search for a minimum value of free energy ΔG of a system and give an equivalent result. However, the last method using enthalpy $\Delta H^{\circ}{}_{T}$, entropy $\Delta S^{\circ}{}_{T}$ and heat capacity $C_p(T)$ has more advantages because it combines heat and equilibrium calculations. A typical example is the determination of the adiabatic flame temperature, where enthalpy of reaction serves as the criterion of the heat balance.

4 Exploiting the GPRO-program for complex equilibria calculations

Modelling Mechanism of Formation Nitrogenous Oxides by the Combustion of Fossil Fuels

Modern combustion processes of fossil fuels meet the relevant requirements for cost-effective operation and avoidance of enviromental pollution. In article some results of the basic study of the formation and reduction NO_x in high temperature combustion processes are presented. The obtained results demonstrate the use of the sophisticated methods of thermodynamics as one of the most important tools by the study of the combustion processes for a better understanding of the mechanism of formation of nitrogen oxides, one of the most important pollutants in combustion of fossil fuels[8-16].

Example 1:

In this example is a demonstration of the use of the GPRO-software program as method for prediction of complex combustion reactions and equilibrium gas composition including NO-oxydes formation.

The high temperature furnace is fired with natural gas and air (no air preheating). The question was: calculate

Table 1: Results of GPRO-analysis of the natural gas combustion by different air - index and without air preheating

Equilibrium data for methane combustion (λ=0,74...2,2)[1]										
$CH_4 + 2\lambda O_2 + 7{,}52\lambda N_2$										
Air index	0,74	0.84	0,94	1,00	1,10	1,30	1,60	1,80	2,00	2,20
CO (%)	6,90	4,44	1,95	0,95	0,30	0,04	0,002	0,0	0,0	0,0
CO_2 (%)	4,77	6,29	7,69	8,49	8,40	7,44	6,16	5,51	4,99	4,71
NO (%)	0,0021	0,017	0,112	0.23	0,345	0,334	0,200	0,130	0,087	0,066
H_2O (%)	18,09	18,99	19,01	18,52	17,28	14,94	12,32	11,03	9,98	9,42
O (ppm)	1,04	14,20	133	258	282	111	15	5	1	0
O_2 (%)	0,00	0,00	0,127	0,53	1,75	4,32	7,28	8,75	9,93	10,56
N_2 (%)	64,97	67,79	70,02	70,89	71,78	72,90	74,03	74,58	75,02	75,25
H_2 (%)	5,27	2,47	0,81	0,37	0,11	0,02	0,00	0,00	0,00	0,00
$\Sigma_{(input)}$ (mole)	8,04	9,00	9,25	10,52	11,47	13,37	16,23	18,14	20,04	21,24
$\Sigma_{(output)}$ (mole)	8,56	9,32	10,10	10,59	11,49	13,37	16,23	18,14	20,04	21,24
T_{adb} (K)	2023	2143	2233	2231	2151	1955	1712	1584	1482	1421

[1] air index

the equilibrium gas composition and the adiabatic flame temperature for the air-index in range $0{,}74 \le \lambda \le 2{,}2$ and compare the obtained results of the flame temperature with similar reference data known in the literature (normally presented in graphically form).

In **table 1** and **figure 1** the computed values for the gas equilibrium are given. The adiabatic flame temperature calculation show values slightly above the compared data.

Thermodynamic evaluation of carburizing atmospheres

The accuracy of the gaseous atmosphere control in the steel carburizing furnaces has been remarkably improved owing to the application of the computer control system and the development of new measuring techniques, for example: oxygen and/or carbon sensors. The atmosphere in carburizing furnaces are consists of: air + methane or other hydrocarbons and involves the gases CO, CO_2, H_2, H_2O, N_2. The four first gases are interdependent in a reversible reaction, commonly called the water-gas reaction:

$$CO + H_2O = CO_2 + H_2$$

The ratio:

$$K_w = \frac{p_{CO_2} \cdot p_{H_2}}{p_{CO} \cdot p_{H_2O}} \tag{1}$$

is a constant, the value of which depend on the temperature.

The carburizing of steel, i.e. carbon content increasing on the steel surface, occurs through the reaction:

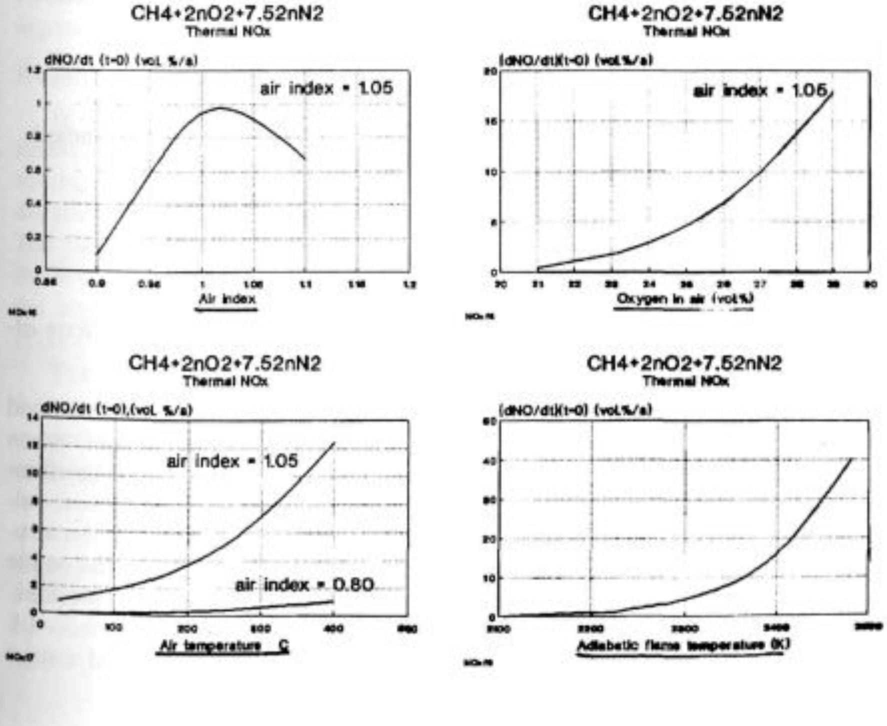

Figure 1: The formation of the nitrogenous oxide NO (model simulation)

Slika 1: Tvorba dušičnega oksida NO (modelne simulacije)

$$2CO = C + CO_2 \qquad (2)$$

For any given temperature, the coresponding equilibrium constant of Boudouard's reaction will determine the carburizing potential of the atmosphere:

$$K = \frac{a_c}{p_{CO} \cdot (p_{CO}/p_{CO_2})} \qquad (3)$$

The carbon potential of on atmosphere is simple to determine if the partial pressure of CO and ratio (p_{CO}/p_{CO_2}) is known. From EMF measurement (**e**lectro**m**otive **f**orce) with the oxygen probe, considering the furnace temperature (p_{CO}/p_{CO_2}) or (p_{H_2}/p_{H_2O}) and measuring the CO - content in the atmosphere is possible to ensure the control of the carburizing process.

Example 2:

The carbon activity in a steel depends on the content of alloying elements, thus every steel composition will have determined carbon potential which corresponding to the atmosphere composition.

In next example three type steels were treated with air + methane atmosphere with the aim to obtain a constant carbon content near the surface of about 1 wt.% C).

Data in **table 2** show, that small deviations in the gas atmospheres (or the change of air + methane ratio) have a remarkable effect on the carbon activity. This model simulation is in good agreement with practical data.

Table 2: Influence of the steel chemistry on the process parameters (Simulation made by GPRO programme by T = 1223K)

Chemistry (%)	Fe+1%C+ 1%Si	Fe+ 1%C	Fe+1%C+ 1%Cr
CO	19.27	19.25	19.24
CO_2	0.0629	0.0717	0.078
H_2O	0.199	0.227	0.248
CH_4	5.17	5.15	5.13
N_2	36.83	36.88	36.92
H_2	38.46	38.42	38.38
O_2 (bar)	$9.4\ 10^{-21}$	$1.16\ 10^{-20}$	$1.46\ 10^{-20}$
EMF(mV)	1173	1167	1162
T_{dp} *) (°C)	-13	-11	-10
a_C	0.818	0.715	0.654
%C	1.03	1.06	1.08
Q_{gas}(m³/h)	1.1	1.1	1.1
Q_{air}(m³/h)	2.094	2.100	2.1045

*) T_{dp} = Dew point temperature

Example 3:

The carburizing of steel is a continuously process within which - due to the kinetics of various reactions - damming up effects may occur leading to non equilibrium CH_4-contents in the furnace atmosphere.

In this case the carburizing reactions under non-equilibrium conditions are modelled.

A mixture of natural gas and air at 1 bar total pressure is introduced into the carburizing furnace heated to 1223 K[5]. The quantity of natural gas and air are $3,1.10^{-4}$ m³/s and $4,2.10^{-4}$ m³/s. Calculate the gaseous equilibrium composition in the furnace atmosphere and the carbon activity assuming graphite as standard state. If the air flow suddenly increased from $4,2.10^{-4}$ m³/s to $5,8.10^{-4}$ m³/s by constant natural gas flow $3,1.10^{-4}$ m³/s in the inlet mixture, determine the new gas equilibrium composition and carbon activity!

Table 3 shows the computed results for gas non-equilibrium composition and obtained energy changes, the preheating energy $H°_T$ - $H°_{289}$, the heat of reaction $H°_R$ and $H°_{total}$ the total heat of the system.

Table 3: Example of input and output of a non-equilibrium composition by the production of endothermic gas from methane and air by T = 1223 K

Air/ methane (m³/s)	$1,1CH_4 + 2\lambda O_2 + 7,52\lambda N_2$			
	$\lambda = 0,157$ $4,2.10^{(-4)}/3,1.10^{(-4)}$ $\alpha^{1)}_{methane} = 0,575$		$\lambda = 0,221$ $5,8.10^{(-4)}/3,1.10^{(-4)}$ $\alpha^{1)}_{methane} = 0,795$	
	X_{inp} (mole)	X_{out} vol.(%)	X_{inp} (mole)	X_{out} vol.(%)
CO	0,0000	17,58	0,0000	19,25
CO_2	0,0000	$4,28.10^{-2}$	0,0000	$7,19.10^{-2}$
CH_4	1,1000	13,40	1,1000	5,80
H_2O	0,0000	0,135	0,0000	0,227
HCN	0,0000	$3,76.10^{-3}$	0,0000	$2,65.10^{-3}$
H_2	0,0000	35,29	0,0000	38,41
N_2	1,1890	33,33	1,6590	36,22
O_2	0,3150	$(5,45.10^{-21})^{2)}$	0,4410	$(1,28.10^{-20})^{2)}$
$a_c^{3)}$	....	1,0000	....	0,714
Σ(mole)	2,604	3,5397	3,200	4,4962
$(H_2/C)^{4)}$	2,00	2,00	2,00	2,00
$H°_T$-$H°_{298}$ (kJ/mol)	92,95		116,77	
$H°_R$ (kJ/mol)	- 14,79		- 22,24	
$H°_{total}$ (kJ/mol)	78,15		94,53	

$^{1)}$ $\alpha_{methane} = \frac{CH4(c)}{CH4(t)}$, $CH_{4(c)}$ = fully cracked CH_4 and

$CH_{4(t)}$ = total CH_4

$^{2)}$ p_{O2} in bar,

$^{3)}$ a_C = carbon activity referred to graphite as standard state

$^{4)}$ $\frac{H_2}{C} = \frac{H_2 + H_2O + 2CH_4}{CO + CO_2 + CH_4}$, λ = air index

Calculation of the decarbirization process of silicon alloyed steels

The use of gaseous atmospheres with a well-defined oxygen potential for the decarburization of low carbon iron-silicon steels in continuous furnaces can be simulated using a thermodynamical model. Equilibrium calculations and practical measurements show that the solubility and carbon activity in Fe-C-Si steels depend on the gaseous atmosphere, temperature and steel composition.

Silicon-iron alloys containing 1 - 3% Si and 0,3 - 1% Al are typical steels for non-oriented sheets and a strict

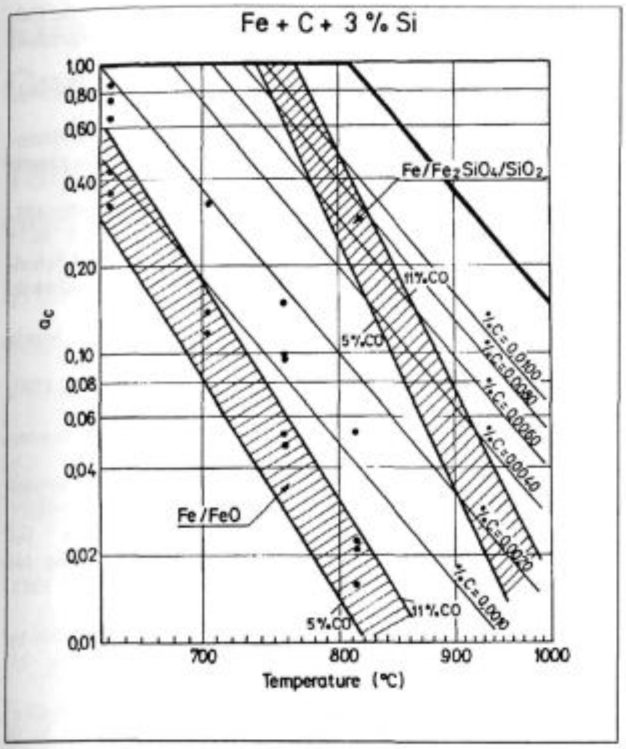

Figure 2: Plot of thermodynamical data for Fe_2SiO_4 as a function temperature calculated with GPRO-program

Slika 2: Diagram termodinamihnih podatkov Fe_2SiO_4 kot funkcija temperature izrahunano s GPRO-programom

control of the decarburization and surface reactions is required. The optimum properties for an electrical steel normally include high permeability with low core loss and minimal aging effects. An important factor in a process control is the formation of a high quality glassy film which is developed through a complex series of processing steps.

Example 4:

In order to clarify the relation between the decarburization atmosphere for the carbon removal during the annealing, the thermodynamical reactions and formation of different oxide phases in the scale have been studied. The first task was the determination of the carbon activity in the decarburization gas atmosphere containing at the start $H_2 + N_2 + H_2O$ in temperature range 600 - 1000°C.

The mathematical model GPRO allows an easy use of thermodynamical data to predict the equilibrium carbon content in electrical steels. It is convenient to use the carbon activity in the gas atmosphere by different partial pressures of CO to present the conditions for the formation of FeO and Fe_2SiO_4 by the different temperature. **Figure 2** shows the results obtained. Having these curves available, it is possible to determine the dew point temperature as the function of the partial pressure ratio H_2O/H_2.

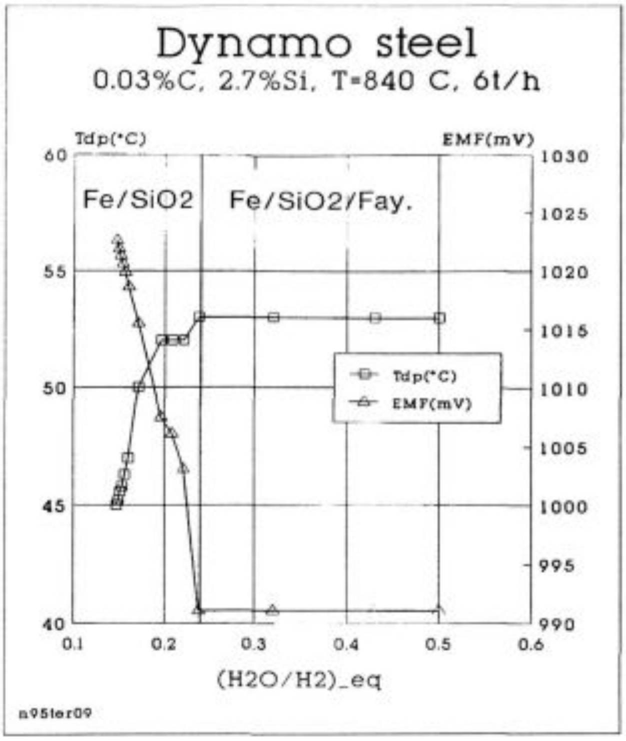

Figure 3: Equilibrium oxide-formation by the decarburization of non-oriented electrical sheets in gaseous atmosphere $H_2 + H_2O + N_2$ (T_{dp} - dew point temperature, EMF (mV) = electromotive force, $(H_2O/H_2)_{eq}$ = equilibrium pressure ratio)

Slika 3: Ravnotežni pogoji tvorbe oksidov med razogljičenjem *neorintitane pločevine v plinski atmosferi* $H_2 + H_2O + N_2$ (T_{dp} - točka rosišča, EMF (mV) = elektromotorna napetost, $(H_2O/H_2)_{eq}$ = ravnotežno razmerje plinov)

As shown on **Figure 3**, the ratio of H_2O/H_2 at which the formation of fayalite actually disappeared is near $H_2O/H_2 = 0,24$ at 840°C.

It is obvious that the pressure ratio H_2O/H_2 and CO_2/CO is interchangeable with the partial pressure of oxygen - p_{O_2} and finally also by means of the relation:

$$\log p_{O_2} = \log\left(\frac{p_{CO}}{a_c}\right)^2 - \frac{11854}{T} - 9{,}090 \qquad (4)$$

which allows the application of the oxygen (carbon) sensor signal (EMF).

5 Conclusions

The use of thermodynamic predictive model offers many advantages over conventional gas atmosphere calculations because of the simplicity for description of chemical reactions in complex systems, the automatic performance of equilibrium computations, of the avoidance plugging wrong numbers in wrong equations and so on. The rational and theoretical basis for the Gibbs energy model used was presented elsewhere[5,17-19]. To summarise, the key features of model calculations for the nitrocarburizing atmospheres are as follows:

- Modern combustion processes of fossil fuels meet strict requirements for cost-effective operation and avoidance of enviromental pollution. This article presents the first results of study into formation and reduction NO_x in high temperature combustion processes.
- The obtained results demonstrate the use of the sophisticated methods of thermodynamics as one of the most important tools for the study of combustion processes to understanding better the mechanism of formation of nitrogen oxides, as one of the most important pollutants in fossil fuels combustion.
- Little is given in disponible references on use of thermodynamical models in the field of active atmospheres. Such mixtures containing both gaseous and condensed components for example: Fe + C + O + H + N are extremly complicated for the numerical calculations. Detailed experimental studies are difficult and also thermodynamical results are mostly presented in the graphical form, which are very useful in research work but of little effectivness in searching solutions for a current practical operation.
- To obtain equilibrium compositions in the real gaseous mixtures by high temperatures, taking into account both energy and material balances, the development of new approaches are strongly required.

6 References

[1] D. R. Gaskel: Introduction to Metallurgical Thermodynamic McGraw-Hill Book Company, (Washington, D.C.), 1973

[2] W. B. Christopher, G. Erriksson: Metallurgical Thermochemical Databases, *Canadian Metallurg. Quat.*, 29, 1990, 2, 105-132

[3] G. Eriksson, K. Hack: ChemSage - A Computer Program for the Calculation of Complex Chemical Equilibria, *Metallurgical Transactions B*, 21B, 1990, 1013-1023

[4] F. D. Richardson, J. H. E. Jeffes: *J. Iron Steel Inst.*, 160, 1948, 261-270

[5] B. Koroušić: Contributions to the Computer Predictions of the Homogene and Heterogene Equilibrium Compositions for Gaseous Atmospheres, *Veitsch-Radex-Rundschau*, 1994, 1-2, 465-542

[6] R. Hoffmann: Aspekte des Kurzzeitnitrierens, *HTM*, 31, 1976, 152-157

[7] H. Henrich, W. Kozlowski, W. Liere: Energieeinsparung und Schadstoffreduzierung an Beheizungseinrichtungen in der Industrie, *Gaswärme International*, 41, 1992, 2/3, 89-100

[8] F. A. Williams: Combustion Theory, Benjamin Cummings, Menlo Park, 1985

[9] K. Hein: Fossil Fuel Utilisation, *Combust. Sci. and Tech.*, 93, 1993, 61, 27-39

[10] R. Haupt, R. Oppenber: Feuerungen in Dampf - und Heisswassererzeugern, *Gaswärme International*, 41, 1992, 10, 445-456

[11] B. Bonn, H. Baumann: Kenntnisstand der N_2O Bildung in verschiedenen Feuerungsanlagen, *VDI Berichte*, 922, 1991, 17, 625-633

[12] H. Schuster: Minderung der NO_x - Emissionen aus Kraftwerksfeuerungen, *VDI-Kolloquium Emissionsminderung bei Feuerungsanlagen* SO_2 - NO_x - Staub Essen, 10-11 November 1983, VDI-Bericht, Nr. 495

[13] Y. H. Song, J. M. Beer, A.F. Sarofim: Reduction of Nitric Oxide by Coal Char at Temperatures of 1250 - 1750 K, *Comb. Sci. Techn.*, 25, 1981, 237

[14] H. Schulz, H. Kremer: Bildung von Stickstoffoxiden bei der Kohlenstaubverbrennung, *Brennstoff Warme Kraft BWK*, 37, 1985, 1/2, 29-35

[15] J. Zel'dovich: The oxidation of nitrogen in combustion and explosions, *Acta Physicochimica URSS*, 21, 1946, 4, 577-628

[16] Y. B. Zel'dovidh, P. Y. Sadovnik, D. A. Frank-Kamentku: Oxidation of Nitrogen in Combustion, (translated by Shelef), Academy of Sciences of USSR, 1947

[17] B. Koroušić: Fundamental thermodynamic aspects of the CaO-Al_2O_3-SiO_2 system, *Steel res.*, 62, 1991, 7, 285-289

[18] B. Koroušić: Study of equilibrium reactions in gaseous nixtures (Part 1. Protective atmospheres), *Rudarsko-Metalurški zbornik*, 1993, 1-2, 5-17

[19] B Koroušić, M. Stupnišek: A thermodynamic evaluation of nitrocarburizing atmospheres, *Steel res.*, 66, 1995, 8, 349-352

Kovine, zlitine, tehnologije/30/1996/6/527-530

Fusion of Low Carbon Steel Scrap in the Middle Carbon Steel Melt

Taljenje niskougljičnog čeličnog otpatka u talini srednje ugljičnog čelika

V. Grozdanić,[1] Metallurgical faculty Sisak, Croatia

Prejem rokopisa - received: 1996-10-01; sprejem za objavo - accepted for publication: 1996-11-04

A quasi three-dimensional mathematical model of fusion of cylindrical steel scrap in converter melt was developed. The model was solved using the implicit alternating direction method. The obtained algorithm was programmed in ASCII FORTRAN for the computer SPERRY 1100/72. In the model temperature dependent thermophysical properties of material were incorporated. That gives to the model a nonlinearity. On the basis of the model it was concluded that the addition of 1% of low carbon steel scrap decreases the temperature of a middle carbon steel melt for cca 20°C. This is in good agreement with experimental data from literature. The mathematical model was tested for one-dimensional exact solution using the Bessel functions. A good agreement was found.

Key words: fusion, steel scrap, mathematical model

Razvijen je i istražen kvazitrodimenzijski matematički model taljenja valjkastog čeličnog otpatka u talini kod konverterskog procesa. Matematički model riješen je implicitnom metodom promjenljivog smjera. Dobiveni algoritam programiran je u programskom jeziku ASCII FORTRAN za računalo SPERRY 1100/72. U matematički model inkorporirana su temperaturno ovisna toplofizička svojstva materijala, što modelu daje nelinearnost. Na temelju matematičkog modela zaključeno je da 1% niskougljičnog čeličnog otpatka snizi temperaturu srednje ugljične čelične taline za cca 20°C, što se dobro slaže s eksperimentalnim podacima iz literature. Matematički model testiran je na jednodimenzionalnom egzaktnom rješenju pomoću Besselovih funkcija. Konstatirano je njihovo međusobno dobro slaganje.

Ključne riječi: taljenje, čelični otpadak, matematički model

1 Introduction

From the increase of the share of metalic scrap in the charge, an increased economy of steel manufacturing in the converter processes is expected. The share of steel scrap should approach that in the openhearth process. Steel scrap, usually as low carbon steel refuse, is a very economical means of melt cooling. Iron ore is only better means of cooling. Data in ref.1 show that 1% of steel scrap decreases the bath temperature for 12 to 15°C, while 1% iron ore decreases the temperature for 30 to 40°C. However, production expirience shows that steel scrap is better than iron ore. For example, by using steel the quantity of metal ejected from the converter is diminished, the resistance of refractory lining is increased and a better utilization of excess heat in the bath obtained. The regime of scrap fusion depends in significant degree on scrap size, and affects the bath temperature, the slag forming processes, as well as the oxidation of carbon and the metal desulfurization. For instance, small sized scrap melts faster and cools quickly the bath. This decreases the rate of slag forming, carbon oxidation, desulfurization, and lower the quantity of blown oxygen. Very large pieces of scrap don't melt completly during the processing in the oxygen converter. A mathematical model of low carbon steel scrap melting in the carbon steel melt was developed and tested with the aim to determine the optimal scrap size. Since the bath temperature is above 1550°C the so-called diffusion melting is not considered. In **figure 1** the investigated system is illustrated. It consists of a volume element of melt in which cylindrical steel scrap is immersed.

2 Mathematical model

For the start of the melting of a cylindrical scrap piece in a volume element of melt in **figure 1** the Fourier's partial differential equation of heat conduction has the form[2]:

$$\frac{\partial T}{\partial t} = a\left(\frac{\partial^2 T}{\partial r^2} + \frac{1}{r}\frac{\partial T}{\partial r} + \frac{\partial^2 T}{\partial z^2}\right) \tag{1}$$

Since for the horizontal axis of the system r = 0 the equation (1) is modified according to L'Hospital's in the form:

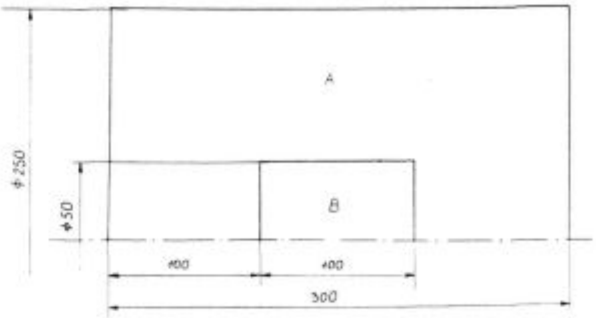

Figure 1: Volume element of melt with cylindrical steel scrap

---

[1] Dr. Sc. Vladimir GROZDANIĆ
University of Zagreb
Metallurgical faculty Sisak, Aleja narodnih heroja 3,
4000 Sisak, Croatia

$$\frac{\partial T}{\partial t} = a\,(2\frac{\partial^2 T}{\partial r^2} + \frac{\partial^2 T}{\partial z^2}) \qquad (2)$$

The basic assumption for the validity of the differential equations (1) and (2) is that scrap piece is immersed is physicaly realistic since the difference in density of steel scrap (7860 kg/m^3) and melt (7507 kg/m^3) is very small. Considering the system in **figure 1**, it can be concluded that mathematical model is quasi three-dimensional. In the time t = 0 the temperature of the melt is T_L, and that of the scrap piece is T_s. The initial temperature at the steel scrap/melt boundary interface is obtained by solving the Fourier's differential equation for heat flow through the contact area of two semifinite medias[3]:

$$T_i = T_s + \frac{T_L - T_s}{1 + \frac{k_s}{k_m}\sqrt{\frac{a_m}{a_s}}} \qquad (3)$$

On the contact steel scrap/melt area a continuous heat flow occurs with boundary condition of the fourth kind:

$$k_m \frac{\partial T_m}{\partial n} = k_s \frac{\partial T_s}{\partial n} \qquad (4)$$

In developing the model it was asummed that thermal properties of low carbon steel scrap (0,2% C) and middle carbon steel melt (0,6% C) are temperature dependent[4].

3 Implicit alternating direction method

The differential heat flow equations (1) and (2) with the corresponding initial and boundary conditions were numerically solved using the implicit alternating direction method[5] and dividing the time interval into two steps.

In the first half of the time interval the equation is solved implicitly for the z and explicitly for the r direction. The procedure is reversed in the second half of time interval.

Consequently, for the differential equation (1) and first half of time interval Δt/2 we obtain:

$$\partial_r^2 T^n_{i,j} + \frac{T^n_{i,j+1} - T^n_{i,j-1}}{2 r_j \Delta r} + \partial_z^2 T^*_{i,j} = \frac{1}{a_{i,j,n}} \frac{T^*_{i,j} - T^n_{i,j}}{\Delta t/2} \qquad (5)$$

Whereas for the second Δt/2 we obtain

$$\partial_r^2 T^{n+1}_{i,j} + \frac{T^{n+1}_{i,j+1} - T^{n+1}_{i,j-1}}{2 r_j \Delta r} + \partial_z^2 T^*_{i,j} = \frac{1}{a_{i,j,n}} \frac{T^{n+1}_{i,j} - T^*_{i,j}}{\Delta t/2} \qquad (6)$$

The numerical solution of the differential equation (2) of heat flow for first Δt/2 is:

$$4\,\frac{T^n_{i,2} - T^n_{i,1}}{(\Delta r)^2} + \partial_z^2 T^*_{i,1} = \frac{1}{a_{i,j,n}} \frac{T^*_{i,1} - T^n_{i,1}}{\Delta t/2} \qquad (7)$$

and for second Δt/2:

$$4\,\frac{T^{n+1}_{i,2} - T^{n+1}_{i,1}}{(\Delta r)^2} + \partial_z^2 T^*_{i,1} = \frac{1}{a_{i,j,n}} \frac{T^{n+1}_{i,1} - T^*_{i,1}}{\Delta t/2} \qquad (8)$$

The solution of equations (1) and (2) for the net point (i, j) in the melt and scrap piece as well as for net points on their boundary surface are given in Appendix 2.

Generally it holds:

$$\begin{aligned}
&b_1v_1+c_1v_1 &&= d_1\\
&a_2v_1+b_2v_2+c_2v_3 &&= d_2\\
&\quad a_3v_3+b_3v_3+c_3v_4 &&= d_3\\
&\text{--------------}&&\\
&\qquad a_iv_{i-1}+b_iv_i+c_iv_{i+1} &&= d_i \quad (9)\\
&\text{------------------}&&\\
&\qquad a_{N-1}v_{N-2}+b_{N-1}v_{N-1}+c_{N-1}v_N &&= d_{N-1}\\
&\qquad a_Nv_{N-1}+b_Nv_N = &&\quad d_N
\end{aligned}$$

where v is the unknown temperature, and N is a real number. On the base of the presented algorithm of fusion a computer program was written in ASCII FORTRAN and solved on SPERRY 1100/72 computer.

4 Discusion

The simulation of fusion of a low carbon steel scrap in the carbon steel melt is carried out by space steps $\Delta z = \Delta r = 1$ cm and the time step $\Delta t = 30$ s till $t_{max} = 630$ s. The initial melt temperatures of 1700°C for the melt, 25°C for the scrap piece and 883°C for the boundary surface were assumed. On the basis of succesive temperatures prints out for particular net points the fusion time of 540 s was obtained for a low carbon steel cylinder of size ϕ 50 x 100 mm. The weight of the scrap piece was 4,3% of total weight of the melt. Thus, it can be concluded that 1% of steel scrap decrease the temperature of steel melt for 20 to 22°C, a value in good agreement with published experimental data[1]. Three-dimensional mathematical model of fusion of scrap piece was tested through the one-dimensional exact solution of the fusion of the low carbon steel cylinder and a good agreement was established. The derivation of the exact solution using Bessel functions is given in Appendix 3.

5 Conclusions

A quasi three-dimensional mathematical model of fusion of low carbon steel scrap piece in carbon steel melt in oxygen converter was developed. The model was checked in the base of experience data. The simulation of the fusion is carried out on cylindrical piece of diameter of 50 mm and length of 100 mm. The fusion time of 540 s was calculated. Also it has been established that the addition of 1% of steel scrap decrease the melt temperature for cca 20°C, a value in good agreement with experimental data, and also with the exact one-dimensional solution of the equations, which are the model base.

Appendix 1

Abbreviations used:

a - temperature conductivity

a_i, b_i, c_i, d_i - coefficients adjoining to unknowns in tridiagonal system of algebric equations
c_p - specific heat at constant pressure
k - thermal conductivity
n - vertical direction
r - space coordinate
t - time
T - temperature
v_i - unknown in system of simultaneous algebric equations
z - space coordinate

Appendix 2

Constant whivh appear in tridiagonal coefficients

$$p_1 = \frac{a\Delta t}{2(\Delta r)^2}$$

$$p_2 = \frac{a\Delta t}{4r_j\Delta r}$$

$$p_3 = p_1 - p_2$$

$$p_4 = p_1 + p_2$$

$$p_5 = \frac{\Delta t(k_A + k_B}{2c(\Delta r)^2}$$

$$p_6 = \frac{\Delta t(k_A + k_B}{4cr_j\Delta r}$$

$$c = \frac{k_A}{a_A} + \frac{k_B}{a_B}$$

$$q_1 = \frac{a\Delta t}{2(\Delta z)^2}$$

$$q_2 = \frac{k_A\Delta t}{c(\Delta t)^2}$$

$$q_3 = \frac{k_B\Delta t}{c(\Delta t)^2}$$

$$q_4 = \frac{\Delta t\ (k_A + k_B)}{2c(\Delta z)^2}$$

$$q_5 = \frac{k_A\Delta t}{c(\Delta r)^2}$$

$$q_6 = \frac{k_B\Delta t}{c(\Delta r)^2}$$

Tridiagonal coefficients

1. Point (i,j) in the melt or scrap piece

– first Δt/2:
$a_i = c_i = -q_1$
$b_i = 1 + 2q_1$
$$d_i = p_3T^n_{i,j-1} + (1-2p_1)T^n_{i,j} + p_4T^n_{i,j+1} \quad (10)$$
– second Δt/2:
$a_j = -p_3$
$b_j = 1 + 2p_1$
$c_j = -p_4$
$$d_j = q_1T^*_{i-1,j} + (1-2q_1)T^*_{i,j} + q_1T^*_{i+1,j} \quad (11)$$

2. Point (i,j) on the boundary surface parallel to r axis separating the materials A (left) and B (right)

– first Δt/2:
$a_i = -q_2$
$b_i = 1 + q_2 + q_3$
$c_i = -q_3$
$$d_i = (p_5-p_6)T^n_{i,j-1} + (1-2p_5)T^n_{i,j} + (p_5+p_6)T^n_{i,j+1} \quad (12)$$
– second Δt/2:
$a_j = -(p_5-p_6)$
$b_j = 1+2p_5$
$c_j = -(p_5+p_6)$
$$d_j = q_2T^*_{i-1,j} + (1-q_2-q_3)T^*_{i,j} + q_3T^*_{i+1,j} \quad (13)$$

3. Point (i,j) on the boundary surface parallel z axis separating the materials A (down) and B (up)

– first Δt/2:
$a_i = c_i = -q_4$
$b_i = 1+2q_4$
$$d_i = (q_5-q_6)T^n_{i,j-1} + (1-2p_5)T^n_{i,j} + (q_6+p_6)T^n_{i,j+1} \quad (14)$$
– second Δt/2:
$a_j = p_6 - q_5$
$b_j = 1+2p_5$
$c_j = -(q_6-p_6)$
$$d_j = q_4T^*_{i-1,j} + (1-2q_4)T^*_{i,j} + q_4T^*_{i+1,j} \quad (15)$$

4. Point (i,1) out of the boundary surface

– first Δt/2:
$a_i = c_i = -q_1$
$b_i = 1+2q_1$
$$d_i = (1-4p_1)T^*_{i,1} + 4p_1T^n_{i,2} \quad (16)$$
– second Δt/2:
$b_j = 1+4p_1$
$c_j = 4p_1$
$$d_j = q_1T^*_{i-1,1} + (1-2q_1)T^*_{i,1} + q_1T^*_{i+1,1} \quad (17)$$

5. Point (i,1) on the boundary surface which separates the materials A (left) and B (right)

– first Δt/2:
$a_i = -q_2$
$b_i = 2q_4 + 1$
$c_i = -q_3$
$$d_i = (1-4p_5)T^n_{i,1} + 4p_5T^n_{i,2} \quad (18)$$
– second Δt/2:
$b_j = 4p_5 + 1$
$c_j = -4p_5$
$$d_j = q_2T^*_{i-1,1} + (1-2q_4)T^*_{i,1} + q_3T^*_{i+1,1} \quad (19)$$

Appendix 3

One-dimensional mathematical model of fusion of steel cylinder consists of the solution of a differential equation of heat conduction with adequate initial and boundary conditions

$$\frac{\partial T}{\partial t} = a\,(\frac{\partial^2 T}{\partial r^2} + \frac{1}{r}\frac{\partial T}{\partial r}) \qquad 0<r<1,\ t>0 \quad (20)$$

$T(r,0) = T_0$
$T(1,t) = T_L$
$|T(r,t)| < M$
where M is a positive real number.

It is convenient to consider insted of the equation (20) the equation

$$\frac{\partial T}{\partial t} = \frac{\partial^2 T}{\partial r^2} + \frac{1}{r}\frac{\partial T}{\partial r} \tag{21}$$

and then to repleace t by at.

Applying the Laplace transform[6], we find

$$\frac{d^2\theta}{dr^2} + \frac{1}{r}\frac{d\theta}{dr} - s\theta = -T_0 \tag{22}$$

$\theta(1,s) = T_L/s$, $\theta(r,s)$ is connected.

The general solution of this equation is given in terms of Bessel functions as

$$\theta(r,s) = c_1 J_0(ir\sqrt{s}) + c_2 Y_0(ir\sqrt{s}) + \frac{T_0}{s} \tag{23}$$

Since $Y_0(ir\sqrt{s})$ is unbounded as $r \to 0$, we must choose $c_2 = 0$. Than

$$\theta(r,s) = c_1 J_0(ir\sqrt{s}) + \frac{T_0}{s} \tag{24}$$

From the boundary conditions we find

$$\theta(1,s) = c_1 J_0(i\sqrt{s}) + \frac{T_0}{s} = \frac{T_L}{s} \tag{25}$$

$$c_1 = \frac{T_L - T_0}{sJ_0(i\sqrt{s})} \tag{26}$$

$$\text{Thus}\quad \theta(r,s) = \frac{T_0}{s} + (T_L - T_0)\frac{J_0(ir\sqrt{s})}{sJ_0(i\sqrt{s})} \tag{27}$$

After complex inversion this equation acquires the form

$$T(r,t) = T_0 + (T_L - T_0)\frac{1}{2\pi 1}\int_{\gamma-i\infty}^{\gamma+i\infty}\frac{e^{st}J_0(ir\sqrt{s})}{sJ_0(i\sqrt{s})\,ds} \tag{28}$$

and the final solution is obtained as

$$T(r,t) = T_L - 2(T_L - T_0)\sum_{n=1}^{\infty}\frac{e{-}a\lambda_n^2 t\, J_0(\lambda_n^r)}{\lambda_n J_1(\lambda_n)} \tag{29}$$

where $\lambda_1, \lambda_2, \ldots, \lambda_n, \ldots$ are positive zeros of equation $J_0(\lambda_n) = 0$, which are given in **Table 1**.

Table 1: Zeros of equation $J_0(\lambda_n) = 0$[7].

n	λ_n
1	2,40482 55577
2	5,52007 81103
3	8,65372 79129
4	11,79153 44391
5	14,93091 77086
6	18,07106 39679
7	21,21163 66299
8	24,35247 15308
9	27,49347 91320
10	30,63460 64684

6 References

[1] M. Ja. Madžibožski, Osnovi termodinamiki i kinetiki staleplaviteljnih processov, Viša škola, Kiev, 1986

[2] F. Oeters, Metallurgie der Stahlerstellung, Springer-Verlag, Berlin, 1989

[3] V. Grozdanić, *Metalurgija*, 30, 1991, 1/2, 47-50

[4] V. Grozdanić, *Livarstvo*, 5, 1990, 1, 3-11

[5] J. Douglas, H. H. Rachford, *Trans. Amer. Math. Soc.*, 82, 1956, 421

[6] M. R. Spiegel, Laplace Transforms, McGraw-Hill, New York, 1965

[7] M. Abramowitz, I. A. Stegun (eds.), Handbook of Mathematical Functions with Formulas, Graphs and Mathematical Tables, National Bureau of Standards, Washington, 1964

Kovine, zlitine, tehnologije/30/1996/6/531-537

Equilibrium Grain Boundary Segregation of Antimony in Iron Base Alloys

Ravnotežna segregacija antimona po mejah zrn v zlitinah železa in antimona

R. Mast[1], H. Viefhaus, M. Lucas, H. J. Grabke, Max-Planck-Institute, Düsseldorf, Germany

Prejem rokopisa - received: 1996-10-01; sprejem za objavo - accepted for publication: 1996-11-04

The equilibrium grain boundary segregation of antimony was investigated in iron base alloys (Fe-Sb, Fe-C-Sb, Fe-Ni-Sb) after annealing at temperatures between 550°C and 750°C. Utilizing Auger electron spectroscopy (AES) the concentration of antimony at intergranular fracture faces was determined as a function of bulk concentration and equilibration temperature. The segregation of antimony in Fe-Sb alloys with 0,012 wt.% - 0,094 wt.% Sb was described by the Langmuir-McLean equation. The evaluation leads to the free enthalpy of segregation $\Delta G_{segr.}$ = -19 kJ/mol - T 28 J/mol K. For Fe-0,93 wt.% Sb and Fe-1,91 wt.% Sb a thermodynamic calculation is not possible because of intergranular antimonides had formed. Scanning electron micrographs (SEM) of fractured samples show that the percentage of intergranular fracture increases with an increasing coverage of antimony at the grain boundaries. The addition of carbon to Fe-Sb alloys results in a higher grain boundary cohesion which is caused by two effects of carbon, displacement of antimony from the grain boundaries by carbon and enhanced grain boundary cohesion. In the Fe-Ni-Sb alloys an additional segregation of nickel was found at the grain boundaries but no enhanced antimony segregation, as expected from previous models of other authors, assuming Ni-Sb cosegregation.

Key words: grain boundary segregation, antimony equilibrium segregation, Fe-Sb alloys, Fe-C-Sb alloys, Fe-Ni-Sb alloys, segregation thermodynamics, Langmuir-McLean equation, Auger electron spectroscopy (AES), intergranular fracture, embrittlement, site competition, Charpy impact tests

Ravnotežna segregacija antimona po mejah zrn v zlitinah z železnoosnovno (Fe-Sb, Fe-C-Sb, Fe-Ni-Sb) po žarjenju v temperaturnem področju od 550°C do 750°C. Z metodo spektroskopije Augerjevih elektronov (AES) je bila določena koncentracija antimona na interkristalnih prelomnih ploskvah kot funkcija vsebnosti antimona v osnovnem materialu in ravnotežne temperature. Segregacija antimona v Fe-Sb zlitinah z 0.012 ut.% - 0,094 ut.% Sb je opisana z Langmuir McLeanovo enačbo izračunana je bila prosta entalpija segregacije $\Delta G_{segr.}$ = -19 kJ/mol - T 28 J/mol K. Za zlitini Fe -0,93 ut.% Sb in Fe -0,91 ut.% Sb termodinamični izračuni niso mogoči zaradi tvorbe interkristalnih antimonidov. Posnetek z vrstičnim elektronskim mikroanalizatorjem (SEM) prelomljenih vzorcev kaže, da odstotek interkristalnega preloma narašča z naraščajočo segregirano plastjo antimona na mejah zrn. Dodatek ogljika v Fe-Sb zlitino povzroči večjo kohezijo med posameznimi zrni, ogljik namreč izrine antimon z mej zrn in zviša kohezijo kristalnih mej. V Fe-Ni-Sb zlitinah je bila določena še segregacija niklja na mejah zrn ne pa tudi povečana koncentracija antimona kot je bilo pričakovati po prejšnjih modelih nekaterih avtorjev, ki so predvideli skupno segregacijo Ni-Sb.

Ključne besede: segregacija na mejah zrn, ravnotežna segregacija antimona, Fe-Sb zlitine, Fe-C-Sb zlitine, Fe-Ni-Sb zlitine, termodinamika segregacij, Langmuir McLeanova enačba, spektroskopija Augerjevih elektronov (AES), interkristalni prelom, krhkost, tekmovanje za prosta mesta na površini, Charpyjev udarni preizkus

1 Introduction

The increased usage of low quality scrap in steel production will lead to a higher content of antimony in steels, which may have a deleterious effect on material properties. The presence of antimony (and/or other tramp elements such as P, Sn, S, As) induces temper embrittlement of low alloy ferritic steels by segregation to the grain boundaries during application at higher temperatures[1,2,3]. The driving forces for such an enrichment in a range of a monolayer are the decrease of interfacial energy and the release of elastic energy. Especially the latter effect is important for antimony because of its large atom size compared to iron atoms. Many researches have been shown that the amount of antimony segregation depends on the total composition of the steel. However, there is no uniform evidence how other alloying components, especially nickel[2,4,5], influence antimony segregation.

Therefore, the equilibrium grain boundary segregation of antimony and its effects on material properties were examined in simple iron base alloys to avoid the complex chemistry of multicomponent steels. The degree of coverage was determined by Auger electron spectroscopy (AES) on the intergranular fracture faces after fracture by impact inside the UHV chamber. The influence on the mechanical behaviour was studied by scanning electron microscopy (SEM) and Charpy impact tests.

2 Experimental procedure

The alloys used in this study were melted in a vacuum induction furnace. The chemical compositions are listed in **Table 1**. Small amounts of manganese (0,02 wt.%) were added to each alloy to tie up sulfur, which has a strong tendency for grain boundary segregation[3] and may hinder antimony segregation.

The ingots of the Fe-Sb, Fe-C-Sb and Fe-Ni-Sb alloys were hot forged and then machined into rectangular specimens. The Fe-Sb and Fe-Ni-Sb samples were heat treated by austenitizing at 1060°C for 70-90 min, air

---

[1] Dr.Sc. Ralph MAST
Max-Planck-Institut für Eisenforschung GmbH
Postfach 140 444, 40074 Düsseldorf, Germany

Table 1: Chemical composition of the Fe-Sb, Fe-C-Sb and Fe-Ni-Sb alloys (wt.%)

Alloy	Sb	C	Mn	P	S
Fe-Sb1	0,012	0,005	0,027	0,0015	0,0013
Fe-Sb2	0,049	0,0048	0,027	0,0011	0,001
Fe-Sb3	0,094	0,0057	0,027	0,001	0,0011
Fe-Sb4	0,93	0,006	0,026	0,0013	0,0012
Fe-Sb5	1,91	0,0039	0,028	0,0014	0,0012
Fe-C-Sb1	0,056	0,0043	0,025	<0,002	0,0013
Fe-C-Sb2	0,053	0,0085	0,023	<0,002	0,0013
Fe-C-Sb3	0,052	0,0144	0,023	<0,002	0,0014
Fe-C-Sb4	0,094	0,0057	0,027	0,001	0,0011

Alloy	Sb	Ni	C	Mn	P
Fe-Ni-Sb1	0,049	0,53	0,0035	0,022	<0,002
Fe-Ni-Sb2	0,049	2,85	0,0069	0,024	<0,002

cooling, and then tempering at 780°C for 168 h and water quenching. These two heat treatments were performed in flowing wet hydrogen to decrease the bulk carbon concentration below 10 wt.-ppm.

The Fe-C-Sb alloys were annealed in flowing dry argon to avoid carbon losses. The samples were homogenized at 1060°C for 70 min and air cooled. Afterwards they were recrystallized at 780°C for 2 h and water quenched.

Then all specimens were held at ageing temperatures of 550°C, 600°C, 650°C, 700°C and 750°C for different periods of time, to establish the equilibrium concentration of antimony at the grain boundaries. The time necessary for equilibration at each temperature can be assessed using an equation proposed by McLean[6]. AES measurements confirmed that the calculated time was long enough to reach equilibrium segregation; the conditions of each exposure are listed in **Table 2**.

Table 2: Conditions for the establishment of segregation equilibria

Ageing Temperature/ Ageing Time	Exposure Conditions
550°C/600 h	vacuum/quenched in water
600°C/140 h	vacuum/quenched in water
650°C/ 50 h	flowing argon/quenched in water
700°C/ 5 h	flowing argon/quenched in water
750°C/ 2 h	flowing argon/quenched in water

The amount of grain boundary segregation was to be measured by AES, which is conducted in UHV to avoid surface contamination. After cooling to about -120°C the cylindrical notched specimens were fractured by impact in the UHV chamber of the spectrometer. The fracture surface was then imaged by operating the electron beam in a scanning electron microscope (SEM) mode to distinguish between intergranular and transgranular areas. Auger spectra were taken from at least 10 individual grain boundary facets using a cylindrical mirror analyzer (CMA) and the results were averaged. The peak-to-peak heights of antimony (454 eV), nickel (848 eV) and carbon (271 eV) were related to the iron peak at 651 eV. The entire analysis of each fracture face had to be completed within approximately 3 h to prevent contamination effects. The operating conditions were as follows: primary beam energy 5 kV, primary beam current 3×10^{-6} A, and primary beam size 10 µm.

To estimate the degree of coverage of antimony at the grain boundaries, it can be assumed that antimony is uniformly distributed on both fracture faces. This supposition was verified by some AES measurements in which opposite fracture facets were investigated[7]. From LEED studies of surface segregation on Fe-Sb single crystals a calibration factor had been obtained which converts the peak-to-peak height ratio to the degree of coverage[8].

Supplementary surface analytical methods were employed. The binding state of core electrons of segregated antimony was determined by X-ray photoelectron spectroscopy (XPS), while scanning Auger microscopy (SAM) was applied to examine the distribution of segregated elements on grain boundary facets.

The fracture type and the mechanical properties were investigated using SEM (accelerating voltage 20 kV) and Charpy impact tests (DIN 50115).

3 Results and discussion

3.1 Fe-Sb alloys

Typical Auger spectra of transgranular and intergranular areas are represented in **Figure 1**. On transgranular fracture surfaces of the Fe-0,094 wt.% Sb alloy, no antimony peak was observed, since the bulk concentration is below the detection limit of the AES method. The oxygen peak is due to adsorption from the residual atmosphere after breaking the sample. The spectrum taken on a grain surface of the same alloy clearly indicates the enrichment of antimony which is caused by grain boundary segregation.

Figure 2 illustrates that the average coverage of antimony at the grain boundaries increases with increasing bulk concentration and decreasing equilibration temperature. The scatter of the data indicated by the error bars in one curve is rather large (25% - 30% of the mean value) due mainly to the following reasons:

a) The segregation of antimony may be strongly dependent on grain orientation as indicated by surface segregation studies on Fe-Sb single crystals[8].

b) The examined areas have different distances and different surface normals to the cylindrical mirror analyzer (CMA).

c) The degree of coverage is calculated from measurements on only one side of the intergranular fracture face. It was verified by some AES measurements in which opposite fracture facets were investigated that the average grain boundary antimony concentration is nearly the same on both fracture faces[7]. The assumption that an-

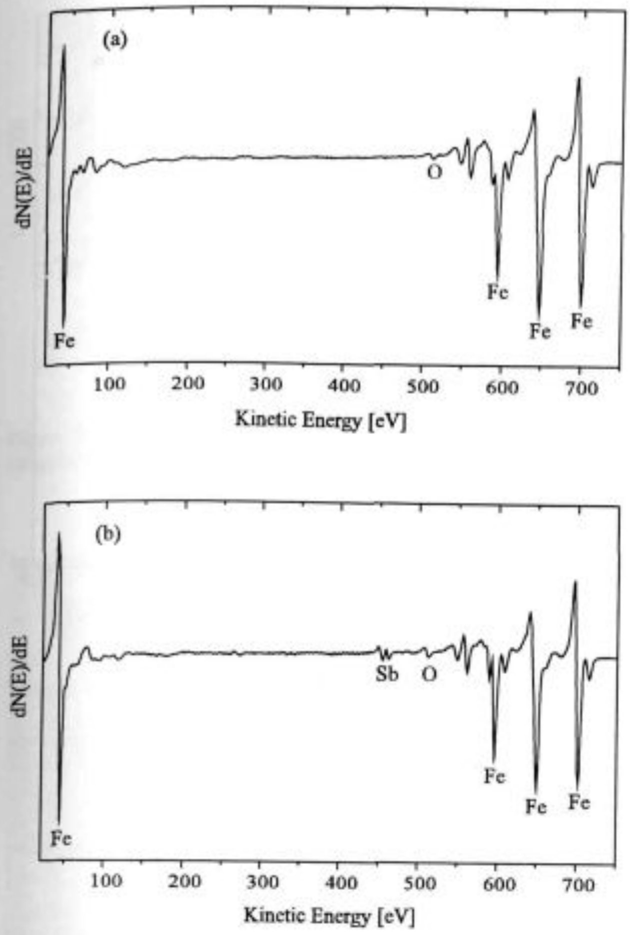

Figure 1: Auger spectra of fracture surfaces of Fe - 0,094 wt.% Sb alloy after annealing at 650°C. a) cleavage facet, b) intergranular fracture surface

Slika 1: AES spekter prelomnih površin Fe - 0,094 ut.% Sb po žarjenju pri 650°C. a) prelomna ploskev, b) interkristalna prrlomna površina

timony is equally distributed is probably not true for each single intergranular area.

In spite of the large scatter of the data, a thermodynamic calculation was attempted, applying the Langmuir-McLean equation

$$\ln\frac{\theta}{1-\theta} - \ln x_{Sb} = -\frac{\Delta H_{segr}}{RT} + \frac{\Delta S^{exs}_{segr}}{R} \qquad (1)$$

which expresses the relationships between bulk concentration (mole fraction) x_{Sb}, temperature T, and degree of coverage θ, at the grain boundaries. The results according to the Langmuir-McLean equation are plotted in **Figure** 3. The estimation yields the segregation enthalpy $\Delta H_{segr.}$ = -19 kJ/mol ± 5 kJ/mol and the segregation entropy $\Delta S_{segr.}$ = 28 J/mol K ± 6 J/mol K. The free enthalpy of segregation in α-iron can be expressed as follows:

$$\Delta G_{segr} = -(19\ \text{kJ/mol} \pm 5\text{kJ/mol}) - T(28\ \text{J/mol K} \pm 6\ \text{J/mol K})$$

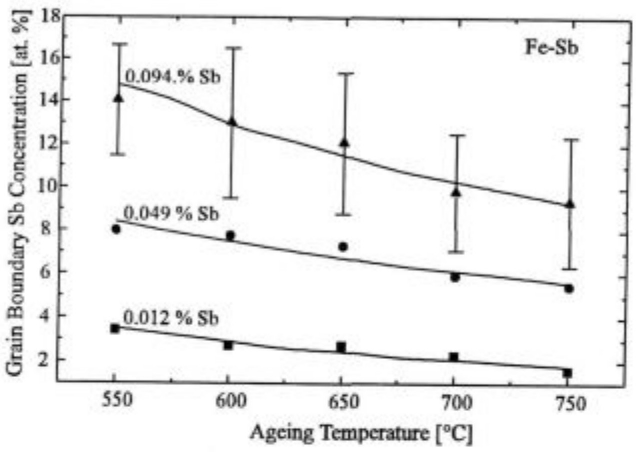

Figure 2: Grain boundary concentration of antimony plotted as a function of equilibration temperature for the alloys Fe - 0,012 wt.% Sb, Fe - 0,049 wt.% Sb and Fe - 0,094 wt.% Sb

Slika 2: Koncentracija antimona na kristalni meji kot funkcija ravnotežne temperature za zlitine Fe - 0,012 ut.% Sb, Fe - 0,049 ut.% Sb in Fe - 0,094 ut.% Sb

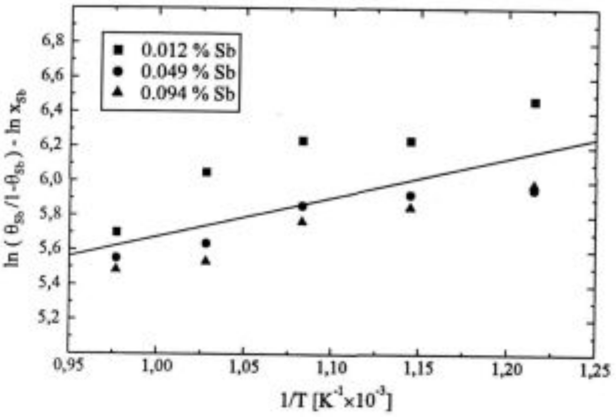

Figure 3: Langmuir-McLean plot of the data in **Figure 2**

Slika 3: Langmuir-McLeanov diagram podatkov iz **slike 2**

The segregation enthalpy value is low compared to values for phosphorus (ΔH_{segr} = -34 kJ/mol)[9] or tin (ΔH_{segr} = -23 kJ/mol)[10], this indicates the low tendency for grain boundary segregation of antimony in iron.

It would be unreasonable in the present thermodynamic calculations to include the AES data for the Fe - 0,93 wt.% Sb and Fe - 1,91 wt.% Sb alloys, since unknown antimonides had formed at the grain boundaries. In **Figure 4**, a typical scanning electron micrograph and the corresponding elemental map for antimony on the same intergranular area of the Fe - 0,93 wt.% Sb alloy indicate star shaped antimonides.

In spite of the low tendency for grain boundary segregation, antimony has a strongly embrittling effect. The relationship between the percentage of intergranular fracture and the grain boundary coverage of antimony is demonstrated in **Figure 5**. With increasing enrichment of antimony at the grain boundaries the fracture mode at

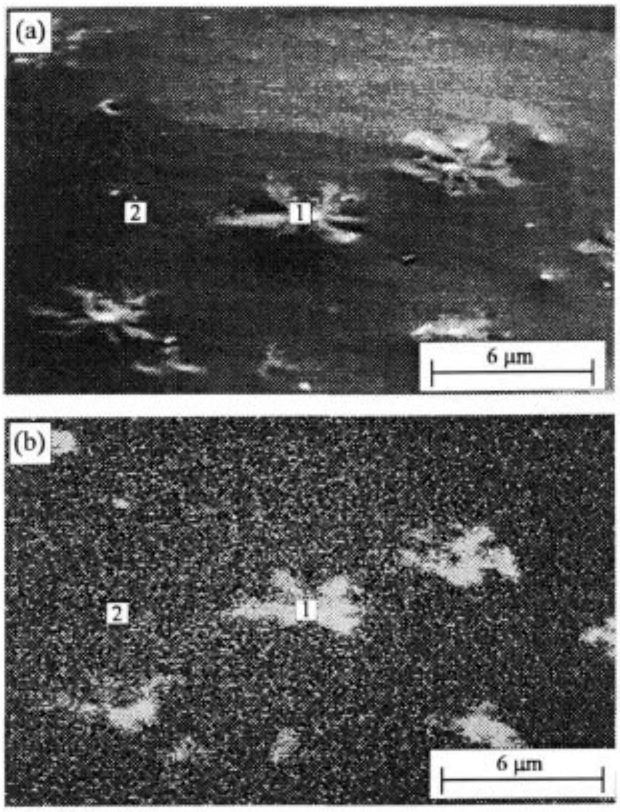

Figure 4: Intergranular antimonides observed in Fe - 0,93 wt.% Sb after annealing at 650°C; a) scanning electron micrograph, b) corresponding scanning Auger image of Sb

Slika 4: Interkristalni antimonidi opaženi v Fe - 0,93 ut.% Sb po žarjenju na 650°C; a) posnetek z vrstičnim elektronskim mikroanalizatorjem, b) vrstični Augerjev posnetek

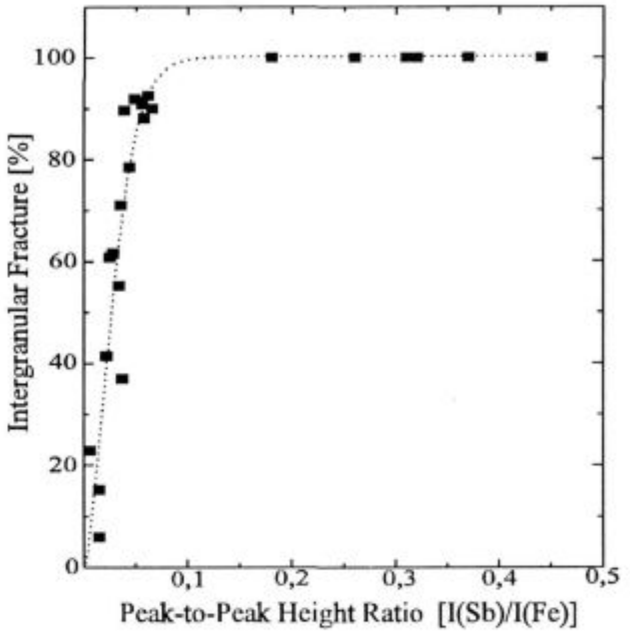

Figure 5: Percentage of intergranular fracture versus peak-to-peak height ratio I(Sb)/I(Fe)

Slika 5: Odstotek interkristalnega preloma v odvisnosti od razmerja višine vrhov I(Sb)/I(Fe)

low temperatures (about -120°C) changes from transgranular to intergranular already at rather low grain boundary concentrations.

The influence of antimony segregation on the mechanical properties was also studied by Charpy impact testing. The transition temperature determined T_T is a measure of the embrittlement of iron base alloys. T_T is defined as the temperature where half of the difference value between the impact work necessary for ductile fracture and the impact work for brittle fracture is reached. For the Fe-Sb alloys a shift of the impact transition temperature to higher values is expected with increasing antimony concentration at the grain boundaries. This supposition is verified in **Figure 6**. For each of the two investigated alloys a higher transition temperature is obtained with increasing coverage of antimony at the grain boundaries. However, the Fe - 0,094 wt.% Sb alloy tempered at 750°C has a lower transition temperature than the Fe - 0,049 wt.% Sb alloy annealed at the same temperature. The observed phenomenon can be explained by the different average grain size of these materials (Fe - 0,049% Sb: 0,21 mm; Fe - 0,094% Sb: 0,08 mm), with increasing antimony concentration the grain size decrease which leads to a higher strength of the material.

One possible way to explain the embrittling behaviour of antimoy is to apply quantum mechanical models[11,12]. The main conclusions of these calculations can be summarized as follows:

The segregated antimony atoms are electronegative with respect to the host metal iron. Consequently electronic charge is transferred from iron to antimony. This charge transfer leaves fewer electrons to participate in

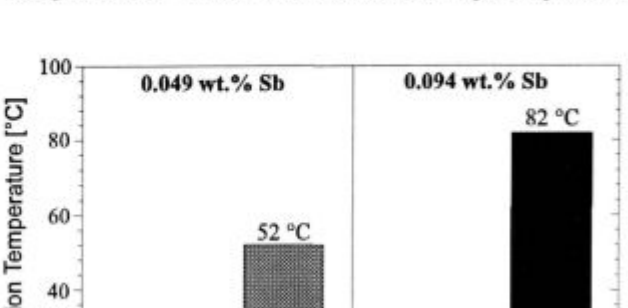

Figure 6: Dependence of the transition temperature on the grain boundary antimony concentration for Fe - 0,049 wt.% Sb and Fe - 0,094 wt.% Sb alloys

Slika 6: Odvisnost koncentracije antimona na mejah zrn od prehodne temperature za zlitine Fe - 0,049 ut.% Sb in Fe - 0,094 ut.% Sb

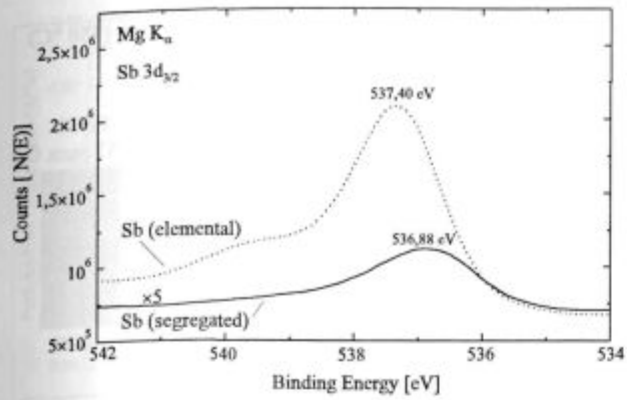

Figure 7: Photolines of pure Sb and segregated Sb in Fe-Sb alloys
Slika 7: XPS krivulje čistega Sb in segregiranega Sb v Fe-Sb zlitini

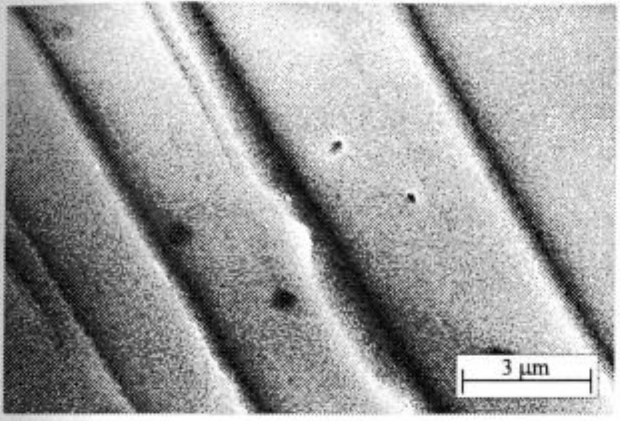

Figure 8: SEM of a faceted grain boundary in Fe - 0,094 wt.% Sb after annealing at 650°C
Slika 8: SEM posnetek facetirane meje v zlitini Fe - 0,094 ut.% po žarjenju na temperaturi 650°C

the iron-iron bonding and these bonds at the grain boundary will be weakened.

XPS measurements on a large area of intergranular fracture of Fe - 0,93 wt.% Sb alloy after annealing at 600°C show that the energies of the Sb 3d electron levels of segregated and pure antimony are distinctly different **(Figure 7)**. The energy shift of about -0,5 eV in comparision to pure antimony indicates an electron transfer to segregated antimony, as expected in the above model.

It is also possible to explain the embrittling behaviour of antimony in another way by taking into consideration that the grain boundaries often are facetted, as illustrated in **Figure 8**. The segregation of antimony induces a reconstruction of the grain faces which results in a decrease of grain boundary cohesion.

On some intergranular areas pores were detected with an average diameter of 2 µm as can be seen in **Figure 9**. An antimony map recorded for the same area, shows antimony enrichment within this pore. Segregated antimony certainly favours the formation of such pores since its surface segregation causes a pronounced decrease of surface energy and such pores will intensity the observed embrittlement of the material.

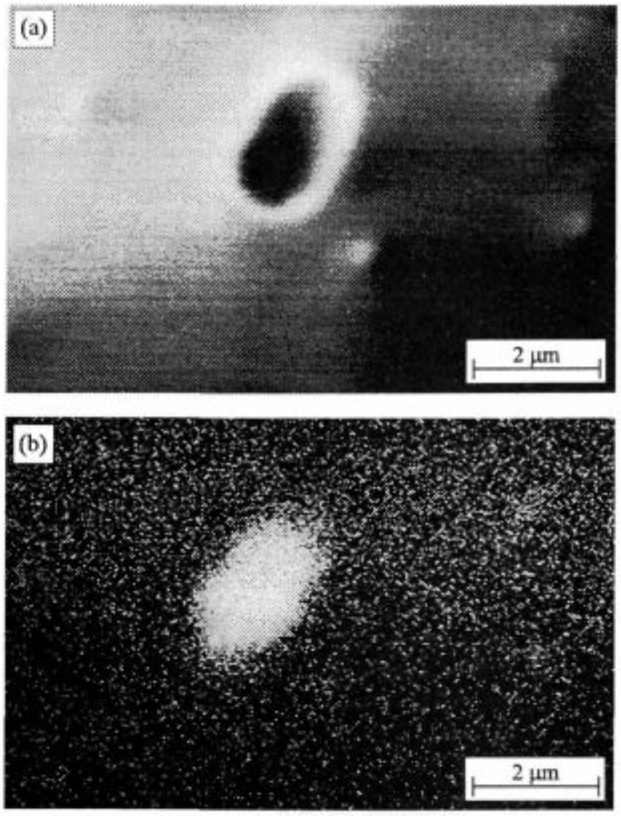

Figure 9: Pore at a grain boundary facet of Fe - 0,094 wt.% Sb after annealing at 600°C; a) SEM, b) corresponding scanning Auger image of Sb
Slika 9: Razpoka v kristalni meji Fe - 0,094 ut.% po žarjenju na temperaturi 600°C; a) SEM posnetek, b) odgovarjajoči SAM posnetek Sb

3.2 Fe-C-Sb alloys

Samples with different antimony and carbon contents were investigated to study the effect of carbon on antimony grain boundary segregation. The fracture faces of the Fe-C-Sb alloys with 0,049 wt.% Sb show transgranular fracture caused by the carbon content. The higher cohesion of these materials compared with corresponding Fe-Sb alloys is due to the fact that antimony is displaced from the grain boundaries by carbon, according to the equation

$$\text{C(dissolved)} + \text{Sb(segregated)} = \text{C(segregated)} + \text{Sb(dissolved)} \qquad (2)$$

The mutual displacement of these two elements corresponding to the displacement equilibria in the systems Fe-C-P[9] and Fe-C-Sn[10], was proven for the Fe-C-Sb alloy with 0,094 wt.% Sb, as shown in **Figure 10**. The average grain boundary concentration of antimony decreases with increasing grain boundary and bulk concentration of carbon. Simultaneously the percentage

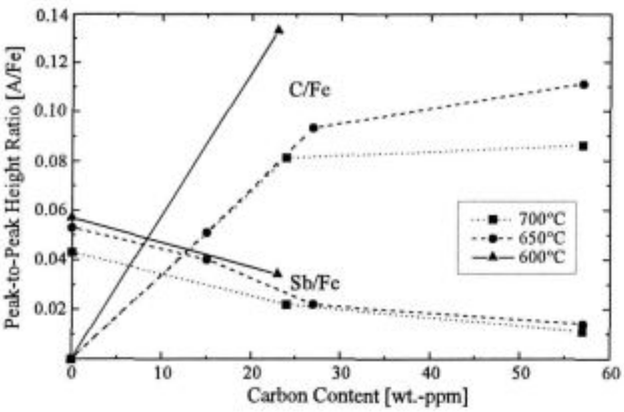

Figure 10: Dependence of the Sb and C grain boundary concentrations on the bulk concentration of carbon in Fe - 0,094 wt.% Sb

Slika 10: Odvisnost koncentracij Sb in C na mejah zrn od koncentracije ogljika v osnovnem materialu Fe - 0,094 ut.% Sb

of transgranular fracture rises with increasing bulk concentration of carbon (**Figure 11**).

The decrease of brittle intergranular fracture of Fe-C-Sb alloys can be explained by the following effects:

a) The strongly embrittling antimony is displaced from the grain boundaries by carbon.

b) The segregated carbon causes a higher grain boundary cohesion.

If energetic interactions between segregated carbon and antimony are neglected, the above mentioned phenomena can be described by considering only the site competition of the two elements

$$\frac{\theta_{Sb}}{1-\theta_{Sb}-\theta_{C}} = x_{Sb}\exp\left(\frac{-\Delta G^{0}_{Sb}}{RT}\right) \qquad (3)$$

$$\frac{\theta_{C}}{1-\theta_{Sb}-\theta_{C}} = x_{C}\exp\left(\frac{-\Delta G^{0}_{C}}{RT}\right) \qquad (4)$$

The de-embrittling effect of carbon was also demonstrated by Charpy impact tests. **Figure 12** illustrates for both Fe-Sb alloys (0,049 wt.% Sb or 0,094 wt.% Sb) tempered at 750°C that the transition temperature shifts to lower values if carbon is added to each alloy.

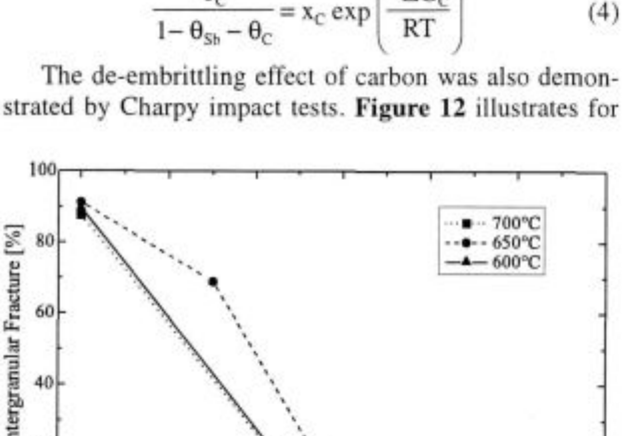

Figure 11: Variation of the percentage of intergranular fracture with bulk concentration of carbon in Fe - 0,094 wt.% Sb

Slika 11: Sprememba odstotka interkristalnih prelomnih ploskev v odvisnosti od koncentracije ogljika v zlitini Fe - 0,094 ut.% Sb

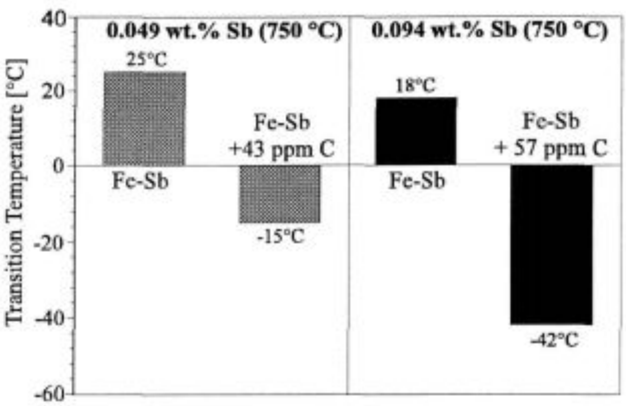

Figure 12: Dependence of the transition temperature on bulk concentration of carbon for Fe - 0,040 wt.% Sb and Fe - 0,094 wt.% Sb after annealing at 750°C

Slika 12: Odvisnost prehodne temperature žilavosti od vsebnosti ogljika v osnovnem materialu Fe - 0,049 ut.% Sb in Fe - 0,094 ut.% Sb po žarjenju na temperaturi 750°C

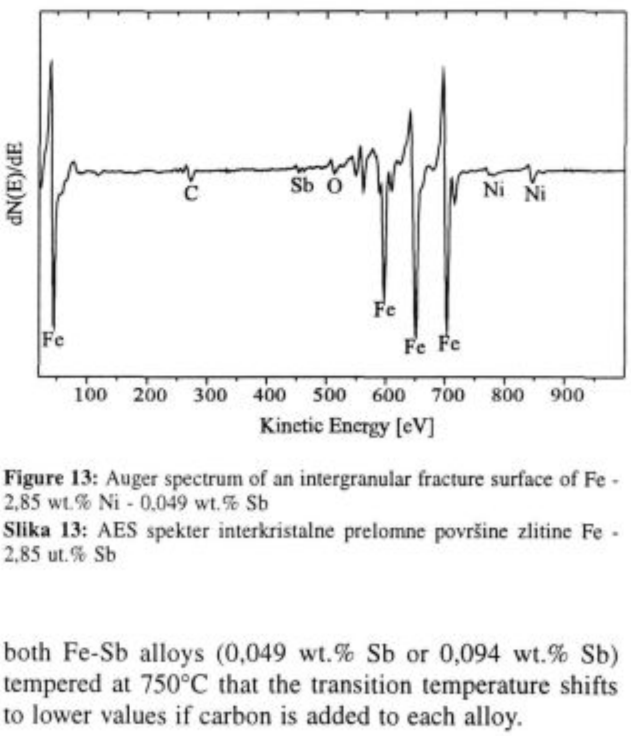

Figure 13: Auger spectrum of an intergranular fracture surface of Fe - 2,85 wt.% Ni - 0,049 wt.% Sb

Slika 13: AES spekter interkristalne prelomne površine zlitine Fe - 2,85 ut.% Sb

3.3 Fe-Ni-Sb alloys

The influence of nickel on the grain boundary segregation of antimony was also investigated for two Fe-Ni-Sb alloys. Auger spectra taken from intergranular areas indicate the enrichment of antimony and nickel; a typical Auger spectrum is shown in **Figure 13**. The temperature dependence of antimony and nickel equilibrium segregation contradicts previous results of other authors[2,4,5] (**Figure 14**). No evidence was found for cosegregation of antimony and nickel or for antimony segregation beeing enhanced by the presence of nickel, as was observed by other authors[2,4]. For the Fe - 0,53 wt.% Ni - 0,049 wt.% Sb alloy the antimony grain boundary concentration is

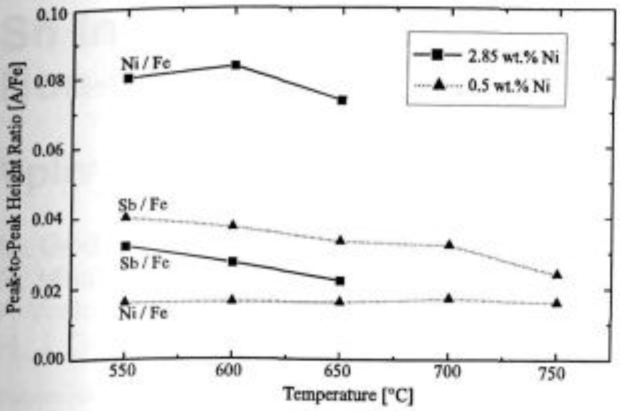

Figure 14: Grain boundary segregation of Sb and Ni plotted as a function of equilibration temperature for two Fe-Ni-Sb alloys

Slika 14: Segregacija Sb in Ni po mejah zrn prikazana kot funkcija ravnotežne temperature za dve zlitini Fe-Ni-Sb

nearly the same at all temperatures as for the same alloy without nickel and is therefore not enhanced by the presence of nickel. Additionally, the amount of nickel segregation is always the same at all temperatures. AES studies on the Fe - 2,85 wt.% Ni - 0,049 wt.% Sb alloy illustrate that the average amount of antimony is lower than in the Fe - 0,53 wt.% Ni - 0,049 wt.% Sb alloy. The grain boundary concentration of antimony increases with decreasing annealing temperature, but the behaviour of nickel is slightly different. After increasing segregation with decreasing temperature the grain boundary segregation of nickel decreases at 600°C. Consequently Guttmann's model of cosegregation does not hold true for the Fe-Ni-Sb system. It was also asserted that the presence of nickel enhances the embrittling behaviour of antimony. Charpy impact tests of Fe-Ni-Sb alloys tempered at 750°C show different results (**Figure 15**). The transition temperature of Fe - 0,049 wt.% Sb and Fe - 0,53 wt.% Ni - 0,049 wt.% Sb alloy is nearly the same, while the transition temperature of Fe - 2,85 wt.% Ni - 0,049 wt.% Sb alloy decreases to a value which is typical for ductile materials. With regard to this result the de-embrittling effect of nickel can be explained by the following effects:

a) Nickel promotes the refinement of grains.

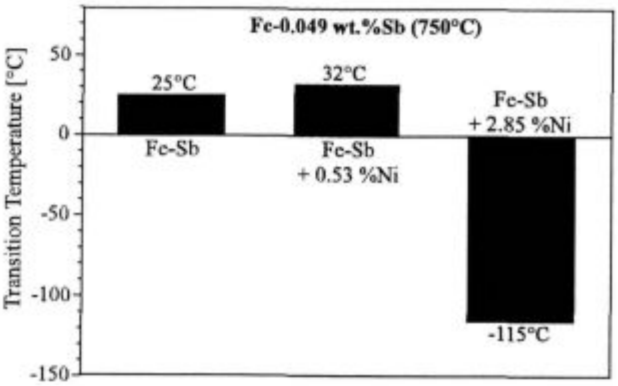

Figure 15: Dependence of the transition temperature on the bulk concentration of nickel for Fe-Ni- 0,049 wt.% Sb alloys after annealing at 750°C

Slika 15: Odvisnost prehodne temperature žilavosti od vsebnosti niklja v Fe-Ni- 0,049 ut.% Sb po žarjenju na 750°C

b) The segregation decrease in antimony may be due to nickel segregation.

Thus the expected severe embrittlement of Fe-Ni-Sb alloys according to earlier investigations was not confirmed.

4 Acknowledgement

The authors are grateful to the European Committee for financial support under contract no. P3455.

5 References

[1] J. Kameda, C. J. McMahon, *Met. Trans. A*, 12A, 1981, 31
[2] C. L. Briant, A. M. Ritter, *Acta Met.*, 32, 1984, 11, 2031
[3] C. L. Briant, H. J. Grabke, *Materials Science Forum*, 46, 1989, 260
[4] P. Gas, M. Guttmann, J. Bernardini, *Acta Met.*, 30, 1982, 1309
[5] A. Wirth, I. Andreoni, G. Gregory, *Surface and Interface Analysis*, 9, 1986, 157
[6] D. McLean, Grain Boundaries in Metals, Oxford University Press., Oxford, 19577, 131
[7] H. Viefhaus, R. Mast, unpublished results
[8] M. Rüsenberg, H. Viefhaus, *Surface Science*, 172, 1986, 615
[9] H. Erhart, H. J. Grabke, *Metal Science*, 15, 1981, 401
[10] W. Jäger, H. J. Grabke, Jin Yu, *Proc. Int. Conf. on 'Residuals and Trace Elements in Iron and Steel*, Portorož, Oct. 1985, ed. by F. Vodopivec, Inst. Metall., Ljubljana, 1986, 217-237
[11] C. L. Briant, R. P. Messmer, *Acta Met.*, 32, 1984, 11, 2043
[12] W. Losch, *Acta Met.*, 27, 1979, 1885

I M T®

INŠTITUT ZA KOVINSKE
MATERIALE IN TEHNOLOGIJE

INSTITUTE OF METALS
AND TECHNOLOGY

1001 LJUBLJANA, LEPI POT 11, SLOVENIJA, POB 431
Phone.: +386 61/125 11 61, Fax: +386 61/213 780

VACUUM HEAT TREATMENT LABORATORY

Vacuum Heat Treatment

Vacuum Heat Treatment is recognised as a high quality cost effective and ultra clean method for processing a wide range of components and materials currently in use in today's industry. The range of our equipment enables us to heat treat most sizes of load, from small batches to work up to 350 mm diameter, 910 mm high, and weight up to 380 kg.

ADVANTAGES

- Clean, bright surface finish
- Minimal distortion
- Minimal post treatment operations, e.g., grinding or polishing

Five years of continual investment has ensured that **VHTL** maintains it position as market leader in the field of high quality sub-contract metal processing.

We operate the latest generation of IPSEN VTTC furnace capable of processing components up to 350 mm in diameter, which in addition to our high pressure, rapid quenching facilities increases the range of materials suitable for Vacuum Heat Treatment.

TYPICAL APPLICATIONS

- Bright Annealing
- Bright Stress Relieving
- Hardening/Tempering
- Brazing/Hardening/Tempering
- Solution Treatment
- Demagnetisation
- Degassing
- Diffusion Treatments
- Sintering

QUALITY ASSURANCE

Quality is fundamental to the **IMT** philosophy. The choice of process, all processing operations and process control are continuously monitored by IMT Quality Control Department.

The high level of quality resulting from this tightly organised activity has been acknowledged by government authorities. industry and International companies.

Kovine, zlitine, tehnologije/30/1996/6/539-543

Sn Influence on the Recrystallization of Non-Oriented Electrical Sheet

Vpliv Sn na rekristalizacijo neorientirane elektro pločevine

M. Godec[1], M. Jenko, IMT Ljubljana, Slovenija
R. Mast, Max-Planck-Institut für Eisenforschung, Düsseldorf, Germany
F. Vodopivec, IMT Ljubljana, Slovenija
H. J. Grabke, H. Viefhaus, Max-Planck-Institut für Eisenforschung, Düsseldorf, Germany

Prejem rokopisa - received: 1996-10-01; sprejem za objavo - accepted for publication: 1996-11-04

During the recrystallization microalloyed tin in non-oriented silicon steel segregates to the surface and grain boundary and as a surface active element selectively decreases the surface energy of grains, planes of which (100) lie parallel to the surface sheet. This phenomenon can be used to achieve non-oriented electrical steel with improved electromagnetic properties. Auger electron spectroscopy was used to measure the grain boundary and surface segregation of tin in non-oriented electrical steels. The grain boundary segregation of the specimens, which were previously aged at 550°C for different times and were fractured in UHV conditions, was measured. The segregation temperature dependence and its kinetics were followed in polycrystalline specimens in the temperature range from 400°C to 900°C on the grains of known orientations: (100), (111) and (110). In spite of fact that the grain boundary segregation is much smaller compared with surface segregation, both might have an influence on recrystallization and on texture development in electrical steel. The textures of electrical steels were measured by X-ray texture goniometer. The results were presented as orientation distribution functions. The selective grain growth can be achieved by controlled surface segregation by which the electrical properties of non-oriented electrical steel are improved. The best results were obtained by alloying it with 0.05 wt.% Sn.

Key words: non-oriented silicon steel, tin, surface and grain boundary segregation, recrystallization, texture

Kositer, mikrolegiran v neorientirani elektro pločevini, pri rekristalizaciji segregira na površino in meje zrn in kot površinsko aktivni element selektivno zmanjša površinsko energijo zrn, katerih ravnine (100) ležijo vzporedno s površino pločevine. Ta pojav lahko izkoristimo za izdelavo neorientirane elektro pločevine z izboljšanimi elektromagnetnimi lastnostmi. S spektroskopijo Augerjevih elektronov smo zasledovali segregacijo po mejah zrn in na površini neorientirane elektropločevine. Segregacijo po mejah zrn smo merili na vzorcih, ki so bili predhodno starani na temperaturi 550°C različno dolgo in prelomljeni v pogojih UVV. Tudi temperaturno odvisnost segregacije in njeno kinetiko smo zasledovali na polikristalnih vzorcih, v temperaturnem območju od 400°C do 900°C, na zrnih znanih orientacij: (100), (111) in (110). Kljub temu, da je segregacija po mejah zrn veliko manjša od segregacije na površini, pa imata verjetno obe vpliv na rekristalizacijo in tako na razvoj teksture elektro pločevine. Teksturiranost elektro pločevin smo določili z rentgenskim goniometrom. Rezultati so predstavljeni z orientacijskimi porazdelitvenimi funkcijami. S kontrolirano površinsko segregacijo dosežemo selektivno rast zrn, kar izboljša električne lastnosti neorientirane elektro pločevine. Najboljše rezultate smo dosegli pri legiranju z 0.05 mas.% Sn.

Ključne besede: neorientirana elektro pločevina, kositer, površinska segregacija in segregacija po mejah zrn, rekristalizacija, tekstura

1 Introduction

Recrystallization, corrosion, adsorption, catalysis, surface diffusion, adhesion, sintering and some other processes are decisively depended of chemical composition and structure of surface. On the other hand the mechanical properties and the corrosion resistivity of metals and alloys are greatly influenced by the atomic composition of grain boundaries and interfaces[1].

The chemical composition of surfaces and grain boundaries are drastically changed during heat treatment of steels due to the well-known phenomenon called segregation. Some of the alloying elements and also some of the tramp elements in ppm level from IV A to VI A group enrich surface and grain boundaries. Equilibrium segregation is reached by the interaction of free bonds on the surface with the segregating elements. This decreases the surface energy and releases the elastic energy of the lattice[2].

By alloying non-oriented electrical steels with small additions of surface active elements such as Sn, Sb, Te and Se, the texture can be significantly improved[3-9]. Tin, when added in the range of a 0.02-0.1 wt%, can improve magnetic properties, though it is not desirable in steel[10]. During the recrystallization process, tin segregates at the grain boundaries and on the surface. The thickness and structure of the segregated layer depend on the crystallographic orientation[11].Thus, by segregation, the surface energy decreases selectively, and so the difference in the total energy of the grain, which is the driving force for its growth during recrystallization. It is logical to expect a selective effect on grain growth with a different space orientation.

The aim of the present work was to find out the correlation of segregation and the texture development. Surface and grain boundary segregation of tin in non-oriented electrical steel alloyed with 2 wt.% Si and 1 wt.% Al and different contents of tin (0.025, 0.05 and 0.1.wt.%) were determined. The temperature dependence and the kinetics of surface segregation were studied with the emphasis on orientation dependence. The correlation

---

[1] Mag. Matjaž GODEC, dipl.inž.met.
Inštitut za kovinske materiale in tehnologije
1000 Ljubljana, Lepi pot 11, Slovenija

between tin segregation and texture development was ascertained. The segregation of tin during the recrystallization increased the grain growth of (100) grains lying in the plane of the sheet and in the same time decreased the growth of (111) grains.

2 Experimental

Four experimental non-oriented electrical sheets were produced from the same basic material. The compositions of vacuum melted and cast steels are listed in **Table 1**.

Table 1: Chemical composition of steels in wt.%
Tabela 1: Kemijska sestava preiskovanih jekel v mas.%

Steel	C	Mn	Si	S	Al	Sn
A	0.0015	0.24	2.2	0.0005	1.10	0.000
B	0.0025	0.26	2.01	0.0028	1.10	0.027
C	0.0015	0.23	2.02	0.0005	0.95	0.048
D	0.0015	0.23	2.08	0.0004	0.95	0.097

The resulting ingots of about 15 kg weights were hot rolled, at a starting temperature of 1200°C, to the final strip thicknesses of 6 mm and 2.5 mm. The strips were descaled and decarburized in a wet hydrogen (dew point 25°C) for two hours at 840°C.

Segregation was studied "in situ" using Auger Electron Spectroscopy - AES. The tin enrichment on the surface was determined by following the peak height ratio (PHR) of amplitudes between the dominant $Sn(M_5N_{45}N_{45})$ and the $Fe(L_3M_{23}M_{54})$ Auger transitions, located at the 430 and 651 eV kinetic electron energies.

For grain boundary segregation the notched cylindrical specimens of 3.7 mm and 5 mm in diameter and of 3 mm length, were prepared from a 6 mm thick hot rolled strip. The specimens were encapsulated in quartz tubes and were evacuated to 10^{-6} mbar. After they had been normalised for 24 hours at 1000°C, they were aged from 5 to 1000 hours at 550°C. The cylindrical notched specimens were introduced into a UHV chamber of the spectrometer, being cooled to about -120°C, the specimens were fractured by impact. The newly-formed surface was imaged by a scanning electron microscope (SEM). The Auger spectra were taken from as many intergranular fractures as possible and the results were averaged[12-13].

The specimens for surface segregation were prepared from a hot rolled strip of 2.5 mm, descaled, decarburized and, after intermediate annealing (900°C, 1 hour, dry hydrogen), cold rolled to the final thickness of 0.5, 0.2, and 0.1 mm with a cold deformation of 60%. Specimens were secondary recrystallized in-situ during AES measurements in UHV (10^{-10} mbar), as well as in a tube furnace in an argon atmosphere.

The grain orientation was determined by the etch pitting method[14,15]. The specimens with known orientation were heated to 900°C for 10 minutes and cooled down to room temperature. These were then sputter cleaned and annealed in a temperature range of 450°C to 1000°C. The temperature was increased in steps of 50°C every 15 minutes and the AES spectra were recorded in-situ every 3.5 minutes. For the kinetics studies, the specimens were heated to a certain temperature, sputtered to a clean surface and exposed to the same temperature for different periods of time.

The X-ray diffraction method was used for texture measurements. A goniometer using MoKα radiation was applied and the (200), (110) and (211) pole figures were performed. Additionally, orientation distribution functions (ODF) were calculated and texture fibres were plotted.

3 Results and discussion

Tin added into experimental steels was in the range of solubility in α-Fe at all examined temperatures but it was below the detection limit of AES. After the specimens were exposed to higher temperature tin enriched the surface, grain boundaries and interfaces due to equilibrium segregation and its segregation were detectable by AES. All AES spectra were normalised to $Fe(L_3M_{23}M_{54})$ Auger transition at the 651 eV kinetic energy[11].

3.1 Grain boundary segregation

The equilibrium segregation of tin was attained after annealing the specimen alloyed with 0.1% Sn for 200 hours at 550°C (**figure 1**). Considering that tin is equal distributed on both fractured sides, it was estimated a 7% tin monolayer at grain boundaries. The scattering of results was rather large due to the strong dependence of tin segregation to grain boundary orientation[12,16]. Steel alloyed with 0.05% Sn had much less intergranular facets. Evaluated equilibrium segregation was smaller than in steel alloyed with 0.1% Sn. Detailed AES analyses of

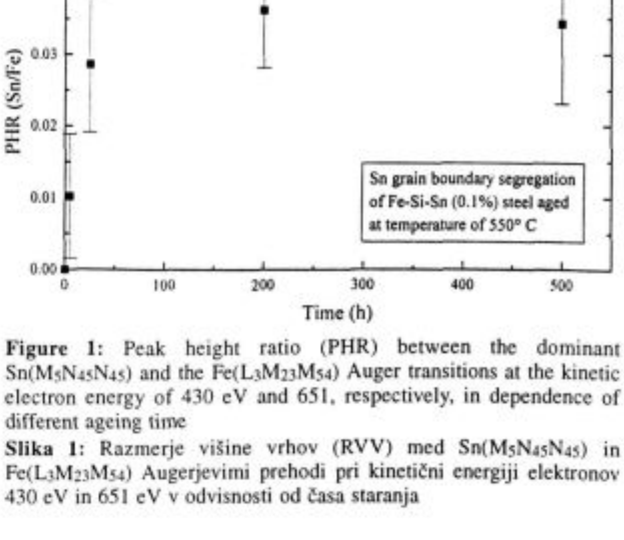

Figure 1: Peak height ratio (PHR) between the dominant $Sn(M_5N_{45}N_{45})$ and the $Fe(L_3M_{23}M_{54})$ Auger transitions at the kinetic electron energy of 430 eV and 651, respectively, in dependence of different ageing time

Slika 1: Razmerje višine vrhov (RVV) med $Sn(M_5N_{45}N_{45})$ in $Fe(L_3M_{23}M_{54})$ Augerjevimi prehodi pri kinetični energiji elektronov 430 eV in 651 eV v odvisnosti od časa staranja free surfaces between inclusion (AlN, Al_2O_3) and matrix clearly indicated that the considerable tin segregation occurs at the interface. The degree of tin segregation at the interface is five times larger than at the grain boundaries.

3.2 Surface segregation

Scanning Auger image (SAM) of non-oriented electrical steel heated to 800°C for 10 minutes was taken. The orientation of individual grains was determined by the method described in our previous publication[15]. **Figure 2** shows SEM and SAM images of surface. A different surface tin segregation on different grains was noticed. Different grain orientation provided different sites for segregated tin atoms. By comparing PHRs Sn/Fe among different specimens one should take care of so called channelling effect especially due to the fact that Auger iron signal is very sensitive to the angle of sample surface and analyser axis[13].

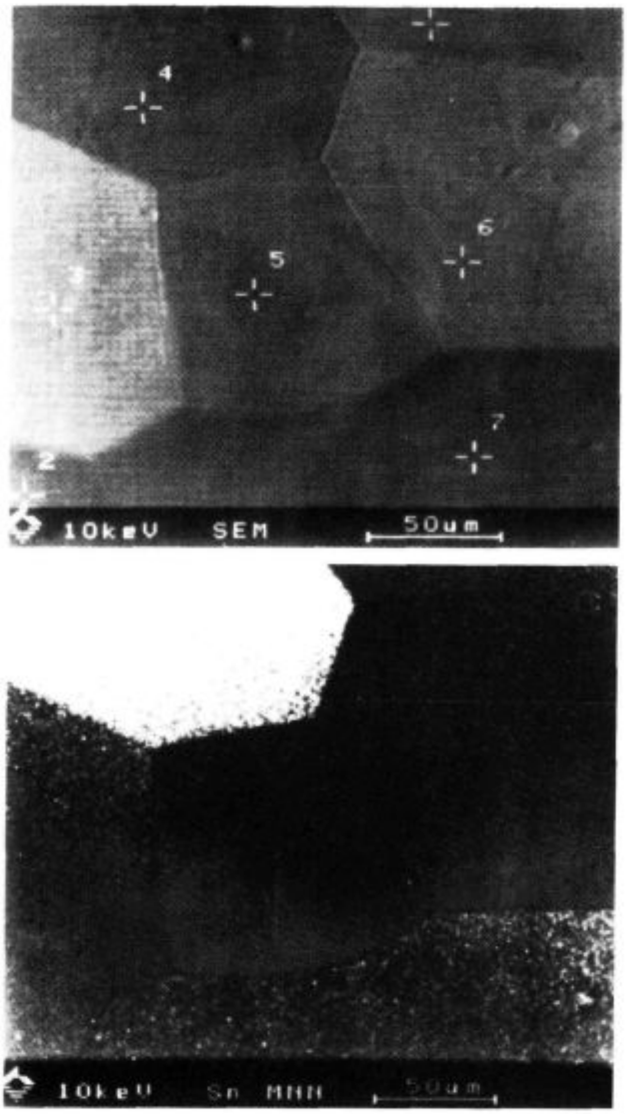

Grain	1	2	3	4	5	7
PHR Sn/Fe	0.23	0.31	0.29	0.40	0.30	0.40
Orientation	(144)	(025)	(118)	(111)	(5913)	(236)

Figure 2: **a)** SEM image of 0.2 mm thick non-oriented electrical steel alloyed with 0.1% Sn, **b)** a SAM image Sn-MNN transition recorded on a same area, **c)** table shows a relation between grain orientation and Sn PHR

Slika 2: **a)** SEM posnetek površine neorientirane elektro pločevine legirane z 0.1% Sn, **b)** SAM posnetek Sn MNN prehoda posnet na istem mestu, **c)** tabela podaja zvezo med orientacijami zrn in RVV

Figure 3 shows the temperature dependence of surface segregation of alloying and tramp elements of non-oriented electrical steel alloyed with 0.05% Sn on different grain orientations - (001) and (111) - respectively. Electrical steel is a multicomponent system and so very complicated to understand the temperature dependence behaviour of surface segregation, therefore the results obtained on binary alloys should be considered[17]. The relations of the surface segregation enthalpies and volume diffusivities are as follows: $\Delta H^0{}_{Si} < \Delta H^0{}_C < \Delta H^0{}_P$ and $D^C{}_V >> D^{Si}{}_V > D^P{}_V$[17].

At lower temperatures (~300°C), C segregated to the surface due to very high diffusion coefficient in comparison to Si and P, although the bulk concentration was at very low 15 ppm. At higher temperatures, C atoms were displaced by Si atoms[18]. The P and S atoms displaced the silicon at higher temperatures[17]. Their bulk diffusion co-

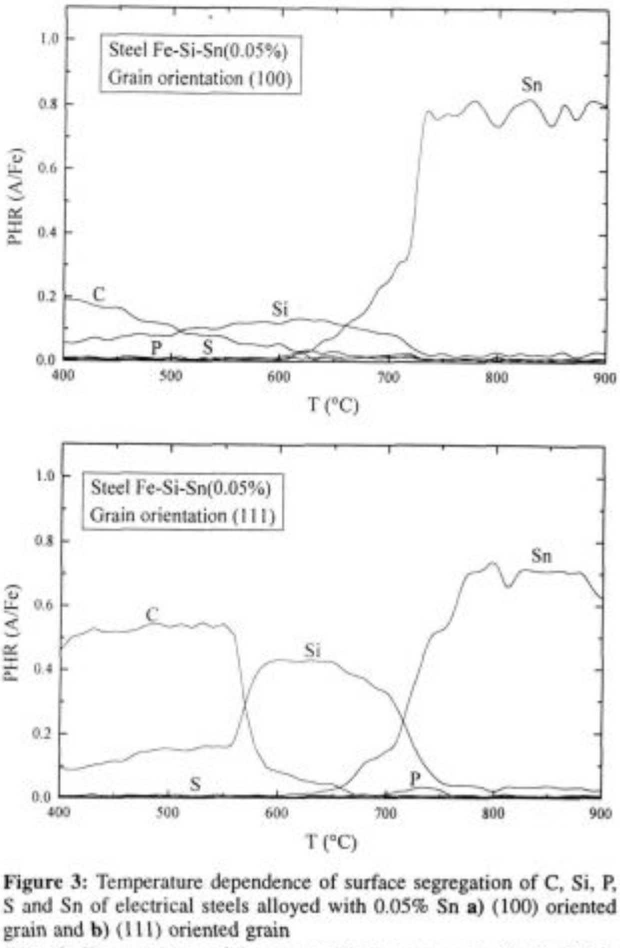

Figure 3: Temperature dependence of surface segregation of C, Si, P, S and Sn of electrical steels alloyed with 0.05% Sn **a)** (100) oriented grain and **b)** (111) oriented grain

Slika 3: Temperaturna odvisnost površinske segregacije C, Si, P, S in Sn za elektro pločevino legirano s 0.05% Sn **a)** zrno (100) orientacije in **b)** zrno (111) orientacije efficient was rather low, but their segregation enthalpy was very high, so tin started segregating significantly above 600°C. The kinetics study confirmed the orientation dependence of tin surface segregation as well as thickness of segregated layer.

It was ascertained[11] that on (100) and (111) faces, the segregation of tin was beyond one monolayer, due to the strong decrease of surface energy. On a surface with a (111) orientation FeSn intermetallic compound of one unit cell thickness was found. Our measurements showed that tin surface coverage dependence on tin bulk concentration and Θ value approached one for (100) and (111) orientation.

3.3 Texture measurements

The textures of 0.5 mm thick electrical steels were measured on the surface and in the middle plane after the half of the sheet thickness were removed. Taking into account that approximately six crystal grains constitute the 0.5 mm thick cross-section steel sheet and the fact that penetration depths of x-rays were less than 0.1 mm one might conclude that there were analysed some grains whose growth was not affected by the surface segregated tin. Nevertheless, there were not more than 10% of such grains.

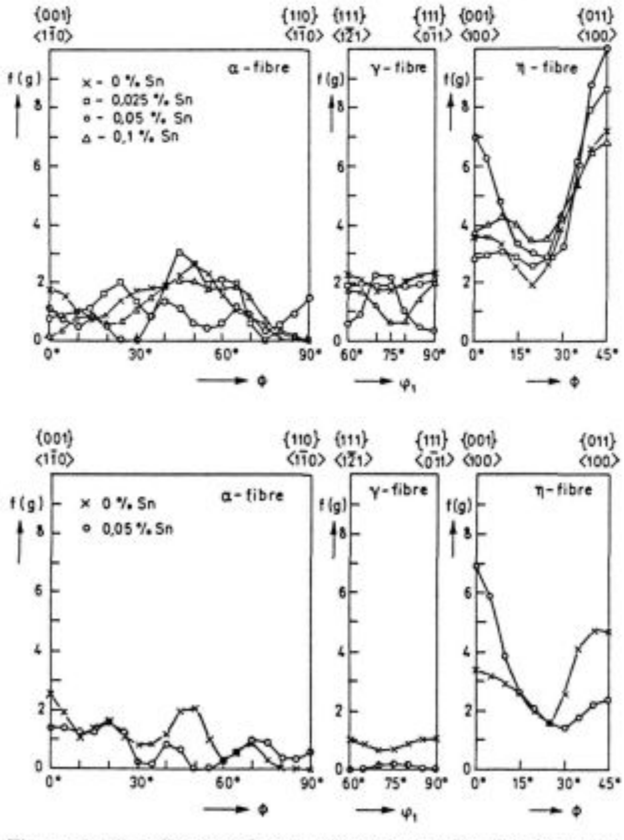

Figure 4: Fibre diagram of recrystallized texture for electrical steels measured **a)** in the middle plane and **b)** on the surface

Slika 4: Diagram vlaken rekristalizacijske teksture za elektro pločevine merjen **a)** v sredini in **b)** na površini

The orientation distribution functions (ODF) f (g) were calculated from the (200), (110) and (211) pole figures. The textures were presented as α, γ and η fibres. **Figure 4** shows texture fibres in the middle plane (a) and on the surface (b) of electrical steels alloyed with and without tin. The volume fraction of grains with the (100) planes measured on the surface and in the middle plane increased to the order of two compared the steel without tin with the steel alloyed with 0.05% tin. Less hard magnetic orientations were found on the surface. Texture development during the recrystallization was. Steel alloyed with 0.05% Sn, which had previously been aged 25 hours at 550°C, compared to the steel without tin, showed an increase of (100) planes parallel to the rolling direction to the order of three.

4 Conclusions

Grain boundary and surface segregation of tin in non-oriented electrical steels were determined. Maximum equilibrium segregation on the surface were reached at 750°C and approached for majority of orientations one monolayer. One iron atom on the surface corresponds to one segregating tin atom. It was proved that thickness of tin segregating layer depended of tin bulk concentration. Tin segregation was controlled by bulk diffusion; thus, the equilibrium enrichment of tin on the surface was slightly faster for a specimen with higher tin contents. The tendency for tin surface segregation was much higher compared to grain boundary segregation. At equilibrium grain boundary segregation only 7 and 3% of tin atoms were found on a grain boundary for steel alloyed with 0.1 and 0.05% Sn, respectively.

Different crystallographic orientations can provide different sites for segregating tin atoms. During the recrystallization tin atoms segregated on the surface and also at the grain boundary and so decreased the surface energy of crystal grains selectively.

The obtained results confirmed our supposition. Tin segregation took place during the recrystallization and decreased the surface energy of crystal grains with (100) and (110) plains parallel to the sheet surface. Textures represented as sections through three-dimensional orientation distribution space in fixed directions showed that volume fraction of magnetically soft grains increased for two times compared to steel without tin. Slightly better textures were obtained near the surface than in the middle plane of 0.5 mm thick steel sheet. The best results were obtained for steel alloyed with 0.05% Sn. We suppose that only a certain level of segregation promotes desired selective grain growth.

5 References

[1] H. Viefhaus, *Analytica Chimica Acta*, 297, 1994, 43-53

[2] H. J. Grabke, V. Leroy and H. Viefhaus, *ISIJ International*, 35, 1995, 2, 95

[3] Lyudkovsky, P. K. Rastogi and M. Bala, *Journal of Metals*, 1, 1986, 18

[4] H. Shimanaka, T. Irie, K. Matsumura, K. Nakamura, *J. Magn. Magn. Mat.*, 19, 1980, 63

[5] M. Jenko, F. Vodopivec, H. J. Grabke, H. Viefhaus, B. Praček, M. Lucas and M. Godec, *Steel Research*, 65, 1994, 11

[6] M. Jenko, F. Vodopivec, B. Praček, M. Godec, D. Steiner, *J. Mag. Mag. Mat.*, 133, 1994, 229

[7] M. Jenko, F. Vodopivec, H. J. Grabke, H. Viefhaus, M. Godec and D. Steiner Petrovič, *Journal De Physique IV*, 5, 1995, C7-225

[8] S. Nakashima, K. Takashima, J. Harase and K. Kuroki, *J. Japan Inst. Metals*, 55, 1991, 12, 1392-1399

[9] Lyudkovsky and P. Rastogi, *Metallurgical Transactions A*, 15 A, 1984, february, 257

[10] K. Iwayama, K. Kuroki, Y. Yoshitomi, K. Homma and T. Wada: *J. Appl. Phys.*, 55, 1984, 2134

[11] H. Viefhaus and M. Rüsenberg, *Surface Science*, 159, 1985, 1-23

[12] R. Mast, H. J. Grabke, M. Jenko and M. Lukas, in print

[13] V. Rüsenberg, H. Viefhaus; *Surf. Sci.*, 172, 1986, 615

[14] Beguinot and P. Lesbats, *Metalography*, 10, 1977, 115-119

[15] M. Godec, M. Jenko, F. Vodopivec, M. Ambrožič, Đ. Mandrino, L. Kosec, M. Lovrečič Saražin, *Kovine, zlitine, tehnologije*, 28, 1994, 1-2, 105-109

[16] W. Jager, H. J. Grabke, R. Möller, *4th International Conference*, Portorož Jugoslavija, 1985

[17] H. J. Grabke, V. Leroy and H. Viefhaus, *ISIJ International*, 35, 1995, 2, 95-113

[18] H. De. Rugy and H. Viefhaus, *Surface Science*, 173, 1986, 418-438

Kovine, zlitine, tehnologije/30/1996/6/545-549

Corrosion Resistance of NdDyFeB Basic Alloys

Korozijska obstojnost osnovnih zlitin NdDyFeB

S. Kobe Beseničar[1], IJS Ljubljana, Slovenija
L. Vehovar, IMT Ljubljana, Slovenija
B. Saje, Magneti d.d. Ljubljana, Slovenija

Prejem rokopisa - received: 1996-10-01; sprejem za objavo - accepted for publication: 1996-11-04

Nd-Dy-Fe-B-X (X = Zr, Hf) alloys were exposed to severe corrosion conditions and the corrosion rates were followed by various techniques (electrochemistry, Tafel extrapolation method). The weight loss was measured over a period of 10 weeks in a wet corrosion chamber. Corrosion products were analysed using X-ray diffraction and the microstructures were investigated by optical microscopy and on SEM - EDS. In aggresive media, such as diluted NaCl or H_2SO_4, the differences between the corrosion rates were small. The lowest potential difference between the anodic phase (corrosion products) and the matrix, acting as cathode, was observed in Nd-Dy-Fe-B-Zr alloys. Corrosion rates in fresh water were 0,30 mm/year for Nd-Dy-Fe-B alloy and 0,02 mm/year for Nd-Dy-Fe-B-Zr alloy. The same trend was shown on samples exposed to conditions of simulated condensed atmospheric humidity. The highest cumulative weight loss occurred with pure Nd-Dy-Fe-B alloys and the lowest with the alloy improved by ZrO_2 addition. The corrosion rates for three different alloys were 0,089 mm/year for Nd-Dy-Fe-B alloy, 0,072 mm/year for Nd-Dy-Fe-B-Hf alloy and 0,063 mm/year for Nd-Dy-Fe-B-Zr alloy.

Key words: corrosion, Nd-Fe-B alloys, permanent magnets

Osnovne zlitine Nd-Dy-Fe-B-X (X = Zr, Hf) smo izpostavili agresivnim korozijskim pogojem in zasledovali korozijski proces z različnimi metodami (elektrokemija, Taflova ekstrapolacijska metoda). V vlažni komori smo merili izgubo teže v obdobju desetih tednov. Korozijske produkte smo analizirali z uporabo X -žarkovne difrakcije ter opazovanjem mikrostrukture z optično mikroskopijo in elektronskim mikroskopom opremljenim z EDS. V agresivnih medijih kot sta NaCl in H_2SO_4 so bile razlike v korozijski hitrosti med različnimi zlitinami majhne. Najmanjšo razliko potenciala med anodno fazo (korozijski produkt) in matrico, ki deluje kot katoda, smo opazili pri zlitini Nd-Dy-Fe-B-Zr. Korozijska hitrost v vodi je bila 0,30 mm/leto pri zlitinah Nd-Dy-Fe-B in 0,02 mm/leto pri zlitinah Nd-Dy-Fe-B-Zr. Enako tendenco smo opazili pri eksperimentih, pri katerih so bile zlitine izpostavljene pogojem, ki so simulirali nasičeno zračno vlago. Najvišja kumulativna izguba teže je bila dosežena s čistimi Nd-Dy-Fe-B zlitinami in najnižja z Nd-Dy-Fe-B-Zr zlitinami. Korozijske hitrosti za različne zlitine so bile 0,089 mm/leto za zlitino brez dodatkov, 0,072 mm/leto za zlitino z dodatkom HfO_2 in 0,063 mm/leto za zlitino z dodatkom cirkon oksida.

Ključne besede: korozija, Nd-Fe-B zlitine, trajni magneti

1 Introduction

Among the rare earth based permanent magnets, Nd-Fe-B magnets have assumed an important position due to their outstanding magnetic properties[1,2] and their use is still on growing in different fields of application[3]. However, corrosion has been a problem with Nd-Fe-B magnets, because phases rich in rare earth elements are easily oxidised in air, especially in humid air[4,5]. Since corrosion can deteriorate seriously the magnetic properties and on the other hand, can also be detrimental to magnetic circuits, much effort has been made to improve the corrosion resistance of Nd-Fe-B magnets. Even coating and plating are not the perfect solution to this problem, because they can be imperfect and allow the penetration of reacting species such as moisture to the magnet surface[6]. Searching for a better resistance of the material itself, various referred possibilities have been studied.

Narasimhan et al.[7] reported that raising the oxygen content to between 0,6 to 3,5% significantly improved the corrosion resistance; Kim and Jacobson reported that the addition of Al, Dy or Dy_2O_3 improved the corrosion resistance in humid air[4], while Tenaud, Vial, Sagawa[8] and Hirosawa et al.[9] used V and Mo to improve the basic corrosion resistance of Nd-Fe-B magnets. Kobe et al. reported on the beneficial influence of ZrO_2 addition not only to the increased coercivity, but also to the corrosion resistance of the Nd-Dy-Fe-B magnets[10]. Previously Nakamura[11] attained better corrosion resistance of the Nd-rich phase by the substitution of Fe with Co and Zr, and Sagawa et al.[12] improved the corrosion resistance by addition of Co and Al. Kim et al.[6] influenced the corrosion resistance by varying the amount of O, C and N in the basic composition of Nd-Fe-B magnets.

On the basis of the promising results in our previous work[10], we continued our studies on the influence of ZrO_2 and HfO_2 additions on improving the corrosion resistance of the basic Nd-Dy-Fe-B alloy with the composition $Nd_{15}Dy_1Fe_{76}B_8$. The corrosion resistance was followed over experimental periods during which the samples were exposed to various severe corrosion conditions.

2 Experimental

The basic alloys used fot the corrosion experiments were prepared by arc melting the alloys NdFe, DyFe, FeB and Fe powder in a pure Ar atmosphere. In order to prevent the oxidation Ti sponge was used as a getter for oxygen. Three different batches were prepared: **A** - samples without other additives, **B** - 1 wt.% hafnia was

---

[1] Dr. Spomenka KOBE BESENIČAR
Inštitut Jožef Stefan, Jamova 39
1001 Ljubljana, Slovenija

added before arc melting, **C** - 1 wt.% of zirconia was added prior to arc melting. Samples were remelted three times in order to attain a better homogeneity. Buttons of melted alloys were sliced and polished to discs, dimensionally appropriate for the corrosion tests.

The investigations were focused on general corrosion resistance, based on electrochemical determinations of the possible passivity of electrode surfaces, or active corrosion. Moreover, service conditions were simulated by exposing the test specimens in a wet corrosion facility (DIN 5017), with the aim of establishing the effect of chemical composition and microstructure on the corrosion rate and the form of corrosion.

The potentiodynamic anodic polarisation measurements were performed using an EG and G-PAR potentiostat and "Softcorr 352" software. Experiments were carried out in fresh water and in various aqueous test-solutions containing low concentrations of aggressive ions such as Cl^- and SO_4^{2-}. Such media could only represent approximative atmospheric conditions in the industrial environment. Electrochemical determination of corrosion rates were performed by the Tafel plot technique.

After exposing the samples to various corrosion conditions they were characterised by optical and electron microscopy (SEM/EPMA JEOL, JXA 840 A). Phases in corrosion products were identified using EDS and WDS analysis facilities and an X-ray diffractometry (Philips 1710).

3 Results and discussion

3.1 Effect of the HfO_2 and ZrO_2 additives on the corrosion rate of Nd-Dy-Fe-B alloys

The example of the anodic polarisations curves presented in **Figure 1** indicates that all of the three materials cannot achieve passivity. The overall shape of the curves indicates that the materials undergo active corrosion. It is evident that the potentiodynamic scans did not reveal any significant feature, such as a passive region where passivation is spontaneous, the pitting potentional or the critical anodic current. The conclusion from the anodic potentiodynamic scans of the materials carried out in different solutions was that no significant passivation occurred.

Table 1: Corrosion rates of alloys in different media at 20°C

Material	Media	Corrosion rate (mm/year)
NFB	fresh water	0,300
NFB-HfO_2	fresh water	0,530
NFB-ZrO_2	fresh water	0,022
NFB	0,09 M NaCl	2,120
NFB-HfO_2	0,09 M NaCl	2,710
NFB-ZrO_2	0,09 M NaCl	2,650
NFB	0,17 M NaCl	2,650
NFB-HfO_2	0,17 M NaCl	3,260
NFB-ZrO_2	0,17 M NaCl	3,150
NFB	0,5 M H_2SO_4	303,0
NFB-HfO_2	0,5 M H_2SO_4	274,0
NFB-ZrO_2	0,5 M H_2SO_4	237,8

Due to such polarisation behaviour of the materials, corrosion rate measurements were performed by the Tafel plot technique. The corrosion rates of the materials tested when exposed in various media are presented in **Table 1** and graphically in **Figure 2**.

From these results it can be concluded that chloride ions drastically promote corrosion. As their concentration increases, so does the rate of corrosion. The corrosion process is also particularly dramatic in acid solutions containing SO_4^{2-} ions, which represent very aggressive industrial atmosphere. The corrosion rates of all materials in fresh water are relatively favourable. In addition, the results of this investigation showed that a defined trend which favours a NDFB-ZrO_2 material exists (**Figure 3, Table 1**).

The same trend among the materials was observed by exposure in a wet corrosion facility, but a substantial improvement of the corrosion properties by addition of ZrO_2 was not achieved. Results are presented in **Table 2**.

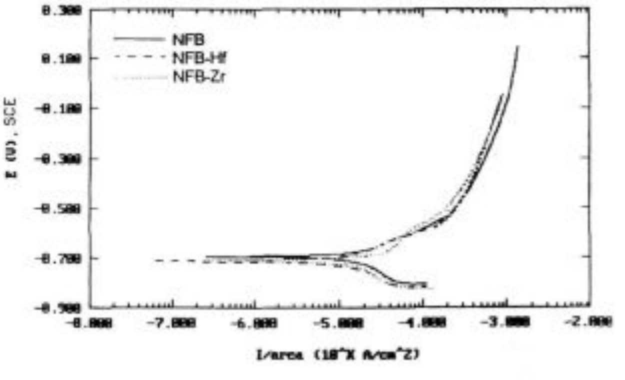

Figure 1: Potentiodynamic polarisation curves for three types of alloys tested in fresh water, 20°C

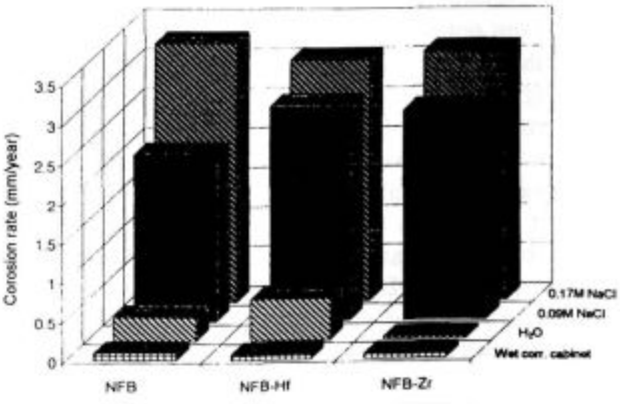

Figure 2: Corrosion rates of the materials exposed in various media presented graphically

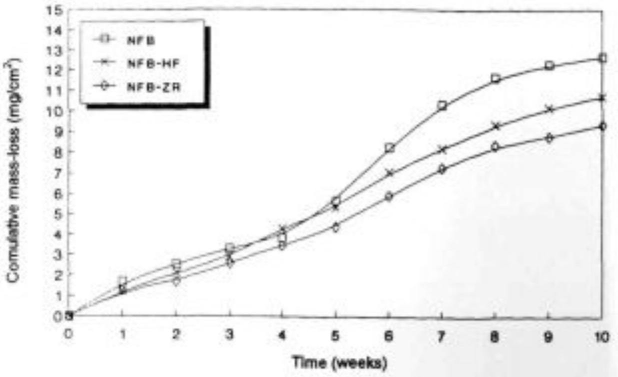

Figure 3: Cumulative mass-loss of different alloys during 10 weeks of exposure in a wet corrosion chamber

Table 2: Corrosion rates of alloys exposed in a wet corrosion cabinet

Material	Environment	Corrosion rate (mm/year)
NFB	Wet corrosion chamber	0,089
NFB-HfO_2	Wet corrosion chamber	0,072
NFB-ZrO_2	Wet corrosion chamber	0,063

3.2 Microstructural study

Cross section of the samples A, B, C were ground and polished with diamond paste. The polished surfaces were examined by optical microscopy and electron microscopy (SEI and BSEI). The phases present were analysed using EDS standardless quantitative analyses.

Figure 4: Microstructures (cross sections) of sample without any addition (A) and sample with 1 wt.% of HfO_2 (B) (385 x)

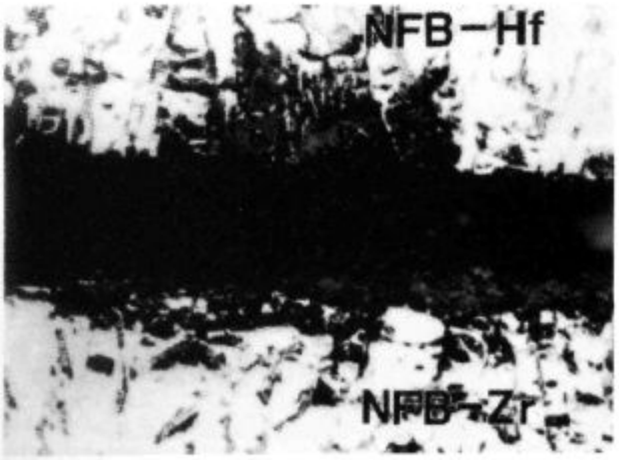

Figure 5: Microstructures (cross sections) of sample with HfO_2 (B) and sample with ZrO_2 (C) (385 x)

Figure 4 shows a comparision of the microstructures (cross sections) of sample without any addition (A) and sample with 1 wt.% of HfO_2 addition (B). **Figure 5** shows the cross sections of the polished surfaces of samples with HfO_2 (B) and ZrO_2 (C) addition. There is an obvious difference in the level of corrosion attack between the three samples. The most aggressive corrosion proceeds in samples A. In samples B and C the corrosion products are located mainly on the surface, especially in samples C, where no deep corrosion in the bulk material was observed. The reason for such local corrosion is supposed to be the presence of particular phases.

More detailed analyses of the phases present were obtained by electron microscopy. **Figure 6** shows the combined BS/SE image of an SEM micrograph of sample A and spectra of phases P_1 and P_2. The phases present in the corrosion products of sample A were found to be combined Nd, Dy and Fe oxides. The ratio between Nd and Fe oxides differs in the phases P_1 and P_2. The results of standardless quantitative analyses (ZAF correction program) are presented in **Table 3**.

Table 3: The results of standardless quantitative analyses of the oxide phases

	Nd_2O_3 (wt.%)	Dy_2O_3 (wt.%)	FeO (wt.%)
Phase P_1	43,35	30,18	24,47
Phase P_2	07,69	-	92,31
Phase P_{11}	37,55	24,73	37,72
Phase P_{12}	11,99	-	88,01

In samples B a Hf-Fe rich phase was detected. The combined BS/SE image of the SEM micrograph of sample B and the corresponding spectrum of phase P_6 are shown in **Figure 7**. Other phases present are the matrix phase P_5 ($RE_2Fe_{14}B$) and RE -rich phase P_7.

In samples C a Zr-Fe -rich phase was found, mostly on the phase boundaries between the hard magnetic $RE_2Fe_{14}B$ phase (P_5) and the RE -rich phase (P_7). A combined BS/SE image of the SEM micrograph of sample C and the corresponding spectrum of Zr-Fe -rich phase P_9 are shown in **Figure 8**. The SEM micrograph of the same sample showing different phases in the corroded area and the corresponding spectra of these phases are presented in **Figure 9**. In samples C, the barrier based on the Zr-Fe -rich phase, which exists between the

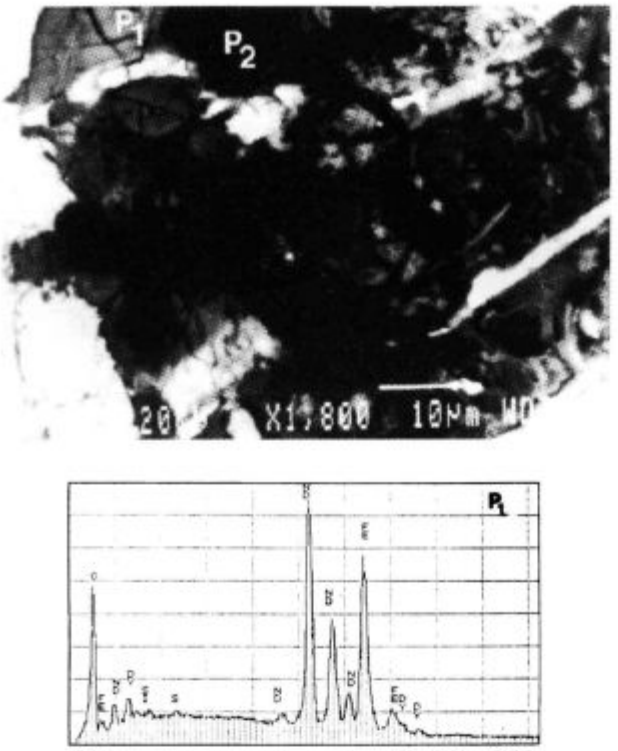

Figure 6: Combined BS/SE image of SEM micrograph of sample A and spectra of phases P_1 and P_2

corrosion products (in the RE -rich phase) and the hard magnetic matrix phase, prevents the propagation of corrosion. Phase P_{10} shown on SEM micrograph **(Figure 9)** illustrates this tentative explanation. The results of standardless analyses of the Zr-Fe -rich phases found are presented in **Table 4**.

Table 4: The results of standardless quantitative analyses of Zr-Fe -rich phases

	Zr	Fe	Nd
Phase P_9	44,22	54,02	05,76
Phase P_{10}	37,28	54,35	08,38

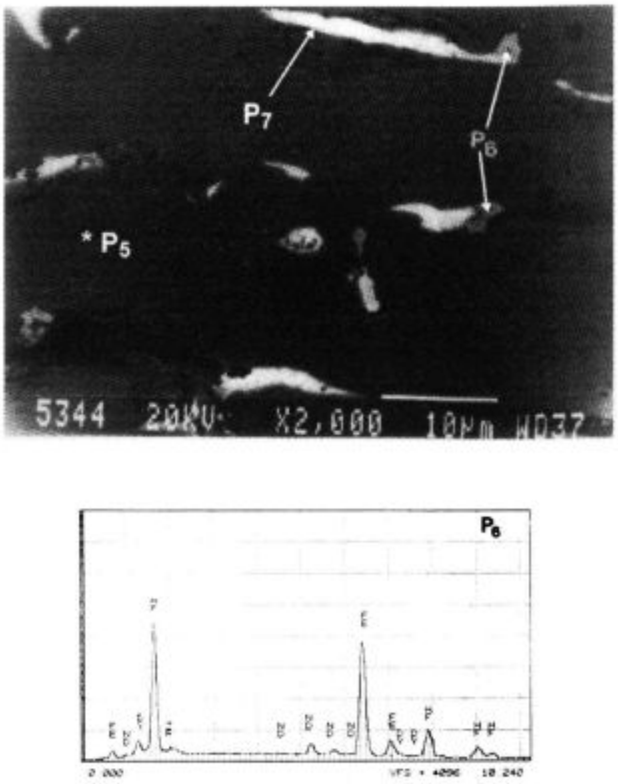

Figure 7: Combined BS/SE image of SEM micrograph of sample B and corresponding spectra of Hf-Fe -rich phase P_6

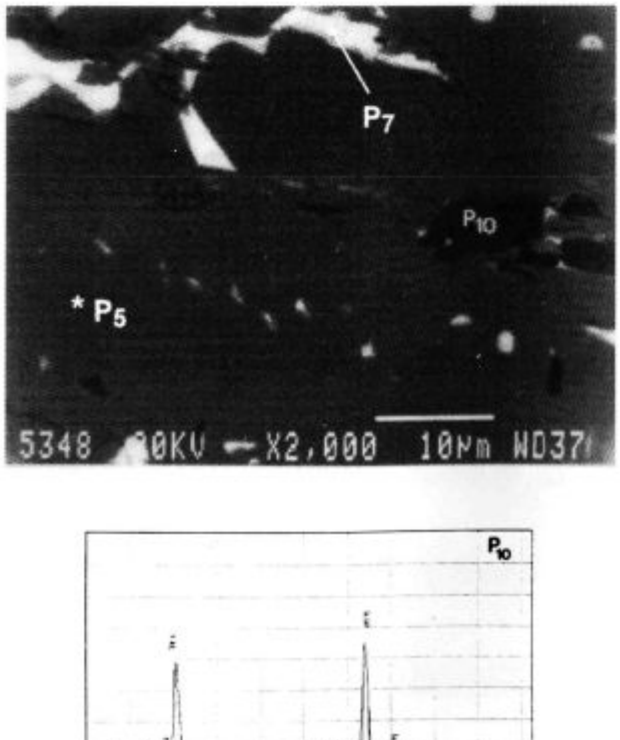

Figure 8: Back scattered image of SEM micrograph of sample C and the corresponding spectrum of Zr-Fe -rich phase P_{10}

4 Conclusion

The results of the corrosion experiments and analyses of RE-Fe-B-X alloys, as well as analyses ot the corrosion products and microstructural observation and analyses show, that zirconia addition gives the most promising re-

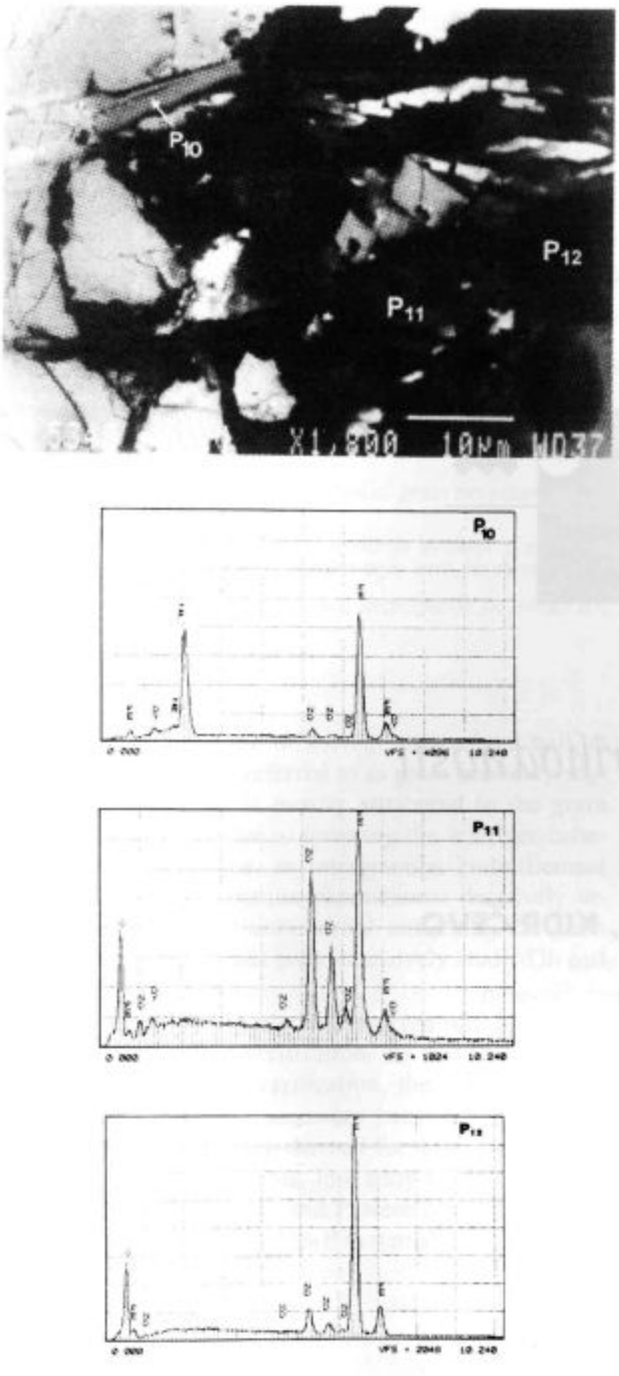

Figure 9: SEM micrograph of sample C showing various phases in the corroded area and the corresponding spectra of phases P_{10}, P_{11} and P_{12}

sults in corrosion protection of the basic material. Corrosion rates in fresh water were 0,30 mm/year for Nd-Dy-Fe-B alloy and 0,02 mm/year for Nd-Dy-Fe-B-Zr alloy. The same trend was shown when the samples were exposed to conditions where condensed atmospheric humidity was simulated. The highest cumulative weight loss occured with pure Nd-Dy-Fe-B alloys and the lowest with the alloy improved by ZrO_2 addition.

A tentative explanation for the difference is that the change in microstructure is obviously responsible for improving the corrosion resistance of Nd-Dy-Fe-B-Zr alloy. The reason for local corrosion is the presence of particular phases, (Fe-Hf, Fe-Zr) acting as an anode, with considerable potential difference between these and the matrix. A tentative explanation for the formation of Fe-Hf and Fe-Zr -rich phases is that in the samples with HfO_2 and ZrO_2 addition, during the arc melting process most probably Nd from Nd -rich phase reduces both oxides and Hf or Zr -rich phases are formed. They act as the barrier between the corrosion products (in the RE -rich phase) and the hard magnetic matrix phase and to some extent prevent the propagation of corrosion.

The improvement of the corrosion resistance of basic material itself can contribute significantly to the stability of coated magnetic material.

5 References

[1] M. Sagawa, S. Fujimura, N. Togawa, H. Yamamoto, Y. Matsuura, *J. of Appl. Phys.*, 55, 1984, 2083

[2] J. Croat, J. Herbst, J. Lee, F. Pinkerton, *J. of Appl. Phys.*, 55, 1984, 2078

[3] M. Hersch, Permanent Magnet Demand Fuels Continued Market Growth, PCIM, July 1994, p 26

[4] A. Kim, J. Jacobson, *IEEE Trans. on Mag.*, 23, 1987, 5,2509

[5] A. Kim, *Journ. of Material Eng.*, 11, 1989, 1, 95

[6] A. S. Kim, F. E. Camp, S. Constantinides, Corrosion of Electronic and Magnetic Materials, ASTM STP 1148, Ed. P. J. Peterson, Am. Soc. for Testing and Materials, Philadelphia, 1992, p 68

[7] K. Narasimhan, C. Willman, E. Dulis, *US Patent*, No. 4588439, 1986

[8] P. Tenaud, F. Vial, M. Sagawa, *IEEE Trans. on Magn.*, 26, 1990, 5, 1730

[9] S. Hirosawa, S. Tomizawa, S. Mino and A. Hamamura, *IEEE Trans. on Mag.*, 26, 1990, 5, 1960

[10] S. Kobe Beseničar, J. Holc, G. Dražič, B. Saje, *IEEE Trans. on Mag.*, 30, 1994, 2, 693

[11] H. Nakamura, A. Fukuro, T. Yoneyama, *Proc. of the 10th Inter. Workshop on Rare Earth Magnets and Their Application*, Kyoto, Japan, 1989, p 315

[12] M. Sagawa, S. Fujimura, H. Yamamoto, S. Hirosawa, *Japanese Patent*, No. 6338555, 1988

Kovine, zlitine, tehnologije/30/1996/6/551-555

Some Aspects of Impurity Grain Boundary Segregation in Low Alloy Cr-Mo-V Steels

Segregacije nečistoč v nizko legiranih Cr-Mo-V jeklih

J. Janovec[1], Institute of Materials Research, Košice, Slovakia
V. Magula, Welding Research Institute, Bratislava, Slovakia
P. Ševc, Institute of Materials Research, Košice, Slovakia

Prejem rokopisa - received: 1996-10-04; sprejem za objavo - accepted for publication: 1996-11-01

The present work is focused on theories of grain boundary segregation. An overview of different approaches to solution of surface enrichment phenomenon is given in the first part. The second part is devoted to the verification of introduced theories by means of experimental results.

Key words: low alloy steels, phosphorus, grain boundary segregation, non-equilibrium segregation, kinetics

V članku so predstavljene teorije različnih avtorjev o segregaciji po mejah zrn. V prvem delu je podan pregled različnih razlag obogatitve prostih površin. V drugem delu smo obravnavane teorije verificirali z eksperimentalnimi rezultati.

Ključne besede: nizko legirana jekla, segregacija po mejah zrn, neravnotežne segregacije, kinetika segregacije po mejah zrn

1 Introduction

Enrichment of solute or solvent atoms from bulk at the grain boundaries is referred to as grain boundary segregation. Segregation is mostly attributed to the grain boundary weakening due to lowering the interface cohesion. As a consequence, an intergranular embrittlement occurs. Because segregation phenomenon decisively influences properties of commertial materials, the grain boundary segregation has been intensively studied in last decades[1-8].

The present work deals with segregation theories[9-15] and their experimental verification. By use of multicomponential alloys in the verification, the introduction of some simplifications is necessary because the segregation theories were mostly derived for binary or ternary solid solutions. For example, low alloy steels containing Fe, Cr, Mo, V, Mn, Si, C and P were considered to be binary Fe-P or ternary Fe-Mo-P systems[13-15].

2 Segregation theories

2.1 Non-interactive equilibrium segregation

The theory of equilibrium segregation for dilute binary solid solution Fe-I (Fe - solvent, I - solute impurity) was derived by McLean to be the grain boundary analogous of Langmuir adsorption at free surfaces[1,16]. The Langmuir-McLean isotherm yields:

$$\frac{C_I^{Eeq}}{1-C_I^{Eeq}} = \frac{C_I^B}{1-C_I^B} \exp\left(-\frac{\Delta g_I}{kT}\right), \qquad (1)$$

where C_I^{Eeq} is the equilibrium grain boundary concentration of impurity, C_I^B is the bulk concentration of impurity, Δg_I is the free energy of impurity segregation, and k is the Boltzmann constant.

The equilibrium segregation kinetics can be calculated as[1]:

$$\frac{C_I^E(t) - C_I^{E0}}{C_I^{Eeq} - C_I^{E0}} = 1 - \exp\left[\frac{4D_I t}{(\alpha_I^E)^2 (d^E)^2}\right] \operatorname{erfc}\left(2\frac{\sqrt{D_I t}}{\alpha_I^E d^E}\right), \qquad (2)$$

where $C_I^E(t)$ is the grain boundary concentration of impurity for the time t, $C_I^{E0} = C_I^E(t=0)$ is the initial concentration of impurity, d^E is the grain boundary thickness, D_I is the diffusion coefficient of impurity, and $\alpha_I^E = C_I^{Eeq}/C_I^{E0}$ is the enrichment factor.

2.2 Interactive equilibrium segregation (co-segregation)

Guttmann[4,17] modified the Langmuir-McLean isotherm to be suitable for the calculation of interactive equilibrium segregation in ternary Fe-M-I systems. He assumed for this system an attractive interaction between the impurity I and the solute metalic element M. If the M-I competition for convenient sites at the grain boundary exists, impurity grain boundary concentration can be calculated according to:

$$\frac{C_i^{Eeq}}{1 - C_I^{Eeq} - C_M^{Eeq}} = \frac{C_i^B}{1 - C_I^B - C_M^B} \exp\left(-\frac{\Delta g_i}{kT}\right), \ i=I, M \qquad (3)$$

The interaction leading to the M-I co-segregation was defined in terms of segregation free energy, Δg_i, i = I, M:

$$\Delta g_I = \Delta g_I^0 - 2\alpha_{FeI} C_I^{Eeq} + \alpha'_{MI} (C_M^{Eeq} - C_M^B), \qquad (4)$$

$$\Delta g_M = \Delta g_M^0 - 2\alpha_{FeI} (C_M^{Eeq} - C_M^B) + \alpha'_{MI} C_I^{Eeq}, \qquad (5)$$

where Δg_I^0 and Δg_M^0 are the free energies of segregation for I and M in their respective binary systems with

---

[1] Dr.Sc. Jozef JANOVEC
Institute of Materials Research, Slovak Academy of Sciences
Watsonova 47, 04353 Košice, Slovakia

Fe, while α'_{MI} and α_{FeI} are the relative chemical interaction energies between M-I and Fe-I, respectively. For non-competitive segregation the following expression was obtained[17,18]

$$\frac{C_i^{Eeq}}{1-C_i^{Eeq}} = \frac{C_i^B}{1-C_i^B} \exp\left(-\frac{\Delta g_i}{kT}\right), \quad i=I, M \tag{6}$$

where Δg_i has the same meaning as in the previous case.

Kinetics of interactive segregation can be described by means of the regular solution model proposed by Seah[18]. In the model it is assumed a local equilibrium between concentrations of impurity at the grain boundary, $C_I^E(t)$, and in adjacent bulk layers, $C_I^B(t)$. Then

$$\frac{C_I^E(t)}{1-C_I^E(t)} = C_I^B(t) \exp\left(-\frac{\Delta g_I}{kT}\right) \tag{7}$$

The combination of equations (4) and (7) is frequently used in kinetic calculations, as firstly by Tyson[19].

In recently proposed theories, the grain boundary segregation is assumed to be a bulk-diffusion-controlled process. There are also kinetic models favouring other controlling mechanisms, for instance the fast diffusion path[20,21] or the grain boundary diffusion[22,23]. Du Plessis and Van Wyk[24], for instance, proposed a model considering the chemical potential gradient as a driving force of the grain boundary segregation.

2.3 Non-equilibrium segregation

Non-equilibrium segregation theory was established by Aust et al.[25] and Anthony[26]. They supposed that vacancies and impurities form vacancy-impurity complexes with a binding energy higher than the thermal energy. The controlling mechanism of non-equilibrium segregation is the vacancy concentration gradient. The higher temperature the higher is the equilibrium concentration of vacancies. The temperature decrease during rapid cooling leads to a loss of vacancies along grain boundaries due to their annihilation. This process is in accordance with the tendency to achieve a lower equilibrium concentration of vacancies at lower temperature. The vacancy concentration decrease near the grain boundaries results in the dissociation of vacancy-impurity complexes in this region. In the interior of grains, where less vacancy sinks are present, the concentrations of vacancies and vacancy-impurity complexes decrease lesser. Consequently, the diffusion of the complexes from interior to the grain boundaries occurs due to the concentration gradient between these two areas. The process leads to an excessive impurity concentration near the grain boundaries and causes the non-equilibrium segregation.

The model of non-equilibrium segregation was proposed by Faulkner[6] and extended by Xu Tingdong[27]. When a sample is held at the solution-treatment temperature T_0 and then quickly cooled to the lower temperature T, the maximum of the impurity grain boundary concentration C_I^{Nmax} induced during holding at the temperature T is calculated as[6,27]:

$$C_I^{Nmax} = C_I^B \left(\frac{E_b}{E_f}\right) \exp\left(\frac{E_b - E_f}{kT_0} - \frac{E_b - E_f}{kT}\right), \tag{8}$$

where E_b is the vacancy-impurity atom binding energy and E_f is the energy of vacancy formation. The kinetic equation of non-equilibrium segregation has a form[27]:

$$\frac{C_I^N(t) - C_I^{N0}}{C_I^{Nmax} - C_I^{N0}} = 1 - \exp\left[\frac{4D_c t}{(\alpha_I^N)^2 (d^N)^2}\right] \operatorname{erfc}\left(2\frac{\sqrt{D_c t}}{\alpha_I^N d^N}\right), \tag{9}$$

where $C_I^N(t)$ is the grain boundary concentration of impurity for time t, $C_I^{N0} = C_I^N(t=0)$ is the initial concentration of impurity, D_c is the diffusion coefficient of complexes, d^N is the thickness of grain boundary, and $\alpha_I^N = C_I^{Nmax}/C_I^{N0}$ is the enrichment factor. The equation (9) is used for times of impurity diffusion shorter than the critical time. The critical time t_c is given by[27]

$$t_c = \frac{\gamma^2 \ln(D_c/D_I)}{4\delta (D_C - D_I)} \tag{10}$$

where γ is the average austenite grain size and α is the critical time constant[28]. For times of impurity diffusion longer than the critical time the process of desegregation occurs.

The concentration level of impurity at grain boundaries during the desegregation can be calculated according to[29,30]:

$$C_I^N(t) = C_I^B + \frac{1}{2}[C_I^N(t_C) - C_I^B] \cdot$$
$$\cdot \left[\operatorname{erf}\left(\frac{d^N/2}{[4D_I(t-t_c)]^{1/2}}\right) - \operatorname{erf}\left(\frac{-d^N/2}{[4D_I(t-t_c)]^{1/2}}\right)\right]; \quad t>t_c \tag{11}$$

The process in which the desegregation is dominant can only occur when $C_I^N(t_c) > C_I^{Eeq}$ for a given temperature. It means the desegregation is limited by reaching the equilibrium grain boundary concentration. The migration of grain boundaries during austenitizing and recrystallization can also contribute to the non-equilibrium segregation in term of a sweep effect. The nature of this phenomenon resides in embedding and subsequent dragging of solute species by moving grain boundary. As a consequence the grain boundary enrichment of solute species occurs[31,32].

2.4 Segregation under stress

Stress and thermal energy does not affect the equilibrium grain boundary concentration of impurities during the tempering (aging) significantly, but it influences segregation kinetics. Grain boundary segregation of impurities with higher diffusivity can be enhanced effectively by applied stress. Atoms of some impurities (e.g. carbon, nitrogen, boron) fastly occupy the convenient sites on grain boundaries and they prevent subsequently due to competition effect the segregation of other elements[33-35].

Shinoda and Nakamura[36] studied the grain boundary segregation of phosphorus in low carbon steel during long-term tempering and subsequent aging under stress at the same temperature. In the first step of aging under tension (compression) phosphorus grain boundary concentration increases (decreases), then its value approximate to the initial one[36]. Changes in impurity concentration at the grain boundaries oriented normal to the applied stress ΔC_I^S can be calculated as follows[37]:

$$\Delta C_I^S = \frac{4\phi C_I^{S0} D_I \rho \sigma \Delta t}{\gamma^2 RT}, \qquad (12)$$

where ϕ is a numerical factor of the order of unity, C_I^{S0} is the initial grain boundary concentration of impurity, ρ is the specific volume of alloy, σ is the stress related to the grain boundary, and Δt is the aging time under stress.

3 Verification of segregation theories

To verify the above described theories the phosphorus grain boundary segregation in five low alloy steels was investigated, **Table 1**. Schedules of heat treatment and phases identified in individual investigated steels termed 1, 2, 3, 4, and 5 are given in **Table 2**. Grain boundary concentrations of relevant elements were calculated after Davis et al.[38] from Auger spectra. Peaks of P_{120eV}, S_{152eV}, Mo_{186eV}, C_{272eV}, N_{379eV}, V_{473eV}, Cr_{529eV} and Fe_{703eV} were used in calculation. The peak of oxygen was not considered because of additional adsorption of this element on freshly fractured surface. Parameters, at which Auger spectra were achieved are given in Ref.[13,15].

Table 1: Chemical composition of investigated steels in wt.%

Steel	C	P	Mn	Si	Cr	Mo	V	Ni	S
1	0.110	0.004	0.525	0.385	2.685	0.694	0.355	-	0.010
2	0.100	0.014	0.700	0.270	2.620	0.690	0.330	-	0.007
3	0.110	0.027	0.665	0.340	2.700	0.733	0.357	-	0.010
4	0.060	0.013	0.650	0.290	2.660	0.700	0.310	-	0.009
5	0.160	0.014	0.460	0.290	2.700	0.640	0.300	0.060	0.015

Table 2: Schedules of heat treatment and phases identified in investigated steels

Steel	Heat treatment	Phases identified
1	1250°C/0.75h, water quenching, 680°C/20 h, water cooling, Ferrite+M_7C_3+MC aging at 500°C for 0.33h,1h,5h,150h	
2		
3		
4	1250°C/0.16h, water quenching, 680°C/20h, water cooling, aging 580°C for 5 min and 150h	Ferite+M_7C_3+MC
5	welding cycle: T_{max}=1300°C $\Delta t_{8/5}$=30s, 580°C/100h	Ferrite+M_3C+M_7C_3
	welding cycle: T_{max}=1300°C, $\Delta t_{8/5}$=30s, 600°C/120s under stress(strain rate 300mm.h^{-1})	Ferrite+M_3C

Phosphorus grain boundary concentrations measured for steels 1, 2, 3 aged at 500°C for different times showed the best fit with McLeans non-interactive kinetic equation (2), (**Figure 1**). The segregation can be characterized as slow, because after 150 h aging the equilibrium was not reached for any of the steels. A completely different situation was observed for steel 4 aged at 580°C

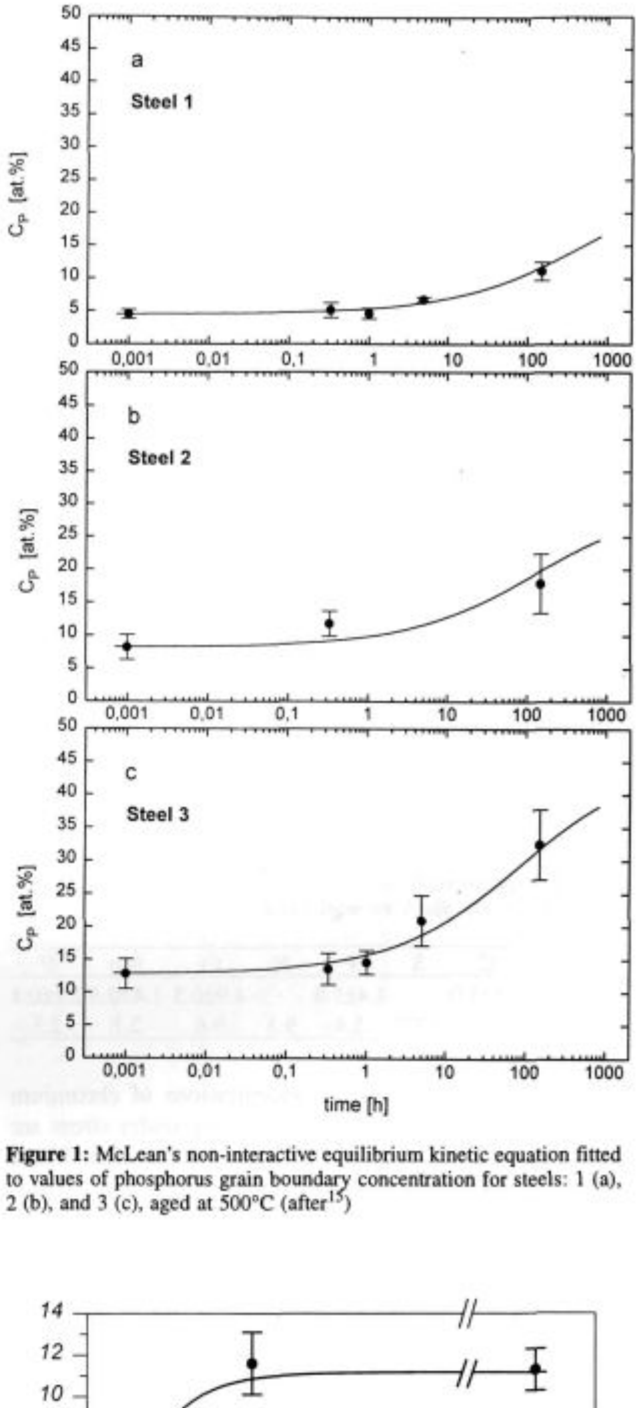

Figure 1: McLean's non-interactive equilibrium kinetic equation fitted to values of phosphorus grain boundary concentration for steels: 1 (a), 2 (b), and 3 (c), aged at 500°C (after[15])

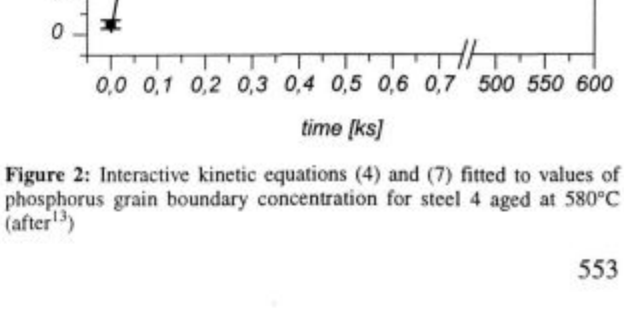

Figure 2: Interactive kinetic equations (4) and (7) fitted to values of phosphorus grain boundary concentration for steel 4 aged at 580°C (after[13])

(Figure 2). Here, the measured values of phosphorus grain boundary concentrations correlate with the curve, calculated according to equations (4) and (7). The equilibrium was reached after 5 min, and that indicates to very rapid segregation process. The obtained results showed that both rate of equilibrium segregation and also participations of interactions in this process are temperature dependent. McLean's non-interactive kinetic theory seems to be available for the description of segregation kinetics at lower aging temperatures (slower segregation rates) and interactive equations are more convenient for higher ones (accelerated segregation rates).

In **Figure 3** Auger spectra for the steel 5 after tempering (a) and short-term aging under stress (b) are shown. For loaded state the peaks of C, S, N, and Cr were evidently higher than for tempered one **(Table 3)**. Differences between carbon, sulphur and phosphorus grain boundary concentrations for the loaded state can be explained by different diffusivity of these elements in iron at 600°C[20,39,40]. Atoms of carbon and sulphur diffuse faster than phosphorus atoms and occupy earlier convenient sites at grain boundaries. Site competition between P-C and P-S[5,41] make impossible an additional phosphorus enrichment at grain boundaries. With prolonging the aging an increase in phosphorus and a decrease in carbon grain boundary concentrations occur because of carbide precipitation[5,42,43].

Table 3: Experimentally measured grain boundary concentrations of C, S, P, N, Cr, Mo, and V for steel 5 in at.%

	C	S	P	N	Cr	Mo	V
tempered	9.5±1.0	-	4.4±1.6	-	4.9±0.5	1.4±0.5	2.7±0.4
stressed	26.9	17.7	5.4	9.3	9.6	2.1	2.5

Higher grain boundary concentrations of chromium and nitrogen in the first period of aging under stress are probably caused by Cr-N interactive segregation. Misra and Balasubramanian[34,35] supposed a Cr-N co-segregation (stressing up to 5 min at 580°C) due to strong chemical interaction between these elements. After reaching the maximum coverage (depending on aging temperature), a continuous decrease in Cr and N grain boundary concentrations occurs.

The shape of carbon peaks **(Figure 3)** indicates the occurence of carbide particles on the grain boundaries[44]. Then, also peaks of alloying elements, preferentially Cr, must originate partially from these particles[45-47]. Reflexes originating from intergranular carbide particles mostly influence the achieved spectra and they can not be neglected in interpretation of grain boundary segregation in multicomponential alloys.

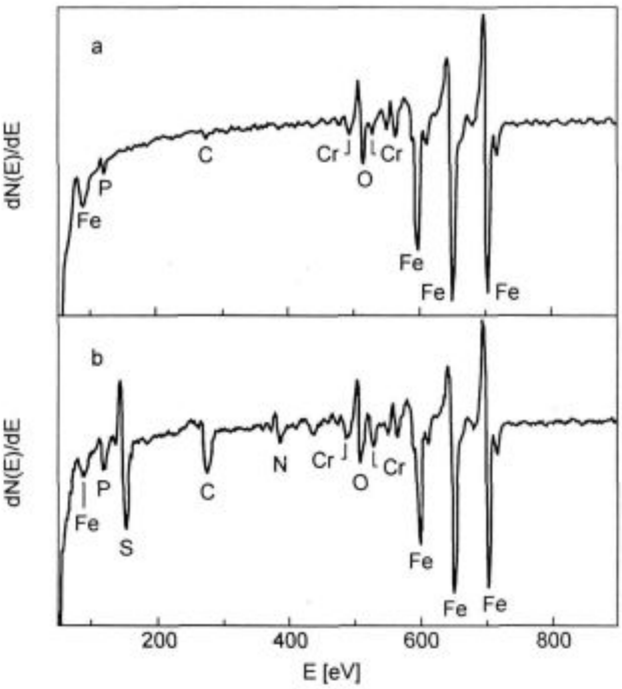

Figure 3: Characteristic Auger spectra taken on intergranular facets of steel 5: **a)** tempered at 580°C for 100 h, **b)** aged under stress for 120 s at 600°C

4 Concludig remarks

An overview of the theories of grain boundary segregation is given in the present work. The verification of the theories for multicomponential Cr-Mo-V low alloy steels leads to the following findings:

1. The McLean's non-interactive equation is the most convenient for the description of equilibrium segregation kinetics at lower temperatures (500°C), while the interactive equations are more suited for the description of equilibrium segregation kinetics at higher temperatures (580°C)

2. In comparision with unstressed aging, the higher rates of C, S, N and Cr grain boundary segregation in the first period of the aging under stress (600°C) were observed

3. In the investigated multicomponential steels, an influence of carbide particles on achieved Auger spectra can not be neglected.

Acknowledgment - This study was supported by the Grant Agency of Slovak Republic under grant No. 2/2001/96.

5 References

[1] D. McLean, *Grain Boundaries in Metals*, Chap. V., Oxford Univ. Press, London 1957
[2] M. P. Seah, *Proc. Roy. Soc. Lond. A*, 349, 1976, 535
[3] C. J. McMahon, Jr., *Mater. Sci. Engng.*, 25, 1976, 233
[4] M. Guttmann, *Surf. Sci.*, 53, 1975, 213
[5] H. Erhart and H. J. Grabke, *Metal Sci.*, 15, 1981, 401
[6] R. G. Faulkner, *J. Mater. Sci.*, 16, 1981, 373
[7] C. Uebing, *Surface Segregation of Nonmetallic Solutes on Metals and Alloys*, HRC Review, Wiley, New York 1996

[8] P. Lejček and S. Hofmann, *Solid State Mater. Sci.*, 20, 1995, 1

[9] J. Yu and C. J. McMahon, Jr., *Metall. Trans.*, 11A, 1980, 277

[10] C. L. Briant and H. J. Grabke, *Mater. Sci. Forum*, 48, 1989, 253

[11] M. Jenko, F. Vodopivec, H. J. Grabke, H. Viefhaus, B. Praček, M. Lucas and M. Godec, *Steel. Res.*, 65, 1994, 500

[12] B. Ule and V. Leskovšek, *Kovine zlitine tehnologije*, 29, 1995, 417

[13] P. Ševc, J. Janovec and V. Katana, *Scripta Metall. Mater.*, 31, 1994, 1673

[14] P. Ševc, J. Janovec, M. Koutník and A. Výrostková, *Acta Metall Mater.*, 43, 1995, 251

[15] P. Ševc, J. Janovec, M. Lucas and H. J. Grabke, *Steel Res.*, 66, 1995, 537

[16] M. P. Seah and E. D. Hondros, *Proc. R. Soc. Lond. A*, 335, 1973, 191

[17] M. Guttmann and D. McLean, in *Interfacial Segregation* (edited by W. C. Johnson and J. M. Blakely), American Society for Metals, Metals Park, Ohio 1979, p. 261

[18] M. P. Seah, *Acta Metall.*, 25, 1977, 345

[19] W. R. Tyson, *Acta Metall.*, 26, 1978, 1471

[20] G. Luckman, R. A. Didio and R. W. Graham, *Metall. Trans.*, 12A, 1981, 253

[21] M. Mackenbrock and H. J. Grabke, *Mater. Sci. Technol.*, 8, 1992, 541

[22] M. Militzer and J. Wieting, *Acta Metall.*, 37, 1989, 2585

[23] M. Militzer and J. Wieting, *Scripta Metall. Mater.*, 28, 1993, 1043

[24] J. du Plessis and G. N. van Wyk, *J. Phys. Chem. Solids*, 50, 1989, 237

[25] K. T. Aust, J. S. Armijo, E. F. Koch and J. H. Westbrook, *Trans. Am. Soc. Metals*, 60, 1967, 360

[26] T. R. Anthony, *Acta Metall.*, 17, 1969, 603

[27] Xu Tingdong, *J. Mater. Sci.*, 22, 1987, 337

[28] Song Shenhua, Xu Tingdong and Yuan Zhexi, *Acta Metall.*, 37, 1989, 319

[29] Xu Tingdong and Song Shenhua, *Acta Metall.*, 37, 1989, 2499

[30] Song Shenhua and Xu Tingdong, *J. Mater. Sci.*, 29, 1994, 61

[31] M. Menyhard and L. Uray, *Scripta Metall.*, 17, 1983, 1195

[32] T. Abe, K. Tsukada, H. Tagawa and I. Kozasu, *ISIJ Int.*, 30, 1990, 444

[33] C. L. Briant, *Acta Metall.*, 36, 1988, 1805

[34] R. D. K. Misra and T. V. Balasubramanian, *Acta Metall. Mater.*, 38, 1990, 1263

[35] R. D. K. Misra and T. V. Balasubramanian, *Acta Metall. Mater.*, 38, 1990, 2357

[36] T. Shinoda and T. Nakamura, *Acta Metall.*, 29, 1981, 1631

[37] T. Shinoda and T. Nakamura, *Acta Metall.*, 29, 1981, 1637

[38] L. E. Davis, N. C. McDonald, P. W. Palmberg, G. R. Riach and R. E. Weber, *Handbook of Auger Electron Spectroscopy*, 2nd edn., Phys. Electronics Industries, Minnesota 1976

[39] G. Seibel, *Mem. Sci. Rev. Met.*, 61, 1964, 413

[40] J. Kučera and K. Stránsky, *Mater. Sci. Engng.*, 52, 1982, 1

[41] R. D. K. Misra and P. Rama Rao, *Mater. Sci. Technol.*, 9, 1993, 497

[42] S. Suzuki, *Z. Metallk.*, 82, 1991, 883

[43] H. J. Grabke, R. Möller, H. Erhart and S. S. Brenner, *Surf. Interf. Anal.*, 10, 1987, 202

[44] J. Janovec, P. Ševc and M. Koutník, *Kovine zlitine tehnologije*, 29, 1995, 40

[45] J. Janovec, V. Magula and A. Holy, *Kovové Mater.*, 30, 1992, 44 (In Slovak)

[46] J. Kočík and E. Keilová, *Mater. Sci. Forum*, 97-99, 1992, 337

[47] R. C. Thomson and H. K. D. H. Bhadeshia, *Mater. Sci. Technol.*, 10, 1994, 193

slovenske železarne

ŽELEZARNA JESENICE

ACRONI

ELEKTRO PLOČEVINE IN TRAKOVI

NERJAVNA JEKLA

MIKROLEGIRANA JEKLA

VISOKO OGLJIČNA JEKLA za poboljšanje

IZDELUJE:

- nerjavna jekla
- jeklo za elektro pločevino
- nelegirana in legirana jekla
  - – za poboljšanje
  - – za cementacijo
- nelegirana, mikro in malolegirana konstrukcijska jekla

- toplo valjane pločevine, trakove in lamele
- hladno valjane pločevine, široke in vzdolžno razrezane trakove
- hladno oblikovane profile
- kovinske podboje za vrata
- izsekance
- varnostne ograje

NUDIMO TUDI STORITVE:

- prevaljanje
- izsekovanje (štancanje)
- krojenje
- ravnanje
- toplotne obdelave pločevin

SŽ ŽJ ACRONI d.o.o. Cesta železarjev 8, 4270 Jesenice, tel. centrala: +386 64 861-441,
tel. direktor: 861-443, tel. komerciala: 861-474, fax: 861-379, telex: 37219 ZELJSN SI **Slovenija**

Kovine, zlitine, tehnologije/30/1996/6/557-564

Mechanical Properties of High Temperature Vacuum Brazed HSS on Structural Carbon Steel with Simultaneous Heat Treatment

Mehanske lastnosti visokotemperaturno vakuumsko spajkanih in istočasno toplotno obdelanih spojev

V. Leskovšek[1], D. Kmetič, B. Šuštaršič, IMT Ljubljana, Slovenija

Prejem rokopisa - received: 1996-10-01; sprejem za objavo - accepted for publication: 1996-11-04

The high temperature vacuum brazing process, at the HSS austenitization temperature makes it possible to carry out simultaneously the brazing of HSS on structural carbon steel and heat treatment. The advantages of this process are: increased strength of brazed joints and toughness of the part, optimum hardness and cutting edge strength for a given combination working part/cutting tool. The process is economical when used in modern mass production methods, irrespective of the number of metals to be joined and heat treated. The adaptability makes the process so economical.

Key words: high temperature vacuum brazing, hardness, microstructure, shear strength, tensile strength, vacuum heat treatment

Postopek visoko temperaturnega vakuumskega spajkanja v enokomorni vakuumski peči s homogenim plinskim ohlajanjem pod visokim tlakom vodimo v območju avstenitizacije hitroreznih jekel. Prednost tako izdelanih rezilnih orodij je predvsem v doseganju želene žilavosti nosilnega dela iz konstrukcijskega jekla, v doseganju optimalne trdote rezila izdelanega iz hitroreznega jekla ter njegove odpornosti proti otopitvi pri dani kombinaciji del/orodje. Trdnostne lastnosti vezne plasti so odvisne od dodajnega materiala, tehnologije izdelave in pogojev vakuumske toplotne obdelave. Uporaba tega postopka je ekonomična, če moramo spojiti in vakuumsko toplotno obdelati le nekaj ali pa večje število orodij.

Ključne besede: visoko temperaturno vakuumsko spajkanje, trdota, mikrostukture, strižna trdnost, natezna trdnost, vakuumska toplotna obdelava

1 Introduction

High temperature vacuum brazing is a method of joining of metals by means of heat and filler metal in vacuum at temperatures above 900°C, yet below the melting point of the joined metals, and with no use of fluxes. The products are defect-free joints with very high bonding strength that can even reach the strength of the joined metal in many cases (e.g. steel, nickel or cobalt alloys).

The high temperature vacuum brazing of HSS on structural carbon steel with simultaneous heat treatment is performed in single chamber vacuum furnaces, with uniform high-pressure gas quenching at the austenitization temperature of HSS. In this work high temperature brazed joints of HSS and structural carbon steel with simultaneous heat treatment were investigated. Two brazing alloys based on Ni-Cr-Si and copper were applied as filler metals. The shear strength of an overlap joint and the tensile strength of a but joint as well as, the microstructure and fracture surface were investigated.

The advantages of the process are, the requested toughness of the carrying part from structural carbon steel and the optimum hardness and cutting edge strength of HSS for the given combination of working part/cutting tool. Such mechanical properties of cutting tools manufactured in the conventional way from HSS can only be obtained by an additional tempering operation.

Other advantages of the high temperature vacuum process are energy savings, the omittance of expensive tool steels and their cleaning, as well as, few parts are to be joined or hundreds of thousands when it is economical to use vacuum brazing with modern mass production methods. The adaptability makes vacuum brazing of increasing use in the metal-joining processes.

2 Basic factors affecting the mechanical properties of the brazed joint

The strength of the filler metal is one of the main factors influencing the strength properties of the brazing joint, since it is a direct measure for the strength properties of the joints. Therefore, joints brazed with nickel-base filler metal are stronger than those brazed with copper-base filler metal.

The narrow joint clearance causes a high capillary filling pressure; therefore, the gap should be parallel over the whole length of the joint. Only in this way by increased capillary filling pressure the filler metal can be aspired into the gap. The most favourable joint clearance for high vacuum temperature brazing is approximately 0 - 100 μm, when measured at the brazing temperature. **Figure 1** shows schematically the relation between joint clearance and the tensile strength of the joint for flux brazing and high temperature brazing[1].

---

[1] Vojteh LESKOVŠEK, dipl.inž.
Inštitut za kovinske materiale in tehnologije
1000 Ljubljana, Lepi pot 11, Slovenija

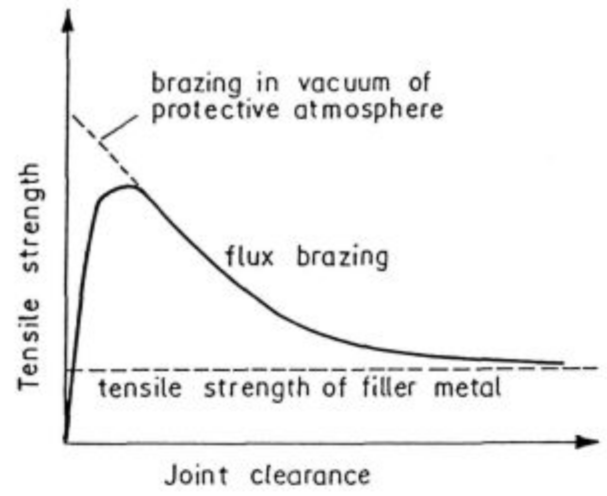

Figure 1: Relation between the joint clearance and the tensile strength of the joint[1]

Slika 1: Odvisnost med širino špranje in natezno trdnostjo spoja

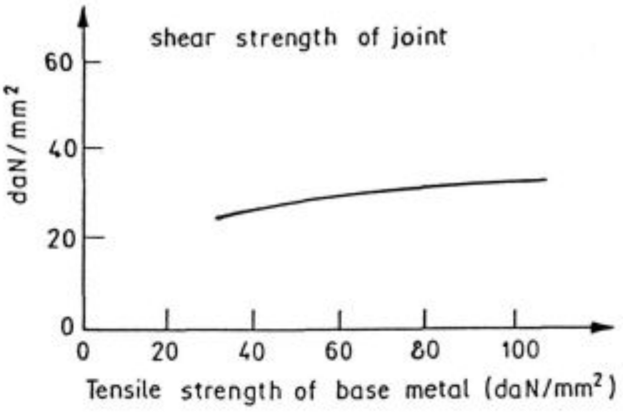

Figure 3: Shear strength of the brazing joints as a function of the tensile strength of the base metal[1]

Slika 3: Strižna trdnost spajkanega spoja v odvisnosti od natezne trdnosti osnovne kovine

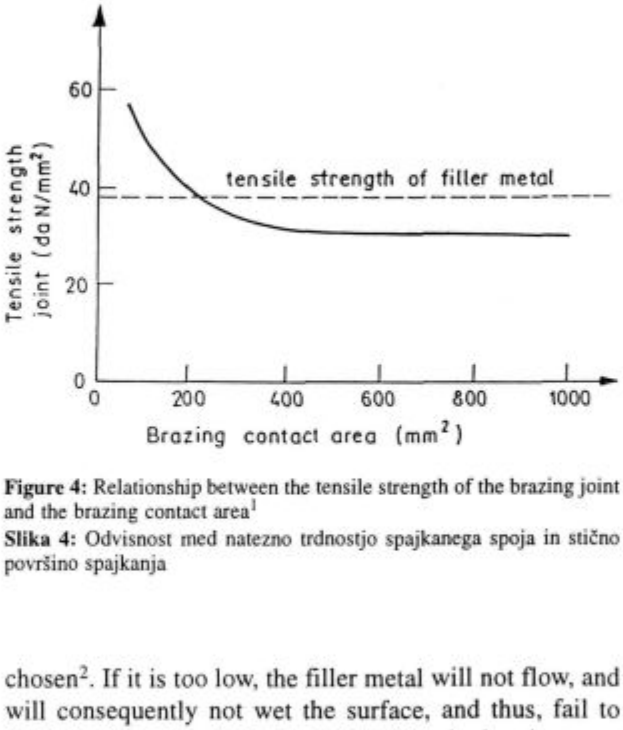

Figure 4: Relationship between the tensile strength of the brazing joint and the brazing contact area[1]

Slika 4: Odvisnost med natezno trdnostjo spajkanega spoja in stično površino spajkanja

The tensile strength of a brazing joint increases with the increasing tensile strength of the base metal, if all other conditions such as filler metal and joint clearance are the same, (**Figure 2**). The tensile strength of the base metal has no influence on the shear strength of the brazing joint, (**Figure 3**). In this case, only the properties of the filler metal are dominant. The tensile strength of the brazing joint decreases with the increase of the brazing contact area, (**Figure 4**). This can be explained by the fact that the chance for the formation of blowholes increases with the contact area, especially if the flow path for the filler metal also increases. However, the loadability of the piece is increased by increasing the contact surface of brazing.

To achieve the desired strength properties for the brazing joint, the exact brazing temperature has to be chosen[2]. If it is too low, the filler metal will not flow, and will consequently not wet the surface, and thus, fail to bond the base metal. On the other side, the brazing temperature must not be exceedingly high, as the alloyed elements in the filler metal might evaporate or undesired changes of the base metal could take place.

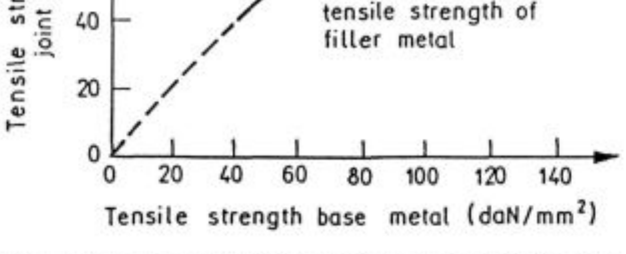

Figure 2: Tensile strength of the brazing joint as a function of the tensile strength of the base metal[1]

Slika 2: Natezna trdnost spajkanega spoja v odvisnosti od natezne trdnosti osnovne kovine

In some cases longer soak time at the brazing temperature after the melting of the filler metal also contributes to increase the strength properties. In this case, the diffusion zone is larger that results in higher strength properties of the joint as long as no brittle intermetallic phases are formed[2]. Investigations have shown that even with small quantities of impurities[1] in the filler metals, the mechanical properties are decreased significantly. The brazing joint becomes brittle because of the formation of brittle layers between the filler metal and the base metal.

3 Experimental procedure

Experiments were performed on high temperature vacuum brazed joints of the HSS W. No. 1.3343 and M15 (AISI) and the structural carbon steel W. No. 1.1141 (DIN) with simultaneous heat treatment. The filler metals used in this process were two brazing alloys manufactured by the Nicrobraz Wall Colmonoy firm (LM, 30) based on Ni-Cr-Si and water-atomised copper powder with the required brazing properties, **(Table 1)**.

Table 1: Chemical composition of base metals and filler metals (in wt%)

Tabela 1: Kemijska sestava jekel in dodajnih materialov (v ut.%)

Material	C	Si	Mn	P	S	Cr	W	Mo	V	Co
1.3343	0,89	0,35	0,29	0,018	0,018	4,2	6,3	4,9	1,8	-
1.1141	0,14	0,27	0,32	0,007	0,012	0,1	-	-	-	-
M15(AISI)	1,5	-	-	-	-	4,5	6,5	3,5	5,0	5,0
LM	7% Cr; 4,5% Si; 3;0% Fe; 2,1% B; max.0,06% C; bal. Ni									
30	19% Cr; 10,2% Si; max.0,10% C; bal. Ni									
Cu	99,8% Cu									

To get a higher strength of the joint or to make the fixturing of parts to be brazed easier, a lap joint should be selected. This joint should be designed to obtain the same stability under load of the joint and of the base metal. The lap length is then function of the tensile strength of the base metal and the shearing strength of the joint:

$$U = \frac{R_m \cdot t}{\tau} \qquad (1)$$

where U = length of the lap in mm,

R_m = tensile strength of base metal in Nmm^{-2},

τ = shearing strength of the joint in Nmm^{-2},

t = thickness of base metal in mm.

If, in addition, a safety factor and an impairment of the joint caused by small brazing errors is taken into account, then the length of the lap should be 3 to 6 times the thickness of the base metal. Generally, three times the base metal is sufficient for metals of low tensile strength; six times should be used for metals of high tensile strength[1].

The but joint is used for thicker parts (t > 2 mm) if a lap joint is not possible[1]. In contrast to soldering, the stability under load of this type of joint is often sufficient for practical use if the parts are brazed.

Experiments[3] were performed on shear specimens with single and fourfold overlap, **(Figure 5)**. The lamellae from HSS and structural carbon steels were, finely ground after rough machining. Measurements showed that the surface roughness R_a = 0.44 µm in the longitudinal direction was equal for both surfaces.

The test specimen with but joint shown in **Figure 6** was used for the tensile test.

For the brazing of the shear and tensile test specimens with the but joint the clearance of 80 µm was chosen. The brazing temperature was 1120°C for specimens brazed with the filler metals LM and Cu, and 1160°C for those brazed with the filler metal 30. After diffusion heat treatment, the specimens were cooled in nitrogen flow at the pressure under 5 bar abs, and than double tempered at 550°C, **(Figure 7)**. The brazing was performed in a vacuum 5 x 10^{-2} mbar. Shear and tensile specimens with but joints were used for metalographical and mechanical research.

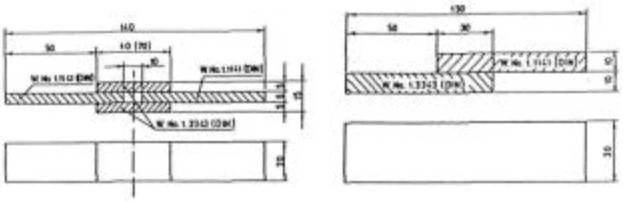

Figure 5: Shear specimens with single and four-fold overlap
Slika 5: Strižna preizkušanca z enkratnim in štirikratnim prekritjem

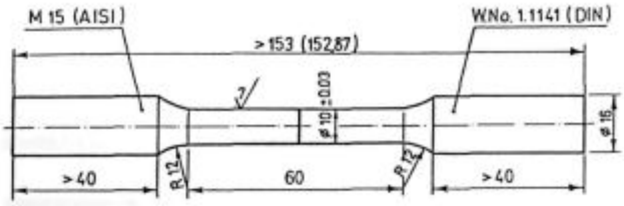

Figure 6: Tensile test specimen with but joint
Slika 6: Natezni preizkušanec s čelnim spojem

For the investigation of endurance of brazing joint, two paper knives with the dimensions of 425x117x10 mm and one knife with the dimension 560x117x10 mm, were manufactured from HSS W. No. 1.3343 steel and their bearing parts from the steel W. No. 1.7131 (DIN) steel, **(Figure8)**. The filler metal marked LM was used for these knives and considering the knives' shape, a lap joint with 80 µm clearance was chosen. The brazing temperature was 1190°C. After diffusion heat treatment, the knives were cooled in a nitrogen flow at a pressure under 5 bar abs, followed by double tempering at 540°C, **(Figure 7)**. The brazing was performed in a vacuum, 5 x 10^{-2} mbar.

4 Results and discussion

4.1 Mechanical tests

Next to the required properties of structural carbon steel and HSS, the most important property is the bond strength between them. Mechanical tests were performed on fourteen shear specimens with a single and four-fold overlap and length of the lap of 2 to 6 times the thickness of the base metal and three tensile test specimens brazed with LM and Cu filler metal.

The joint clearance for high temperature vacuum brazing was among 50-70 µm for the specimens brazed with fillers LM and 30, and 20-50 µm for the specimens

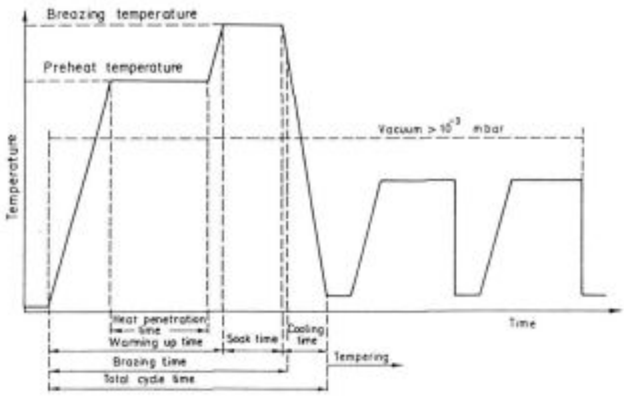

Figure 7: High temperature brazing with simultaneous heat treatment process model

Slika 7: Model visoko temperaturnega vakuumskega spajkanja z istočasno toplotno obdelavo

brazed with the copper filler. Data regarding specimens characteristics and the shear strength obtained by the Instron tensile testing machine are summarised in **table 2**.

Table 2: Specimens characteristics and the shear strength

Tabela 2: Karakteristike preizkušancev in strižne trdnostip rekrovnih spojev

Sample	Filler metal	Overlap	Length of the lap	Shear strength Nmm^{-2}
A/1	LM	four-fold	3 x t	> 30
A/2*	LM	four-fold	3 x t	27
A/3	LM	four-fold	6 x t	> 30
A/4*	LM	four-fold	6 x t	18
A/5	LM	single-fold	3 x t	> 71
A/6	LM	single-fold	2 x t	> 210
B/1	30	four-fold	3 x t	> 30
B/2*	30	four-fold	3 x t	27
B/3	30	four-fold	6 x t	> 20
B/4	30	single-fold	3 x t	> 60
C/1	Cu	four-fold	3 x t	> 32
C/2	Cu	four-fold	6 x t	> 62
C/3	Cu	single-fold	3 x t	> 66
C/4	Cu	single-fold	2 x t	> 205

* Samples fractured in bond layer; C/1- the middle lamellae made from W. No. 1.1141, end lamellae made from W.No. 1.3343; C/2 all lamellae made from W.No. 1.3343, because of gliding in the chucks, there was no destruction of the sample; C/3- all lamellae made from W. No. 1.1141.

Results in **table 2**, show that rupture of samples, in general, appeared in the structural carbon steel and not in the bond layer, **(Figure 9)**, since the shear strength of brazed joints was greater than the tensile strength of the structural carbon steel. The sample where the middle lamellae were from the steel W. No. 1.1141, was an exception since the fracture appeared simultaneously on both middle lamellae.

The shear strength is dependent upon the overlap shape and the lap length. The maximal shear strength was obtained on samples with a single-fold overlap and with the lap length 2 times the thickness of the base metal. On samples brazed with filler metal LM slightly higher values were obtained.

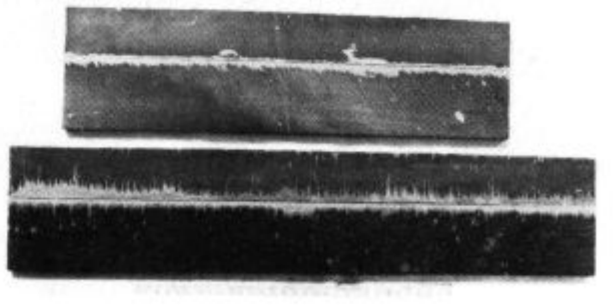

Figure 8: Paper knives manufactured by high temperature vacuum brazing with simultaneous heat treatment process to achieve a hardness of 64 Hrc

Slika 8: Noža za rezanje papirja izdelana po postopku visoko temperaturnega vakuumskega spajkanja in istočasno toplotno obdelana na 64 HRc

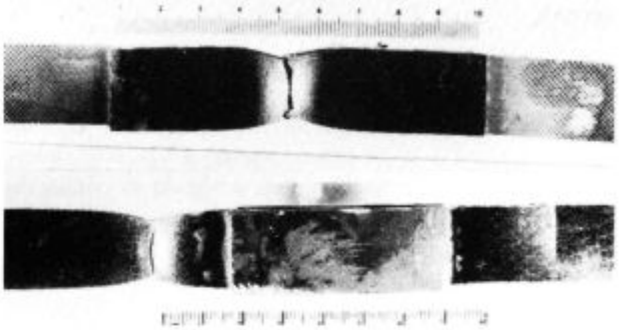

Figure 9: Shear specimens B/1 and C/1 with a four-fold overlap after the tensile test

Slika 9: Strižna preizkušanca B/1 in C/1 s štirikratnim prekritjem po trgalnem preizkusu

After vacuum heat treatment that corresponded to austenitizig and tempering temperatures for HSS M15 (AISI), the strength of the tensile test specimen with but joint was a little lower than that for structural carbon steel. The fractures propagated mostly within the bond layer and partly also in structural carbon steel and HSS. By tensile tests, the strength of specimens with but joint was strongly influenced by defects in the bond layer (sample C/8*). During tensile tests we did not notice any elongation or reduction of area on the samples. Results of tensile tests are presented in **table 3**.

Table 3: Strength of the tensile test specimen with but joints

Tabela 3: Natezne trdnosti čelno spajkanih preizkušancev

Sample	Filler metal	R_e (Nmm^{-2})	R_m (Nmm^{-2})
A/8	LM	330	445
C/7	Cu	340	475
C/8*	Cu	325	345

* defects in the bond layer

After mechanical tests, a metallographical examination was performed. On the single or four-fold overlap

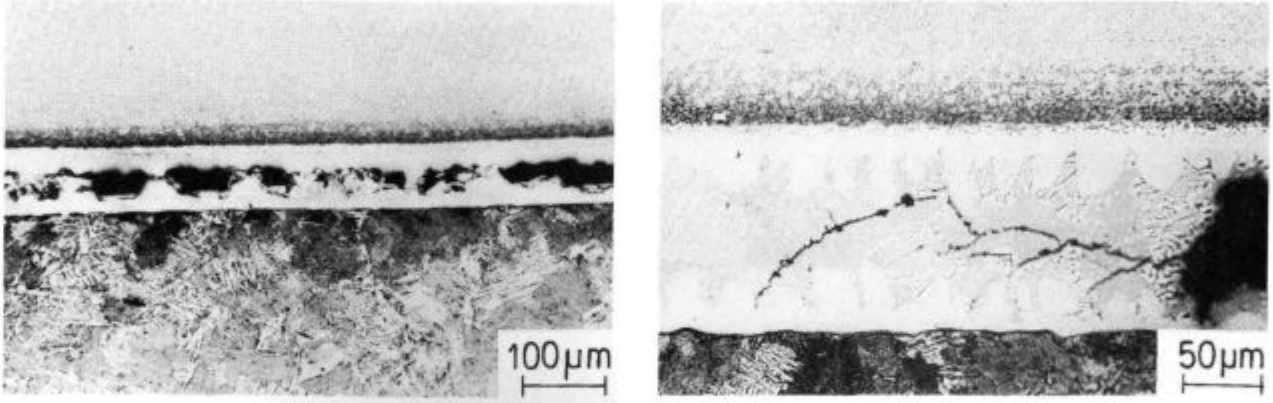

Figure 10: Initial microcrack area propagating through the eutectic phase is in the microporous regions, sample A/2
Slika 10: Inicial za nastanek mikrorazpok, ki potekajo po eutektični fazi, so mikroporozna mesta, preizkušanec A/2

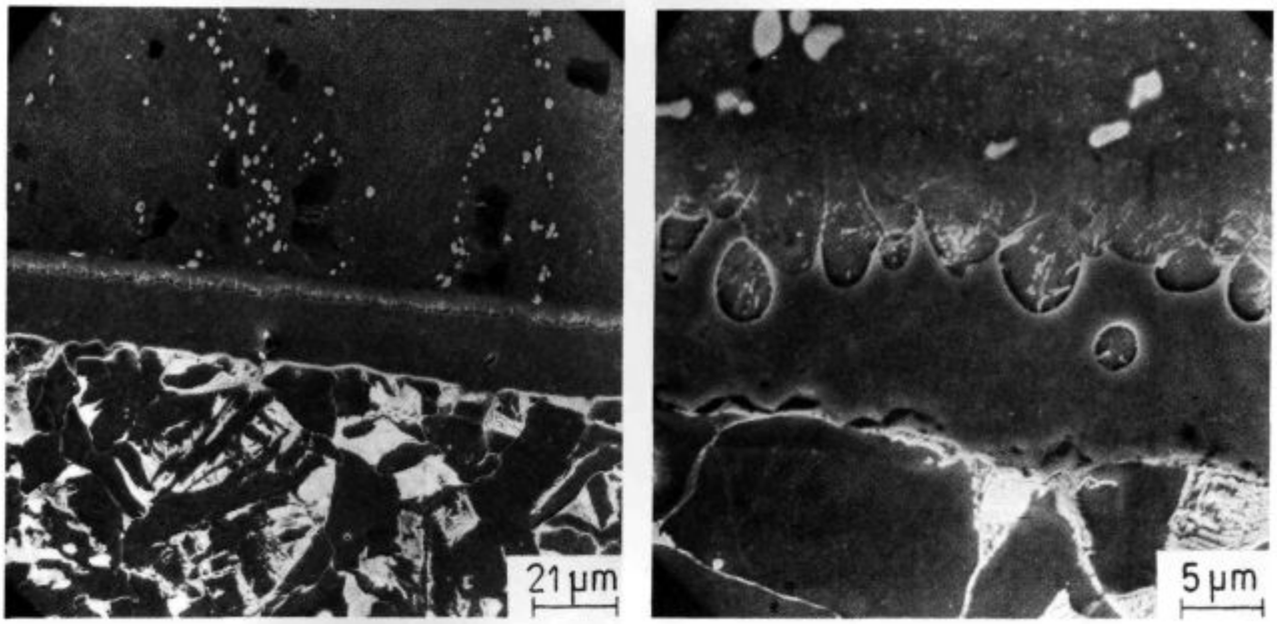

Figure 11: Microstructure of the bond layer in specimen C/7
Slika 11: Mikrostruktura vezne plasti na preizkušancu C/7

specimens, where fractures appeared in the structural carbon steel, only sporadic microcracks were found in the bond layer. On specimens with fracture in the bond layer, areas with microporosity were noticed, without exception, where microcracks initiated. On specimens brazed with the fillers LM and 30, the fracture cracks propagated through the eutectic phase of the bond layer, **(Figure 10)**.

As mentioned above, the diffusion of carbon from HSS to structural carbon steel took place; and consequently, the microstructure along the bond layer/structural carbon steel consisted of pearlite and bainite. On specimens brazed with copper, cracks appeared at the bond layer/structural carbon steel, respectively, **(Figure 11)**. Tensile test specimens fractured in this region, as well. Although carbon is not soluble in copper, the diffusion of carbon from HSS throughout the copper bond layer to structural carbon steel cannot take place, the mi-

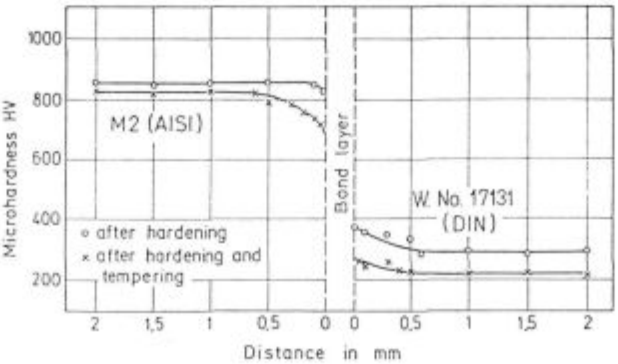

Figure 12: Vickers microhardness on transition from the bond layer to HSS and structural carbon steel
Slika 12: Potek mikrotrdote HV na prehodu iz vezne plasti v hitrorezno in konstrukcijsko jeklo

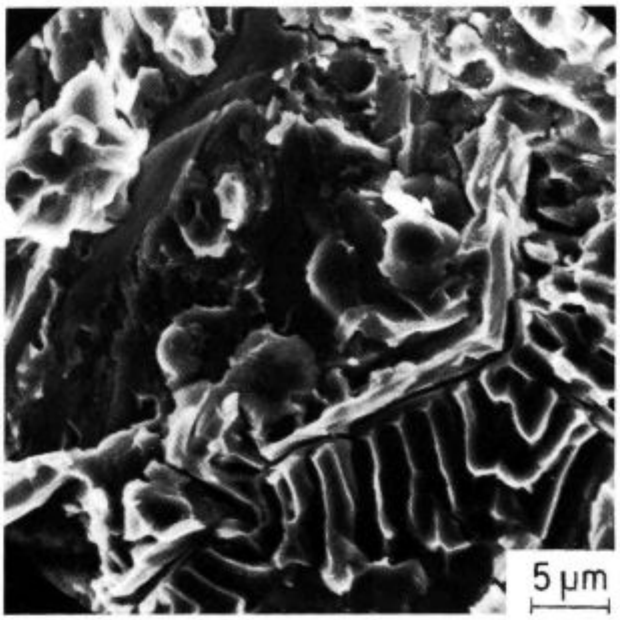

Figure 13: Fracture through an area of eutectic and austenite phase, sample A/8
Slika 13: Prelom preko eutektika in avstenitne faze, preizkušanec A/8

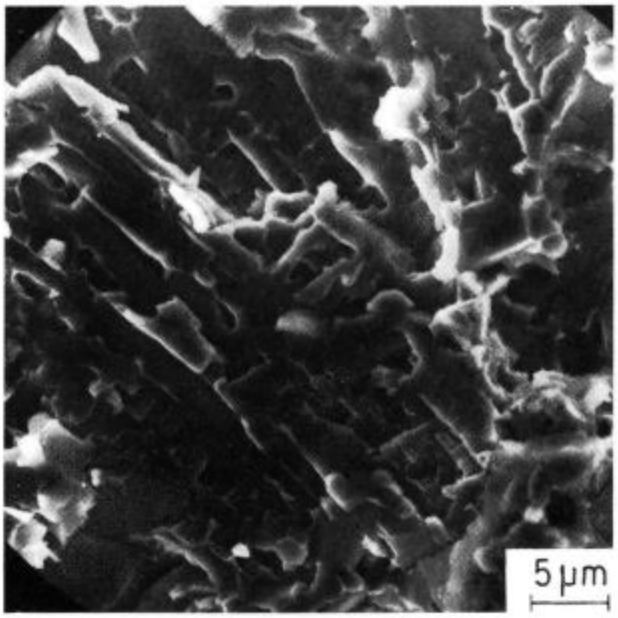

Figure 14: Fracture surface of the specimen B/2
Slika 14: Prelomna površina preizkušanca B/2

crostructure along the bond layer/structural carbon steel consisted of ferrite and bainite with traces of pearlite.

On the paper knife, the microhardness was measured across the bond layer to HSS and the structural carbon steel. The diffusion annealing was carried out with the aim to affect hardness at its transition across the bond layer and **Figure 12** shows the microhardness profile obtained. It shows that the HSS hardness is decreased, while it is increased in the structural carbon steel.

The morphology of fracture surfaces is very heterogeneous. On the specimens brazed with the fillers LM and 30, it was possible to identify fracture surfaces that propagated in dendrit's area from those propagated in the eutectic phase and in austenite, **(Figs 13 and 14)**.

Ductile fracture on specimens brazed with copper propagated mostly within bond layer, **(Figure 15)**. Inclusions of copper oxide were found in the dimples.

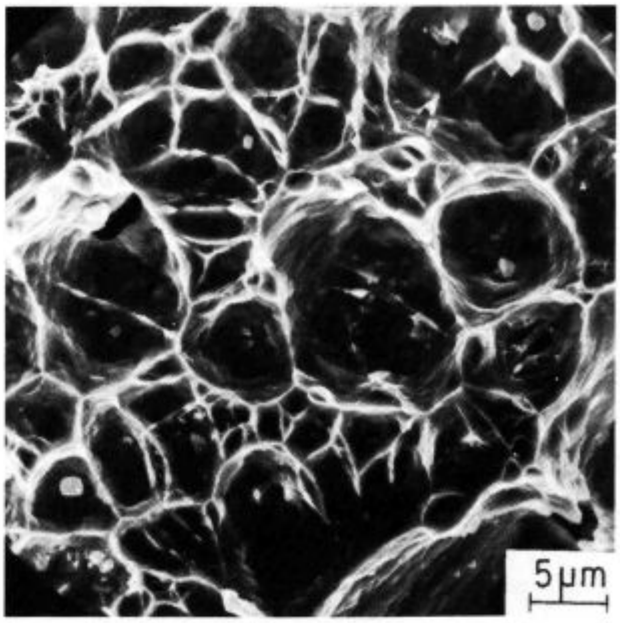

Figure 15: Fracture surface of the specimen C/7 brazed with Cu
Slika 15: Prelomna površina preizkušanca C/7 spajkanega s Cu - v jamicah so vključki bakrovega oksida

4.2 Microstructural characterisation

The used filler metals, structural carbon steel and HSS were examined by optical and scanning electron microscopy. The microstructure of the W. No. 1.1141 (DIN) structural carbon steel consisted of ferite-pearlite and bainite with a hardness of 145 HV10. The microstructure of the W. No. 1.3343 HSS consisted of a matrix of tempered martensite containing small carbide precipitates. The size of austenite grains was among 17 and 13 SG depending on the austenitization temperature and the hardness 64 HRc.

Figure 16 shows the microstructure of the bond layer between the HSS and the structural carbon steel on hardened and tempered specimens A/1 and B/2. The specimens were brazed with the fillers LM and 30.

In the bond layer polygonal grains formed because of the diffusion during brazing. The diffusion at the HSS/bond layer border seams to be quicker; therefore, more of this phase is found in the bond layer along the HSS. Along the structural carbon steel/bond layer, the bond layer was homogenous. The specimen B/2 was examined by SEM, **(Figure 17)**.

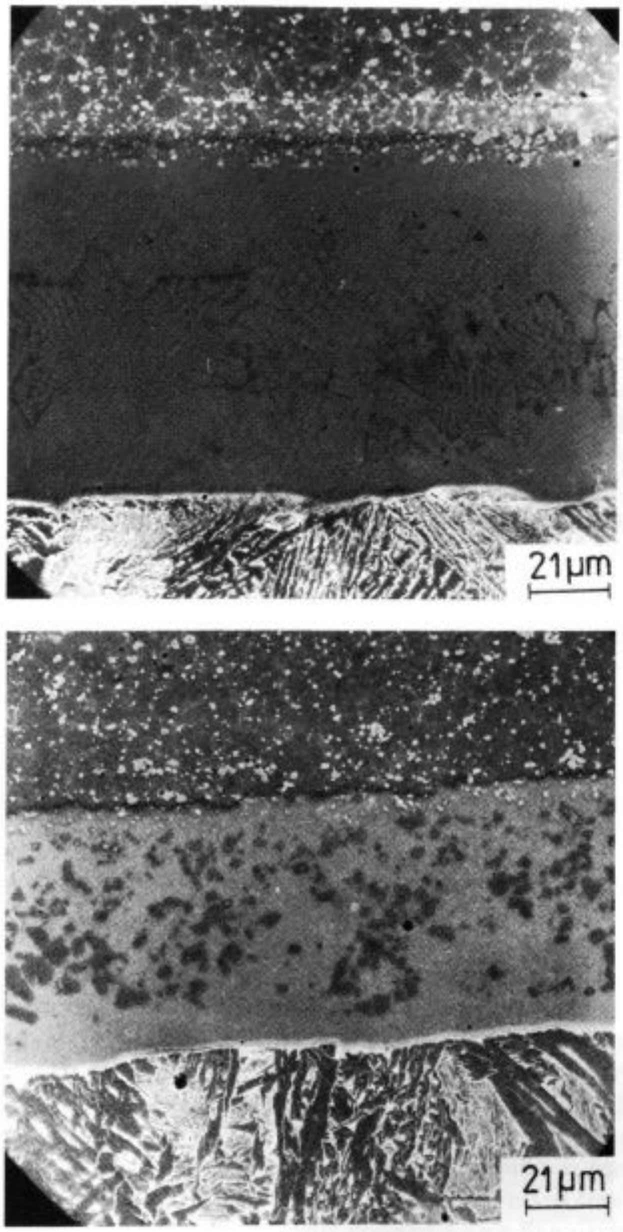

Figure 16: Microstructure of the high temperature brazed and simultaneously heat treated joints of HSS and structural carbon steel, samples A/1 and B/2
Slika 16: Mikrostruktura vezne plasti na preizkušancih A/1 in B/2

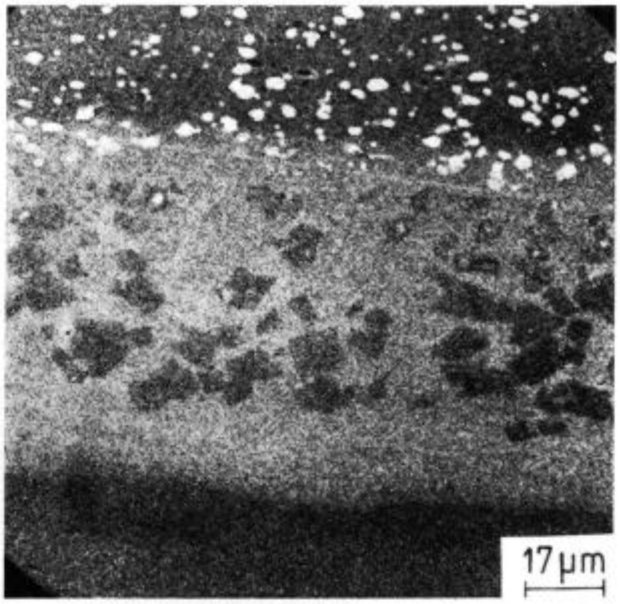

Figure 17: SEM micrograph of high temperature brazed joint, specimen B/2
Slika 17: Mikrostuktura vezne plasti preizkušanca B/2 posneta s SEM

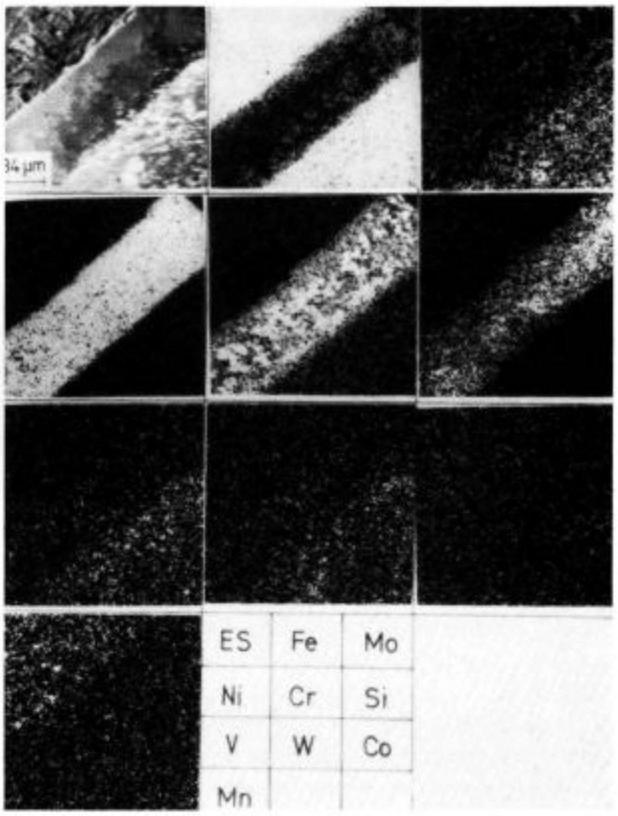

Figure 18: Distribution elements in the bond layer, sample B/2
Slika 18: Porazdelitev elementov v vezni plasti na preizkušancu B/2

A detailed investigation in EPMA showed that the larger polygonal grains present along the central line of the bond layer were a phase solidification grains rich in Cr, containing also Ni and Si with traces of W, Mo and V. The smaller grains were carbides, (**Figure 18**). The intermetallic phase was hard. The measured microhardness was 500-600 HV. The average matrix microhardness was 195 HV.

In the microstructure at the HSS/bond layer border, the effects of the diffusion processes were clearly noticeable. In the thin layer of HSS only carbides particles were noticed, martenzite matrix was transformed because of diffusion into austenite. This microstructure was very similar to that in the bond layer, (**Figure 17**).

At the bond layer/structural carbon steel border, diffusion of Cr, Ni and Si to structural carbon steel occurred. The hardened and tempered samples brazed with filler metal LM and 30 showed along this border a thin layer rich in carbon, (**Figure 16**) with microstructure consisting of a small amount of pearlite and bainite. The diffusion of carbon was more rapid on the samples brazed with the filler LM.

The microstructure of W. No. 1.7131 (DIN) structural carbon steel used for bearing part of paper knives consisted of tempered martensite and bainite. Austenite grains were coarse, due to the high austenitization temperature. The microstructure of the W. No. 1.3343 HSS consisted of a matrix of tempered martensite containing small carbide precipitates and the size of austenite grains of 14 SG. The microstructure of the bond layer was identical as in hardened and tempered samples brazed with filler metal LM.

5 Conclusion

Mechanical tests and metallographic observations were carried on high temperature vacuum brazed and simultaneously heat treated shear specimens with single and four-fold overlap and tensile test specimens with but joint. Two Ni-Cr-Si brazed metals as well as copper served as filler metal. During the heat treatment, rapid diffusion processes occurred between the liquid and the hard phase, especially along the HSS border. By use of Ni-Cr-Si based filler metal the formation of intermetallic phases, eutectic phases and carbides in the bond layer, and a net of eutectic carbides and voids on the austenite net along the bond layer/HSS border, were observed.

The mechanical properties of the bond layer depend on specimen design, manufacture and heat treatment conditions. The bond layer must be as thin and as homogenous as possible and must shows no porosity or microcracks. Intermetallic phases and carbides cannot be eliminated, due to the speed of the diffusion processes, which are very high on the HSS heat treatment temperature.

6 References

[1] J. W. Bouwman, High Temperature Vacuum Brazing, *Ipsen Instruction Manuals*

[2] V. Leskovšek, D. Kmetič, J. Gnamuš and G. Rihar: High temperature vacuum brazing of HSS on construction steel with simultaneous heat treatment, *Vuoto*, 20, 1990, 2, 512- 515

[3] D. Kmetič, V. Leskovšek, J. Žvokelj and J. Gnamuš: Trdnostne lastnosti visokotemperaturno spajkanih spojev v vakuumu, *KZT*, 27, 1993, 1-2, 69-73

Kovine, zlitine, tehnologije/30/1996/6/565-572

Discontinuous Al-SiC Composites Formed by a Low Cost Chemically Activated Infiltration Technique

Pridobivanje in kemijska infiltracija poroznih SiC vzorcev z Al-Si talino

V. M. Kevorkijan[1], zasebni raziskovalec, Maribor, Slovenija

Prejem rokopisa - received: 1996-10-01; sprejem za objavo - accepted for publication: 1996-11-04

In this work, the preparation of porous SiC preforms from SiC particles, platelets and whiskers have been demonstarted. Near net shape preforms, prepared by vacuum casting, were sintered and then covered by SiO_2 layer using a cost effective oxidation in air at 1175 K for 10h. Surface engineered SiC preforms were than pressureless infiltrated in nitrogen atmosphere (96 vol% N_2 + 4 vol% Ar) by a Al-Si melt containing 0.5 - 3 wt% Mg. Based on this, a mathematical model of spontaneous infiltration of a porous ceramic preform has been suggested. The role of magnesium and nitrogen atmosphere was quantitatively evaluated among the other important processing parameters (porosity of preform, the specific surface area, etc.) collected in a new term named preform infiltrability. Moreover, the influence of the above listed parameters on the infiltration rate (expressed as infiltration length and function of time) has also been demonstrated. The optimal conditions for spontaneous and cost effective pressureless infiltration of porous SiC preforms by molten aluminium alloy has been selected and experimentaly confirmed.

Key words: porous SiC preforms, vacuum casting, pressureless infiltration, infiltration kinetics, infiltrability of porous preforms

V delu je opisana izdelava poroznih SiC vzorcev z vakuumskim vlivanjem in njihovo sintranje do poroznih predoblik, sestavljenih iz SiC delcev različne oblike: okrogli, heksagonalne ploščice in kratka vlakna. Z oksidacijo na zraku smo prevlekli površino poroznih SiC predoblik s tanko plastjo SiO_2 in izboljšali omočljivost med SiC in Al talino. V nadaljnjem delu smo infiltrirali porozne keramične vzorce z Al-Si-Mg talino v dušikovi atmosferi (96 vol% N_2 + 4 vol% Ar) pri normalnem tlaku. Na podlagi pridobljenih rezultatov smo razvili matematični model infiltracije, ki opisuje kinetiko procesa v funkciji poroznosti in specifične površine pripravljenih poroznih vzorcev, vsebnosti dušika v atmosferi in sestave Al zlitine. Model je osnova za nadaljnji razvoj tehnologije priprave Al-SiC kompozitov s spontano oz. nizkotlačno infiltracijo poroznih SiC vzorcev.

Ključne besede: porozne SiC predoblike, vakuumsko vlivanje, spontana infiltracija, kinetika infiltracije, infiltrabilnost poroznih predoblik

1 Introduction

The need for high strength, lightweight, and high stiffness materials has, in recent years, attracted much interest to the development of the manufacturing processes of metal matrix composites (MMCs)[1]. The most important limitation of the fabrication of MMCs by liquid-phase processes resides in the compatibility between the reinforcement and the matrix[2]. This compatibility is particularly important in the case of aluminium-based composites, because Al is usually covered with a thin oxide layer that prevents wetting, and when uncovered, it readily reacts with most ceramics to form intermetalics. In particular, liquid aluminium reacts with SiC to produce aluminium carbide and free silicon. Wettability and reactivity determine the quality of the bond between both materials and, therefore, greatly influence the final properties of the composite.

In many instances the properties of a reinforced metal have been shown to provide a performance advantage over a monolithic metal, but the high cost of producing the composite has prohibited widespread commercial use. Liquid-metal processes have the potential to be more economical; hovever, the non-wetting nature of many ceramics by molten aluminium, which results in poor ceramic/metal interfaces and incomplete infiltration, has been an obstacle.

Melt infiltration is a popular technique for fabricating MMCs, as it allow near-net shape fabrication of components and material with a high reinforcing phase content. The molten metal may penetrate the porous preforms either under the action of an external force (pressure casting[3] and vacuum assisted liquid infiltration process[4]) or through a capillary pressure which is created once the molten metal wets the ceramic surface (pressureless infiltration[5]).

Several pressure casting methods have been used for preparing MMCs. The operating principle of a hydrostatic pressure infiltration device[6] is to use pressurised gas to force molten metal into an evacuated die. Another pressure casting technique is relatively simple[7]: pre-heating the particle aggregate in a special mould and then adding 3 MPa pressure to the molten metal poured on the particle aggregate so as to encourage penetration which results in a metal-particle composite. Recently, a bottom mixing process has also been suggested, where an evacuated packed bed in the bottom of a crucible is covered with a melt, and than stirrer shears the interface between the particles and the melt, resulting in incorporation[8].

Different fabrication methods using vacuum techniques for cast-in-place hardfacing of casting were also described[9]. In these processes, aluminium poured into a sand mould is drawn by vacuum into a porous layer of

---

[1] Dr. Varužan M. KEVORKIJAN
Lackova 139
2341 Limbuš, Slovenija

reinforcing phase (named - preform) placed on a wall of the mould cavity.

A recent molten metal process is the Lanxide Corp. Primex^{TM} pressureless infiltration process[10,11]. In this process a packed bed of ceramic powder is infiltrated by an Al-Mg alloy, without any applied pressure, in a nitrogen atmosphere. The resulting composite, which has a packed bed density of about 55 vol.-%, can than be diluted in the appropriate matrix alloy. Ceramic particles of SiC and Al_2O_3, with particle size as fine as about 1 μm have been infiltrated in this way, and at infiltration rates of up to the order of centimetres per minute under specific processing conditions. Processing details of the Primex^{TM} route are proprietary, but it would appear to be a very competitive process for higher volume fraction composites. The Lanxide Corporation has made extensive efforts to protect this very valuable technology and has well over 100 U.S. patents and over 1500 foreign patents pending, with nearly 50 U.S. patents and over 100 foreign patents being issued or allowed by the middle of 1989.

In this work, the preparation of porous SiC preforms made by SiC particles, platelets and whiskers have been demonstrated. The surface of SiC preforms has been covered by SiO_2 layer using cost effective oxidation in air. Chemically treated preforms were than pressurelless infiltrated by an Al-Mg alloy in nitrogen atmosphere. The conditions for spontaneous (as used, spontaneously means without the aid of any externally applied pressure or vacuum), pressureless infiltration, which include the use of a magnesium containing alloy and a nitrogenous atmosphere have been already well documented in literature, by the inventors[12]. However, the offered explanation is semi-empirical based on the well known role of magnesium which decreases the surface tension of a molten aluminium alloy. As stated by inventors[12], this alone does not induce spontaneous infiltration, but a nitrogen atmosphere may cause a further reduction in the surface tension, thus promoting wetting. Additionally, the reactivity of magnesium induces interfacial reactions with solid ceramic surfaces. These reactions typically are not sufficient to promote spontaneous wetting, but again in combination with a nitrogen atmosphere they may change or be altered, thus allowing the observed infiltration. These results clearly demonstrated that the combination of magnesium in the alloy and a nitrogeneous atmosphere leads to the spontaneous infiltration of aluminium alloy into ceramic fillers. However, little information is available on the effect of a nitrogen atmosphere on wetting. Some authors[13] found that when fabricating aluminium alloy matrix composites via compocasting, the use of a nitrogen atmosphere and a bubble-degassing step with nitrogen yielded composites with much lower porosity than those produced similarly with argon, but these results may not be assciated with enhanced wetting.

In the present paper a mathematical model of spontaneous infiltration of a porous ceramic preform has been suggested. The role of magnesium and nitrogenous atmosphere was quantitatively evaluated among the important processing parameters (porosity of the preform, the specific surface area, surface tension and the contact angle). Moreover, the influence of above listed parameters on the infiltration rate (expressed by the infiltration length as a function of time) has been also demonstrated. In this way, the optimal conditions for spontaneous and cost effective pressureless infiltration of porous SiC preforms by molten aluminium alloy were selected and experimentaly confirmed.

2 Pressureless infiltration - theoretical considerations

A. Capilllary Law

Spontaneous infiltration of a liquid into a porous medium takes place when the liquid wets the solid. Otherwise, a minimum external pressure should be applied. This threshold pressure P (also called capillary pressure) is related to the contact angle θ and the particle size through the so-called capillary law or Laplace equation:

$$P = 6\lambda\gamma_{lv}\cos\theta\, V_p/((1-V_p)D) \tag{1}$$

where γ_{lv} is the liquid-vapor surface tension, λ a factor which depends on the geometry of the particles, D the mean diameter of the particles, and V_p the particulate volume fraction. Note that product ($-\gamma_{lv}\cos\theta$) is the work of immersion W_i defined as the change in the free energy on immersing the solid in the liquid. The work of immersion can be written in terms of the threshold (or capillary) pressure through the following expression:

$$W_i = P\,(1-V_p)/S_s\rho V_p \tag{2}$$

where S_s is the specific surface area (the surface area per unit mass of porous preform) and ρ is the density of the particulate. Unfortunately, the Laplace equation describes the situation for a cylindrical tube, a very crude model for the types of porous media under consideration here. This model, for example, cannot be applied to irregularly shaped pores where the effect of both pore geometry and network cooperatively combine with contact angle hysteresis[14]. However, White[15] derived a specialized expression based on the Laplace equation relating the pressure, P required to prevent capillary rise in porous media for which the specific surface area S_s, solid density ρ, surface tension γ_{lv}, contact angle θ, and porosity α, are known:

$$P = (1-\varepsilon)\,\rho\, S_s\gamma_{lv}\cos\theta\,/\varepsilon \tag{3}$$

B. Darcy's Law

The flow of an incompressible fluid through a porous medium is governed by Darcy's law[16]. For unidirectional flaw, and neglecting any effect of gravity, Darcy's law can be written as

$$v_o = -(k/\mu)(dP/dx) \tag{4}$$

where v_0 is the superficial velocity of the fluid (the velocity of the fluid as measured by the volumetric flow rate per unit cross sectional area where the cross section is taken perpendicular to the average direction of flow), μ the viscosity of the liquid, dP/dx the pressure gradient at the infiltration front, and k the intrinsic permeability. It has been found empirically that the intrinsic permeability k of a porous medium is proportional to the square of the mean particulate diameter[17]

$$k = aD^2 \tag{5}$$

where the constant a must be determined experimentally.

The superficial velocity v_0 can be related to the actual velocity in the porous medium (dx/dt) by means of the particulate volume fraction V_p:

$$v_o = (1-V_p)\,dx/dt \tag{6}$$

Combining Eqs. (4) and (6) and integrating, the expression for the infiltration length, L as a function of time and the pressure drop in the liquid metal #9P can be written as:

$$L = [2kt\Delta P/\mu(1-V_p)]^{1/2} \tag{7}$$

On the other hand, for pressureless infiltration the pressure drop should be at least equal to the threshold (or capillary) pressure (Eq. 3). Under conditions of constant permeability and constant capillary pressure, Eqs. (3) and (7) can be combined to obtain the following relationship between infiltration length L, time t, and other processing parameters:

$$L = (1/\varepsilon)\,[2ktW_iS_s\rho(1-\varepsilon)/\mu]^{1/2} \tag{8}$$

Note that W_i (work of immersion) is equal - $\gamma_{lv}\cos\theta$.

The Eq. (8) can be simplified introducing that $\varepsilon^{-1}\sqrt{2kS_s\rho(1-\varepsilon)}$ is the infiltrability of porous preform Q:

$$L = Q\,[W_i/\mu]^{1/2}t^{1/2} \tag{9}$$

Again, it's important to note that Eq. (9) is valid under conditions of constant infiltrability and porosity of ceramic filler, constant work of immersion and, finally, constant viscosity of the melt, which is very difficult to obtain in practice.

In spite of this considerable limitation, Eq. (9) can be successfully used in combination with Eq. (3) in order to designe the simple mathematical criterion for an early stage of pressureless infiltration of porous ceramic preform. Moreover, using this procedure, the parameters of pressureless infiltration can be selected to satisfied both proceesing requirements: spontaneous infiltration at acceprtable infiltration rate.

3 Materials and experimental procedures

Preparation of porous SiC preforms

For the purpose of this study, three basic SiC morphologies - particles, platelets and whiskers in several size ranges (**Table 1**) were used for preforms preparation. Photomicrographs of used powders are compared in **Fig. 1**. A diagram outlining the preform production process is shown in **Fig. 2**.

Table 1: Characteristics of SiC phases used

	Particles	Platelets	Whiskers
	HSC 1200 Microgrits Superior Graphite	SiC Platelets Millenium Materials, Inc.	M-Grade SiC_w Advanced Refractory Technologies, Inc.
Chemistry:	Stoichiometric SiC	Stoichiometric SiC	Stoichiometric SiC
Crystalographic Structure:	Primary phase Beta	Primary phase Beta	Primary phase Beta
Diameter range (µm):	2-12	35-40	whisker length 15-20
Thickness (µm):	/	3-5	1-2
Aspect ratio:	/	8-10	10-12
Purity:	97-99 wt% SiC	<1000 ppm of metallic impurities	<1000 ppm of metallic impurities
Particulate Content (%):	~100	5-10	5-10
Oxygen (%) by Leco	1.0	0.68	1.1
Free Carbon(%):	1.0	0.01	0.53
Specific Gravity (g/cm^3):	3.21	3.21	3.21

Preform infiltration

The experimental lay-up used in this work consisted of an aluminium alloy ingot, measuring about ϕ50 x 30 mm, placed on the top of a porous ceramic preform. The filler material had a height that was great enough to prevent full infiltration under the process conditions (i.e. more-or-less infinite column of filler material). After processing, the amount of infiltration (distance from alloy/filler interface) was measured, and the composite was sectioned and examined both macro- and microstructurally. The alloy/filler pairs were than placed into a controlled atmosphere furnace within a refractory vessel (a 99.9% sintered alumina). The furnace was evacuated to ~1 Pa at room temperature and back-filled with an nitrogen-containing atmosphere until a positive flow was obtained. Note that all experiments were conducted under a slight positive pressure that was achieved by bubbling the exit gas through a 25 mm column of oil. Following the procedure developed in Lanxide, the furnace was ramped to temperature at a rate of 200°C/h, held at temperature for the specified time (e.g. at 800-1000°C for 10 to 24 h for full infiltration of the speciments) and allowed to cool to 675°C, at which time the samples were removed from the furnace and cooled to room temperature. Various combinations of magnesium-containing aluminium alloys, silicon carbide porous preforms, nitrogen-containing gases, and temperature/time conditions were employed to study the effect of various process variables on the infiltration kinetics.

Because the infiltration of the porous preforms occurs in a nitrogenous atmosphere (at least about 10 volume percent nitrogen and the balance a non-oxidizing gas under the process conditions), aluminium nitride precipitates may form within the aluminium alloy matrix.

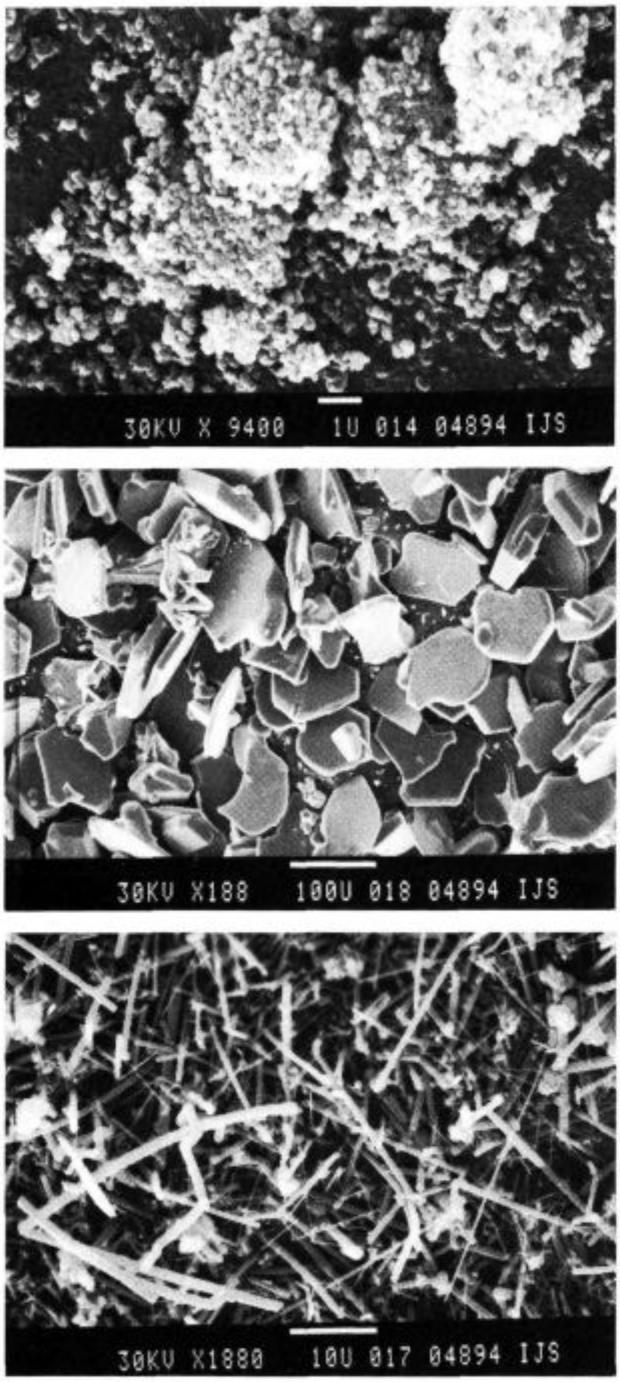

Figure 1: Photomicrographs of used SiC morphologies: a) HSC 1200 Microgrits Superior Graphite, b) SiC Platelets, Millenium Materials, Inc. and c) M-Grade SiC whiskers, Advanced Refractory Technologies, Inc.

Slika 1: SEM fotografije SiC uporabljenih delcev: a) SiC prah -HSC 1200 Microgrits Superior Graphite, b) SiC ploščice, Millenium Materials, Inc. in c) SiC whiskerji - M-Grade, Advanced Refractory Technologies, Inc.

The per cent weight gain provides a measure of the amount of aluminium nitride that forms during processing. For comparison, the total conversion of pure aluminium to aluminium nitride produces a weight gain of 52%. Moreover, because this experimental arrangement produced a constant volume of composite in all cases where full infiltration occured, the weight gains of different experiments could be directly compared.

4 Results and discussion

Preform preparation

SiC preforms, containing whiskers, platelets or particles, were fabricated by vacuum casting in a variety of shapes and with a uniform microstructure. The characteristics of these preforms are listed in **Table 2**.

Table 2: Characteristics of SiC- whiskers, platelets and particles preforms made by vacuum casting method

CHARACTERISTIC	PREFORM		
	Particle's grade	Platelet's grade	Whisker's grade
Average bulk density (g/cm^3)	1-2.25	1-2.25	1-2.25
Preform diameter (cm)	3-10	3-10	3-10
Preform height (cm)	2-5	2-5	2-5
BET-Specific surface area (m^2/g)	1.5-5.9	2.0-2.5	3.5-3.8
Porosity (vol%)	30-70	30-70	30-70

Infiltration experiments

The critical process conditions for pressureless infiltration of porous SiC preforms with molten aluminium

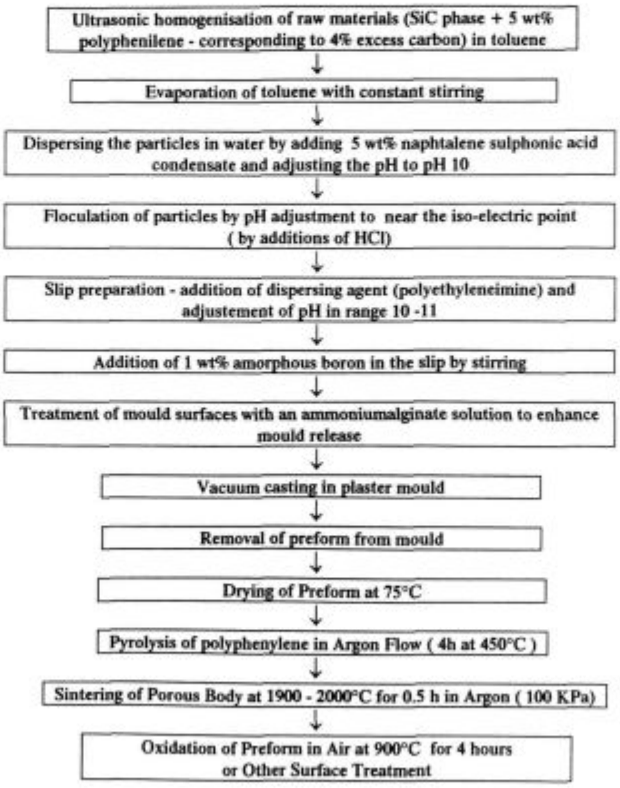

Figure 2: Preform fabrication process

Slika 2: Proces pridobivanja poroznih predoblik

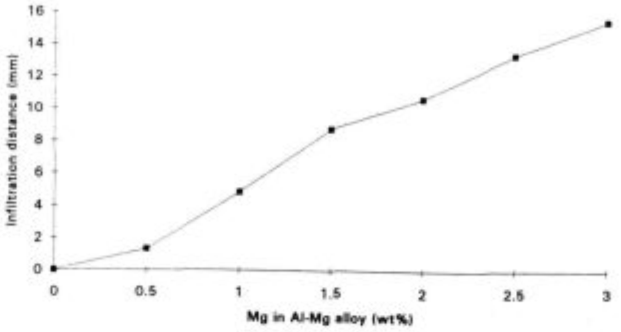

Figure 3: Relationship between magnesium content in an Al-10Si-Mg alloy and iniltration distance (process conditions - 5 h dwell at 1175 K, nitrogen atmosphere with 4 vol% Ar) measured in SiC particle grade preform

Slika 3: Odvisnost globine infiltracije od vsebnosti magnezija v Al-10Si-Mg zlitini (eksperimentalni pogoji - 5 h pri 1175 K, atmosfera dušika s 4 vol% Ar) za porozne SiC predoblike pripravljene iz SiC prahu

alloys were found to be: (i) the alloy composition, (ii) the atmosphere composition, (iii) the process temperature and time and (iv) the infiltrability of the preforms.

The influenece of alloy composition (specifically the magnesium content) on infiltration distance is plotted in **Fig. 3**. The collected results are in agreement with data previously reported by Aghajanian et al.[12] The new data also confirm the linear relationship between magnesium content and amount of infiltration proposed by Aghajanian et al.[12].

The effect of nitrogen content of the atmosphere on the infiltration process was determined by conducting experiments in atmospheres ranging from 100% N_2 to 100% Ar. It was found that no infiltration occured in 100% Ar, only partial infiltration occured in 10% N_2+90% Ar and full infiltration occured when the nitrogen content exceeded 20-30 vol%. As reported[11], at high percentages of N_2, where infiltration was rapid, little nitride formed, whereas in dilute atmospheres, where infiltration was slow, observable levels of AlN formed. In a similar fashion, the process temperature significantly affects the quantity of nitride that forms within the aluminium alloy matrix. **Figure 4** plots unit weight gain versus process temperature for samples using alloy Al-10Si-3Mg, preforms made by SiC grit and process conditions of a 5 hour dwell at temperature in 95% N_2/4% Ar. Results also demonstrate that increased process temperature results in increased nitride formaton whichincrease becames significant and nearly linear for temperatures higher than 1125 K.

At a constant magnesium level and a fixed nitrogen content, several others process variables can affect the infiltration behaviuor. **Fig. 5** plots the infiltration distance against temperature for otherwise constant process conditions. It is evident that infiltration increased in an approximatively linear manner with the temperature. Additionally, the data show that there is a threshold temperature required to initiate the pressureless infiltration for a given set of process parameters. Although limited, the data presented in **Fig. 6** suggest that the threshold temperature changes with the process conditions (the preform infiltrability, the alloy composition and the nitrogen content in the processing atmosphere).

One can also conclude that the process temperature affects the quantity of AlN that formed within the aluminium alloy matrix. **Fig. 7** plots the unit weight gain against temperature for different SiC grade preforms. The results demonstrate that as the process temperature increases, the quantity of AlN that forms also increases. These results are in well agreement with reported data[12] and confirm that the increase in AlN content is approximately exponential over the temperature range investigated.

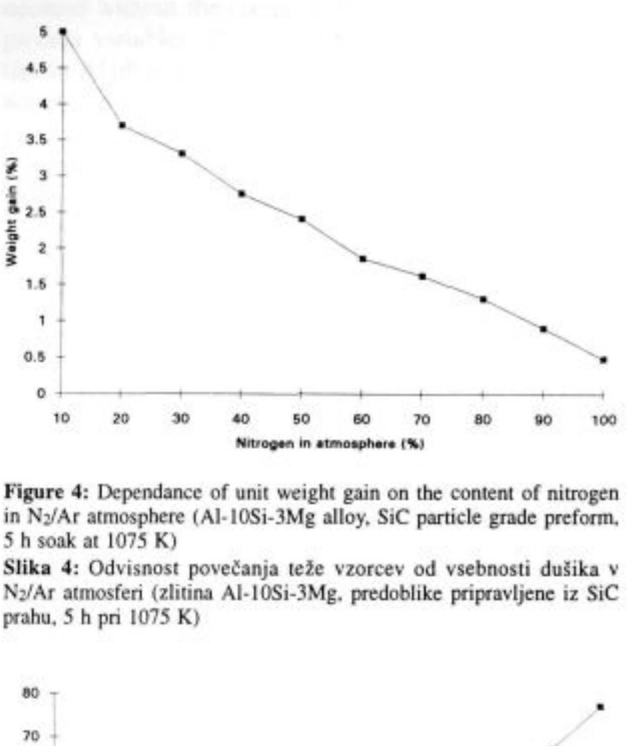

Figure 4: Dependance of unit weight gain on the content of nitrogen in N_2/Ar atmosphere (Al-10Si-3Mg alloy, SiC particle grade preform, 5 h soak at 1075 K)

Slika 4: Odvisnost povečanja teže vzorcev od vsebnosti dušika v N_2/Ar atmosferi (zlitina Al-10Si-3Mg, predoblike pripravljene iz SiC prahu, 5 h pri 1075 K)

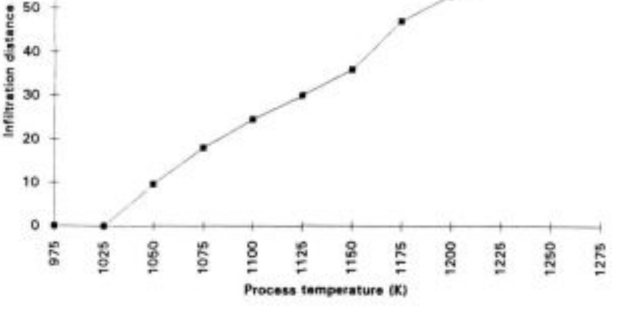

Figure 5: Variation of infiltration distance with process temperature (Al-10Si-3Mg alloy, SiC particle grade preform, 5 h soak at temperature in a nitrogen atmosphere with 4 vol% Ar)

Slika 5: Odvisnost globine infiltracije od temperature (zlitina Al-10Si-3Mg, predoblike pripravljene iz SiC prahu, 5 h pri delovni temperaturi v dušikovi atmosferi s 4 vol% Ar)

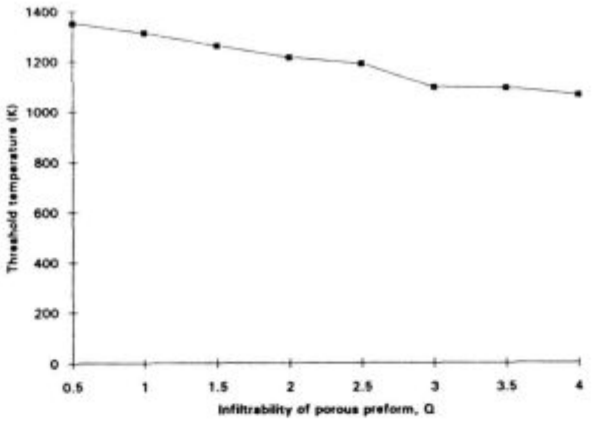

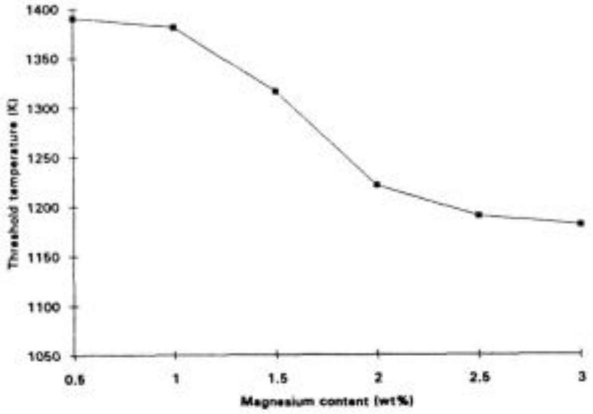

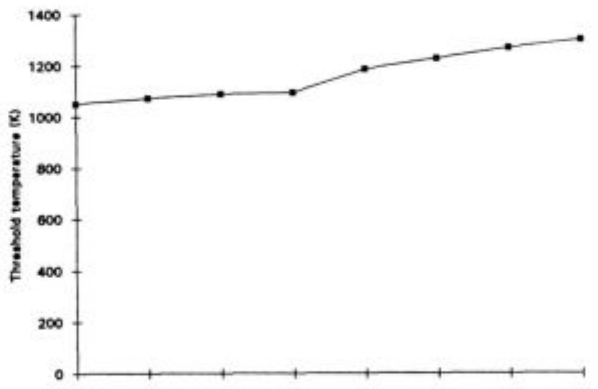

Figure 6a: Relationship between threshold temperature and infiltrability of porous SiC particle grade preforms (Al-10Si-3Mg alloy and a 5 h soak at temperature in nitrogen atmosphere with 4 vol% Ar)

Slika 6a: Odvisnost temperature začetka infiltracije od infiltrabilnosti poroznih predoblik, pripravljenih iz SiC prahu (zlitina Al-10Si-3Mg, 5 h pri delovni temperaturi v dušikovi atmosferi s 4 vol% Ar)

Figure 6b: Relationship between threshold temperature and magnesium content in Al-10Si alloy (SiC particle grade preform and a 5 h soak at temperature in nitrogen atmosphere with 4 vol% Ar)

Slika 6b: Odvisnost temperaturnega praga od vsebnosti magnezija v Al-10Si zlitini (predoblike pripravljene iz SiC prahu, 5 h pri delovni temperaturi v dušikovi atmosferi s 4 vol% Ar)

Figure 6c: Relationship between threshold temperature and nitrogen in processing atmosphere (Al-10Si-3Mg alloy, SiC particle grade preforms and a 5 h soak time at 1125 K)

Slika 6c: Odvisnost temperaturnega praga za porozne predoblike pripravljene iz SiC prahu, od vsebnosti dušika v delovni atmosferi (zlitina Al-10Si-3Mg, 5 h pri delovni temperaturi)

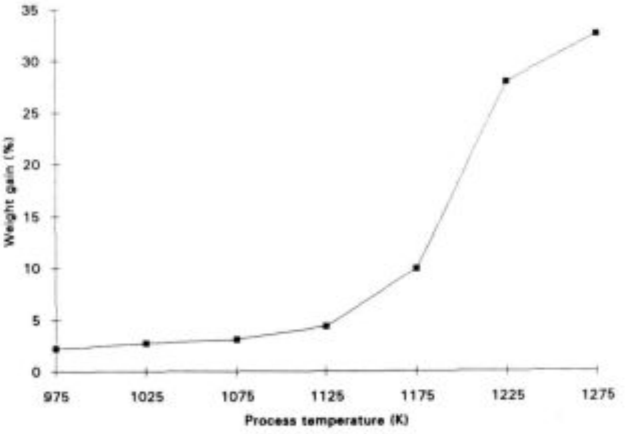

Figure 7: Relationship between process temperature and AlN formation (unit weight gain) in aluminium alloy matrix (obtained using alloy Al-10Si-3Mg, SiC particle grade preform and a 5 h soak at temperature in nitrogen atmosphere with 4 vol% Ar)

Slika 7: Odvisnost temperature infiltracije od deleža nastalega AlN (izraženega kot povečanje teže analiziranih vzorcev) v Al zlitini (zlitina Al-10Si-3Mg, predoblike pripravljene iz SiC prahu, 5 h pri delovni temperaturi v dušikovi atmosferi s 4 vol% Ar)

The effect of the infiltrability of porous preforms (see Eq. (9)) on the infiltration process was studied using preforms with different porosity and specific surface area. Note that the preform infiltrability, defined as $\alpha^{-1}\alpha 2kS_s\rho(1-\alpha)$, could be expressed as a function of specific surface area (S_s) and porosity (α) taking into account Eq. (5):

$$Q = \text{const.}\ \varepsilon^{-1} S_s \sqrt{\rho}(1-\varepsilon) \qquad (10)$$

Fig. 8 plots the infiltration distance against preform infiltrability. The changes in the infiltrability of porous preforms were obtained by ranging their porosity and specific surface area. In order to meet these requirements, the preforms were prepared using selected sintering conditions. The results demonstrate that all experimental data fit well with the proposed process kinetics expressed by Eq. (9) for otherwise constant process conditions. Moreover, Eq. (9) seems to be valid for very different morphology of SiC particles.

However, the Eq. (9) also, in some matter, presents a serious problem. There is a very complex correlation between preform porosity and its real specific surface area. Usually, BET technique is used to determine S_s. It should be noted, however, that a method based upon gas adsorption at the surface whose area is to be measured may not provide the right value to be inserted in Eq.(9). In fact, as reported[14], the specific surface area relevant in the wetting of particulates by aluminium could be much lower than that given by the BET technique.

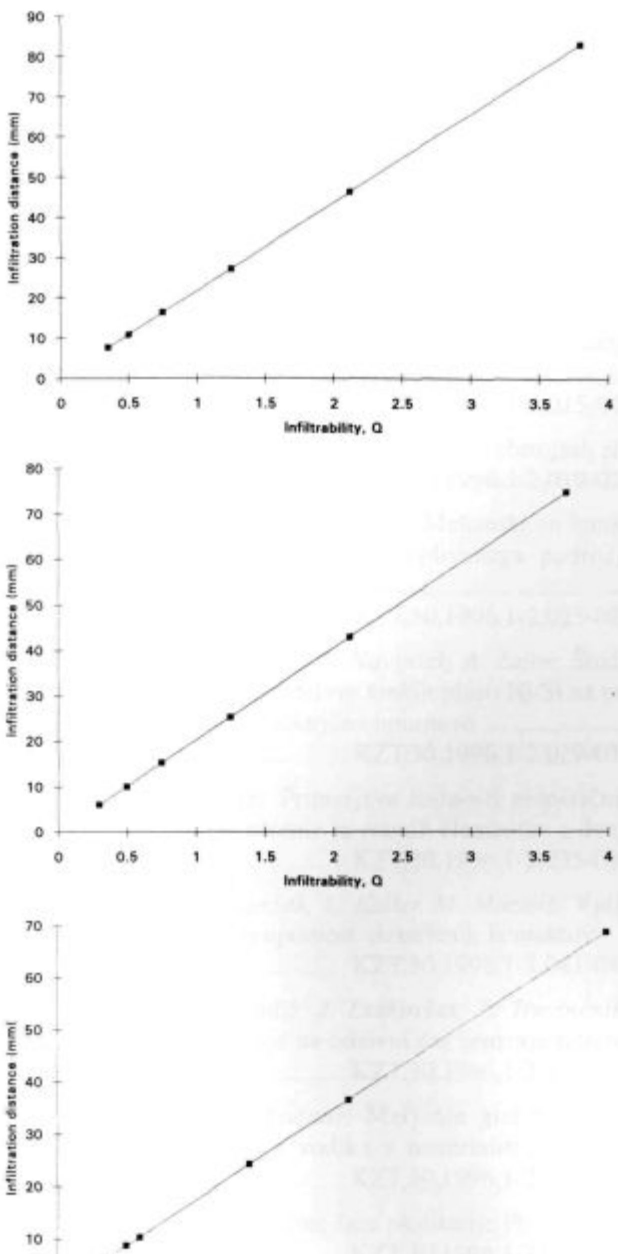

Figure 8: Dependence of infiltration distance on infiltrability of different porous preforms (Al-10Si-3Mg alloy, a 5 h soak at 1175 K a nitrogen atmosphere with 4 vol% Ar) for - a) SiC particle grade preform, b) SiC platelets grade preform, and c) SiC whisker grade preform

Slika 8: Odvisnost globine infiltracije od infiltrabilnosti poroznih predoblik, pridobljenih iz: a) SiC prahu, b) SiC ploščic in c) SiC whiskerjev (zlitina Al-10Si-3Mg, 5 h pri 1175 K, dušikova atmosfera s 4 vol% Ar)

5 Concluding remarks

A process for the production of porous SiC preforms consisting particles, platelets or whiskers is reported. It involves the vacuum casting of specialy prepared slip and sintering of green body to the porous specimen. Following this procedure, vacuum cast preforms in a variety of sizes, with high dimensional and compositional reproducibility, and with uniform characteristics were fabricated.

Porous preforms were sucessfully pressureless infiltrated using the Primex^{TM} method originaly developed by Lanxide, Inc.

The results presented in this article demonstrate that the combination of magnesium in the Al alloy, the nitrogeneous processing atmosphere (with at least 25 vol% N_2) and several porous preform characteristics (specifically the porosity and specific surface area) summarised in term preform infiltrability leads to the pressureless infiltration of molten aluminium alloy into ceramic filler.

The collected data have confirmed that no infiltration occured without the correct combination of above listed process variables. This means that the magnesium content in Al alloy and the content of nitrogen in processing atmosphere should be combined with correctly designed porous preform characteristics.

The results of present work demonstrate the infuence of preform porosity and its specific surface area on the infiltration length. The infiltration kinetics were shown to be strongly affected by preform infiltrability for otherwise constant process conditions. In addition to kinetics, it was found that experimental data fit well the proposed expression for the infiltration length as a function of preform infiltrability, work of adhesion, viscosity of the melt and processing time. Moreover, the experimental results demonstated that the suggested equation is operative for the different morphology of SiC particulate used in this work. However, the influence of preform surface composition, which should affectsthe work of adhesion, and the viscosity of the melt is matter of the further experimental efforts.

6 Acknowledgements

The porous ceramic preforms have been infiltrated using the laboratory feasibilities of the partners on Brite Euram project BE96-3925 (proposal). The authors also thank to Slovene Ministry of Science and Technology, Impol from Slovenska Bistrica and Nova Kreditna Banka Maribor for their financial support.

This research is the part of basic scientific project: "Preparation and Characterisation of Discontinuously Reinforced Al-SiC MMCs" fully financed by Slovene Ministry of Science and Technology.

7 References

[1] D. J. Lloyd, *Intern. Materials Reviews*, 39, 1994, 1-23

[2] T. S. Srivatsan, I. A. Ibrahim, F. A. Mohamed, and E. J. Lavernia, *J. Mater. Sci.*, 26, 1991, 5965-78

[3] A. Mortnesen and T. Wong, *Met. Trans. A*, 21A, 1990, 2257

[4] F. Folgar, *Ceram. Engng. Sci. Proc.*, 9, 1988, 579

[5] J. T. Burke, M. K. Aghajanian and M. A. Rocazella, *Proc. Int. SAMPE Symp.*, 34, 1989, 2440

[6] J. A. Cornie, A. Mortensen and M. C. Flemings, *Proc. of ICCM-VI* (ed. F. L. Mathews, et al.), 1987, 2.297-2.319

[7] S. Nagata, A. Kitahara, S. Akiyama, and H. Ueno, *Trans. AFS*, 93, 1985, 49-54

[8] S. Caron and J. Masounave: in *"Fabrication of particulates reinforced metal composites"*, (ed. J. Masounave and F. G. Hamel), Materials Park, OH, ASM International, 1990, 107-113

[9] K. G. Davis and J. G. Magny., *Trans. AFS.*, 89, 1981, 385-402

[10] A. W. Urquhart, *Mater. Sci. Eng.*, A144, 1991, 75

[11] M. K. Aghajanian, M. A. Rocazella, J. T. Burke and S. D. Keck, *J. Mater. Sci.*, 26, 1991, 447-454

[12] US Pat. 4 828 008

[13] J. W. McCoy, C. Jones and F. E. Warner, *Sampe Q.*, 19, 1988, 2, 37

[14] R. Sharma, *Colloids Surf.*, 16, 1985, 87

[15] L. R. White, *J. Colloid Interface Sci.*, 90, 1982, 536

[16] J. Bear: in *Dinamics of Fluids in Porous Media*, Dover Publication, New York, NY, 1988

LETNO KAZALO - INDEX
KOVINE ZLITINE TEHNOLOGIJE, 30, 1996, 1-6

Kronološko kazalo

Avtorsko kazalo